Measuring luminosity and the $t\bar{t}Z$ production cross section with the CMS experiment

Dissertation
zur Erlangung des Doktorgrades
an der Fakultät für Mathematik, Informatik und Naturwissenschaften
Fachbereich Physik
der Universität Hamburg

vorgelegt von

Joscha Knolle

Hamburg

2020

Gutachter der Dissertation:	PD Dr. Andreas Meyer Prof. Dr. Johannes Haller Prof. Dr. Jonathan Butterworth
Zusammensetzung der Prüfungskommission:	Prof. Dr. Elisabetta Gallo Prof. Dr. Johannes Haller PD Dr. Andreas Meyer Dr. Kai Schmidt-Hoberg Prof. Dr. Günter Sigl / Prof. Dr. Sven-Olaf Moch
Vorsitzender der Prüfungskommission:	Prof. Dr. Günter Sigl / Prof. Dr. Sven-Olaf Moch
Datum der Disputation:	25.06.2020
Vorsitzender des Fach-Promotionsausschusses Physik:	Prof. Dr. Günter Sigl
Leiter des Fachbereichs Physik:	Prof. Dr. Wolfgang Hansen
Dekan der Fakultät für Mathematik, Informatik und Naturwissenschaften:	Prof. Dr. Heinrich Graener

in memory of

Rolf Knolle

(1958–2018)

“Gone don’t always mean that you disappear,
’cause inside all of us you’re still here.”
— Lukas Graham

Abstract

Measurements of the luminosity and of top quark pair production in association with a Z boson ($t\bar{t}Z$) in proton-proton collisions with the CMS experiment at the LHC are presented.

The luminosity measurement of the CMS experiment is calibrated with the Van der Meer (VdM) method, based on data collected during beam separation scans. A calibration of the length scale is performed using data from constant-separation scans. The bias of the VdM method due to the assumption of factorisable proton densities of the beams is estimated with an improved method using the transverse densities as determined from beam-imaging scan data. The performance is evaluated with dedicated simulation studies. Both studies lead to a significant reduction of the systematic uncertainty for the measurement of the integrated luminosity.

Measurements of $t\bar{t}Z$ production in proton-proton collisions at a centre-of-mass energy of 13 TeV are performed using events with three charged leptons where the Z boson is identified in its decay to two oppositely charged leptons. The first differential $t\bar{t}Z$ production cross section measurement as a function of kinematic properties of the Z boson is presented, based on a dataset corresponding to an integrated luminosity of $77.5\,\mathrm{fb}^{-1}$ collected in 2016 & 2017. An extended differential measurement as a function of top quark observables is presented using the full Run 2 dataset, corresponding to an integrated luminosity of $137\,\mathrm{fb}^{-1}$. It includes a kinematic reconstruction of the $t\bar{t}$ system and allows to probe the QCD production mechanism. Within current experimental uncertainties, the measured differential cross sections are found to be in good agreement with standard model predictions.

Zusammenfassung

Messungen der Luminosität und der Top-Quark-Paarproduktion in Assoziation mit einem Z-Boson ($t\bar{t}Z$) in Proton-Proton-Kollisionen mit dem CMS-Experiment am LHC werden gezeigt.

Die Messung der Luminosität des CMS-Experiments wird mit der Van-der-Meer-Methode (VdM-Methode) kalibriert, die auf Daten von Strahltrennungsscans beruht. Eine Bestimmung der Längenskala wird mit den Daten von Scans konstanter Trennung durchgeführt. Die Verzerrung der VdM-Methode aufgrund der Annahme faktorisierbarer Protonendichten für die Strahlen wird mit einer verbesserten Methode ermittelt, die die aus den Daten von Beam-Imaging-Scans rekonstruierten transversalen Dichten benutzt. Die Ergebnisse werden mit umfassenden Simulationsstudien evaluiert. Beide Studien führen zu einer signifikanten Verbesserung der systematischen Unsicherheit der Messung der integrierten Luminosität.

Messungen von $t\bar{t}Z$-Produktion in Proton-Proton-Kollisionen bei einer Schwerpunktsenergie von 13 TeV werden mit Ereignissen durchgeführt, die drei geladene Leptonen beinhalten, wobei das Z-Boson aus seinem Zerfall zu zwei gegensätzlich geladenen Leptonen identifiziert wird. Die erste differenzielle Wirkungsquerschnittsmessung von $t\bar{t}Z$-Produktion als Funktion kinematischer Eigenschaften des Z-Bosons wird gezeigt, basierend auf einem Datensatz, der einer integrierten Luminosität von 77,5 fb^{-1} entspricht und in 2016 & 2017 aufgezeichnet wurde. Eine erweiterte differenzielle Messung als Funktion von Top-Quark-Observablen mit dem vollständigen Run-2-Datensatz, der einer integrierten Luminosität von 137 fb^{-1} entspricht, wird gezeigt. Die Messung beinhaltet eine kinematische Rekonstruktion des $t\bar{t}$-Systems und erlaubt die Untersuchung des QCD-Produktionsmechanismus. Innterhalb der gegenwärtigen experimentellen Unsicherheiten stimmen die gemessenen differenziellen Wirkungsquerschnitte gut mit Vorhersagen des Standardmodells überein.

Contents

Introduction

"Pulchra sunt, quae videntur,
pulchriora, quae sciuntur,
longe pulcherrima, quae ignorantur."
— Nicolaus Stenonis, 1673 [1]

"Fair are the things seen,
fairer those understood,
fairest by far those not yet grasped."
— Nicolas Steno, 1673, own translation

It is the human nature to strive for an understanding of the basic principles that govern our world. In the opening remarks to an anatomical demonstration in Copenhagen in 1673, the anatomist and geologist Nicolas Steno discussed his motivation for research as a quest for knowledge. He addresses the need to be sceptic about prior beliefs to avoid a bias in the interpretation of new observations. Steno, who later became a Catholic bishop for Northern Germany, ultimately understood the expansion of knowledge as a path towards God.

Almost 350 years later, our understanding of the world we live in has evolved dramatically. Still, science continues to be driven by an urge for an ever deeper understanding of the fundamental laws of nature. High energy physics is one of the fields that reach out into the unknown, as it attempts to describe the elementary particles and the forces that govern the universe and its origin. With the CERN Large Hadron Collider (LHC), the world's largest particle accelerator ever built, particle physics has a powerful tool at hand to probe our understanding of fundamental interactions and to look for new particles, to further advance our knowledge.

The standard model of particle physics (SM) is a very successful theory of elementary particles and their interactions. With the discovery of the Higgs boson in 2012 [2, 3], all elementary particles predicted by the SM have been discovered. Measurements of particle physics processes confirm SM predictions with unprecedented precision. So far, no signs of new elementary particles beyond the SM have been found. But the more the experimental results confirm the SM, the stronger the urge grows to go beyond the known and to further test the limits of the SM.

The topics of my thesis are the luminosity measurement and the measurement of top quark pair production in association with a Z boson ($\mathrm{t\bar{t}Z}$) in proton-proton collisions with the CMS experiment at the LHC.

The luminosity of a collider is a property which quantifies the rate of collisions created at the experiment. A precise measurement of the luminosity is a prerequisite for precise cross section measurements. At the CMS experiment, the luminosity measurement is calibrated with the Van der Meer (VdM) method, which is based on beam separation scans called VdM scans. To improve the precision of the measured luminosity, I studied the experimental effects that impact the results of the VdM method the most: The length scale calibration uses the precision of the track and vertex reconstruction of the CMS silicon tracker to improve the precision on the beam positions during the VdM scans. The factorisation bias of the VdM method arises from the assumption of factorisable transverse profiles of the beams. To correct for this bias, the transverse beam proton densities are determined from vertices reconstructed with the CMS experiment during beam-imaging scans. I improved the beam-imaging method and complemented it with dedicated simulation studies to assess the precision of the factorisation bias estimation.

Cross section measurements of $\mathrm{t\bar{t}Z}$ production are the first direct probes of the top quark–Z boson coupling, and allow to constrain deviations from the SM prediction for this coupling. I have contributed to the inclusive and differential $\mathrm{t\bar{t}Z}$ production cross section measurement using proton-proton collisions at a centre-of-mass energy of $\sqrt{s} = 13\,\mathrm{TeV}$ corresponding to an integrated luminosity of $77.5\,\mathrm{fb}^{-1}$ recorded in 2016 & 2017 with the CMS experiment [E]. The differential cross section is presented as a function of the Z boson transverse momentum, and of the angle between the Z boson and its decay lepton, boosted to the Z boson rest frame.

Furthermore, I extended the differential $\mathrm{t\bar{t}Z}$ production cross section measurement to include a kinematic reconstruction of the $\mathrm{t\bar{t}}$ system. Based on the full Run 2 dataset corresponding to an integrated luminosity of $137\,\mathrm{fb}^{-1}$, the differential cross section is presented as a function of the invariant masses of the $\mathrm{t\bar{t}Z}$ and the $\mathrm{t\bar{t}}$ system, of the top quark transverse momentum, and of the rapidity and azimuthal angle differences both between the top quark and the top antiquark, and between the top quark and the Z boson.

The thesis consists of three parts: In Part 1, an overview of the SM (Chapter I) and of the CMS experiment (Chapter II) is given. The luminosity measurement of the CMS experiment is described in Part 2, with a discussion of the concept of luminosity and its measurement (Chapter III), and my results for the length scale calibration (Chapter IV) and the factorisation bias estimation (Chapter V). The cross section measurements of $t\bar{t}Z$ production are presented in Part 3, with an introduction to top quark physics (Chapter VI), an overview of the inclusive cross section measurement (Chapter VII), and the results of my differential cross section measurements using Z boson (Chapter VIII) and top quark observables (Chapter IX).

My contributions to the calibration of the luminosity measurement have been included in preliminary results of the CMS experiment [A–D, F].

The $t\bar{t}Z$ production cross section measurement using 2016 & 2017 data has been performed in close collaboration with research groups in Ghent and Vienna. The results have been published by the CMS experiment [E], and are also documented in the theses of Illia Khvastunov [4] and Daniel Spitzbart [5]. My specific contribution to the publication was the first measurement of the differential cross section.

Part 1.

Fundamentals of particle physics

Figure 1.1

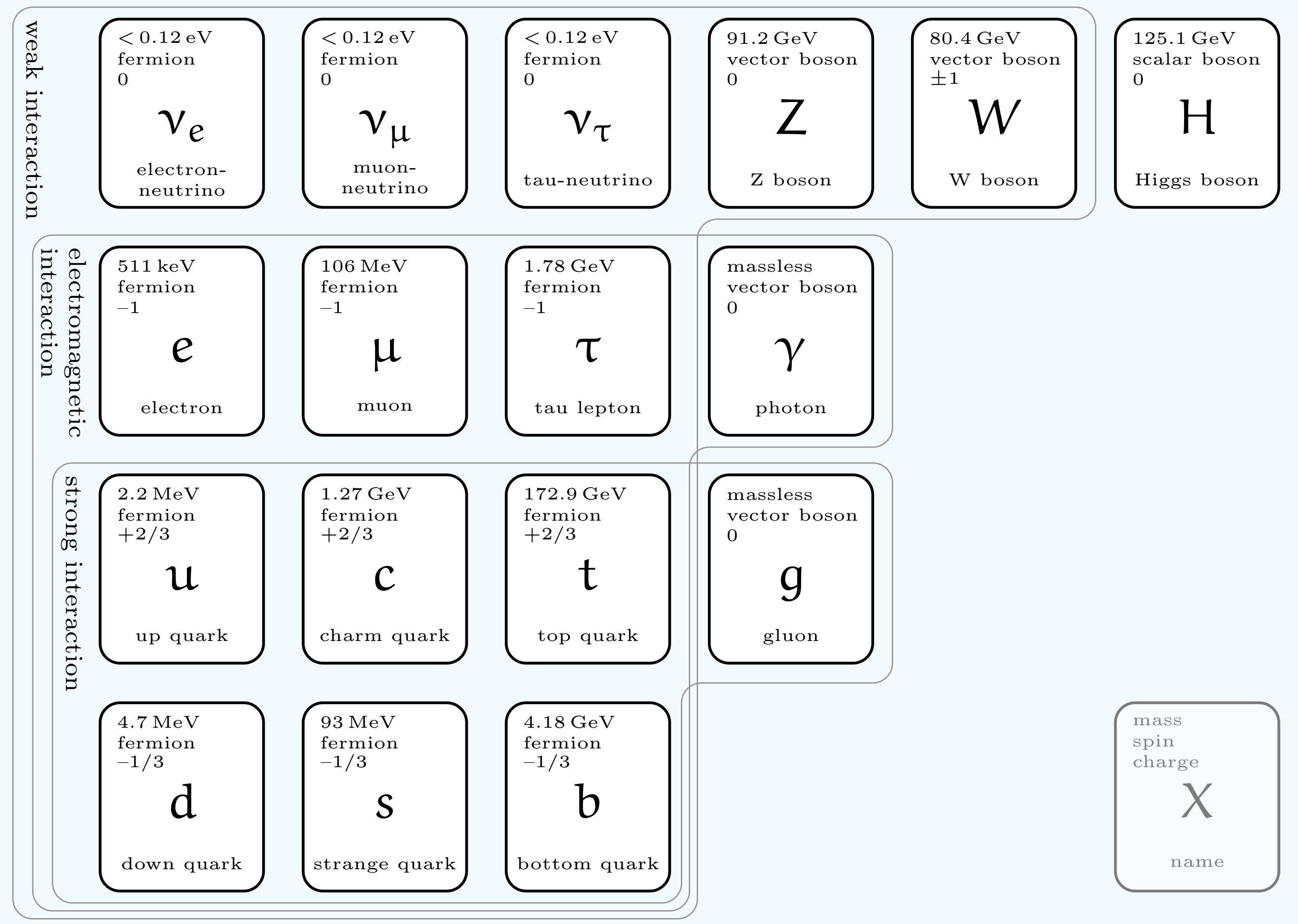

Elementary particles described by the standard model of particle physics, with measured mass [6, 7], spin denoted as scalar boson (spin 0), fermion (spin 1/2), or vector boson (spin 1), and electric charge.

I. Standard model of particle physics

The standard model of particle physics (SM), developed since the 1960s [8–15], is a quantum field theory (QFT) that describes the dynamics and interactions of elementary particles. The fundamental forces of the SM are the strong, the electromagnetic, and the weak interactions. The elementary particles described by the SM are divided into fermions, vector bosons, and scalar bosons. Fermions have spin $1/2$ and are the constituents of matter. The fermions are the quarks and the leptons, where the leptons are divided into charged leptons and neutrinos. Throughout this thesis, the term “lepton” will be used exclusively to refer to charged leptons. Vector bosons have spin 1 and are the mediators of the fundamental forces. The four types of vector bosons are the gluons (the mediators of the strong force), the photon (the mediator of the electromagnetic force), and the $W^{\pm}$ and Z bosons (the mediators of the weak force). The only scalar boson with spin 0 is the Higgs boson, related to the Brout-Englert-Higgs (BEH) mechanism. The particle content of the SM is summarised in Figure 1.1.

In this chapter, a brief summary of the SM with a focus on aspects of relevance to this thesis is given. More detailed introductions can be found e. g. in References [16–20].

1.1. Strong interaction

Quantum chromodynamics (QCD) is the QFT that describes the strong interaction between the particles that carry a colour charge, which are the six quarks q and the eight gluons g. The colour charge of the quarks has three possible values, and correspondingly the antiquarks $\bar{q}$ carry one of three “anti-colour” charges. The six quark flavours are:

- up u, charm c, and top t (“up-type” quarks),
- down d, strange s, and bottom b (“down-type” quarks).

Up-type quarks have an electric charge of $+2/3$, and down-type quarks of $-1/3$. The massless gluons form a colour octet and carry both a colour and an anti-colour charge. The strong interaction is described by quark–gluon couplings and gluon self-couplings, as depicted in Figure 1.2.

Figure 1.2

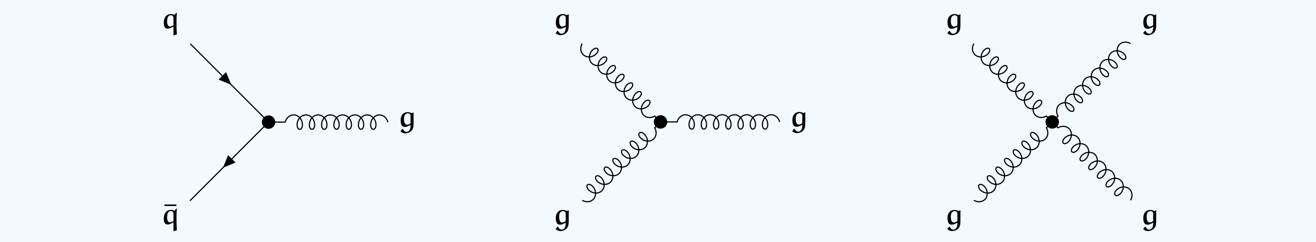

Interaction vertices of quantum chromodynamics. All Feynman diagrams in this thesis were created with the TikZ-Feynman software [21].

Figure 1.3

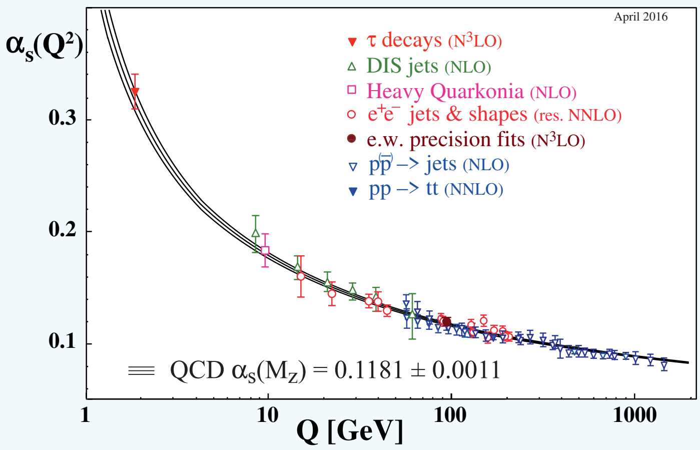

Summary of measurements of α_s at different energy scales Q, taken from Ref. [6].

Measurements of the interaction strength of the strong interaction α_s at different energy scales are summarised in Figure 1.3. The interaction strength decreases with larger momentum transfer. This behaviour is called the "running" of α_s and is described by a renormalisation group equation (RGE). The QCD scale $\Lambda_{\mathrm{QCD}} \approx 200\,\mathrm{GeV}$ [19] describes the energy scale at which the RGE formally diverges. Because of the strong value of α_s at energies below Λ_{QCD}, coloured particles cannot exist as free particles, and thus quarks are confined to colour-neutral bound states called hadrons ("confinement"). Conversely, due to the small value of α_s at large energies, quarks in high energy interactions can be described as free particles ("asymptotic freedom"), and matrix element calculations for such interactions can be approximated with a perturbative expansion in terms of α_s.

The proton p is a bound state of two up quarks and one down quark, called "valence quarks". Each of its quarks has a different colour such that the proton is colour neutral. It is a stable particle with an electric charge of +1. In addition to its valence quarks, the proton consists of a "sea" of particles, gluons and quarks, dynamically generated by the strong interaction between the valence quarks. Jointly, valence quarks and sea particles are referred to as the "partons" of the proton. The cross section σ of a proton-proton scattering process $\mathrm{pp} \to \mathrm{X}$ at a centre-of-mass energy $\sqrt{s}$ is calculated using a factorisation into soft and hard interactions:

$$\sigma(\mathrm{pp} \to \mathrm{X})(s) = \sum_{\alpha,\beta} \int_0^1 \mathrm{d}x_1 \int_0^1 \mathrm{d}x_2\, f_\alpha(x_1, \mu_\mathrm{F}) f_\beta(x_2, \mu_\mathrm{F}) \cdot \hat{\sigma}(\alpha\beta \to \mathrm{X})\big(x_1 x_2 s, \mu_\mathrm{F}, \mu_\mathrm{R}\big). \tag{1.1}$$

Figure 1.4

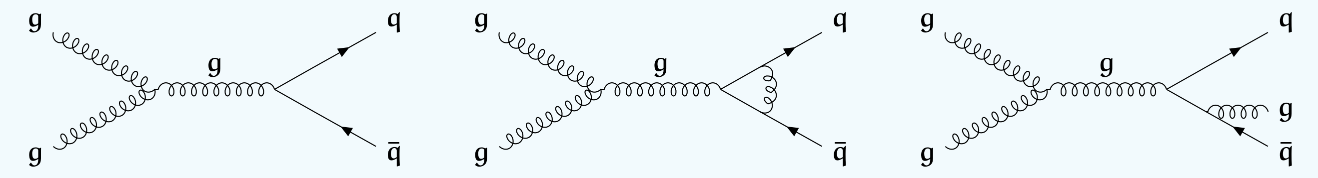

Example contributions to $q\bar{q}$ production at LO (left), and at NLO with a loop correction (centre) and with soft gluon emission (right).

The hard interaction is described by the partonic cross section $\hat{\sigma}$ between two specific partons α, β which carry fractions x_1, x_2 of the total proton momentum. The calculation is evaluated for the factorisation scale μ_F and the renormalisation scale μ_R that serve as cut-offs to avoid infrared and ultraviolet divergences, respectively. The parton distribution functions (PDFs) describe the soft interaction inside the protons, including infrared divergencies in the initial state up to μ_F, where $f_\alpha(x, \mu_\mathrm{F})$ gives the probability to find the parton α with the momentum fraction x inside a proton.

Figure 1.5

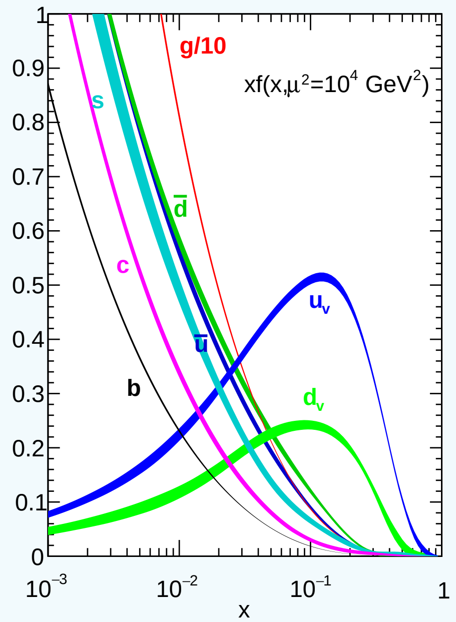

Proton PDFs evaluated at 100 GeV, taken from Ref. [22].

The partonic cross section $\hat{\sigma}$ is evaluated in perturbative QCD. A calculation using only contributions with the lowest order in α_s is of leading-order (LO) accuracy. Similarly, next-to-leading order (NLO) accuracy denotes calculations that additionally include contributions with the second lowest order in α_s, e. g. additional internal loops or the emission of additional soft particles which cannot be measured independently in an experiment. Example diagrams for LO and NLO contributions to quark pair production ($q\bar{q}$) are shown in Figure 1.4.

The proton PDFs cannot be calculated from a perturbative QCD calculation and are extracted from experimental measurements instead. For the extraction of proton PDFs, especially measurements of deep-inelastic scattering (DIS) in electron-proton collisions performed at the DESY Hadron-Electron Ring Accelerator (HERA) [23] as well as fixed-target DIS experiments are used. As an example, the NNPDF3.1 proton PDFs at next-to-next-to-leading order (NNLO) accuracy [22] are shown in Figure 1.5 for a factorisation scale of 100 GeV. It is found that the gluon PDF has by far the largest density, and that the probability for a gluon to be found at a particular value of relative momentum x rises steeply towards lower values of x. It is for this reason that proton-proton collisions at the CERN Large Hadron Collider (LHC) are predominantly gluon-gluon interactions.

When quarks and gluons are produced in high-energy interactions, they create a shower of additional quarks and gluons via the strong interaction. When the energy of these particles falls below a certain scale, they will combine to form colour-neutral hadrons (“hadronisation”), resulting in a collimated stream of hadrons called “jet”. The jet approximately inherits energy and momentum from the initial parton. Jets are defined by a jet algorithm which is used in cross section calculations to define the final state of a process, and in measurements to group the measured hadrons. Here, the anti-k_T jet clustering algorithm [24, 25] is applied which iteratively combines the closest pair of objects to a jet with a fixed maximum jet cone size, starting from the hadrons with the largest momentum. The anti-k_T algorithm is collinear- and infrared-safe, i. e. the splitting of particles into two or more particles with the same total momentum or the addition of arbitrarily soft particles, both of which are regular features of hadronisation, do not change the result of the clustering.

1.2. Electroweak interaction

Quantum electrodynamics (QED) is the QFT that describes the electromagnetic interaction between the electrically charged fermions—quarks and leptons—and the photon. The three leptons ℓ^- are the electron e^-, the muon μ^-, and the tau lepton τ^-, with an electric charge of -1 and no colour charge, and the corresponding antileptons ℓ^+ have an electric charge of $+1$. The massless photon has no electric charge, and thus the electromagnetic interaction is described by fermion–photon interactions only, as depicted in Figure 1.6.

Figure 1.6

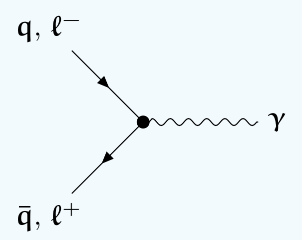

Interaction vertex of quantum electrodynamics.

The electromagnetic interaction strength α_em slowly increases with smaller momentum transfer or larger distance, with $\alpha_\mathrm{em} \approx 1/137$ at zero momentum transfer and $\alpha_\mathrm{em} \approx 1/129$ at the mass scale of the Z boson [26]. Since α_em is significantly smaller than unity, cross section calculations for QED processes can be performed using perturbative expansions.

The weak interaction is the only interaction that involves all fermions—quarks, leptons, and neutrinos—, and is mediated by the $\mathrm{W}^\pm$ and Z bosons. Neutrinos have neither an electric charge nor a colour charge, and there is one neutrino ν_ℓ for each lepton flavour ℓ. In the SM, the neutrinos are treated as massless particles, although the observation of neutrino oscillations requires neutrinos with a small but nonzero mass [27, 28]. The

Figure 1.7

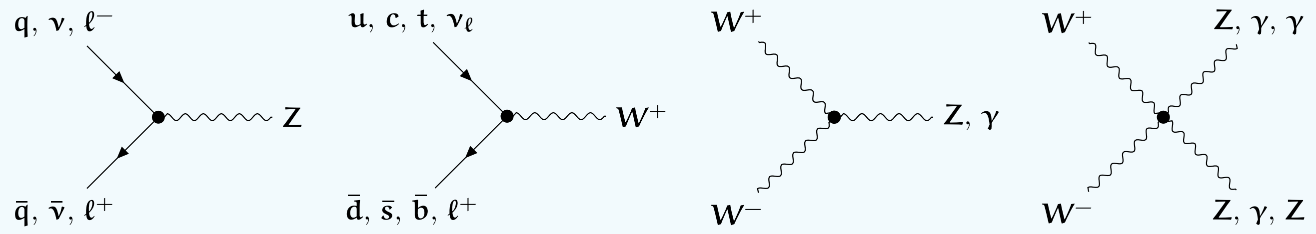

Interaction vertices of the weak interaction.

$W^{\pm}$ and Z bosons have a mass of 80.4 GeV and 91.2 GeV [6], and the $W^{\pm}$ bosons carry an electric charge of ± 1.

Due to the mass of the mediators, the weak interaction is a short-range force at energy scales smaller than the mediator masses and has a much smaller interaction strength compared to the electromagnetic or strong interaction. The Z boson mediates the neutral weak interaction and couples to fermions and antifermions of the same flavour. The $W^{\pm}$ bosons, or short W bosons, mediate the charged weak interaction which is the only interaction in the SM that can change the flavour of particles. They couple to a neutrino and a lepton, or to an up-type and a down-type quark. In addition, W and Z bosons couple to each other, and W bosons, due to their electric charge, also couple to photons. All interaction vertices are summarised in Figure 1.7.

The couplings of the W bosons define the three "generations" of fermions, which are:

1. the electron-neutrino, the electron, the up quark, the down quark;
2. the muon-neutrino, the muon, the charm quark, the strange quark;
3. the tau-neutrino, the tau lepton, the top quark, the bottom quark.

The generations are ordered by mass, i. e. the leptons and quarks of the second generation have a higher (lower) mass than the leptons and quarks of the first (third) generation, respectively. The W bosons couple only to leptons and neutrinos of the same generation, and preferably to quarks of the same generation. Flavour mixing between quarks in charged weak interactions is described by the Cabibbo-Kobayashi-Maskawa (CKM) matrix [29–31], whose elements $V_{\alpha\beta}$ are multiplied onto the interaction strength, such that $|V_{\alpha\beta}|^2$ quantifies the transition probability between the up-type flavour α and the down-type flavour β. From a global fit to experimental results sensitive to the CKM matrix elements, the absolute values of the nine elements are found to be:

$$V_{\mathrm{CKM}} = \begin{pmatrix} |V_{\mathrm{ud}}| & |V_{\mathrm{us}}| & |V_{\mathrm{ub}}| \\ |V_{\mathrm{cd}}| & |V_{\mathrm{cs}}| & |V_{\mathrm{cb}}| \\ |V_{\mathrm{td}}| & |V_{\mathrm{ts}}| & |V_{\mathrm{tb}}| \end{pmatrix} = \begin{pmatrix} 0.974 & 0.225 & 0.004 \\ 0.224 & 0.974 & 0.042 \\ 0.009 & 0.041 & 0.999 \end{pmatrix} \quad [6]. \tag{1.2}$$

Figure 1.8

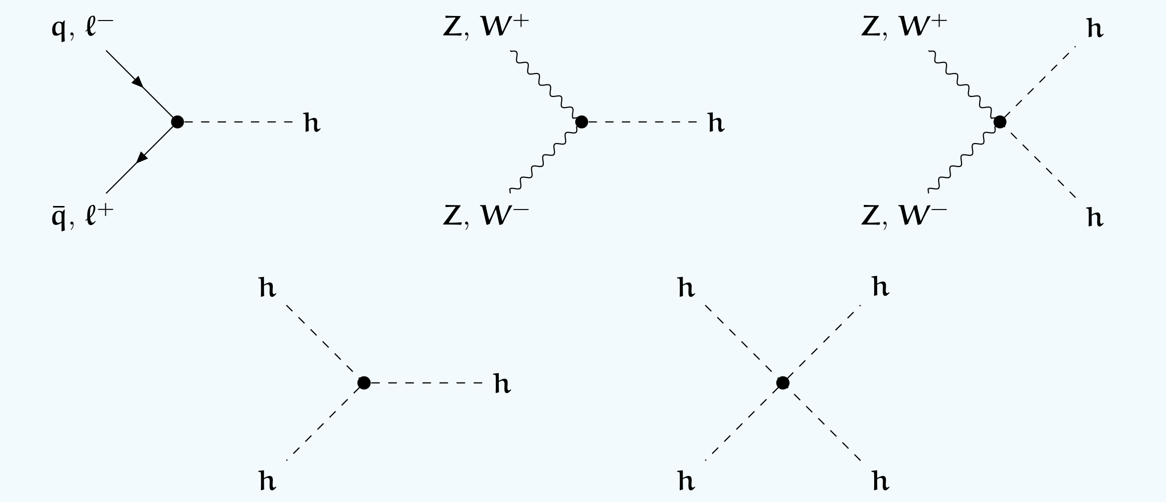

Interaction vertices of the Higgs boson.

Thus, couplings between quarks of different generations and a W boson are highly suppressed, especially for couplings that involve a third-generation quark. Since the charged weak interaction is the only possible interaction that allows elementary particles to decay to lighter particles, the CKM matrix has important consequences for the decays of the third generation fermions. The top quark decays almost exclusively to a W boson and a bottom quark, whereas the decay of the bottom quark to lighter quarks is suppressed resulting in a very long lifetime of hadrons that contain bottom quarks of the order of 1 ps [6].

The electromagnetic and weak interactions are unified in the electroweak interaction at the mass scale of the W and Z bosons. This is facilitated by the Brout-Englert-Higgs (BEH) mechanism [10–13] which introduces a Higgs field that interacts with the electroweak vector fields and with the fermions. Due to the form of the self-interactions of the Higgs field, it has a nonzero vacuum expectation value such that a spontaneous symmetry breaking occurs at the energy scale of electroweak symmetry breaking. Due to the interactions of the Higgs field and the electroweak vector fields, the W and Z bosons acquire a mass which explains the huge difference in the electromagnetic and electroweak interaction strength. The interactions of the Higgs field and the fermions are called Yukawa couplings and give rise to mass terms proportional to the Yukawa coupling constant y_f specific to each fermion. A third consequence of the electroweak symmetry breaking is the Higgs boson, a scalar boson with no electric charge and no colour charge which couples to all massive particles, i. e. the W and Z bosons, the leptons, and the quarks, as depicted in Figure 1.8, with interaction strengths proportional to the masses of the particles.

1.3. Physics beyond the standard model

The standard model of particle physics has been very successful in the prediction and description of particle physics phenomena. Especially at high energy collider experiments, the SM provides a robust theory that is continuously probed at increasing precision, with no significant deviations found so far. Outside of collider experiments, however, clear evidence exists of phenomena that cannot be described by the SM. Thus, a model of particle physics beyond the SM, or “new physics”, is required.

Neutrino oscillations, i. e. the spontaneous conversion of neutrino flavours into each other, have been observed in dedicated neutrino observatories [27, 28]. A theoretical description of neutrino oscillations requires neutrinos to have a nonzero mass which contradicts the SM expectation [17]. Current cosmological observations constrain the neutrino masses to be very small, $\sum m_\nu < 0.12\,\mathrm{eV}$ [7]. An extension of the SM is required that includes the neutrino masses. The huge mass differences observed for the elementary particles, with the top quark mass of $m_\mathrm{t} = 172.9\,\mathrm{GeV}$ [6] being at least twelve orders of magnitude higher than the neutrino masses, raise additional questions about the underlying fundamental reason for these very different mass scales [32].

Astrophysical observations rooting back to the 1930s [33] conclusively show that visible matter only accounts for a fraction of the matter content of the universe. Most recent cosmological measurements [7] estimate the energy content of the universe to be composed of about 5 % of ordinary matter, 26 % of dark matter, and 69 % of dark energy. Dark matter accounts for gravitationally interacting matter required to explain observations at galactic scales, and several extensions of the SM provide new elementary particles that could explain dark matter [34]. Dark energy is required to explain the accelerating expansion of the universe and is not easily accounted for by particle physics models. Another astrophysical observation is the matter-antimatter asymmetry, i. e. the absence of large amounts of antimatter in the universe, whereas equal production of matter and antimatter is expected from the SM [35].

After the successful description of the unification of the electromagnetic and weak interactions, the possibility of a “grand unified theory” (GUT) is explored which would provide a common description of the strong and the electroweak interactions. From an extrapolation of the energy evolution of the interaction strengths, grand unification would be expected to appear at an energy scale of $\Lambda_\mathrm{GUT} \approx 10^{16}\,\mathrm{GeV}$. Going further, the unification with gravity, the fourth fundamental force, could lead to a “theory of everything”. As the gravitational interaction strength is much smaller than those of the other interactions, the impact of gravity on particle physics interactions would only be noticeable at energies above the Planck scale of $\Lambda_{\mathrm{Pl}} \approx 10^{19}\,\mathrm{GeV}$ [17]. Attempts to formulate a QFT of gravity are known as quantum gravity [36].

Several new physics models, i. e. extensions of the SM that address one or more of the open questions, have been proposed. Notable examples are supersymmetry, which introduces a new symmetry that relates fermions and bosons [37], and extra dimensions, which extend the four spacetime dimensions with additional dimensions of finite size or warped shape [38]. Many of these models predict new elementary particles to appear at energy scales close to the collision energy of the LHC. Due to the absence of experimental evidence for new physics at the LHC, the search for deviations from SM expectations in precision measurements of SM observables gains importance in the quest for new physics. An important approach is the SM effective field theory (SMEFT) [39–41] which extends the SM with all possible higher order couplings between the SM fields. Such couplings can e. g. arise as the effective description of virtual particles with a mass much higher than the energy reach of the LHC. An interpretation of SM measurements then allows to constrain possible contributions from new physics in a model-independent way.

II. The CMS experiment at the LHC

1.4. The Large Hadron Collider

Figure 1.9

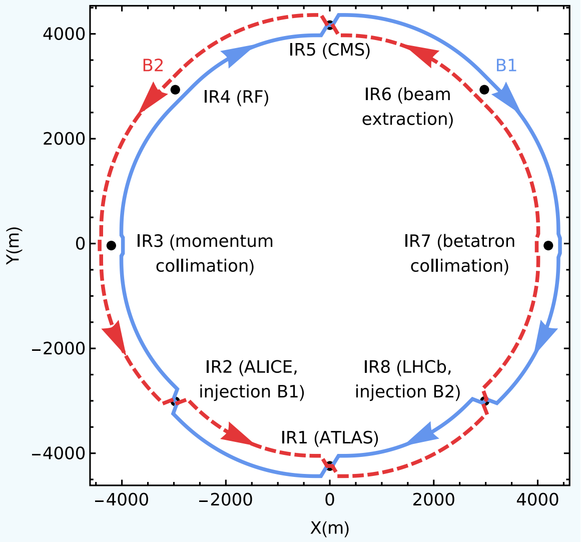

Schematic view of the LHC and its interaction regions, with exaggerated ring separation, taken from Ref. [42].

The Large Hadron Collider (LHC) [43] is a circular hadron accelerator and collider with a circumference of 26.7 km, located at CERN in Switzerland and France. It is designed to accelerate and collide proton beams at a centre-of-mass energy of $\sqrt{s} = 14\,\text{TeV}$, as well as to be operated with heavy-ion beams. The two beams are accelerated in two separate rings, realised with a twin-bore magnet design, and crossed at four interaction points (IPs) located within the interaction regions (IRs) defined in Figure 1.9.

Four main experiments are performed at the IPs: The ATLAS experiment [44] at IP1 and the CMS experiment [45] at IP5, i. e. at opposite sites of the LHC ring, are general-purpose detectors optimised for data-taking at the highest achievable proton-proton luminosities as well as for heavy-ion collisions. Lower collision rates are provided to the LHCb experiment [46] at IP8, designed primarily for measurements related to the physics of B hadrons, and the ALICE experiment [47] at IP2, which targets measurements related to heavy-ion physics.

For proton-proton (pp) collisions, two bunched proton beams are injected into the LHC at an energy of 450 GeV, accelerated to the collision energy, subsequently crossed for many hours to deliver collisions to the experiments, and finally dumped. One such “fill”, from injection to beam dump, defines the smallest unit of data-taking with a constant beam setup. At 25 ns bunch spacing, the LHC orbit has up to 3564 possible bunch positions per beam, of which up to 2808 positions are filled during injection. A bunch crossing number (BCID) between 0 and 3563 is assigned to each crossing of two bunches at the interaction point. Due to the layout of the interaction points, the same bunch pairs collide at the interaction points of the ATLAS and CMS experiments.

At the LHC, data-taking periods alternate with periods during which the accelerator and the experiments are shut down, providing time for maintenance and upgrades of the machines. The LHC started operations with several data-taking periods from 2009 to 2013 ("Run 1"), including pp collisions at $\sqrt{s} = 7$ and $8\,\text{TeV}$. After a shutdown of 2.5 years, LHC operations commenced in 2015 with pp collisions at $\sqrt{s} = 13\,\text{TeV}$. The data-taking periods between 2015 and the shutdown at the end of 2018 ("Run 2") include pp collisions as well as a heavy-ion collision programme: collisions of lead ions with lead ions (PbPb) and with protons (pPb and Pbp) at different energies, as well as "reference" proton-proton collisions at the same per-nucleon collision energy $\sqrt{s_{\text{NN}}}$, and one pilot fill with collisions of Xenon ions [48]. After the current shutdown, four years of data-taking between 2021 and 2024 ("Run 3") are planned, possibly reaching the design collision energy of 14 TeV in pp collisions. Beyond 2024, a shutdown with major upgrades of both accelerator and experiments to the High-Luminosity LHC (HL-LHC) is foreseen [49, 50].

1.5. The Compact Muon Solenoid

The Compact Muon Solenoid (CMS) experiment [45, 52] is designed to measure all particles originating from collisions in the interaction region over the full solid angle. To this end, it employs a cylindrical layout with a central "barrel" part and two "endcap" parts on both sides. The detector consists of a sequence of subsystems arranged in layers of increasing distance to the nominal interaction points. The subsystems are, from inside out, a silicon tracker, an electromagnetic calorimeter (ECAL), a hadron calorimeter (HCAL), a superconducting solenoid, and muon systems. The general structure is depicted in Figure 1.10.

A right-handed coordinate system of the CMS detector is defined with respect to the nominal interaction point such that x points radially inward with respect to the LHC, y vertically upward, and z in the flight direction of the counter-clockwise moving beam. The azimuthal angle ϕ is defined in the (x, y) plane, and the polar angle θ between this plane and the z axis. For a particle with energy E and momentum $\vec{p}$, rapidity y and pseudorapidity η are defined as:

$$y = \frac{1}{2} \ln \frac{E + p_z}{E - p_z} \approx \eta = \frac{1}{2} \ln \frac{|\vec{p}| + p_z}{|\vec{p}| - p_z} = -\ln \tan \left(\frac{\theta}{2} \right). \tag{1.3}$$

Figure 1.10

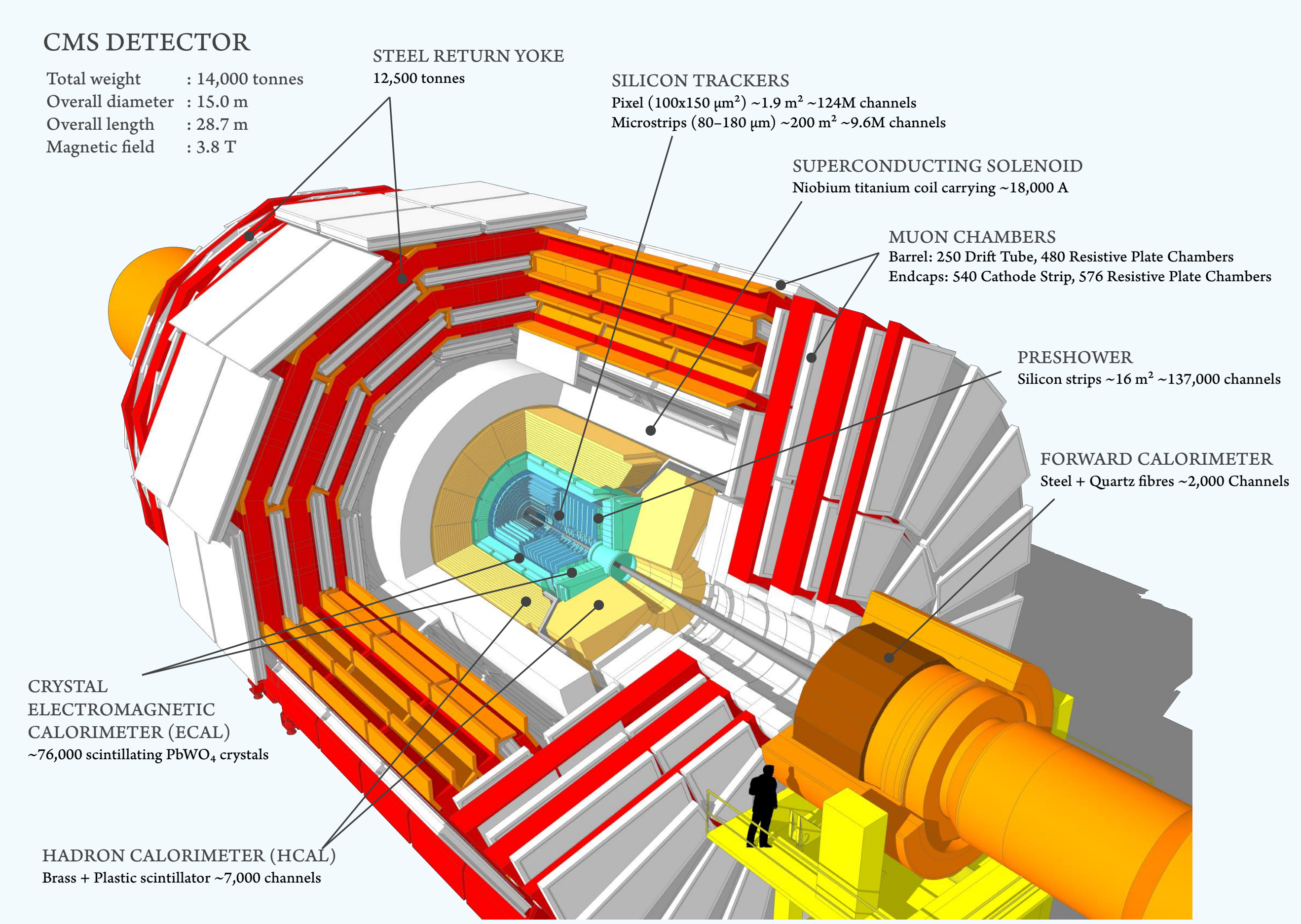

Schematic view of the CMS detector with the upgraded pixel detector, taken from Ref. [51].

The approximate equality $y \approx \eta$ is exact for massless particles. Since the longitudinal momenta of the colliding partons are unknown for individual collisions, rapidity is a useful quantity as rapidity intervals Δy are invariant under Lorentz boosts along the beam direction. "Transverse" as in transverse energy E_{T} and transverse momentum p_{T} always refers to the plane transverse to the beam direction, i. e. to the (x, y) plane.

The basic particles that can be measured with the CMS detector are electrons and muons (including their antiparticles), photons, and neutral and charged hadrons. Each subdetector provides measurements of different properties of specific particles, and the combination of the measurements allows to identify the particle type. Starting from the interaction region, particles first reach the tracker in which the trajectories of charged particles are measured. Due to the encompassing magnetic field, the trajectories are bent and thus their reconstruction allows to measure the electric charges and momenta of the charged particles. In the ECAL, electrons and photons are absorbed and their energy is measured. Similarly, hadrons are absorbed in the HCAL and their energy is measured. Muons traverse the calorimeters and reach the muon chambers, where their trajectories are measured [53].

The design of the subsystems ensures high resolutions and efficiencies for the measurement of these particles. The main properties of the detector are summarized in the following.

- The **superconducting solenoid** is 13 m long with an internal diameter of 6 m, and provides a strong magnetic field of 3.8 T inside. To saturate the magnetic field to the outside, the solenoid is encompassed into a steel flux return yoke.
- The **muon system** comprises three different types of gaseous particle detectors integrated into the steel yoke. Four layers of drift tubes are installed in the barrel part covering the pseudorapidity range $|\eta| < 1.2$ of the detector, and four layers of cathode strip chambers in the endcap part covering $0.9 < |\eta| < 2.4$, such that the full pseudorapidity range $|\eta| < 2.4$ is instrumented with four muon system layers in a row. These are complemented with resistive plate chambers installed both in the barrel and endcap region up to a pseudorapidity of $|\eta| < 1.6$.
- Inside the solenoid and closest to the interaction region, the **tracker** consists of finely segmented silicon pixel and silicon strip detectors. The original silicon pixel detector consisted of three layers of pixel modules at radii of 4.4, 7.3, and 10.2 cm, and two layers in the endcaps, with about 66 million sensors of size $150 \times 100\,\mu\text{m}^2$. Between the data taking periods in 2016 and 2017, an upgraded pixel detector was installed with four barrel layers at radii of 3.0, 6.8, 10.2, and 16.0 cm, and three endcap layers, with about 124 million sensors in total [54, 55]. The silicon strip detector consists of ten layers of strip modules in the barrel, and twelve layers in the endcaps, with about 9.6 million strip sensors between 80 and 180 µm wide. With a length of 5.8 m and a diameter of 2.6 m, the tracker covers the pseudorapidity range of $|\eta| < 2.5$.
- The **ECAL** is a homogenous, fine-grained calorimeter made from high-density lead tungstate crystals encompassing the tracker. In the barrel, the crystals have a transverse size of $2.2 \times 2.2\,\text{cm}^2$ or 0.0174×0.0174 in the (η, ϕ) plane, and are arranged in eight supermodules (four on both sides of $\eta = 0$), covering a pseudorapidity range of $|\eta| < 1.479$. In the endcap, slightly larger crystals with a front size of $2.9 \times 2.9\,\text{cm}^2$ cover the pseudorapidity range $1.479 < |\eta| < 3.0$. A **preshower** detector, consisting of a two-layer sampling calorimeter of lead radiators with silicon strip sensors, is

installed in the pseudorapidity range $1.653 < |\eta| < 2.6$ in front of the endcap ECAL modules to enhance the electromagnetic shower.

- The **HCAL** between the ECAL and the solenoid is a sampling calorimeter with brass radiators and scintillator sensors. Inside the magnet, the barrel and endcap parts cover the pseudorapidity ranges $|\eta| < 1.3$ and $1.3 < |\eta| < 3$, respectively. It is complemented with an outer part integrated as first layer in front of the muon chambers inside the steel yoke. The transverse size of the HCAL read-out towers is 0.087×0.087 in the (η, ϕ) plane for $|\eta| < 1.6$, and 0.17×0.17 for $|\eta| > 1.6$. The forward reach of the HCAL is extended with the forward hadron calorimeter (HF), consisting of iron radiators and quartz-fibre sensors that cover the pseudorapidity range up to $|\eta| < 5$. It measures both the electromagnetic and the hadronic shower in towers with a cross section of mostly 0.175×0.175 in the (η, ϕ) plane.

Particles are reconstructed from the subdetector measurements with the particle flow algorithm [53]. It combines the energy clusters measured by the calorimeters and the tracks reconstructed from the tracker and muon system measurements to identify all particles. Due to the high granularity of the tracker and the ECAL, the particle flow reconstruction provides very precise energy and momentum measurements. In Section 1.6, the reconstruction of the different types of particles is discussed in more detail.

A two-step **trigger system** is employed to select collision events for offline storage. This is necessary due to the huge bunch crossing rate of up to 40 MHz compared to an event rate of 100 Hz that can be processed by the offline computing systems. Given that the inelastic proton-proton scattering cross section is several orders of magnitude higher than the cross sections for the production of heavy particles, the task of the trigger is to select collision events based on physics interest over the bulk of inelastic scattering events. The first trigger step is the **level-1 trigger** (L1), a hardware system that uses all muon systems and the calorimeters to select events based on a fast basic identification of measured particles. The L1 system reduces the event rate to about 100 kHz. Events that passed the L1 trigger are further processed by the **high-level trigger** (HLT), a software-based system that uses measurements from all subdetectors to perform a sophisticated event reconstruction close to the final reconstruction. An "HLT path" is a set of reconstruction and selection steps targeting a specific event signature. With a suite of HLT paths, the event rate is reduced to about 100 Hz [56].

The distribution of measured collision events is compared to theory predictions by means of Monte Carlo (MC) samples, i. e. a simulation of collision events including both the hard scattering process and the interaction of the final-states particles with the CMS detector. The generation of MC events is discussed in Section 1.7.

1.6. Event reconstruction

During one bunch crossing, more than one collision can take place. In Run 2, this "pileup" was large, with 32 collisions per bunch crossing on average during the proton-proton collisions data-taking in 2017 & 2018 and maximum values of about 60 [57], as shown in Figure 1.11. Pileup is a big challenge for the reconstruction of particles from a collision event, as e. g. a pileup of more than 20 results in typically more than 1000 charged particles traversing the tracker [58]. Thus, carefully calibrated reconstruction algorithms are required to distinguish particles originating from different collisions.

Figure 1.11

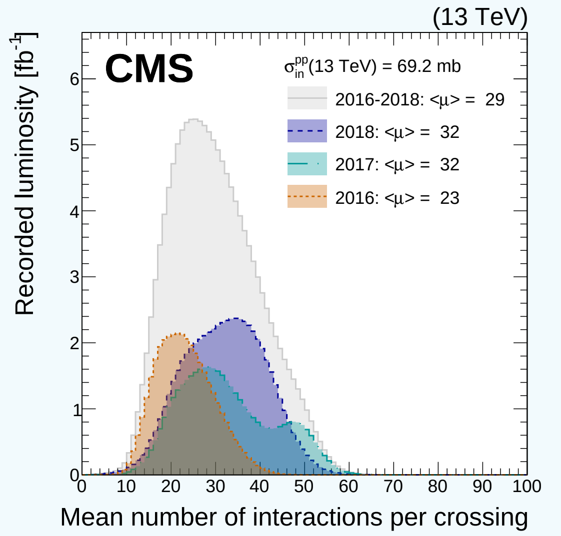

Pileup distribution for proton-proton collisions in 2016–2018, taken from Ref. [57].

Track and vertex reconstruction The precise reconstruction of charged particle tracks from the tracker measurements is required for a precise measurement of charged particle momenta. The subsequent combination of tracks to interaction vertices provides a crucial input for pileup mitigation and for the identification of long-lived particle decays which result in particles originating from displaced vertices.

Tracks are reconstructed from fits to geometrically matched combinations of hits, i. e. the signals from individual pixel and strip sensors. To reduce the combinatorial complexity, an iterative procedure is applied where each iteration uses loosened selection criteria on the track quality compared to the iteration before. This ensures that "easy" tracks, e. g. from particles with relatively large transverse momenta, are reconstructed first, and in subsequent iterations the more difficult ones.

For the vertex reconstruction, the selected tracks are clustered into groups based on a geometric matching along z. The positions of the interaction vertices are then determined by fits to all clusters with at least two tracks [58].

Figure 1.12

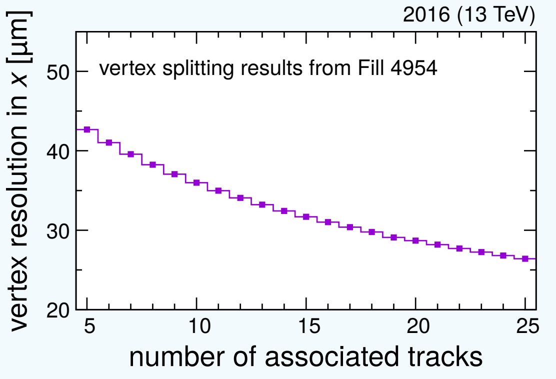

Vertex resolution determined for vertices reconstructed in a specific LHC fill, data provided by Ref. [59].

The precision of the vertex reconstruction is evaluated with the vertex-splitting method [58]. For each vertex, the associated tracks are divided into two equal-sized sets which are refitted as separate vertices. The distribution of differences between the positions of the two refitted vertices is then used to estimate the resolution of the vertex positions. In Figure 1.12, the vertex resolution in x determined in an example fill from the 2016 data-taking, i. e. using the original CMS pixel detector, is shown. The resolution is better for vertices with a larger number of associated tracks, and is about 32 µm for vertices with 14 associated tracks [59].

The "beam spot" is a description of the 3D profile of the luminous region, the space in which the LHC beams collide. Its position and widths can be inferred from a fit to the distribution of vertex positions collected over a series of several crossings [58].

For events with more than one vertex, the vertex with the largest associated transverse momentum is defined as the leading interaction vertex, and all other vertices are denoted as pileup vertices. For this evaluation, all tracks associated to a vertex are clustered to track jets with the anti-k_T algorithm [24, 25], and the sum of transverse momenta of all track jets and of the missing transverse momentum, defined as the negative vector sum of those track jets, is computed [57].

Particle flow candidates The particle flow (PF) algorithm [53] is employed for the reconstruction and identification of the particle candidates: electrons, muons, photons, charged and neutral hadrons. These PF candidates are further used for dedicated selections of electrons, muons, photons (which are not discussed here), and jets (clusters of charged and neutral particles typically resulting from the hadronisation of a single parton). Inputs to the PF algorithm are the reconstructed tracker tracks, measured calorimeter clusters, and tracks reconstructed from the muon system measurements.

Jet reconstruction Jets are clustered from all reconstructed PF candidates using the anti-k_T algorithm [24, 25] with a distance parameter of $R = 0.4$. To reject jets originating from detector noise or misreconstructions, identification criteria are applied based on the constituents of the jets, i. e. how many particles and how much energy is contributed from the different kinds of PF candidates to the jet [60].

To mitigate the effect of pileup in the jet reconstruction, the "charged hadron subtraction" scheme is applied. First, charged hadrons that originate from a pileup vertex are not included in the jet clustering. This removes a large fraction of charged particles from pileup. Second, to account for neutral pileup particles, a correction based on the jet area [61, 62] is applied to the four-momenta of the reconstructed jets on an event-by-event basis. Finally, identification criteria are applied based on the tracks associated with the PF candidates clustered in a jet as well as on jet shape observables to reject jets originating from pileup vertices [57].

Jet energy corrections are applied to correct for residual energy contributions from pileup, for the detector response to hadrons, and for differences between jets reconstructed in measured data and in simulated MC events. The resolution of the jet energy measurement is determined both in data and MC, and the energy of reconstructed jets in MC events is smeared such that both resolutions match [63].

Tagging of jets originating from bottom quarks The long lifetime of hadrons containing a b quark ("b hadrons") of the order of 1 ps results in a decay that is displaced between a few mm and up to 1 cm with respect to the interaction vertex and can be reconstructed as a "secondary" vertex. Additionally, b quarks have a larger mass and harder hadronisation compared to lighter quarks, resulting in decay products with an on average larger momentum transverse to the jet axis and a larger number of tracks associated with the jet. About 20 % of b hadrons have a soft electron or muon among their decay products.

To identify jets originating from b quarks ("b jets"), these properties are exploited in b tagging algorithms. The output of the algorithms are discriminator values for all jets, where larger discriminator values correspond to a higher likelihood for the jet to be a b jet. A minimum value on the discriminator value is defined for a reconstructed jet to be considered as b jet. The performance of a b tagging algorithm is evaluated in terms of the b jet efficiency, i. e. the fraction of all true b jets which are selected as b jets, and the misidentification probability, i. e. the fraction of light jets (originating from gluons or u, d, s quarks) or c jets which are selected as b jets.

Here, the DeepCSV [64] and the DeepJet [65] b tagging algorithms are used which are both based on deep neural networks. While DeepCSV uses information from a preselected secondary vertex and preselected tracks as well as kinematic properties of the jet, DeepJet does not require a preselection and uses information from a larger number of secondary vertices, tracks, and neutral hadrons, as well as the kinematic properties of the jet.

Figure 1.13

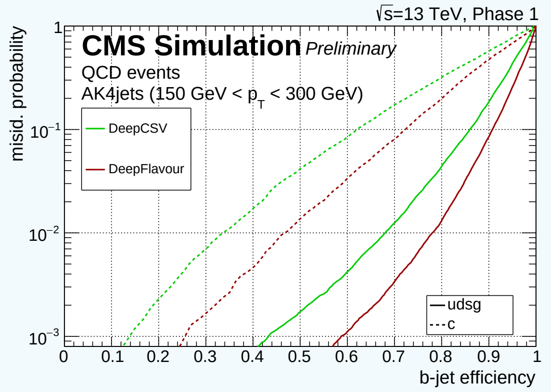

Misidentification probability for light jets (udsg) and c jets, and b jet efficiency, taken from Ref. [66].

In Figure 1.13, the performance of both algorithms is compared for jets from simulated events with a transverse momentum of $150\,\text{GeV} < p_{\text{T}} < 300\,\text{GeV}$. At the same misidentification probability, the DeepJet algorithm has a higher b jet efficiency than the DeepCSV algorithm. A minimum value of the discriminator value is chosen for both algorithms corresponding to a light jet misidentification probability of about 1 %.

The b tagging efficiencies for all jet flavours are measured both in data and MC samples. To correct for differences observed between data and MC samples, the simulated events are reweighted with per-jet scale factors [64].

Muon reconstruction Muons are reconstructed with the PF algorithm from a matching of tracks in the tracker and in the muon chambers. These muon candidates can originate from prompt muons produced in the interaction at the leading vertex, from the decays of light- and heavy-flavour hadrons, or from the misidentification of charged hadrons. A further selection of muon candidates is performed to suppress candidates from misidentification and light-flavour hadrons, based on the quality of the reconstructed track and on the matching between the tracks in the tracker and the muon system.

To distinguish between prompt muons and muons from heavy-flavour hadron decays, the isolation of the reconstructed muons is evaluated. The relative PF isolation is defined as the scalar sum of the transverse momenta of all reconstructed PF candidates within a cone around the muon, divided by the lepton transverse momentum. The cone size is defined by a maximum distance in $\Delta R = \sqrt{\Delta\phi^2 + \Delta\eta^2}$, where both fixed and transverse momentum dependent maximum distances are used [67]. A correction is applied to account for neutral particles from pileup in the cone.

The efficiencies of each step of the muon reconstruction and identification are measured both in data and in MC samples with a “tag-and-probe” method, where events with two muons are selected whose invariant mass is compatible with the Z boson mass. One muon, the “tag”, is then required to pass tight selection criteria. The resolution of a specific reconstruction or selection step is given by the fraction of other muons, the “probes”, that pass the respective reconstruction or selection criteria. To account for differences in the efficiencies observed between data and MC samples, per-muon scale factors are derived to reweight the simulated events [68].

Electron reconstruction Electrons are reconstructed with the PF algorithm from a matching of tracks in the tracker and energy clusters in the ECAL, taking into account the large amounts of bremsstrahlung emitted by the electrons as they traverse the tracker material. Apart from prompt electrons produced in the interaction at the leading vertex, electron candidates can originate from photon conversions, from misidentified jets, or from the decays of heavy-flavour hadrons. Identification criteria are developed based on the matching between the track and the ECAL clusters, the shape of the electromagnetic shower in the ECAL (which tend to be smaller than hadronic showers), HCAL deposits (to veto jets), and properties of the track. A multivariate analysis (MVA) classifier is trained to discriminate between prompt and background electrons, and provides a discriminant for each reconstructed electron. Similar to muons, the relative PF isolation can be evaluated for electrons to further suppress electrons originating from heavy-flavour hadron decays.

A tag-and-probe method is employed to determine the reconstruction and identification efficiencies for electrons. Per-electron scale factors are derived to reweight the simulated events to match the efficiency measured in data [69].

Missing transverse momentum reconstruction Neutrinos which are produced in the collision or are created subsequently in the decays of other particles do not interact with any of the subdetectors and leave the experiment unobserved. Their presence can, however, be inferred if a momentum imbalance is observed in the transverse plane. While the longitudinal momentum of the initial state of the partonic interaction is generally unknown, the transverse momentum of the initial state is zero. Thus, due to momentum conservation, the sum of momenta in the transverse plane of all reconstructed particles is expected to be zero except for events where unobserved particles were created.

Missing transverse momentum is defined as the negative vector sum of the transverse momenta of all PF candidates,

$$\vec{p}_{\mathrm{T}}^{\,\mathrm{miss}} = -\sum \vec{p}_{\mathrm{T}}, \qquad p_{\mathrm{T}}^{\mathrm{miss}} = |\vec{p}_{\mathrm{T}}^{\,\mathrm{miss}}|, \tag{1.4}$$

including the PF candidates not identified as physics objects (electrons, muons, photons, or hadrons), called “unclustered energy”. In the computation of the missing transverse momentum, overlap between reconstructed leptons and jets is removed, and all jet energy corrections are applied [70].

1.7. Event simulation

To facilitate a comparison of QFT predictions and measured data as well as to improve the understanding of the detector response, collision events are generated for different interaction processes predicted from theory including a simulation of the detector response. The event generation is based on the Monte Carlo (MC) method [71], and the set of simulated events generated for a specific process is referred to as a MC sample. A factorisation approach is employed to split the generation in separate steps: matrix element calculation, parton shower, and detector simulation.

The **matrix element (ME) calculation** uses a PDF set for the description of the initial state and a MC generator for the calculation of the partonic interaction. Here, the MadGraph5_aMC@NLO software [72] is used to generate events for most processes, including the top quark pair production in association with a Z boson ($\mathrm{t\bar{t}Z}$) signal process, at LO or NLO accuracy in QCD. For top quark pair production ($\mathrm{t\bar{t}}$) and top quark pair production in association with a Higgs boson ($\mathrm{t\bar{t}H}$), as well as some other background processes, the POWHEG software [73, 74] at NLO accuracy is used. For both generators, the NNPDF3.0 [75] and NNPDF3.1 [22] proton PDFs are used as inputs.

The **parton shower (PS) simulation** is performed with the PYTHIA 8 software [76, 77]. Soft initial and final state radiation (ISR and FSR), as a higher-order correction to the ME calculation, is added using a probabilistic approach for a “splitting” of the partons. Since hard ISR and FSR can also be generated in the ME calculation, a matching between the ME calculation and the PS simulation is performed in which the overlap of additional emissions is removed [78]. The hadronisation of all partons is simulated starting from an energy scale of 1 GeV, using a phenomenological model tuned to experimental data. An underlying event is added, accounting for interactions of multiple partons and of the beam remnants [79–82].

The final step is a **full detector simulation** based on the GEANT4 software [83]. It includes a full geometrical model of the CMS detector including “dead regions” like cables and support structures. The passage of all created particles through the detector and the response of the detector material is simulated. Experimental data is used to parameterise the response of the different subdetectors. Additionally, a simulation of the trigger system and of the electronic readout system is performed. In the end, the simulated events are available in the same format as the measured data and are then reconstructed with the same methods.

Part 2.

Luminosity measurement

Figure 2.1

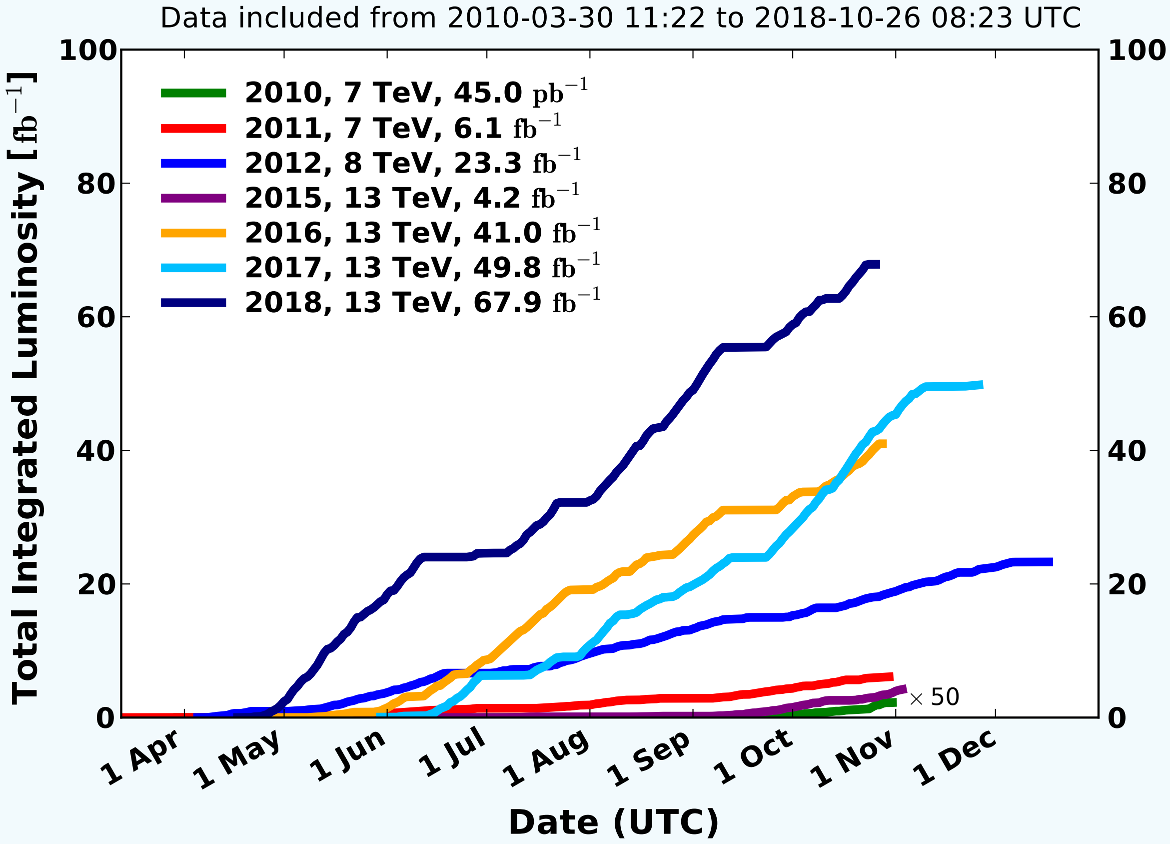

Integrated luminosity of proton-proton collisions at $\sqrt{s} = 7$, 8, and 13 TeV delivered to the CMS experiment in Run 1 (2010–2012) and Run 2 (2015–2018), taken from Ref. [84].

III. Luminosity of collider experiments

2.1. Overview

Luminosity is a key property of a particle collider. For the observation of a collision process $\alpha\beta \to \mathrm{X}$, the event rate $\mathrm{d}N/\mathrm{d}t$ is obtained from the instantaneous luminosity $\mathcal{L}$ of the collider and the cross section σ of the process:

$$\frac{\mathrm{d}N}{\mathrm{d}t}\Big(\alpha\beta \to \mathrm{X}\Big) = \mathcal{L} \cdot \sigma\Big(\sqrt{s}; m_\mathrm{X}, g_{\alpha\beta\mathrm{X}}, \dots\Big). \tag{2.1}$$

The value of σ can be calculated from the underlying interaction theory, and generally depends on the centre-of-mass energy $\sqrt{s}$ of the collision and other parameters like the mass m_X of the final-state particles and the coupling strength $g_{\alpha\beta\mathrm{X}}$ between the initial- and final-state particles. The cross section can also be measured from a collision experiment, by counting the number of events N_events of this process collected during a data-taking period (corrected for backgrounds, acceptance, and efficiency). This event yield is proportional to σ, with the integrated luminosity $L = \int \mathrm{d}t\, \mathcal{L}$ as proportionality constant:

$$\sigma = \frac{N_\mathrm{events}}{L}. \tag{2.2}$$

As the cross section is both calculable and measurable, the comparison of the two values can be used to extract theory parameters from the measurement. The precision of the accordingly measured parameters depends on the precision of the three ingredients: the measurement of the process itself (N_events), the luminosity measurement (L), and the theory calculation. It should thus be the target of the luminosity measurement to match the precision of the other two [85].

In general, the luminosity of a collider can be estimated from machine parameters. For two beams with N_1 and N_2 particles, distributed in the plane transverse to the beam direction according to normalised particle distributions $f_1(x,y)$ and $f_2(x,y)$, and circulating at a revolution frequency ν, the instantaneous luminosity is given by:

$$\mathcal{L} = \nu N_1 N_2 \int \mathrm{d}x \int \mathrm{d}y\, f_1(x,y) \cdot f_2(x,y) = \frac{\nu N_1 N_2}{A_{\text{overlap}}}. \tag{2.3}$$

The integral is called the overlap integral, and its inverse A_{overlap} describes the effective area in which the collisions take place. Here, it is assumed that the two beams collide "head on", i. e. at zero crossing angle. While ν is accurately known for a collider, and the number of particles can be measured precisely via the beam currents, the limited knowledge of the overlap area at the collision points limits the precision of the luminosity estimation [86].

For precision cross section measurements, collider experiments perform precision measurements of reference processes with well-known cross sections such that the inverse of Equation (2.2) can be employed to measure the luminosity.

At electron-positron colliders, Bhabha scattering $e^+e^- \to e^+e^-$ constitutes a process with a cross section known to a high accuracy from perturbative QED calculations. Since the event signature is simple and easy to detect, and the event rate is large, the luminosity can be measured with high precision. At the CERN Large Electron-Positron Collider (LEP), the integrated luminosity was measured from Bhabha scattering events with an uncertainty of better than 0.1 % [87–90]. The current luminosity uncertainty of the modern B factories SuperKEKB [91] and BEPCII [92–94] is about 0.7 %. In the case of the Belle II experiment at SuperKEKB, the dominant source of uncertainty is the precision of $\sqrt{s}$, required in the Bhabha scattering cross section calculation, i. e. a machine parameter.

The luminosity measurement at hadron colliders is more complicated due to the composite nature of the proton and the non-perturbativity of QCD at small energies. While at the DESY Hadron-Electron Ring Accelerator (HERA), the bremsstrahlung process $ep \to ep\gamma$, predictable from QED calculations, could still be used to reach a luminosity uncertainty in electron-proton and positron-proton collisions of as low as 1.7 % [95, 96], the precise luminosity measurement in proton-proton and proton-antiproton collisions poses a much bigger challenge.

At the CERN Intersecting Storage Rings (ISR), the world's first proton-proton collider, Simon van der Meer proposed in 1968 to use simple beam separation scans to estimate the beam overlap area [97], such that Equation (2.3) could be used to compute the luminosity. In the formulation of Carlo Rubbia from 1977 [98], the argument reads as follows: For a detector which measures a rate R proportional to the instantaneous luminosity, the measured rate with the two beams separated in the transverse plane by $(\Delta x, \Delta y)$ is, in generalisation of Equation (2.3), described by:

$$R(\Delta x, \Delta y) = \mathcal{N} \int \mathrm{d}x \int \mathrm{d}y\, f_1(x, y) \cdot f_2(x + \Delta x, y + \Delta y) \tag{2.4}$$

with a normalisation constant $\mathcal{N}$. This can be used to express the beam overlap area in terms of the rate at head-on collisions, $A_{\mathrm{overlap}} = \mathcal{N}/R(0,0)$. To obtain $\mathcal{N}$, Equation (2.4) is integrated over the beam separations:

$$\begin{aligned} \int \mathrm{d}\Delta x \int \mathrm{d}\Delta y\, R(\Delta x, \Delta y) &= \mathcal{N} \int \mathrm{d}x \int \mathrm{d}y\, f_1(x, y) \cdot \int \mathrm{d}\Delta x \int \mathrm{d}\Delta y\, f_2(x + \Delta x, y + \Delta y) \\ &= \mathcal{N}, \end{aligned} \tag{2.5}$$

where the last equality holds for integrals from $-\infty$ to ∞. Thus, A_{overlap} can be computed from:

$$A_{\mathrm{overlap}} = \frac{\int \mathrm{d}\Delta x \int \mathrm{d}\Delta y\, R(\Delta x, \Delta y)}{R(0,0)}. \tag{2.6}$$

For the special case of factorisable particle densities, $f_i(x, y) = f_i^x(x) \cdot f_i^y(y)$, this simplifies to:

$$A_{\mathrm{overlap}} = \frac{\int \mathrm{d}\Delta x\, R(\Delta x, 0)}{R(0,0)} \cdot \frac{\int \mathrm{d}\Delta y\, R(0, \Delta y)}{R(0,0)} = 2\pi \Sigma_x \Sigma_y. \tag{2.7}$$

The parameters Σ_x, Σ_y describe the effective widths of the beam overlap area along two orthogonal directions. In the case of particle densities described by Gaussian distributions,

$$f_i^{\chi}(\chi) = \mathrm{Gauss}(\chi; \sigma_{i,\chi}) = \frac{1}{\sqrt{2\pi\sigma_{i,\chi}^2}} \exp\left(- \frac{\chi^2}{2\sigma_{i,\chi}^2} \right), \tag{2.8}$$

with $\chi = x, y$, the effective widths are just the Gaussian widths of the convoluted particle densities, $\Sigma_\chi = \sqrt{\sigma_{1,\chi}^2 + \sigma_{2,\chi}^2}$.

Independent of the functional form of the particle densities, the effective widths can be obtained from so called Van der Meer (VdM) scans in which the two beams are separated in the respective direction and then moved in steps across each other. To allow for the integration in Equation (2.5), the maximal separation has to be significantly larger than the size of the beams.

This VdM method allows to estimate the luminosity for head-on collisions for the special beam conditions of the VdM scan. The measured luminosity can then be used to calibrate the absolute scale of the rate measurement of the luminosity detector, often called the "visible cross section" σ_{vis}, which is independent of the beam conditions. The reference process, used to measure luminosity via Equation (2.2), is thus typically elastic particle scattering, and σ_{vis} incorporates acceptance and efficiency of the detection method used in the specific detector [99].

At the ISR experiments, luminosity measurements based on the VdM method reached a precision of better than 1 % [100–103].

At the proton-antiproton colliders Sp$\bar{\mathrm{p}}$S at CERN and Tevatron at Fermilab, the VdM method could not be applied since sufficient transverse separation of the beams could not be achieved with the steering magnets at the single-ring accelerators. Thus, the luminosity determination had to rely on measurements of scattering processes or on the estimation from machine parameters [99]. The best achieved precision was 3 % at the Sp$\bar{\mathrm{p}}$S [104] and 4.3 % at Tevatron [105].

Presently, two hadron-hadron colliders are operating with proton-proton collisions and heavy-ion collisions, the Relativistic Heavy Ion Collider (RHIC) at BNL and the Large Hadron Collider (LHC) at CERN. Experiments at both colliders use the VdM method to calibrate their luminosity measurement for the different collision configurations [99]. At RHIC, a luminosity precision of about 3 % has been reached for proton-proton collisions [106]. The precision of the luminosity measurements of the LHC experiments for the Run 1 proton-proton collisions at $\sqrt{s} = 8\,\mathrm{TeV}$ ranges between 1.2 % and 2.6 % [107–110], where the best precision of 1.2 % was achieved at the LHCb experiment by combining the VdM calibration with results from a beam-gas imaging method. Preliminary results for the luminosity measurement of the Run 2 proton-proton collisions at $\sqrt{s} = 13\,\mathrm{TeV}$ yield uncertainties between 1.7 % and 3.4 % [A–C, F, 111, 112]. The measurements of the CMS experiment are discussed in Section 2.2.

For future operation of the LHC at even higher instantaneous luminosity, the luminosity measurements are challenged by the much higher expected collision rates. A proposal to combine the strengths of the VdM method—not to depend on the accuracy of theory predictions and especially the knowledge of the proton PDFs—and of measuring a well-defined physical final state—which allows to determine reconstruction efficiencies from data—is called "Z counting": The fiducial cross section for the Drell-Yan process $\mathrm{pp} \to \mathrm{Z} \to \mu^+\mu^-$ is measured in a low-pileup run using a precise luminosity determination from VdM scans, and then used in regular data-taking for the measurement of the luminosity, employing an in-situ determination of the muon reconstruction efficiency [113, 114]. The development of new methods towards the precise determination of corrections to the VdM method, as discussed in Chapters IV and V, thus serves also the precision luminosity measurements in the future.

2.2. Luminosity measurements at CMS

At the CMS experiment, a two-step procedure is employed to measure the luminosity: First, the VdM method is used to calibrate the absolute luminosity scale of one or more luminosity detectors ("luminometers"). One or more LHC fills with special beam optics are provided once per data-taking period during which VdM scans and other beam separation scans take place (the "VdM campaign"). Using the VdM scans from these fills, the visible cross section of the luminometers is obtained from the rate measurements via:

$$\sigma_{\mathrm{vis}} = \frac{2\pi\Sigma_x\Sigma_y R(0,0)}{\nu N_1 N_2} = \frac{\int \mathrm{d}\Delta x\, R(\Delta x, 0) \int \mathrm{d}\Delta y\, R(0, \Delta y)}{\nu N_1 N_2 R(0,0)}. \tag{2.9}$$

The LHC revolution frequency is $\nu = 11\,245\,\mathrm{Hz}$. Uncertainties in the calibration arise from the measurement of the beam currents N_1, N_2, from uncertainties in the VdM scan evaluation, from the knowledge of the beam separation scale Δx, Δy, and from the assumption of factorisable beam shapes in Equation (2.7).

Second, the rate of the luminosity detectors is integrated over the whole data-taking period and normalised with the calibrated σ_{vis} to obtain the integrated luminosity of the dataset. Uncertainties in the integration arise from changes of the detector response at different pileup ("linearity") and over time ("stability").

In Run 2, the luminosity at the CMS experiment has been measured for proton-proton collisions at $\sqrt{s} = 13\,\mathrm{TeV}$ [A–C, F] and at $\sqrt{s} = 5.02\,\mathrm{TeV}$ [115], as well as for proton-lead collisions at $\sqrt{s_{\mathrm{NN}}} = 8.16\,\mathrm{TeV}$ [D]. In the following, the different sources contributing to the uncertainty of the measured integrated luminosity in pp collisions at $\sqrt{s} = 13\,\mathrm{TeV}$ are introduced. In Table 2.1, the different uncertainty contributions are summarised and compared to the results of the ATLAS experiment [112].

Beam current measurement The number of protons per beam is obtained from beam current measurements provided by dedicated LHC devices, which measure the magnetic fields induced by the proton beams with fluxgate magnetometers. The Direct Current Current Transformers (DCCTs) provide a precise measurement of the total beam current integrated over all bunches. The Fast Bunch Current Transformers

(FBCTs) provide a time-resolved measurement that is proportional to the charge in each 25 ns bunch slot. By a combination of these two measurements, the per-bunch beam currents can be measured with an accuracy of 0.2 % [F, 116, 117].

Non-colliding protons also contribute to the beam current measurement but not to the luminosity, and have to be subtracted from the measured beam populations. They are referred to as "ghosts" (protons in nominally non-colliding bunch slots) and "satellites" (protons in colliding bunch slots, but outside of the colliding radiofrequency bin). With the Longitudinal Density Monitors (LDMs) of the LHC, which measure the longitudinal distributions of protons in the beams, the ghost and satellite fractions can be measured in empty bunch slots. The ghost charge is also measured from beam-gas imaging events in the LHCb experiment, providing a cross-check for the LDM result. The impact of the ghost and satellites correction on σ_{vis} is about 0.4 %, with an uncertainty of better than 0.1 % [F, 118].

VdM scan evaluation To obtain the effective beam overlap widths from the VdM scan data, the measured rates are fitted as a function of the beam separation. An example fit result is shown in Figure 2.2. The fit model is typically a single- or double-Gaussian function. To account for background contributions (detector noise and beam backgrounds) to the rate measurement, a constant term can be added to the function for the fit [A, B]. Alternatively, the background rates can be measured, either from nominally empty or non-colliding bunches [C] or from a special super-separation scan where the beams are kept at a large transverse separation [F]. The background yields are subtracted from the measured rates before the fit. The fitted function, without the background contribution, is then used to evaluate the integrals in Equation (2.7). Uncertainties arise both from the choice of the fit model and the estimation of the background yields.

Figure 2.2

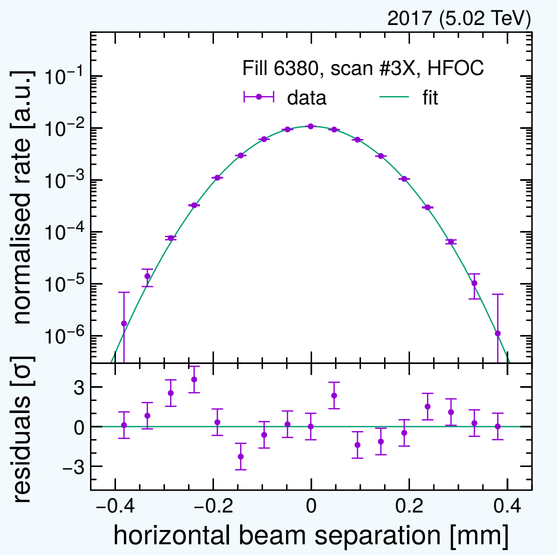

Event rate normalised by beam currents as a function of horizontal separation during a VdM scan in Fill 6380. The data is fitted with a single-Gaussian function. Data provided by Ref. [119].

Typically, several estimates of Σ_x, Σ_y are derived, using different pairs of VdM scans, collisions recorded at different bunch crossings, and different luminosity detectors. The consistency between the separately measured values is used for an uncertainty estimate.

Beam separation scale The VdM fit, as well as the evaluation of other beam separation scans, relies on a precise knowledge of the beam separation at each scan step. To this end, the beam positions inferred from the current settings of the steering magnets ("nominal positions") are corrected for several known effects.

- The absolute beam separation scale is calibrated with special **length scale** scans, exploiting the high precision of the track and vertex reconstruction with the CMS tracker as described in Section 1.6. With a combination of different length scale scan techniques, a length scale contribution to the σ_{vis} uncertainty of 0.2 % has been achieved [F]. The length scale calibration is discussed in detail in Chapter IV.
- Time-dependent movements of the beams away from their nominal orbit, known as **orbit drift**, have been observed, with up to 10 µm movement during a single VdM scan. The LHC beam position monitors (BPMs) are used to measure changes in the beam positions, which can then be corrected for in the VdM fits. An uncertainty is estimated from the comparison of two independent BPM systems [120].
- **Beam-beam deflection** denotes the increase of beam separation due to the electric repulsion of the positively charged protons. It can be calculated analytically and results in σ_{vis} corrections of about 1.5 % [F, 121].

A beam-beam effect correlated with beam-beam deflection is the focusing and defocusing of both beams by the magnet quadrupole moment of the other, known as **dynamic $\boldsymbol{\beta^\star}$ effect**. It results in a separation-dependent increase of the event rate and is corrected from analytic computations [122]. Recently, an inconsistency in the treatment of the beam-beam effects has been noted [123, 124]. Consequently, a combined effort of the LHC and the experiments is underway to update the analytic calculations.

Factorisation bias The VdM method uses Equation (2.7) to obtain σ_{vis} from the effective widths Σ_x, Σ_y measured in two VdM scans performed in orthogonal directions, and thus assumes factorisable beam proton densities. If this assumption is violated, the estimated σ_{vis} value is biased. To correct for this bias, the two-dimensional transverse beam shape is reconstructed from special beam-imaging scans. The uncertainty of the bias estimation can be the dominant contribution of up to 2 % to the uncertainty in the visible cross section [A, F, 115]. In Chapter V, the beam-imaging method employed at the CMS experiment to asses the factorisation bias is discussed, and compared with complementary methods.

Linearity To measure the luminosity in all fills of a data-taking period using a visible cross section σ_{vis} calibrated in one specific fill with its specific beam conditions, detectors for the luminosity measurement are required to have a linear response to the instantaneous luminosity independent of pileup or of the bunch structure of the LHC filling scheme. However, most detectors show some nonlinearity in their response, and thus corrections are determined for these.

Typical nonlinear effects, known as "out-of-time pileup" or "afterglow", are the spill-over of hits from one bunch crossing into the time window of the next crossing, and an exponentially decaying activation of the surrounding detector material, leading to a sizeable increase of the rate measured over several following bunches. Afterglow is determined from rate measurements in nominally empty bunch crossings, and corrections are then applied to the rate measurements in filled bunch crossings [F].

The performance of the linearity corrections for each luminosity detector can be monitored with emittance scans, which are short variants of VdM scans with a small number of steps, performed at the CMS experiment in 2017 and 2018 at the start of all and the end of many fills, i. e. on a daily basis. Thus, the σ_{vis} values obtained from the analysis of emittance scans can be used to analyse changes in the detector response as a function of time. An additional linearity correction is obtained from comparing σ_{vis} values from emittance scans taken at different pileup.

After all linearity corrections have been applied to each detector, the overall linearity of the corrected response is evaluated by cross-detector comparisons. To this end, the ratio of the luminosity as measured by two different luminosity detectors is determined as a function of the instantaneous luminosity during a fill, and a slope in the distribution is determined to quantify the residual nonlinearity between these two detectors. A comparison of the nonlinearity of the different fills of a data-taking period as a function of time shows the time dependence of the linearity, and is used to estimate an uncertainty which can be as large as 1 % [125].

Stability Similarly to the linearity analysis, the emittance scan data and cross-detector comparisons are used to evaluate the stability of the detector response as a function of time, induced e. g. due to radiation damage or operational issues, and to derive corrections. In a cross-detector comparison with three or more detectors, strong disagreements in the luminosity measurement can be attributed to instable response of one detector, such that this detector is excluded from the luminosity measurement for this period. The remaining disagreements between the different detectors that have not been excluded are used to estimate an uncertainty in the luminosity measurement due to instability [125].

Table 2.1

dataset		CMS 2015	CMS 2016	CMS 2017	CMS 2018	CMS 2015–2018	ATLAS 2015–2016	ATLAS 2017	ATLAS 2018	ATLAS 2015–2018
int. luminosity	[fb^{-1}]	2.3	35.9	41.5	59.7	139.5	36.2	44.3	58.5	139.0
total uncertainty	[%]	2.3	2.5	2.3	2.5	1.8	2.1	2.4	2.0	1.7
beam current	[%]	0.4	0.5	0.3	0.2	$0.2^{\dagger}$	0.2	0.2	0.2	$0.1^{\dagger}$
VdM scan fit	[%]		0.3		0.1	0.1	0.5	0.4	0.5	$0.4^{\dagger}$
Σ_x, Σ_y consistency	[%]			1.1	0.5	0.4	0.6	1.2	0.8	0.6
length scale	[%]	0.5	0.8	0.3	0.2	$0.2^{\dagger}$	0.3	0.3	0.4	$0.2^{\dagger}$
orbit drift	[%]	0.4	0.4	0.2	0.1	0.1	0.3	0.4	0.3	$0.2^{\dagger}$
beam-beam effects	[%]	0.6	0.6	0.6	0.2	$0.3^{\dagger}$	0.4	0.4	0.3	$0.4^{\ddagger}$
factorisation bias	[%]	1.5	0.9	0.8	2.0	$1.4^{\ddagger}$	0.4	0.2	0.5	$0.4^{\ddagger}$
linearity	[%]	1.0	1.1	1.5	1.2	$0.7^{\dagger}$	1.6	1.3	1.3	$1.3^{\dagger}$
stability	[%]	1.1	1.7	0.7	0.6	0.5	0.9	1.3	0.8	0.6

Contributions to the uncertainty of the luminosity measurement of the CMS [A–C, F] and ATLAS [112] experiments for the proton-proton collision datasets recorded at $\sqrt{s} = 13\,\mathrm{TeV}$. For the combined 2015–2018 luminosity, †partial and ‡full correlation of the uncertainties of the different years is denoted.

2.3. Van der Meer campaigns in Run 2

The LHC fills of a VdM campaign during which the VdM scans and other beam separation scans are performed have special beam optics, with zero crossing angle, a large value of $\beta^{\star}$, and large beam emittances. This increases the transverse size of the bunches σ_b to about 90 µm which makes precise measurements of the size of the beam overlap region by variation of beam separation possible. Filling schemes with a small number of isolated bunches well-separated over the orbit are used, thus minimising long-range beam-beam interactions away from the collisions, and allowing afterglow effects from one collision to decay before the arrival of the next bunch. The beam currents are reduced to minimise the beam-beam effects. The resulting average pileup is about 0.5 at head-on collisions [112].

In Figure 2.3, the transverse beam positions as a function of time are shown for the VdM campaign of the pp data-taking period at $\sqrt{s} = 13\,\mathrm{TeV}$ in 2017. Other VdM

Figure 2.3

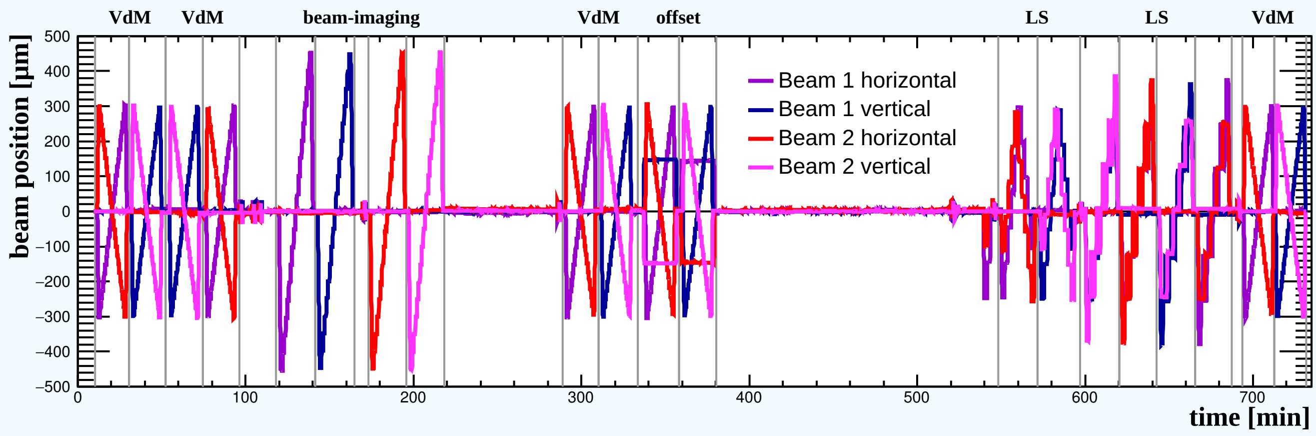

Relative transverse positions of the two proton beams during Fill 6016 as a function of time. Vertical grey lines enclose the separate scans. The scan campaign consists of four VdM scan pairs, one set of beam-imaging scans, an offset scan pair, and two sets of length scale (LS) scans. Taken from Ref. [C].

Figure 2.4

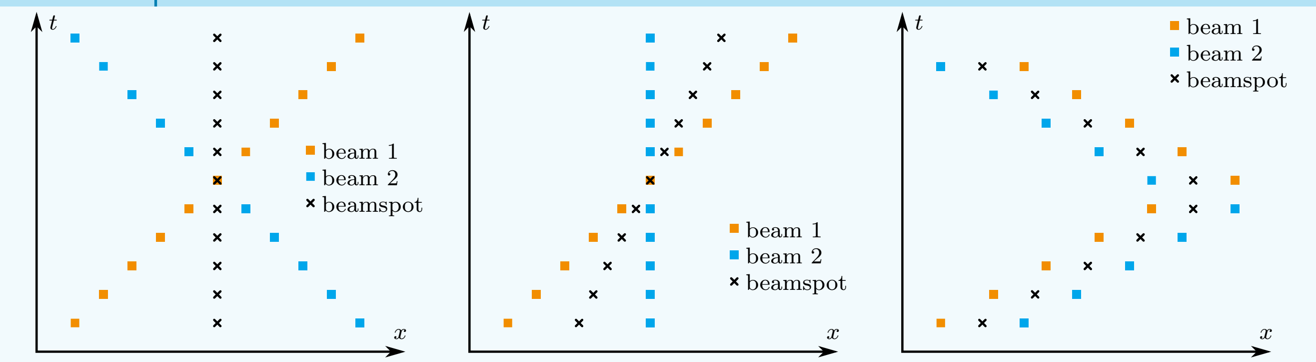

(a) VdM scan (b) Beam-imaging scan (c) Length scale scan

Sketches of the transverse beam position x as a function of time t for three beam separation scan types. The boxes show the positions of the single beams, and the crosses show the beamspot position, i. e. the centre of the beam overlap region.

campaigns have a similar setup. Several different types of beam separation scans are part of the campaign.

- In the **VdM scans**, the beams were initially separated by about $6\sigma_b$ in the transverse plane and then moved in 25 steps of 30 s each across each other, with a step size of about $0.5\sigma_b$. This is shown schematically in Figure 2.4a (with a smaller number of steps). VdM scans are always conducted in pairs of two scans along the horizontal and vertical direction, respectively. For reproducibility checks and monitoring of changes over the course of the fill, several scan pairs are conducted as part of the VdM campaign.

- A **beam-imaging scan** is a variant of a VdM scan with only one moving beam. While one beam is kept at the nominal head-on position, the other beam is offset by about $4.5\sigma_b$ and moved in 19 steps of 46 s each with a step size of $0.5\sigma_b$ across the non-moving beam, as shown schematically in Figure 2.4b (with a smaller number of steps). Four beam-imaging scans, for both beams both horizontally and vertically, form a scan set required for the beam-imaging analysis employed to estimate the factorisation bias, as discussed in Chapter V. Beam-imaging scans can also be analysed with the VdM method to measure σ_{vis}, for which a scan set of four scans is divided into two scan pairs.

- An **offset scan** is a variant of a VdM scan in which the two beams are additionally separated in the non-scanning direction. Here, an additional separation of $3\sigma_b$ was chosen. An offset scan pair can be analysed together with a VdM scan pair as a complementary method to determine the factorisation bias, as discussed in Section 2.11.

- **Length scale scans** are special scans used to calibrate the beam separation scale. In a **constant-separation** length scale scan, the two beams are separated by $1.4\sigma_b$ and moved in simultaneous steps of $1\sigma_b$ across the detector. With 70 s per step, five steps constitute the “forward“ scan, after which the two beams swap positions as the next step and are then moved in four steps “backward“. This is shown schematically in Figure 2.4c, and discussed in Chapter IV. Two of these scans along the horizontal and vertical direction constitute a length scale scan set.

- An alternative strategy for the length scale calibration uses **variable-separation** length scale scans. One such scan consists of 15 steps of 46 s each, grouped into five “miniscans”. Each miniscan has one beam at a fixed position and the other beam scanned across the fixed beam at relative positions of $-1.25\sigma_b$, 0, and $+1.25\sigma_b$. Between the miniscans, the position of the fixed beam is moved by $1\sigma_b$ along the same direction. Four scans are required, for both beams both horizontally and vertically, to constitute a scan set.

In Table 2.2, all VdM campaigns of the CMS experiment in Run 2 and the performed beam separation scans are listed. One special scan type not present in Fill 6016 is the **diagonal scan** and was only performed in the calibration fills for the PbPb data-taking in 2018. It is a VdM scan variant in which the beams move both horizontally and vertically in each step such that the scan axis is rotated by 45° with respect to standard VdM scans. It is used to determine the factorisation bias.

Table 2.2

data-taking period			performed beam separation scans								
type	$\sqrt{s_{\mathrm{NN}}}$	**year**	**fill**	**date**	**VdM**	**BI**	**OS**	**DS**	**cLS**	**vLS**	
pp	13 TeV	2015	4266	2015/08/24	✓	✓			✓		[A]
pp	5.02 TeV	2015	4634	2015/11/19	✓	✓			✓		[115]
PbPb	5.02 TeV	2015	4689	2015/12/03	✓		✓		✓		
pp	13 TeV	2016	4937	2016/05/17		✓					
			4945	2016/05/18	✓				✓		
			4954	2016/05/27	✓	✓			✓		[B]
Pbp	8.16 TeV	2016	5527	2016/11/22	✓				✓		[D]
pPb	8.16 TeV	2016	5563	2016/12/01	✓				✓		[D]
pp	13 TeV	2017	6016	2017/07/08	✓	✓	✓		✓	✓	[C]
pp	5.02 TeV	2017	6380	2017/11/11	✓	✓					
			6381	2017/11/12					✓		
pp	13 TeV	2018	6868	2018/06/30	✓	✓	✓		✓	✓	[F]
PbPb	5.02 TeV	2018	7442	2018/11/13	✓		✓	✓	✓		
			7443	2018/11/14	✓		✓	✓			
			7483	2018/11/29					✓		

VdM campaigns in Run 2 during which beam separation scans for the luminosity calibration of the CMS experiment have been performed. The listed scan types are VdM, beam-imaging (BI), offset (OS), diagonal (DS), constant-separation length scale (cLS), and variable-separation length scale (vLS).

IV. Length scale calibration

2.4. Formalism

The beam separation scale is an essential input to the fit of the measured rate during a VdM scan. For a length scale variation, i. e. a proportional variation of the beam separation scale $\Delta x \to \alpha\Delta x$, unknown to the analyst, the measured effective overlap width Σ_x^{meas} for the simple case of factorisable proton densities of Gaussian shape,

$$\Sigma_x^{\text{meas}} = \int \mathrm{d}\Delta x \,\text{Gauss}(\alpha\Delta x; \Sigma_x^{\text{true}}) = \int \mathrm{d}\Delta x \,\text{Gauss}(\Delta x; \Sigma_x^{\text{true}}/\alpha) = \frac{1}{\alpha}\Sigma_x^{\text{true}}, \tag{2.10}$$

is off with respect to the true width Σ_x^{true} by a factor of α^{-1}, which propagates inversely to the integrated luminosity. An uncertainty on the length scale translates linearly to an uncertainty on the measured integrated luminosity, and the precise knowledge of the length scale is thus an important prerequisite for a precise luminosity measurement.

During a VdM scan, the positions of the beams are predicted from the settings of the corrector dipole magnets which steer the two beams at the CMS experiment's interaction point. Since the steering is done separately in the two transverse planes and for the two beams, four scale factors are required to describe the relation between the actual beam positions $(\tilde{x}_i, \tilde{y}_i)$ and the predicted "nominal" positions (x_i, y_i), defined as:

$$\tilde{x}_i = \alpha_{x,i}\, x_i, \qquad \tilde{y}_i = \alpha_{y,i}\, y_i. \tag{2.11}$$

For the case of VdM scans, both beams are moved for each step n by the same nominal distance $d_n/2$ but in opposite directions, such that the true separation,

$$\Delta\tilde{x}_n = \tilde{x}_{2,n} - \tilde{x}_{1,n} = \alpha_{x,2}\frac{d_n}{2} - \alpha_{x,1}\frac{(-d_n)}{2} = \frac{\alpha_{x,1} + \alpha_{x,2}}{2} d_n = \bar{\alpha}_x d_n, \tag{2.12}$$

only depends on the average scale factor $\bar{\alpha}_x$. The per-beam scale factors are only required for the VdM analysis of the beam-imaging scans during which only one beam is moved. One also defines the difference of the scale factors $\epsilon_x = \alpha_{x,2} - \alpha_{x,1}$, and similarly for y. In general, the understanding of the steering magnets is good such that $\bar{\alpha}_\chi \approx 1$ and $\epsilon_\chi \approx 0$ [126].

To calibrate the length scale, the very precise track and vertex reconstruction of the CMS tracker is used. While the tracker measurements cannot give information on the positions of the two beams separately, the beamspot position, i. e. the centre of the luminous region, can be estimated from the distribution of reconstructed vertices.

In a constant-separation length scale scan, as shown schematically in Figure 2.4c, the beams are kept at a constant transverse separation and moved simultaneously. For a step size d in a scan along x with an initial separation s_0, the nominal and actual positions of the two beams and the beamspot position at step n are

$$\begin{aligned} & x_{1,n} = nd, && x_{2,n} = s_0 + nd, && \bar{x}_i = \frac{x_{1,n} + x_{2,n}}{2} = \frac{s_0}{2} + nd \\ \Rightarrow\quad & \tilde{x}_{1,n} = \alpha_{1,x} nd, && \tilde{x}_{2,n} = \alpha_{2,x} s_0 + \alpha_{2,x} nd, && \tilde{\bar{x}}_n = \frac{\alpha_{2,x} s_0}{2} + \bar{\alpha}_x nd = \frac{\epsilon_x s_0}{4} + \bar{\alpha}_x \bar{x}_n. \end{aligned} \tag{2.13}$$

Thus, the average scale factor can be obtained as the slope of the linear relation between the actual beamspot position, as estimated from the vertex distribution, and the nominal beamspot position, computed from the nominal beam positions.

A second estimator for the beam separation scale is the instantaneous luminosity during a constant-separation length scale scan. While the nominal beam separation is constantly equal to s_0 during the scan, different per-beam scale factors, i. e. in the case of $\epsilon \neq 0$, cause an evolution of the actual separation,

$$\Delta\tilde{x}_n = \tilde{x}_{2,n} - \tilde{x}_{1,n} = \alpha_{2,x} s_0 + \epsilon_x nd = \bar{\alpha}_x s_0 + \epsilon_x \bar{x}_i. \tag{2.14}$$

Assuming factorisable beams of Gaussian shape, the resulting evolution of the event rate in a luminosity detector is:

$$R_n = R(\Delta\tilde{x}_n) = R_0 \exp\left(- \frac{(\Delta\tilde{x}_n)^2}{2\Sigma_x^2} \right) \approx \text{const} \cdot \left(1 - \frac{\bar{\alpha}_x \epsilon_x s_0 \bar{x}_n}{\Sigma_x^2} \right). \tag{2.15}$$

Thus, the scale factor difference can be estimated from the change of the rate during the length scale scan. However, in contrast to the estimation of the average scale factor from the beamspot position, this estimation depends on a precise knowledge of the initial separation, the step size, and the convoluted beam width.

Figure 2.5

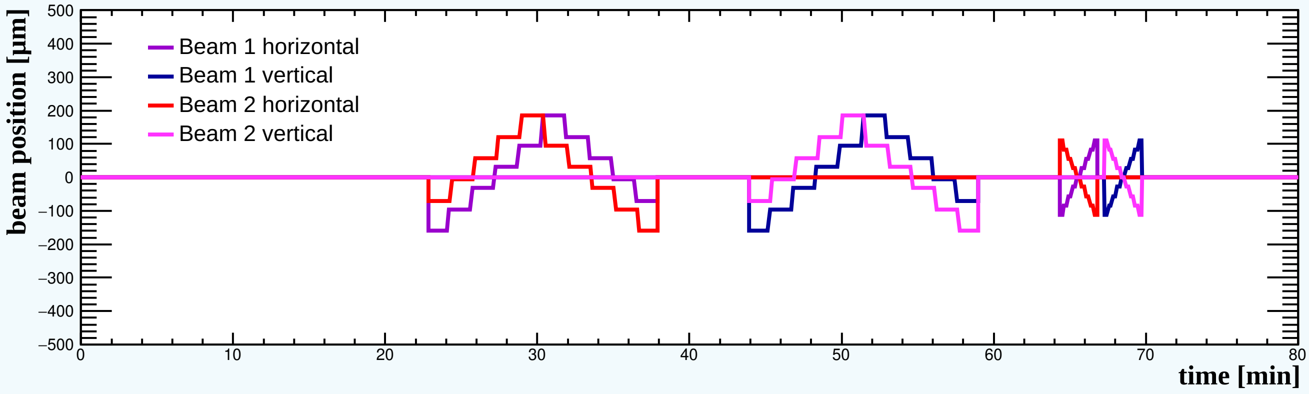

Nominal relative transverse positions of the two proton beams during Fill 6381 as a function of time. The scan campaign consists of a constant-separation length scale scan pair, followed by an emittance scan pair.

2.5. Analysis procedure

The derivation of the average scale factors is discussed using the length scale scan pair from Fill 6381 as example. The nominal beam positions during this fill are shown in Figure 2.5. Two constant-separation length scale scans were performed, in the horizontal and vertical direction, each with both five steps "forward" and "backward".

Reconstructed vertices are selected if they satisfy standard quality criteria, especially a minimal requirement of 14 associated tracks, and belong to the time window of a scan step. Two different methods to define the time window are used, the "timestamp-based" and the "lumisection-based" selection, and yield statistically consistent results. For each scan step, about 200 000 vertices are selected with the lumisection-based selection.

The distribution of the selected vertices along the scanning direction is shown for two steps of the forward horizontal scan in Figure 2.6, and for two steps of the forward vertical scan in Figure 2.7. A Gaussian fit is performed to the binned distribution of vertex positions to extract the mean vertex position which estimates the beamspot position. With about 415 degrees of freedom, the χ^2 of the fit result is about 850 (950) in each step of the horizontal (vertical) scan. The fitted mean is statistically consistent with the average position calculated arithmetically.

A notable difference between the horizontal and vertical scans is the scan direction. While the nominal beam positions increase numerically during the forward scan directions for both scans (cf. Figure 2.5), the measured mean vertex position during consecutive steps of the forward direction only increases for the vertical scan but decreases for the

Figure 2.6

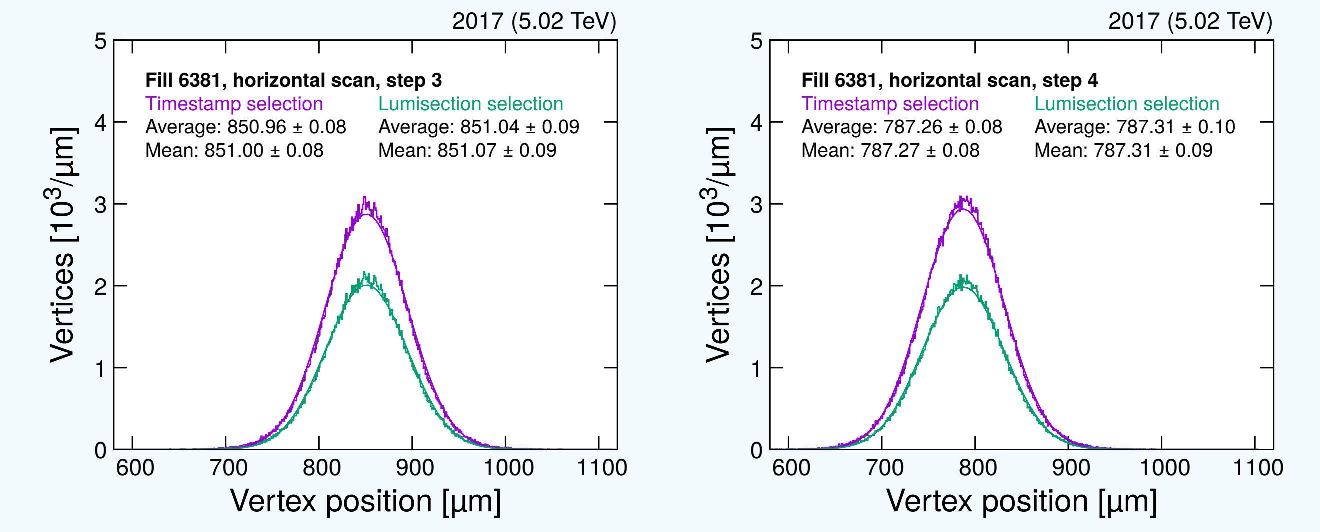

Distribution of reconstructed vertex positions for third (left) and fourth (right) step of the constant-separation length scale scan in horizontal direction in Fill 6381. The data (histogram) is shown alongside a Gaussian fit (line) for both the timestamp-based (violet) and lumisection-based (green) vertex selection. The "average" denotes the arithmetic average of vertex positions, while the "mean" denotes the mean parameter extracted from the Gaussian fit.

Figure 2.7

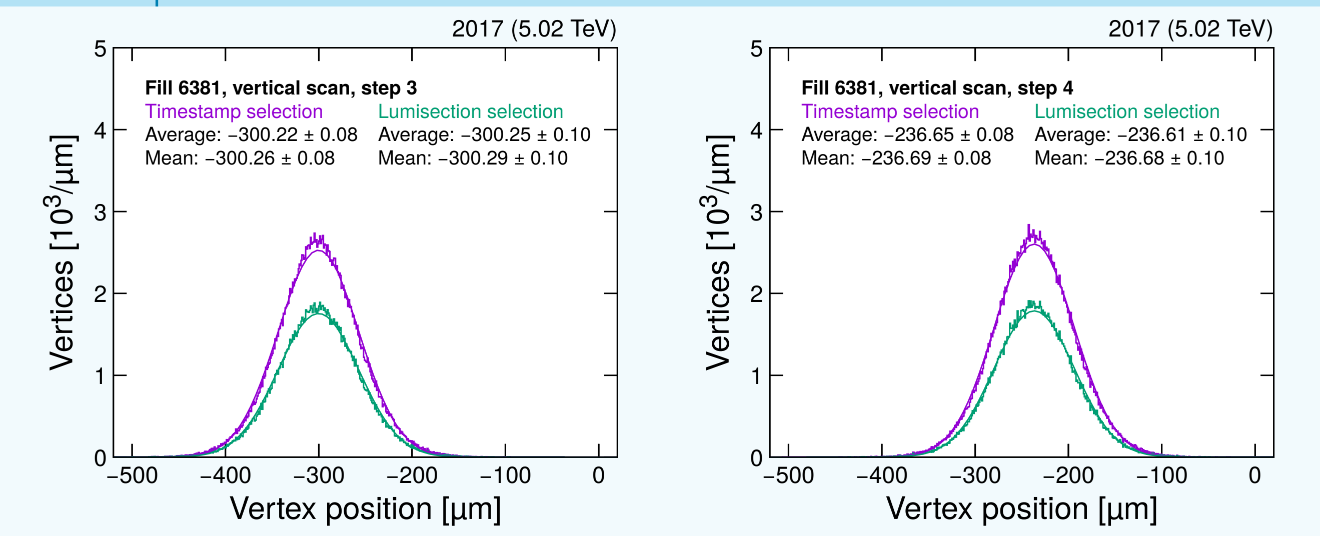

Distribution of reconstructed vertex positions for third (left) and fourth (right) step of the constant-separation length scale scan in vertical direction in Fill 6381. Same definitions as in Figure 2.6.

horizontal scan. This is due to the fact that the horizontal axis of the LHC coordinate system is flipped with respect to the horizontal axis of the CMS coordinate system. To remedy for this, the mean vertex positions extracted from scan steps of the horizontal scan are multiplied by −1 before the next stage of the analysis.

Figure 2.8

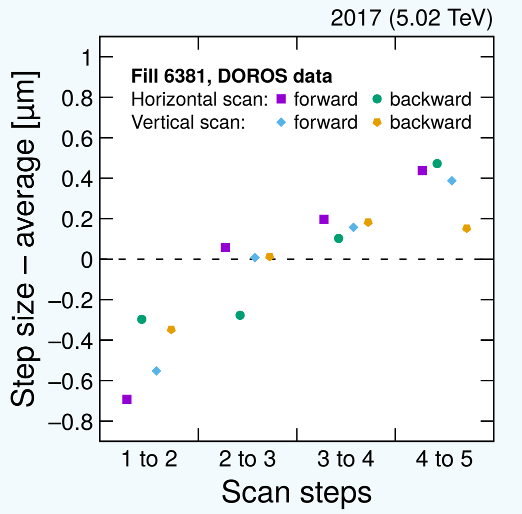

Step sizes measured with the DOROS BPMs during the constant-separation length scale scans in Fill 6381.

Assuming that the step size is the same between all scan steps of the constant-separation length scale scan, the length scale calibration can be performed by the comparison of nominal beamspot position and mean vertex position. However, time-dependent changes of the beam positions, known as orbit drift [120], violate this assumption and can bias the calibration result. To determine orbit drift and correct for it, the beam positions are monitored with the DOROS beam position monitors (BPMs), an LHC system. While the absolute length scale of the DOROS measurements differs from the actual length scale and thus cannot be used to calibrate the length scale of the nominal positions, the DOROS measurement can provide information on a change of the step size of the beamspot. In Figure 2.8, the variation of the step size, defined as the difference of the beamspot positions between two consecutive scan steps, relative to the average step size, is shown separately for both directions of both scans. In all cases, the observed step size increases slightly with subsequent scan steps. The overall variation, however, is small, with a maximum difference between first and last step size of 1.1 µm for the forward direction of the horizontal scan.

The observed orbit drift during the length scale scans is included as a correction to the nominal beamspot positions, such that they correspond to a constant step size when including orbit drift, an approach originally proposed by Reference [127]. In practice, the nominal position of the third step is left unchanged and the observed step size variations are subtracted from or added to the nominal position of the preceding and following steps, respectively.

In Figure 2.9, the difference between the measured and the orbit-drift corrected nominal position is shown as a function of the latter, for both directions of both the horizontal and vertical scan. The difference between the positions is shifted separately for each direction such that the linear fits to the data have zero intercept. The slopes of the linear fits estimate the difference of the average scale factors from unity. With three

Figure 2.9

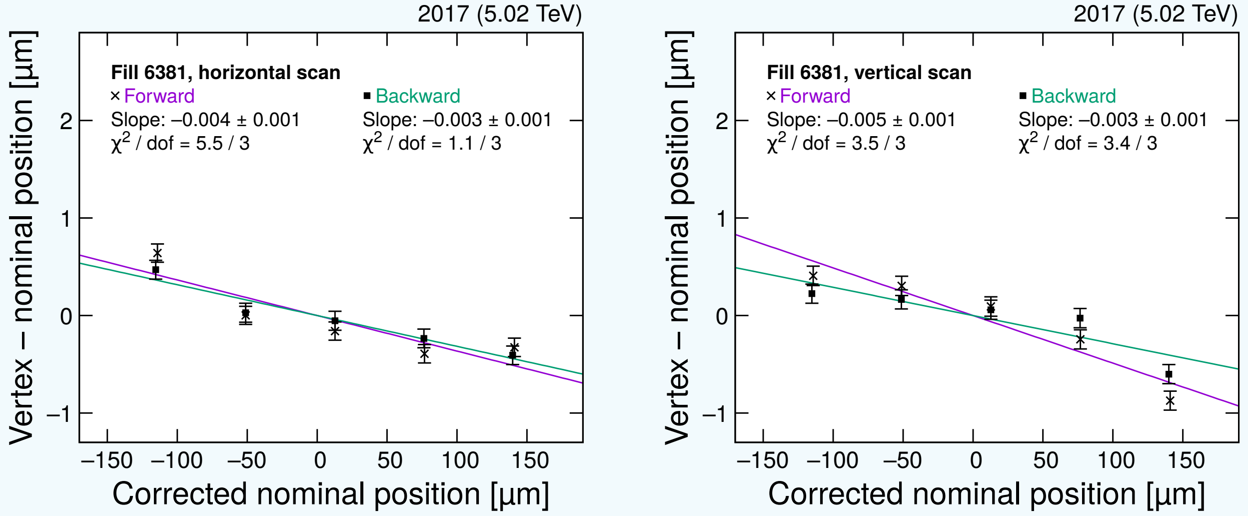

Difference between the mean vertex position (from a Gaussian fit to the vertex distribution obtained with the lumisection-based selection) and the nominal position corrected for orbit drift as a function of the latter, for the horizontal (left) and vertical (right) length scale scans in Fill 6381.

Figure 2.10

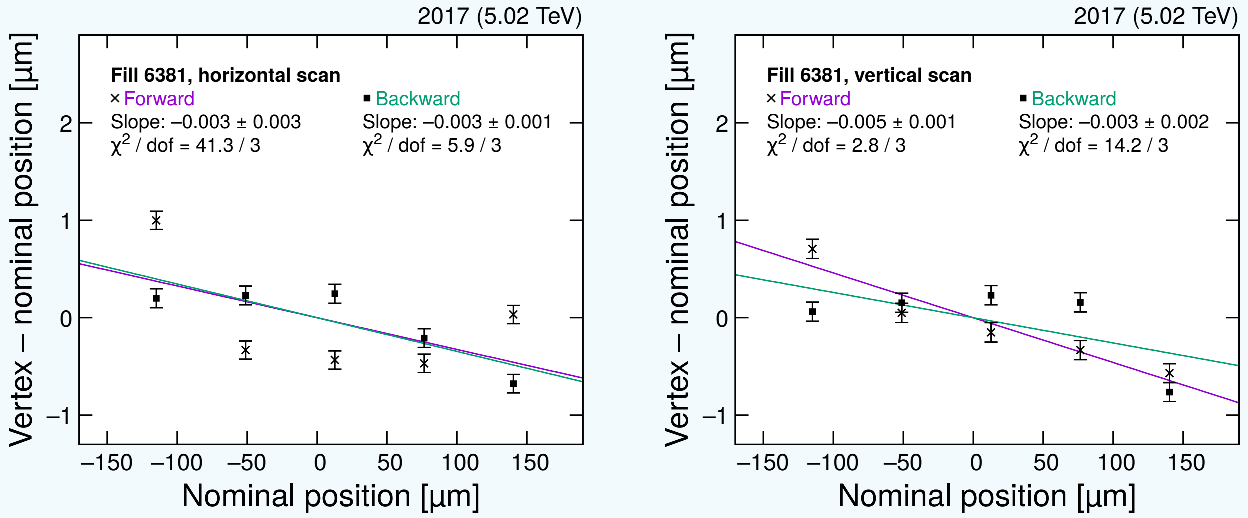

Difference between the mean vertex position (from a Gaussian fit to the vertex distribution obtained with the lumisection-based selection) and the nominal position without orbit drift correction as a function of the latter, for the horizontal (left) and vertical (right) length scale scans in Fill 6381.

Table 2.3

	nominal result		corrected result	
	slope	χ^2/dof	slope	χ^2/dof
horizontal scan				
forward direction	-0.0033 ± 0.0030	41.3 / 3	-0.0036 ± 0.0011	5.5 / 3
backward direction	-0.0035 ± 0.0012	5.9 / 3	-0.0032 ± 0.0005	1.1 / 3
vertical scan				
forward direction	-0.0046 ± 0.0008	2.8 / 3	-0.0049 ± 0.0009	3.5 / 3
backward direction	-0.0026 ± 0.0018	14.2 / 3	-0.0029 ± 0.0009	3.4 / 3

Slopes and χ^2 of linear fits to constant-separation length scale scans in Fill 6381, without (left) and with (right) orbit drift corrections applied to the nominal positions, and using the mean vertex positions from a single-Gaussian fit to the vertex distribution obtained with the lumisection-based selection.

degrees of freedom and the χ^2 of the fit ranging up to about 5.5, the uncertainty in the slope reaches values between 15 % and 30 %. Within these uncertainties, the slopes obtained in the forward and backward direction are consistent.

For comparison, the same measured vertex positions are fitted as a function of the uncorrected nominal positions. The fit results are shown in Figure 2.10, and the comparison is summarised in Table 2.3. The uncorrected fits have a significantly worse fit quality, and subsequently larger uncertainties in the fitted slopes of as large as 100 %. The overall change in the central value of the slope, however, is small.

Table 2.4

	horizontal	vertical
statistical	0.0011	0.0009
consistency	0.0002	0.0010
orbit drift	0.0003	0.0003
total	0.0012	0.0014

Uncertainty contributions to the average scale factors derived for Fill 6381.

The final length scale correction factors are obtained as the average of the results from the forward and backward direction of the fit to the corrected nominal positions using the mean vertex positions from the fit to the lumisection-based selection. To evaluate the uncertainty of these results, different uncertainty sources are considered. In Table 2.4, the uncertainty contributions are summarised.

The statistical uncertainty on the vertex distribution is propagated in the Gaussian fit to the beamspot estimates and subsequently in the linear fit to the uncertainty of the slope. The larger uncertainty of the slopes from the independent fits for the forward and backward direction is used to estimate the statistical uncertainty of the scale factor.

The forward and backward directions of the constant-separation length scale scans are expected to yield the same results. Differences in the slopes indicate remaining experimental inconsistencies of systematic nature. To cover the possible bias from one or both of the results, half the difference between the slopes from the forward and backward scans is assigned as uncertainty.

While the orbit drift correction improves the fit results, a residual bias due to orbit drift effects not assessed by the correction is possible. Thus, the larger difference between the results without and with orbit drift corrections from the forward or backward direction is assigned as additional uncertainty source.

Finally, imperfect tracker alignment can impact the reconstruction of the vertex positions and thus the result of the length scale calibration. As a cross-check, the analysis has been repeated with a dataset using an older tracker alignment setup. The resulting slopes agree within the statistical uncertainties.

The resulting average scale factors are

$$\bar{\alpha}_x = 0.9966 \pm 0.0012 \qquad \text{and} \qquad \bar{\alpha}_y = 0.9961 \pm 0.0014 \tag{2.16}$$

for the horizontal and vertical direction. The visible cross section changes by $-0.7\,\%$ after applying the length scale calibration, with an uncertainty of $0.2\,\%$.

2.6. Results

A precise length scale calibration is an important prerequisite for a percent-level precision of the integrated luminosity measurement, and has thus been an integral part of every luminosity measurement of the CMS experiment throughout Run 2. The resulting corrections on the visible cross section for all proton-proton data-taking periods are shown in Figure 2.11. Constant-separation scans have been performed in all VdM campaigns. Their analysis differs in the treatment of orbit drifts and in the evaluation of systematic uncertainties as the analysis technique was refined over time.

The analysis discussed in Section 2.5 represents the state-of-the-art length scale calibration technique with constant-separation scans. By fully incorporating the observed orbit drifts into the fit of the measured vertex position, the fit quality is improved and better agreement between the forward and backward directions of the scans are found. This significantly improves the uncertainty of the length scale correction compared to previous approaches that only estimated the impact of orbit drift using the observed change in head-on beam positions before and after the full scan.

Figure 2.11

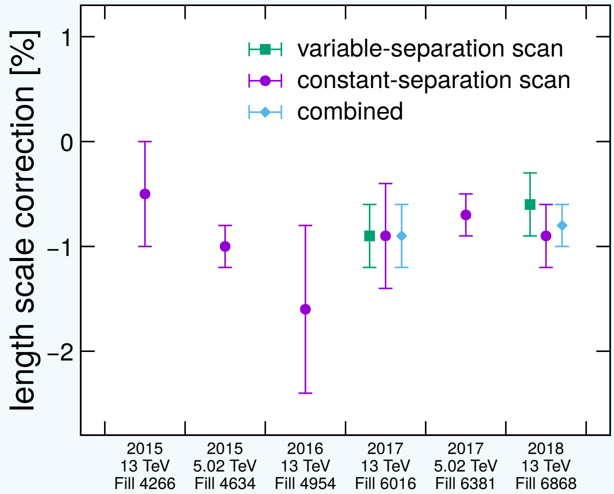

Length scale corrections to the visible cross section for different data-taking periods. The entry for Fill 6381 shows the result from Section 2.5, for the other entries see References [A–C, F, 115].

In addition to the constant-separation scans, variable-separation scans have been performed in the VdM campaigns at $\sqrt{s} = 13\,\text{TeV}$ in 2017 and 2018 [C, F]. They also provide the main length scale calibration method of the ATLAS experiment [112]. Compared to the constant-separation scan, the variable-separation scan has a miniscan for each transverse beamspot position in which one beam is moved in three steps around the head-on position. A fit to the luminosity measured during the miniscan allows to identify precisely the position of the head-on configuration, i. e. the transverse position of the beam that is not performing the miniscan. The linear fit to the measured vertex position as a function of the nominal position then provides separate measurements for the per-beam scale factors.

The average scale factors obtained from the variable-separation scans agree within uncertainties with the results from the constant-separation scans. The combination of the scale factors from both methods results in a reduced systematic uncertainty.

V. Factorisation bias estimation

2.7. Formalism

In the VdM method, two VdM scans in orthogonal transverse directions are performed to measure the width of the beam overlap region along these two directions. Assuming that the two-dimensional beam overlap region can be described as a function that factorises into two one-dimensional functions of the coordinates along the scan directions, two widths suffice to compute the beam overlap area, as described by Equation (2.7). If the width of the beam overlap region in one direction depends on the coordinate along the other direction, this assumption of factorisation does not hold. The estimate of the beam overlap area from the VdM method is then biased.

Non-factorisable normalised transverse beam distributions f_i can be modelled with a two-dimensional Gaussian distribution that includes a correlation parameter ρ_i:

$$\begin{aligned} f_i(x,y) &= \mathrm{Gauss}^{\mathrm{2D}}(x,y;\sigma_{i,x},\sigma_{i,y},\rho_i) \\ &= \frac{1}{2\pi\sigma_{i,x}\sigma_{i,y}\sqrt{1-\rho_i^2}}\exp\left[-\frac{1}{2(1-\rho_i^2)}\left(\frac{x^2}{\sigma_{i,x}^2}+\frac{y^2}{\sigma_{i,y}^2}-2\rho_i\frac{x}{\sigma_{i,x}}\frac{y}{\sigma_{i,y}}\right)\right]. \end{aligned} \tag{2.17}$$

The correlation parameter can take values $|\rho_i| < 1$ and can be interpreted as a rotation of the factorisation axes with respect to the coordinate directions. For a vanishing correlation parameter $\rho_i = 0$, the two-dimensional Gaussian distribution factorises into two one-dimensional distributions,

$$\mathrm{Gauss}^{\mathrm{2D}}(x,y;\sigma_{i,x},\sigma_{i,y},\rho_i=0) = \mathrm{Gauss}(x;\sigma_{i,x})\cdot\mathrm{Gauss}(y;\sigma_{i,y}). \tag{2.18}$$

In addition to the correlation parameter, non-factorisable distributions can also be obtained from sums of Gaussian distributions. The simplest example is a double-Gaussian distribution,

$$\mathrm{DG}^{\mathrm{2D}}(x,y) = w_{\mathrm{N}}\mathrm{Gauss}^{\mathrm{2D}}(x,y;\sigma_{\mathrm{N},x},\sigma_{\mathrm{N},y},\rho_{\mathrm{N}}) + w_{\mathrm{W}}\mathrm{Gauss}^{\mathrm{2D}}(x,y;\sigma_{\mathrm{W},x},\sigma_{\mathrm{W},y},\rho_{\mathrm{W}}), \tag{2.19}$$

This sum of two Gaussian distributions (labelled “narrow” N and “wide” W) with weights $w_{\mathrm{N}} + w_{\mathrm{W}} = 1$ does not factorise if the widths of the two components are different.

During the VdM campaigns performed in proton-proton collisions at $\sqrt{s} = 8\,\mathrm{TeV}$ in April and July 2012, the four LHC experiments found first evidence for non-factorisable beam shapes, affecting the consistency of the beam overlap area measurements from different VdM scan pairs and using different techniques. Consequently, additional VdM scans were performed in November 2012 in fills with an especially tuned injector chain setup to provide proton bunches with a highly Gaussian transverse distribution. The experiments confirmed that the November 2012 VdM scan data can be well described with the assumption of factorisation [107–110].

In Run 2, the LHC experiments started to estimate the factorisation bias via a full reconstruction of the beam proton densities. This allows to compute the transverse profile of the beam overlap region, and to quantify the difference between the beam overlap area obtained from a direct integration (unbiased) and from the widths along the two coordinate directions (biased in the same way as the VdM method).

The CMS experiment employs the **beam-imaging method** [128] to reconstruct the transverse proton densities from a set of four beam-imaging scans. The distribution of the measured vertices collected during all steps of a beam-imaging scan is used as a proxy to the proton density. The parameters of the proton density models can then be extracted from a fit to the vertex data without relying on beam separation information. In this thesis, the beam-imaging method was brought to maturity and applied to all Run 2 datasets. In the following sections, the method and its results are discussed, using the beam-imaging scan sets from Fills 4266 and 4954 as examples. A full account of this work is also given in Reference [I].

The ATLAS and ALICE experiments perform a **beamspot evolution analysis** to reconstruct the three-dimensional proton densities of the two beams. It employs a three-dimensional fit to the reconstructed vertices of each step of a set of VdM and (optionally) offset scans to extract beamspot observables: mean position and width in three coordinates, and tilts between any two coordinates. A fit to this set of observables together with the measured rate as functions of the beam separation is used to estimate the parameters of the proton densities. A complementary method, employed by the ATLAS experiment, is the **offset scan analysis** which uses only the rate measurements during VdM and offset scans to extract the transverse profile of the beam overlap region [129, 130].

Figure 2.12

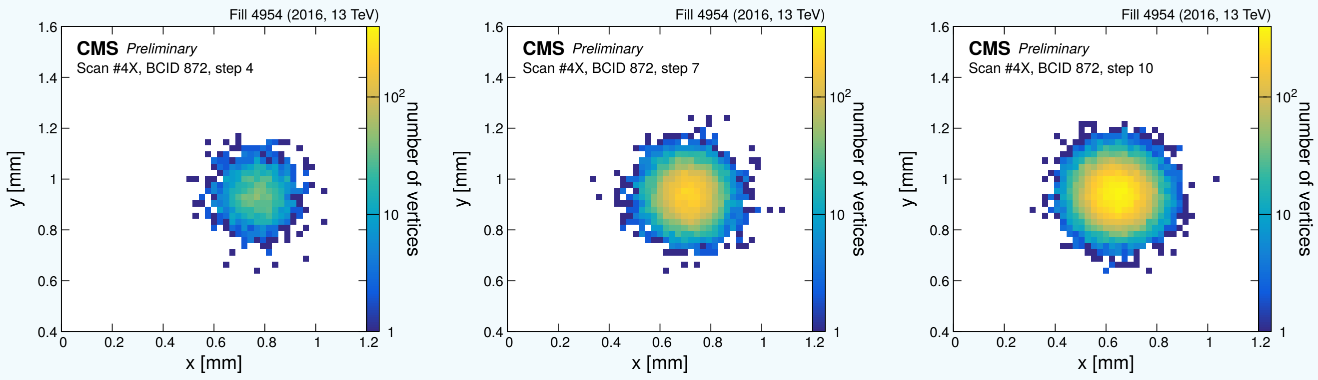

Distribution of vertex positions at the fourth (left), seventh (middle), and tenth (right) step of the beam-imaging scan where the first beam is moved horizontally, recorded for BCID 872 in Fill 4954, published in Ref. [G].

A special technique applied at the LHCb experiment is **beam-gas imaging**. Neon gas is injected into the beam interaction region such that both beam-beam and beam-gas interactions occur for colliding bunch pairs and beam-gas interactions only for non-colliding single bunches. Differentiating the reconstructed vertices from beam-beam and beam-gas interactions by the directions of their associated tracks, the vertex distributions from both kinds of interactions can be fitted separately to obtain the proton densities of the two beams [108, 131, 132].

2.8. Beam-imaging method

In a beam-imaging scan, one beam remains constant at its nominal head-on position while the other beam is moved in steps along one transverse direction, as shown schematically in Figure 2.4b. In each scan step, the transverse distribution of vertices $N_{\mathrm{vtx}}(x, y)$ depends on the two proton densities and the separation of the two beams. In the case of a scan where the first beam moves horizontally, the vertex distribution for a separation Δx can be described by the relation:

$$N_{\mathrm{vtx}}(x, y; \Delta x) \propto \Big[f_1(x + \Delta x, y) \cdot f_2(x, y) \Big] \otimes V, \tag{2.20}$$

where $\otimes V$ denotes a convolution of the beam overlap region with the vertex resolution function. In Figure 2.12, examples of these distributions are shown. The transverse distribution of the vertices combined from all steps of one scan is described by the sum over the per-step distributions,

$$\sum_{\Delta x} N_{\text{vtx}}(x, y; \Delta x) \propto \left[\left(\sum_{\Delta x} f_1(x + \Delta x, y)\right) \cdot f_2(x, y)\right] \otimes V. \tag{2.21}$$

For a small step size, the sum can be approximated by an integral over the beam separation Δx:

$$\begin{aligned}\sum_{\Delta x} N_{\text{vtx}}(x, y; \Delta x) &\approx \left[\left(\int_{-\infty}^{\infty} f_1(x + \Delta x, y)\, \mathrm{d}\Delta x\right) \cdot f_2(x, y)\right] \otimes V \\ &= \left[(\mathcal{M}_x f_1)(y) \cdot f_2(x, y)\right] \otimes V.\end{aligned}$$

Figure 2.13

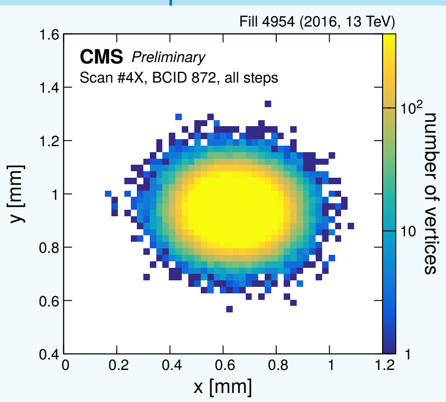

Distribution of vertex positions from all steps of the beam-imaging scan where the first beam is moved horizontally, recorded for BCID 872 in Fill 4954, published in Ref. [G].

Here, $\mathcal{M}_x f_1$ denotes the marginalisation of f_1 along the horizontal direction. On the right-hand side of Equation (2.8), only f_2 depends on x, i. e. the resulting vertex distribution depends only on the non-factorisation present in f_2. Its x dependence is then a direct proxy for the horizontal profile of f_2. Thus, Equation (2.8) is called the “beam image”. An example beam image is shown in Figure 2.13. Four beam images, obtained from four beam-imaging scans for both beams along two orthogonal directions, then allow to extract the complete transverse proton distribution functions of the two beams [128, I].

One complication in the beam-imaging method is the presence of the vertex resolution function in Equation (2.8). It is typically modelled with a two-dimensional Gaussian function without correlation parameter, cf. Equation (2.18). Since the convolution of two Gaussian functions is again a Gaussian function with analytically calculable parameters [133], only Gaussian functions and sums of Gaussian functions are used as proton density models.

In this analysis, normalised sums of up to three Gaussian distributions are considered. Typically, the additional Gaussian components with wider widths facilitate a description of wider tails to the distribution. A description of a flattened central part of the distribution can be achieved with a super-Gaussian function, i. e. a Gaussian-like function with an exponent larger than 2 in the exponential (used e. g. in laser beam optics [134]). However, super-Gaussian functions cannot be convolved analytically with the Gaussian vertex resolution function. To approximate the “flat-top” behaviour of super-Gaussian functions, a Gaussian function with a narrow width and small weight is

Table 2.5

name	symbolic formula		#P
single-Gaussian	SG =	Gauss_M	3
double-Gaussian	DG =	$w_\text{M}\text{Gauss}_\text{M} + w_\text{W}\text{Gauss}_\text{W}$	7
triple-Gaussian	TG =	$w_\text{M}\text{Gauss}_\text{M} + w_\text{W}\text{Gauss}_\text{W} + w_\text{E}\text{Gauss}_\text{E}$	11
"super-Gaussian"	SupG =	$-w_\text{N}\text{Gauss}_\text{N} + w_\text{M}\text{Gauss}_\text{M}$	7
"super-double-Gaussian"	SupDG =	$-w_\text{N}\text{Gauss}_\text{N} + w_\text{M}\text{Gauss}_\text{M} + w_\text{W}\text{Gauss}_\text{W}$	11

Two-dimensional functions used to model the beam proton densities in the beam-imaging method. The last column gives the number of free parameters per beam. The indices represent the main (M), narrow (N), wide (W), and extra-wide (E) components. For all models, the sum of weights is set to one, i. e. one of the weights is not a free parameter.

subtracted from a main single- or double-Gaussian function. These approximations are called SupG ("super-Gaussian") and SupDG ("super-double-Gaussian") here. All fit models used are summarised in Table 2.5.

For the beam-imaging analysis of Fills 4266 and 4954, belonging to the VdM campaigns for the proton-proton data-taking periods at $\sqrt{s} = 13\,\text{TeV}$ in 2015 and 2016, respectively, the vertex selection is similar to the procedure described in Section 2.5. Reconstructed vertices are selected for the analysis if they fulfil standard quality criteria, have at least 14 associated tracks, and belong to the timestamp interval of a beam-imaging scan step. The vertex positions are binned into a two-dimensional histogram, with 38 bins per unit step size in both coordinate directions. The histograms extend to ±10 times the step size away from the average vertex positions of all selected vertices, which ensures that all outliers are included. Typically, not more than 10 % of the maximum total number of 577 600 bins are filled with selected vertices.

A simultaneous fit to the four binned beam images is implemented using the RooFit software [135]. To evaluate the agreement between the fitted model and the data, the two-dimensional residual distributions for all four beam images are computed. To this end, the data histograms are re-binned to reduce the number of bins per axis by a factor of 4, and the fit model prediction for each bin is obtained by integration of the fit function over the area of the bin. The relative residual ("pull") is then obtained as data minus the fit model divided by the statistical uncertainty of the data,

$$\text{pull}(x_i, y_j) = \frac{N_\text{vtx}^\text{data}(x_i, y_j) - N_\text{vtx}^\text{fit}(x_i, y_j)}{\delta(x_i, y_j)}. \tag{2.22}$$

The sum of all relative residuals from all four beam images provides a χ^2 value which can be used to quantify the agreement. The corresponding number of degrees of freedom is the number of filled bins in all four beam images, and is between 10 000 and 13 000 for the beam-imaging datasets of Fills 4266 and 4954.

Here, the collision events recorded at different bunch crossing numbers (BCIDs) are analysed separately, thus providing five independent datasets each for both fills.

A first fit of all datasets is performed with the single-Gaussian (SG) fit model with correlation parameters fixed to zero, $\rho_i = 0$, i. e. a factorisable model. Example residual distributions for one beam image of one BCID are shown in Figure 2.14 for Fill 4266, and in Figure 2.15 for Fill 4954. In addition to the two-dimensional residual distribution, two projections along radial and angular coordinates are shown. For the radial projection, the distance of each bin to the centre of the vertex distribution is computed, and the average relative residual is evaluated for all bins with similar distance. Similarly, for the angular projection, the angle is computed between the positive x axis and the ray from the centre of the vertex distribution through the bin.

For the fit with the factorisable model, both the radial and angular projection from Fill 4266 show a disagreement between data and the fit model. The sinusoidal shape of the radial projection hints at a deviation of the beam shape from a single-Gaussian. Since the fit model is factorisable, angular modulation can only result from different Gaussian widths in the two coordinate directions. The disagreement in the angular projection thus points towards non-factorisable features in the data which cannot be described by the factorisable fit model. For the example from Fill 4954, a qualitatively comparable shape of the projections is observed with an overall better level of agreement, especially in the angular projection. The χ^2/dof values are between 1.29 and 1.34 for the fits to the data from Fill 4266, and between 1.14 and 1.18 for Fill 4954.

Residual distributions for fit results with a SG fit model with the correlation parameter determined by the fit are shown in Figure 2.16 for Fill 4266, and in Figure 2.17 for Fill 4954. For both fills, the radial projection is very similar to the fits with $\rho_i = 0$. However, the angular projections are now much flatter and show a very good agreement between data and the fit model. For Fill 4266, the fitted values of the correlation parameter are $\rho_1 \approx -0.12$ for beam 1 and $\rho_2 \approx -0.04$ for beam 2, with a relative statistical uncertainty of less than 10 % each. Especially the large value of ρ_1 leads to a big difference in the fit result, and to a significant reduction in the χ^2/dof values which are now between 1.13 and 1.20. For Fill 4954, smaller values of $\rho_i \approx -0.05$ are obtained for both beams, resulting in a small change of the fit results and a slight reduction in χ^2/dof to values between 1.10 and 1.14.

Figure 2.14

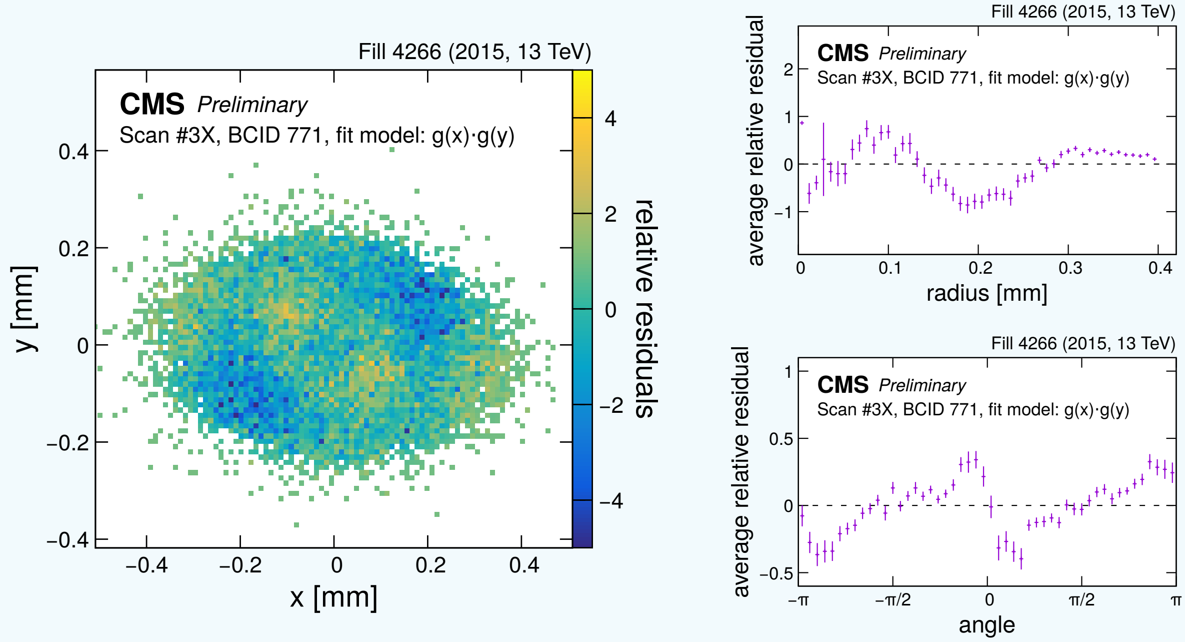

Residual distributions of the SG fit, with $\rho = 0$ fixed, to the beam-imaging scan where the first beam is moved horizontally, recorded for BCID 771 in Fill 4266. Shown is the two-dimensional distribution (left), and its projection to radial (upper right) and angular (lower right) coordinates. Published in Ref. [G].

Figure 2.15

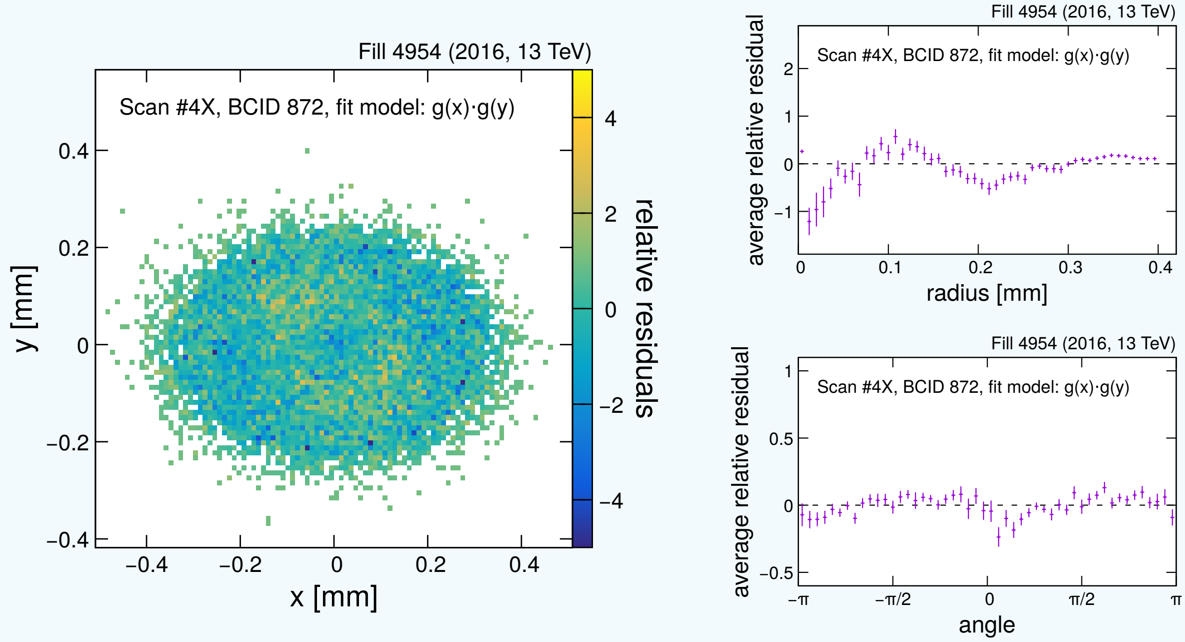

Residual distributions of the SG fit, with $\rho = 0$ fixed, to the beam-imaging scan where the first beam is moved horizontally, recorded for BCID 872 in Fill 4954. Shown is the two-dimensional distribution (left), and its projection to radial (upper right) and angular (lower right) coordinates.

Figure 2.16

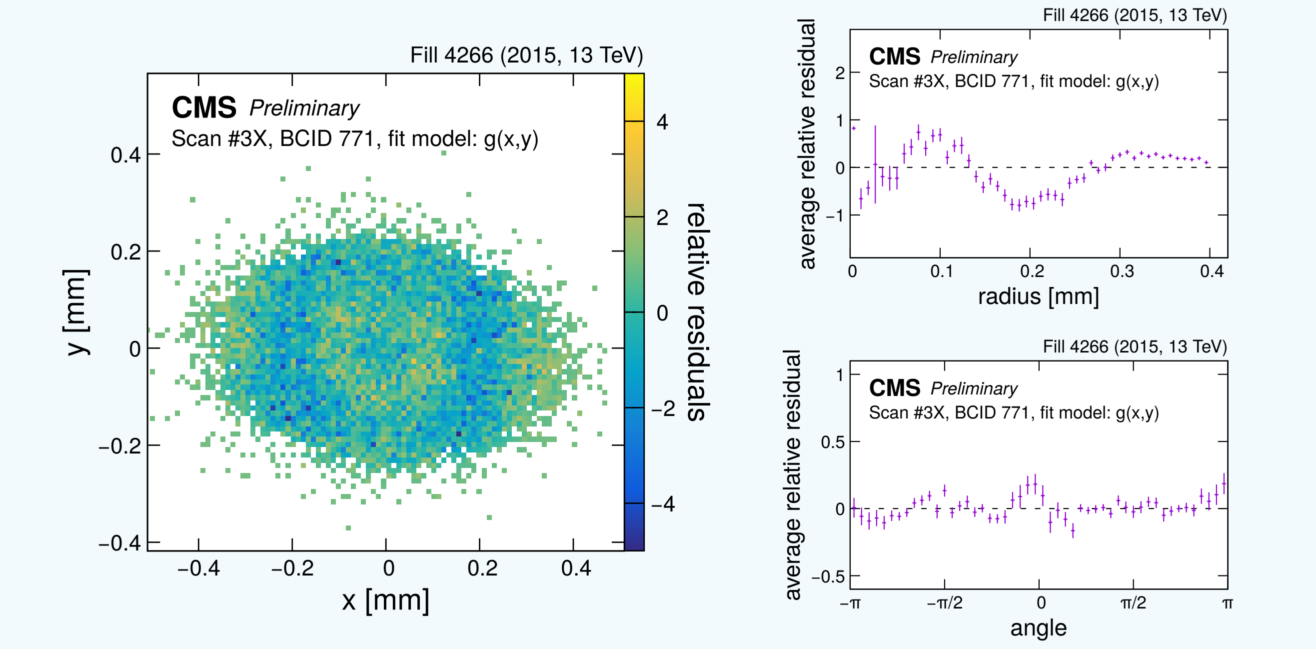

Residual distributions of the SG fit to the beam-imaging scan where the first beam is moved horizontally, recorded for BCID 771 in Fill 4266. Shown is the two-dimensional distribution (left), and its projection to radial (upper right) and angular (lower right) coordinates. Published in Ref. [G].

Figure 2.17

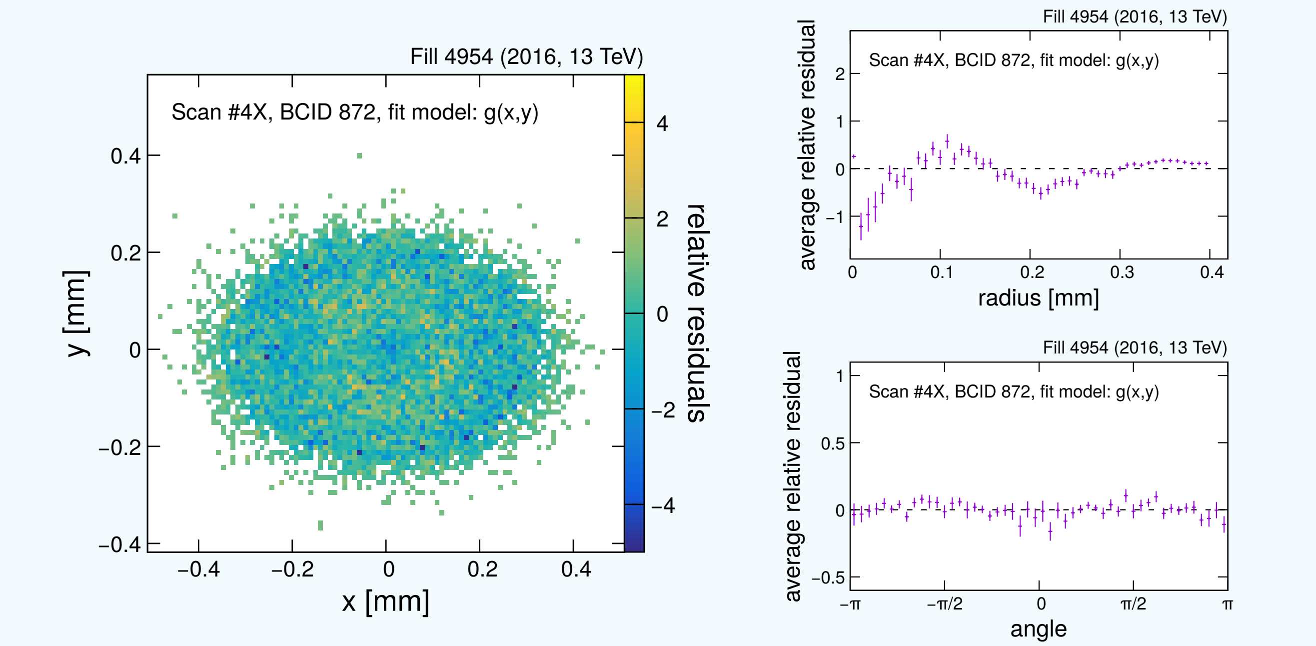

Residual distributions of the SG fit to the beam-imaging scan where the first beam is moved horizontally, recorded for BCID 872 in Fill 4954. Shown is the two-dimensional distribution (left), and its projection to radial (upper right) and angular (lower right) coordinates.

Figure 2.18

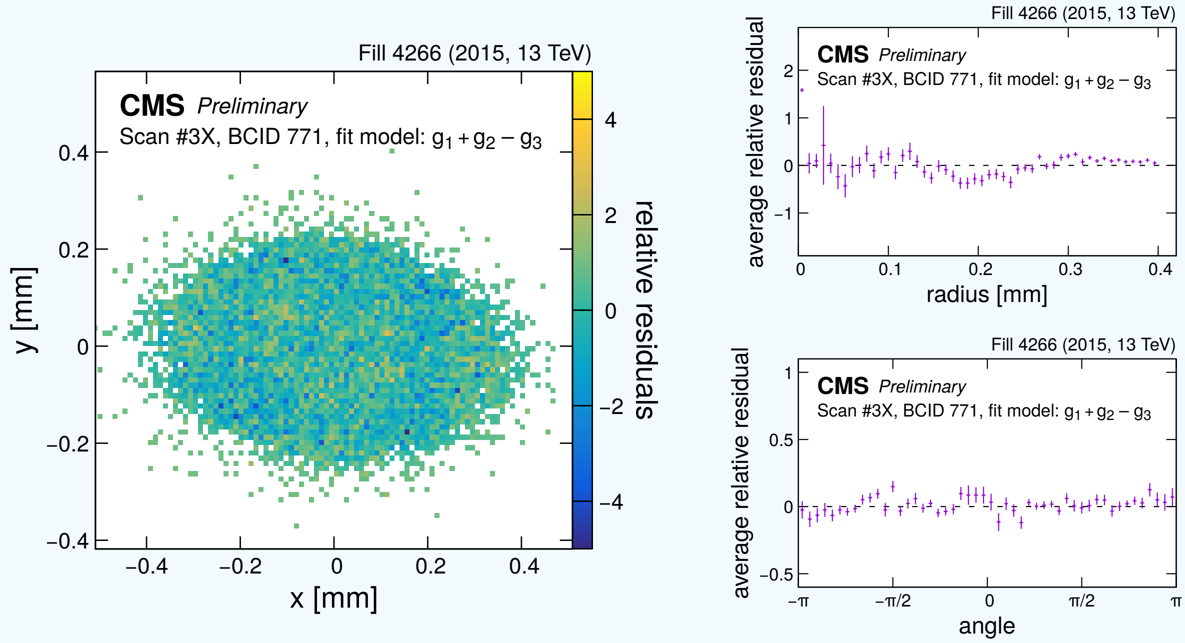

Residual distributions of the SupDG fit to the beam-imaging scan where the first beam is moved horizontally, recorded for BCID 771 in Fill 4266. Shown is the two-dimensional distribution (left), and its projection to radial (upper right) and angular (lower right) coordinates. Published in Ref. [G].

Figure 2.19

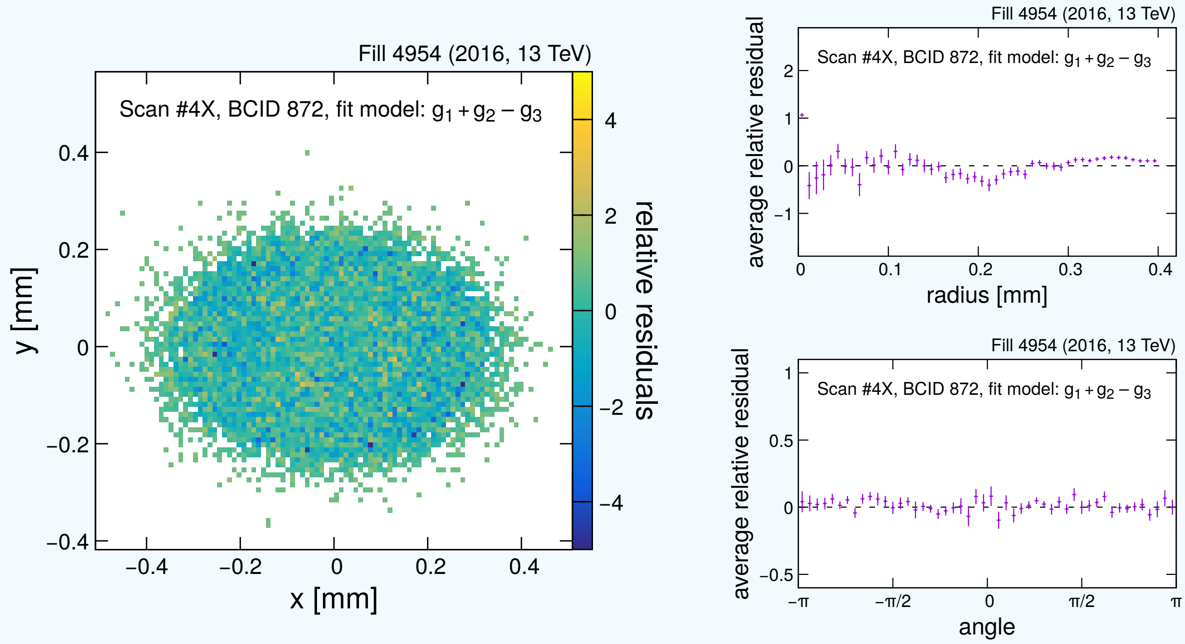

Residual distributions of the SupDG fit to the beam-imaging scan where the first beam is moved horizontally, recorded for BCID 872 in Fill 4954. Shown is the two-dimensional distribution (left), and its projection to radial (upper right) and angular (lower right) coordinates.

To obtain a good description of the radial profile of the data, fits with all models listed in Table 2.5 are performed for all datasets. For a proper convergence of the fits, positive definite model functions are required. While the sums of Gaussian distributions with only positive weights are automatically positive definite, the SupG and SupDG functions have been re-parameterised to ensure definiteness. For a further improvement of the convergence, a two-step fit procedure is applied: The first fit is performed with the SG (DG) model, and the second fit uses the resulting fit parameters as starting values for the positive components of the SupG (SupDG) fit model.

Consistently for both fills and all BCIDs, the SupDG fit model gives the best description of the data. Example fit results are shown in Figure 2.18 for Fill 4266 and in Figure 2.19 for Fill 4954. Both examples show a good agreement of data and the fit model in the radial projection, with only small modulations remaining. The χ^2/dof values range between 0.99 and 1.02 for Fill 4266, and between 1.02 and 1.04 for Fill 4954.

2.9. Bias evaluation

The result of the fits to the beam-imaging data are the transverse proton densities of the two beams. The actual beam overlap area at head-on position $A_{\mathrm{overlap}}^{\mathrm{true}}$ can now be obtained by an integration of the product of the two proton densities. To evaluate the factorisation bias, this is compared to the expected result from the VdM method $A_{\mathrm{overlap}}^{\mathrm{VdM}}$ given these proton densities. For this purpose, toy MC events are generated, reproducing the setup and the statistics of the VdM scans as observed in data. The generated pseudo-data is analysed with the standard VdM method, yielding an estimate for $A_{\mathrm{overlap}}^{\mathrm{VdM}}$ from the product of the two reconstructed beam overlap widths. The factorisation bias is now quoted as the difference between these two results, normalised to the true value, which serves as relative correction to the visible cross section:

$$\sigma_{\mathrm{vis}}^{\mathrm{corrected}} = \sigma_{\mathrm{vis}}^{\mathrm{biased}} \cdot \left(1 + \frac{A_{\mathrm{overlap}}^{\mathrm{VdM}} - A_{\mathrm{overlap}}^{\mathrm{true}}}{A_{\mathrm{overlap}}^{\mathrm{true}}}\right) . \tag{2.23}$$

In Figure 2.20, example results for this procedure are shown, using fit results with the SupDG model from both fills. The MC simulation is repeated 1000 times with the same proton densities, to evaluate the impact of the statistical uncertainty of the VdM scan pseudo-data on the factorisation bias. It is observed that the distribution of factorisation bias estimates can be described by a Gaussian distribution with a small standard deviation of typically 0.1 %. To check the impact of the statistical uncertainty of the beam-imaging data on the factorisation bias estimation as well, the MC simulation

Figure 2.20

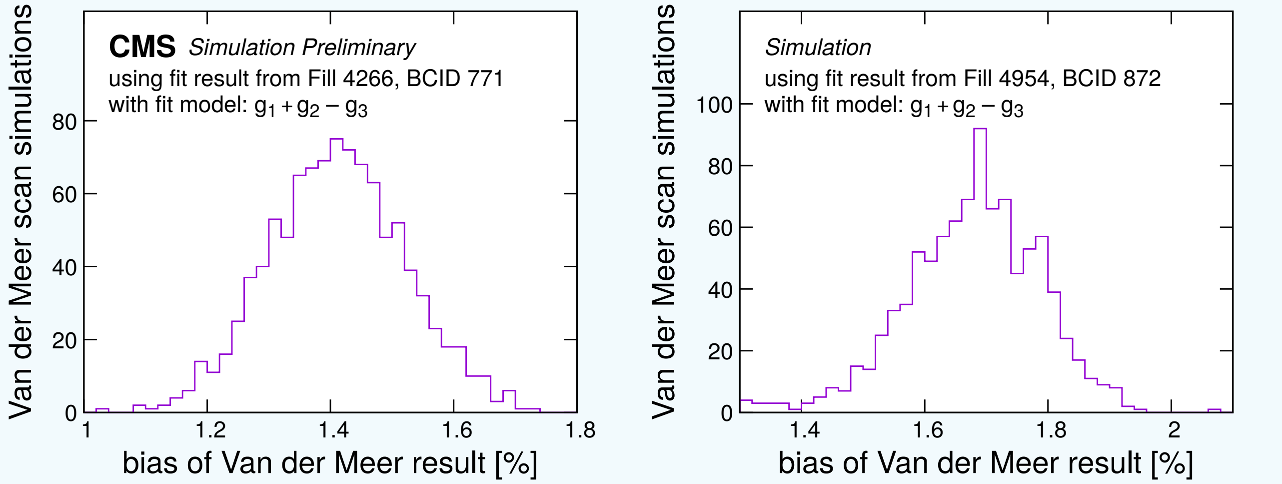

Factorisation bias of VdM results, evaluated for 1000 independent MC simulations of VdM scans, using the SupDG model from a fit to beam-imaging data in Fill 4266 (left, published in Ref. [G]) and Fill 4954 (right).

is repeated 1000 times with varied proton densities, where simultaneously all parameter values are randomly drawn from Gaussian probability distributions with fitted values and fit uncertainties as means and widths. This alternative set of MC simulations results in a distribution of factorisation bias estimates that is in agreement with the nominal distribution, both with respect to the mean value and the spread. Thus, the RMS of the nominal distribution of factorisation bias estimates is used to estimate both the statistical uncertainty from the beam-imaging and the VdM scan data.

For an evaluation of the systematic uncertainty of the factorisation bias estimate, a closure test is performed: Since the SupDG fit model gives the best description of the data, it is assumed that the true proton densities are of SupDG shape. How precisely the beam-imaging method with the SupDG fit model reproduces the factorisation bias of the true model is tested by generating MC pseudo-data for several SupDG toy models and analysing the pseudo-data with a SupDG fit model. The following four steps are performed.

1. A **SupDG toy model**, i. e. a set of parameters for two SupDG functions describing the proton distribution functions of the two beams, is generated. The parameters are drawn from uniform distributions, defined as realistic ranges of values that cover the

Figure 2.21

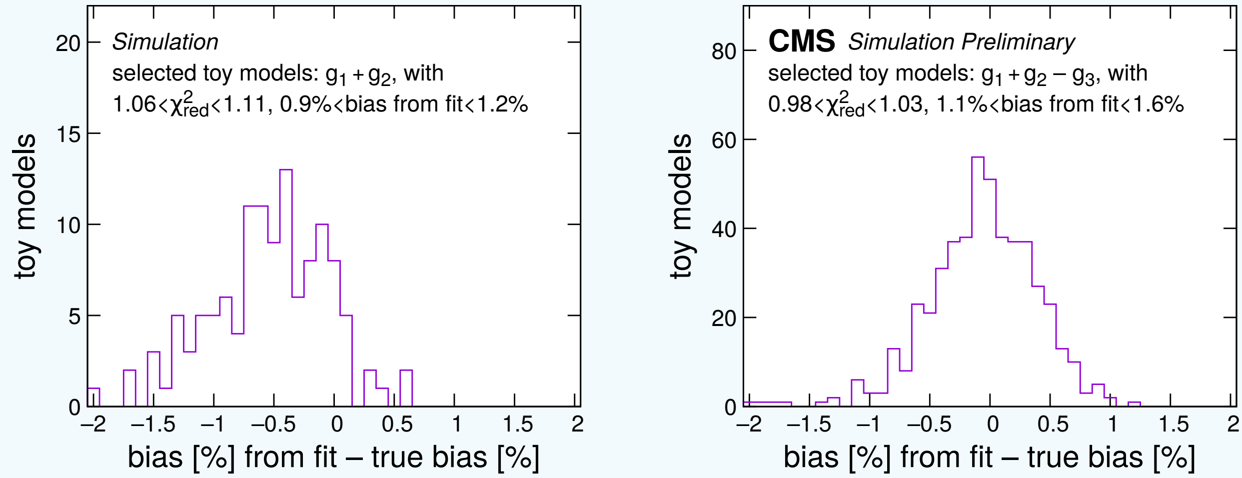

Difference between bias obtained from direct integration of a toy model ("true bias") and from a fit to pseudo-data ("bias from fit") using the DG model (left) and using the SupDG model (right, published in Ref. [G]), for a selection of toys similar to the fit results from Fill 4266.

parameter values obtained in the fits to data. For some parameters of the negative component, the range is defined after the other parameters have been generated and restricted to values for which the resulting function is positive definite. The true factorisation bias is evaluated using this toy model.

2. With the toy model, MC toy events are generated for a set of four beam-imaging scans. This **beam-imaging pseudo-data** represents the statistics and the setup of the beam-imaging scans performed at the CMS experiment.

3. The pseudo-data is fitted with a **DG fit model**, using the same procedure as applied for fits to data. With the fit result, the factorisation bias for the case of a DG fit model is evaluated.

4. The pseudo-data is fitted with a **SupDG fit model**, using the fit results from the DG fit model as starting values for the positive components. With the fit result, the factorisation bias for the case of a SupDG fit model is evaluated.

A comparison of the factorisation bias obtained from a fit result and the true factorisation bias allows to assess the precision of the method. About 28 000 toys, including pseudo-data and both fits, have been generated. To evaluate the accuracy of a set of fit results, the toys with a fit performance similar to the data fits are selected. The fit performance is quantified by the value of the χ^2/dof and by the value of the fitted factorisation bias.

Figure 2.22

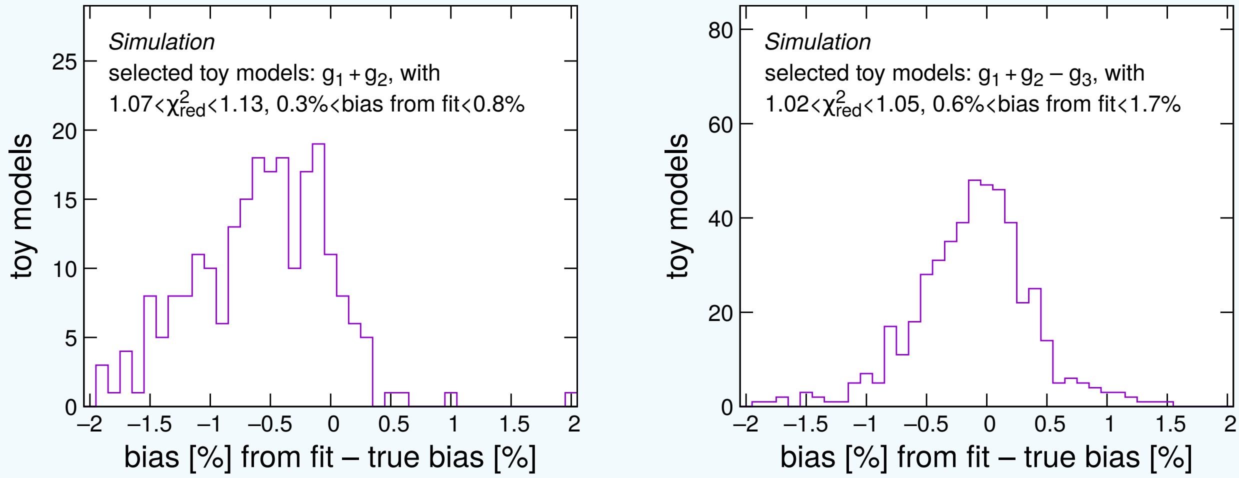

Difference between bias obtained from direct integration of a toy model ("true bias") and from a fit to pseudo-data ("bias from fit") using the DG model (left) and using the SupDG model (right), for a selection of toys similar to the fit results from Fill 4954.

In Figure 2.21, the difference between the fitted and the true bias is shown for toys similar to the fit results from Fill 4266. Fitting the SupDG toys with a DG model results in an underestimation of the factorisation bias, with an average deviation of $-0.55\,\%$. However, using the SupDG fit model, the factorisation bias estimation is unbiased with an average deviation of $-0.06\,\%$ and a spread of $0.45\,\%$.

The same evaluation for toys similar to the fit results from Fill 4954 is shown in Figure 2.22. While the fit results with a DG model are strongly biased with an average deviation of $-0.59\,\%$, the fit results with a SupDG model have a small bias of $-0.11\,\%$ and a spread of $0.49\,\%$. The quadratic sum of average deviation and spread is now used to estimate the systematic uncertainty of the fitted factorisation bias due to the accuracy of the beam-imaging method.

With the knowledge about the accuracy of the beam-imaging method for different fit models, the factorisation bias obtained for different datasets and different fit models can be compared. In Figure 2.23, the estimates for both fills using both DG and SupDG fit models for all five BCIDs each are shown, with error bars showing the combined uncertainty from the MC simulation of VdM scans and from the evaluation of the closure test. The estimates from the DG fit results are consistently smaller than the estimates from the SupDG fit results, as expected from the large bias seen in the closure test. However, with the larger assigned uncertainty, the DG estimates are consistent with the SupDG results everywhere. The spread of the SupDG fit results is small compared

Figure 2.23

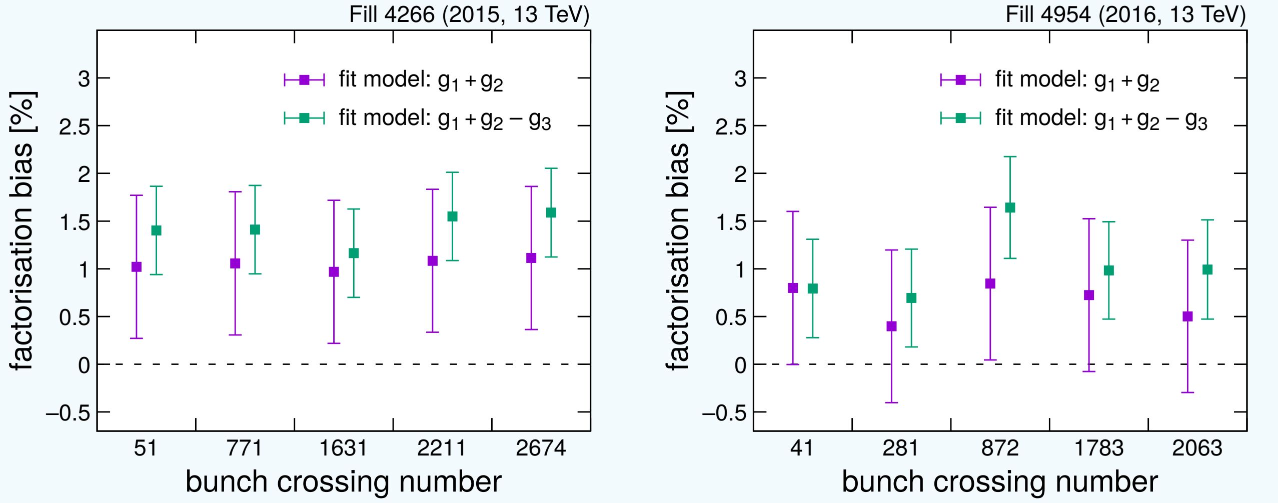

Factorisation bias obtained from fits to the data from Fill 4266 (left) and from Fill 4954 (right) using the DG fit model (violet) and the SupDG fit model (green).

to the assigned systematic uncertainty.

To apply a correction to the visible cross section obtained from the VdM scans, the average of the factorisation bias estimates obtained for the different BCIDs of a fill is used. The final corrections to the visible cross section thus are:

$$1.42\,\% \pm 0.46\,\% \qquad \text{for Fill 4266,} \tag{2.24}$$

$$1.02\,\% \pm 0.53\,\% \qquad \text{for Fill 4954.} \tag{2.25}$$

As additional checks, variations of the beam-imaging dataset are considered, namely

- with a tighter vertex selection with a requirement of at least 24 tracks, resulting in an improved vertex resolution and lower statistics;
- an older tracker alignment setup, to probe the impact of misalignment effects; or
- using four VdM scans instead of four beam-imaging scans. To obtain beam images as in Equation (2.8) from the vertex distributions selected for the steps of a VdM scan, the nominal beam position of one beam is subtracted from the position of all selected vertices, separately for each step. The combination of the modified vertex distributions then resembles the setup of a beam-imaging scan in which the other beam remains at a constant position. This approach introduces an additional dependence on the knowledge of the beam separation scale.

For each variation, the full analysis is repeated including the fits to the beam-imaging data, the evaluation of the factorisation bias, and the evaluation of the toys from the closure test. The resulting factorisation bias estimates are compatible with the nominal

Figure 2.24

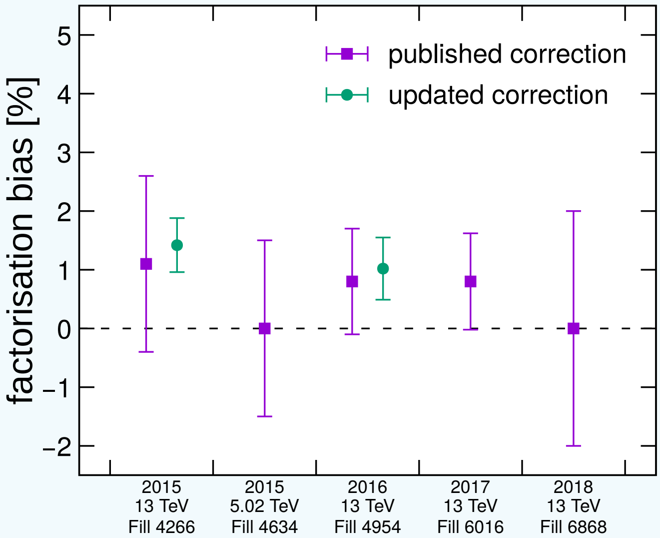

Factorisation bias corrections to the visible cross section for different data-taking periods. For the published corrections, see Ref. [A–C, F, 115]. The updated entries for Fills 4266 and 4954 show the results from this chapter.

estimate, separately for each BCID of both fills.

2.10. Results

In Run 2, the beam-imaging method was the main technique to determine the factorisation bias of the VdM calibration results. Consequently, beam-imaging scans have been performed in the VdM campaigns of all proton-proton data-taking periods, and preliminary results have been published. In Figure 2.24, the factorisation bias estimates from the preliminary luminosity calibrations are summarised together with the updated results for Fills 4266 and 4954 presented here.

The initial luminosity calibration with Fill 4266 used only the DG model for the fit of the beam-imaging data, and estimated a factorisation bias of 1.1 % ± 1.5 % [A]. For Fill 4954, the initial luminosity calibration was extended with the SupDG model for the fit, but it did not use the DG fit model as starting value for its parameters, resulting in a worse performance of the fits with the SupDG model. The factorisation bias was estimated to be 0.8 % ± 0.9 % [B]. In both cases, the uncertainty estimation is based on a comparison of estimates from different fit results and using different fit models, and the factorisation bias constitutes the largest contribution to the calibration uncertainty of the luminosity measurement.

Figure 2.25

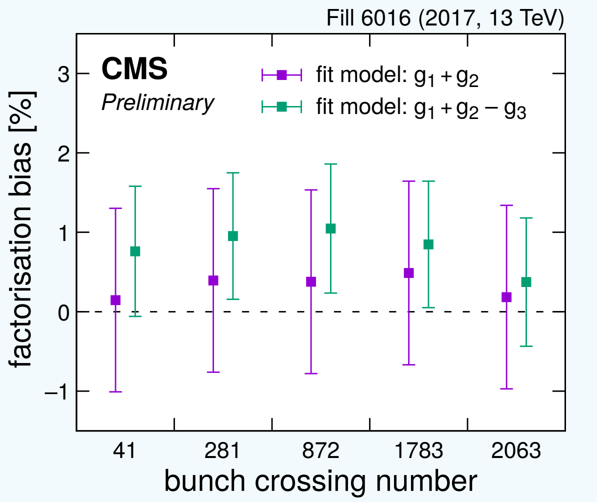

Factorisation bias obtained from fits to the data from Fill 6016 (right) using the DG fit model (violet) and the SupDG fit model (green), published in Ref. [G].

The updated method discussed in this chapter improves the fit results by the introduction of the two-step fit procedure, and supplements the data fits with a dedicated closure test on MC simulations. While the updated factorisation bias estimates are consistent with the preliminary values, the updated method reduces the uncertainty to about 0.5 % for both calibrations.

For the luminosity calibration with Fill 6016, the updated method has been applied already for the preliminary result. However, in contrast to the very good description of the beam-imaging data of Fills 4266 and 4954 with a SupDG model for the proton densities, the fit results here show a much worse agreement of data and fit model, with χ^2/dof values between 1.10 and 1.27. From the evaluation of the closure test, a large bias of −0.33 % with a spread of −0.72 % is found for the factorisation bias estimates from the SupDG fit results. In Figure 2.25, the resulting estimates with their assigned uncertainty are shown. Finally, a factorisation bias correction of 0.8 % ± 0.8 % [C] was applied.

Table 2.6

Fill	χ^2/dof
4266	1.13 – 1.20
4954	1.10 – 1.14
6016	1.39 – 1.50
6868	1.61 – 1.77

Comparison of SG fit results.

The most recent luminosity calibration with Fill 6868 does not use the fit results of the beam-imaging data for a correction of the factorisation bias, as no sufficiently good description of the data by the fit models has been achieved so far. Already with the simple SG fit model, the agreement of data and fit model is much worse compared to other fills analysed, as summarised in Table 2.6. These fit results suggest that the deviation of the beam proton density from the single-Gaussian shape is much larger for Fill 6868. In comparison, the ATLAS experiment reported a small factorisation bias in the same fill [112]. In the preliminary result, the CMS experiment did not apply a correction and assigned an uncertainty of 2 % due to the unknown factorisation bias [F].

2.11. Outlook

The estimation of the factorisation bias with the beam-imaging method, including complex fit models and a closure test for the evaluation of the systematic uncertainty, has been developed in this thesis and applied to the luminosity calibration of the proton-proton collision datasets recorded in 2015 and 2016 at $\sqrt{s} = 13\,\text{TeV}$. Compared to the preliminary calibration results, the precision of the factorisation bias correction has been significantly improved. In contrast, the same method has also been applied to the 2017 and 2018 datasets but does not yield similarly good results. Thus, it is necessary to further investigate the factorisation bias estimation.

Beam separation scale While the beam-imaging method does not use the beam positions or the beam separation scale, it relies on the assumption that the non-moving beam stays at a constant position in each beam-imaging scan. From the effects that impact the beam separation scale introduced in Section 2.2, both orbit drift and beam-beam deflection can lead to violations of this assumption.

The electric repulsion of the two proton beams, called **beam-beam deflection**, depends on the separation of the beams, and thus introduces a change in the position of the non-moving beam over the course of a beam-imaging scan. In Figure 2.26, the analytically calculated beam-beam deflection [121] during a beam-imaging scan from Fill 4954 is shown. The maximal position difference of the non-moving beam between any two steps is less than 4 µm, such that no big impact is expected on the results of the beam-imaging analysis. Correlated to beam-beam deflection is the dynamic $\beta^\star$ effect, describing the defocusing of one beam due to the other beam's quadrupole field. This effect influences the shape of the proton density differently at different separations, which may have an impact on the beam-imaging results. Since both beam-beam deflections and the dynamic $\beta^\star$ effect can be predicted analytically, a correction for the beam-imaging data should be investigated.

Figure 2.26

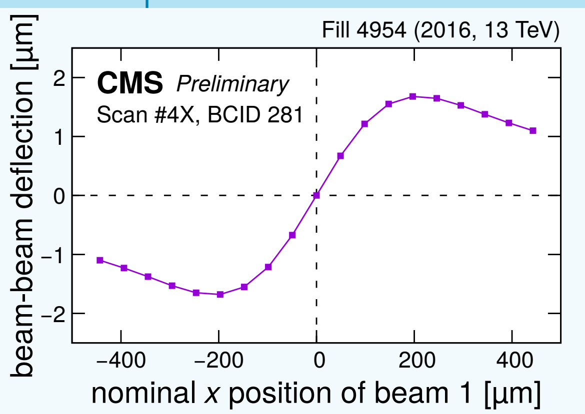

Change of the horizontal position of the non-moving beam due to beam-beam deflection during a beam-imaging scan from Fill 4954, taken from Ref. [G].

Time-dependence of the beam position for fixed machine parameters, the effect known as **orbit drift**, can cause a variation of the position of the non-moving beam over the course of a beam-imaging scan. However, it is typically observed to be small [120] and thus not expected to have a large impact on the quality of the beam-imaging data. In Section 2.5, a method to correct for observed orbit drift has been discussed in the context of the length scale calibration. However, this approach only considers corrections to the beam separation, whereas the beam-imaging method would require a correction for the beam position of only one beam. For a quantitative study of the impact of orbit drift, new orbit drift correction strategies need to be developed.

Method improvements To model the beam image in the fit, a convolution with the two-dimensional vertex resolution function is required, cf. Equation (2.8). The analysis procedure of the beam-imaging method presented here is restricted to proton density models that can be analytically convoluted with a Gaussian function. Additionally, the CPU time of the implemented fit increases drastically with the number of free parameters, such that more complex models built from Gaussian functions—like the normalised sum of four Gaussian functions—are not practical from a computing point of view. Some ideas exist to circumvent this complication and to thus obtain a better description of the data beyond what is possible with the models used so far.

- A numerical implementation of the convolution of two two-dimensional functions would remove the limitation on the initial fit models. However, a good efficiency in terms of CPU time is required such that the full workflow, including necessary iterations for systematic studies, is still feasible.
- The projected residual distributions might be used to derive a correction on the fitted proton densities such that the deviations from data are approximately cancelled. Thus, a simple model like the single-Gaussian function can be fitted and then corrected from its residual shape, without a need for more complex fit models. It remains to be demonstrated though that a meaningful proton density correction can be obtained from the beam image residuals.
- Instead of a convolution of the fit model with the vertex resolution, a deconvolution of the beam-imaging data would allow to fit arbitrary models to the unsmeared beam images. While deconvolution algorithms exist and are widely used (e. g. in astrophysics [136]), their direct applicability to the beam-imaging data needs to be investigated.

Complementary methods To validate the results of the beam-imaging method, the application of complementary methods can be helpful. In the ATLAS experiment, two approaches based on **offset scans** have been applied and are used to estimate the factorisation bias [129, 130].

In Figure 2.27, the event rates measured by the CMS experiment during a VdM scan pair and the subsequent offset scan pair from Fill 6868, performed for the 13 TeV proton-proton data-taking period in 2018, are shown. Since VdM and offset scans test different "slices" of the beam overlap region, a comparison of the measured rates allows to test the assumption of factorisable beam proton distributions. The transverse profile of the beam overlap is reconstructed from a simultaneous fit to all four scan curves. Using single-Gaussian and double-Gaussian fit models, a good description of the measured rates was found. The correlation parameter ρ extracted from this fit is in agreement with the correlation parameter extracted from single-Gaussian fits to the beam-imaging scans in the same fill [F]. Fits with more complex models, as suggested by the beam-imaging results, are, however, limited by the low event rates in the tails of the scan curves of the offset scans.

Figure 2.27

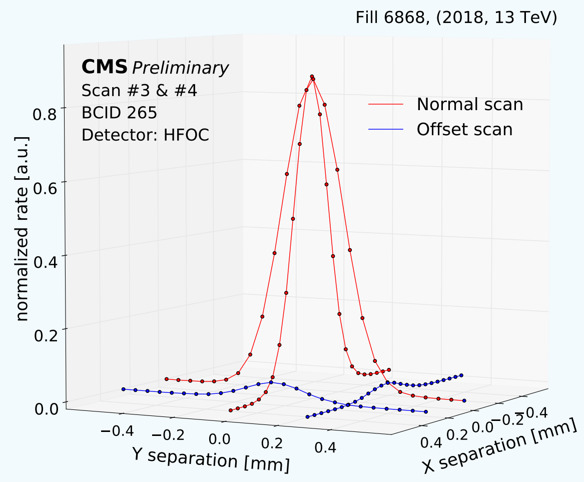

Event rate normalised by beam currents as a function of horizontal and vertical beam separation during VdM and offset scans in Fill 6868, taken from Ref. [G].

The second, more refined approach employed by the ATLAS experiment is to combine the rate measurements with information obtained from fits to the three-dimensional distribution of vertices reconstructed for each scan step. Efforts to apply this **beamspot evolution analysis** at the CMS experiment are underway.

Part 3.

Measurement of the $t\bar{t}Z$ production cross section

Figure 3.1

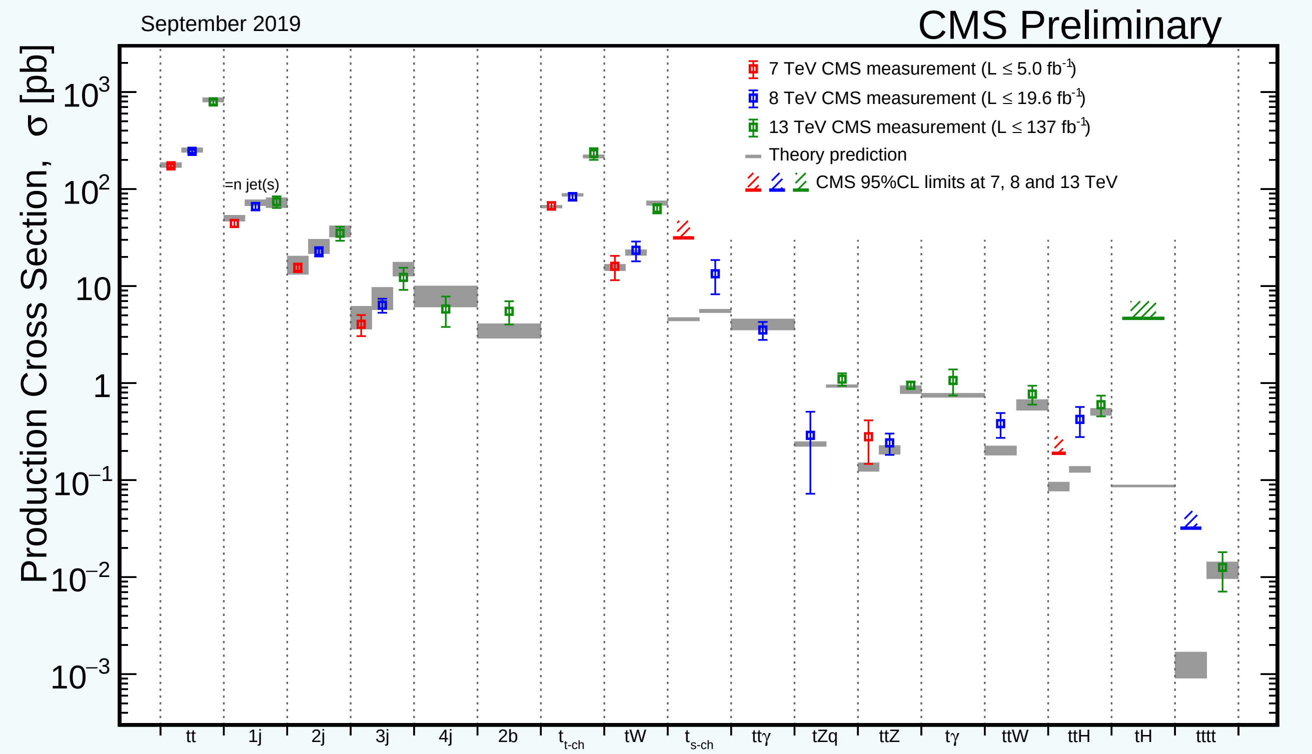

Cross sections for processes involving top quarks, measured at the CMS experiment at $\sqrt{s} = 7\,\text{TeV}$ (red), 8 TeV (blue), and 13 TeV (green), taken from Ref. [137].

VI. Top quark physics

3.1. Associated top quark production

In the 25th year after its discovery at the Tevatron [138, 139], the top quark remains an important object of study for both experimental and theoretical physics. Being the heaviest known elementary particle with a mass of $m_\mathrm{t} = 172.9\,\mathrm{GeV}$ [6], its large Yukawa coupling to the Higgs boson $y_\mathrm{t} = \sqrt{2}m_\mathrm{t}/v \approx 1$ makes the top quark the most important known contributor to loop corrections for any electroweak prediction, including the question of the stability of the electroweak vacuum [140, 141]. Since the top quark decays predominantly to W bosons and bottom quarks, $\mathrm{t} \to \mathrm{W}^+ + \mathrm{b}$, with a decay width of $\Gamma_\mathrm{t} = 1.42\,\mathrm{GeV}$ [6] larger than the QCD scale of $\Lambda_\mathrm{QCD} \approx 200\,\mathrm{MeV}$ [19], the decay precedes hadronisation, and thus all spin information is retained in the decay products. At the same time, Γ_t is sufficiently smaller than m_t, and thus predictions for top quark processes can approximately describe production and decay as factorised ("narrow-width approximation"). Measurements of different production and decay modes then allow to probe our understanding of QCD and electroweak theory via the determination of top quark properties [142, 143].

Top quark production In proton-proton collisions, top quarks are predominantly produced via the strong interaction in pairs ($\mathrm{t\bar{t}}$) or via the electroweak interaction as single top quarks. Example Feynman diagrams for both production modes are shown in Figure 3.2. The cross section for $\mathrm{t\bar{t}}$ production is about three times larger than for single top quark production. Associated top quark production modes, i. e. $\mathrm{t\bar{t}}$ or single top quarks produced together with bosons, have cross sections about three orders of magnitude smaller than the $\mathrm{t\bar{t}}$ production cross section. Together with four top quark production ($\mathrm{t\bar{t}t\bar{t}}$), these processes are sometimes referred to as "rare" top quark production [H].

Figure 3.2

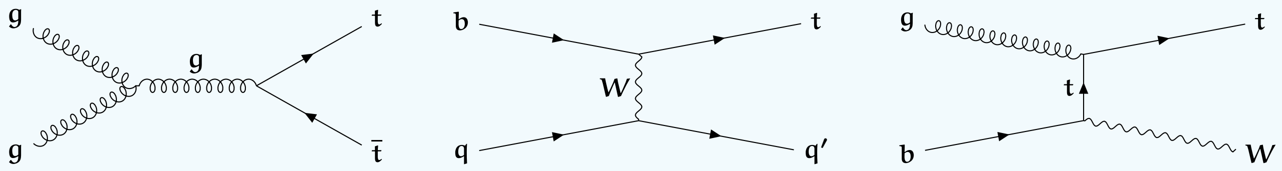

(a) pair production **(b)** t-channel single production **(c)** tW production

Example leading-order Feynman diagrams for top quark pair production (a) and single top quark production via *t*-channel production (b) and as tW production (c).

Top quark decay The decay channels of the top quark are typically classified by the subsequent decays of the W boson. Since the W boson decays to hadronic final states with a branching ratio of about 2/3, $W^{\pm} \to q\bar{q}'$, and to leptonic final states with a branching ratio of about 1/9 per lepton flavour, $W^{-} \to \ell^{-}\bar{\nu}$, the decays of a $t\bar{t}$ pair can be sorted into three channels:

- fully-hadronic decays with six jets;
- semileptonic decays with one lepton, one neutrino, and four jets,
- dileptonic decays with two opposite-sign leptons (of same or different flavour), two neutrinos, and two jets.

In all decay channels, two of the quarks are bottom quarks. Experimentally, leptons in the final state allow for a precise reconstruction of the events and an efficient rejection of background contributions. Thus, while the fully-hadronic decay channel retains the largest branching ratio, precision measurements are typically better feasible in the semileptonic or dileptonic channels [144].

Measurements of top quark production In Run 2 of the LHC, with about 140 fb^{-1} of collisions recorded at $\sqrt{s} = 13\,\mathrm{TeV}$, more than 100 million top quark events have been produced at the collision points of each the ATLAS and CMS experiments. With this wealth of data, the experiments have been able to measure a wide range of top quark production modes in different decay channels, as summarised in Figure 3.1 with results from the CMS experiment.

For **$\mathbf{t\bar{t}}$ production**, with a cross section at $\sqrt{s} = 13\,\mathrm{TeV}$ of about 830 pb, high-precision measurements have been performed in various decay channels for inclusive and differential cross sections, for mass measurements, and to determine other top quark properties. Recent examples of CMS results for $t\bar{t}$ production include the measurement of the inclusive cross section with a precision of 4 % [145], of differential cross sections [146], and of multi-differential cross sections [147], which have been used to extract QCD parameters like the top quark mass and the strong coupling constant, as well as to constrain the parton distribution functions (PDFs) of the proton. Similarly, measurements of **single top quark production** reach very good precision, with measurements of the differential cross sections in t-channel production [148] and the total cross section of tW production [149] as recent examples. Since the cross section measurements are now limited by systematic uncertainties, e. g. on the integrated luminosity [145], dedicated studies of systematic effects are required to further improve the precision of the measurements.

Associated production modes also become accessible for measurements at the LHC, and provide unique opportunities to probe the electroweak couplings of the top quark. Measurements of associated $\mathrm{t\bar{t}}$ production with neutral bosons, i. e. $\mathrm{t\bar{t}}\gamma$, $\mathrm{t\bar{t}H}$, and $\mathrm{t\bar{t}Z}$ production, are the first direct tests of the coupling between the top quark and the photon, the Higgs boson, and the Z boson, respectively. They allow to directly access the electric charge, the Yukawa coupling, and the electroweak dipole moments of the top quark, or to more generally constrain modifications of the Lorentz structure of these couplings, as predicted in many BSM models. The impact of different new physics scenarios on these three processes is discussed in References [150–155].

Evidence for **$\mathbf{t\bar{t}}\boldsymbol{\gamma}$ production** was already found at the Tevatron by the CDF experiment [156]. At the LHC, it has been observed by the ATLAS experiment at $\sqrt{s} = 7\,\mathrm{TeV}$ [157]. High-precision measurements of the inclusive and differential cross section in a fiducial phase space for semileptonic and dileptonic $\mathrm{t\bar{t}}$ decays have been performed at $\sqrt{s} = 13\,\mathrm{TeV}$ by the ATLAS experiment, with all results found in good agreement with the standard model predictions [158, 159].

The observation of **$\mathbf{t\bar{t}H}$ production** has been reported by both the ATLAS and CMS experiments in 2018, combining various decay channels of both Higgs boson and $\mathrm{t\bar{t}}$ pair, and the datasets taken at $\sqrt{s} = 7\,\mathrm{TeV}$, $8\,\mathrm{TeV}$, and $13\,\mathrm{TeV}$ [160, 161]. Because of the special role of the top quark Yukawa coupling for electroweak symmetry breaking, the measurement of $\mathrm{t\bar{t}H}$ as the first direct test of this coupling remains especially important.

Simultaneous measurements of **$\mathbf{t\bar{t}Z}$ and $\mathbf{t\bar{t}W}$ production** have been performed at $\sqrt{s} = 8\,\mathrm{TeV}$ by the ATLAS and CMS experiments, establishing the observation of both processes and constraining deviations from their predicted SM couplings [162, 163]. Similar measurements have been repeated by both experiments at $\sqrt{s} = 13\,\mathrm{TeV}$ [164–166].

In the latest measurement of $\mathrm{t\bar{t}Z}$ production performed by the CMS experiment [E], using $\sqrt{s} = 13\,\mathrm{TeV}$ data collected in 2016 and 2017, the inclusive cross section measurement

Figure 3.3

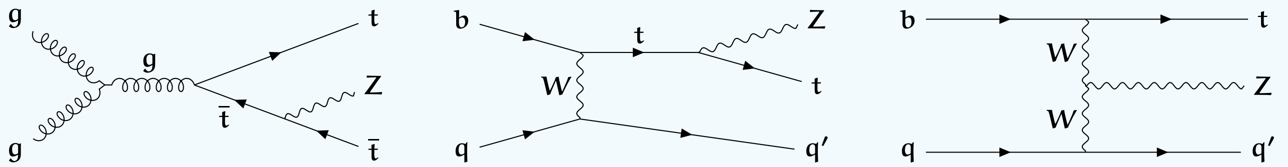

(a) $t\bar{t}Z$ production (b) tZq with tZ vertex (c) tZq with triboson vertex

Examples of leading-order Feynman diagrams for $t\bar{t}Z$ production (a) and for tZq production (b, c).

reaches a precision that is competitive with current cross section predictions and where statistical and systematic uncertainties contribute equally. Additionally, a first differential measurement of the $t\bar{t}Z$ production cross section has been performed. The status of $t\bar{t}Z$ production measurements is further discussed in Section 3.3.

Additional attention is attracted to the measurements of $t\bar{t}Z$ and $t\bar{t}W$ production from both the $t\bar{t}H$ measurement, especially in final states with many leptons, and from dark matter searches (or more general new physics searches) in final states with top quarks and missing energy, since $t\bar{t}Z$ production, with the $Z \to \ell^+\ell^-$ and $Z \to \nu\bar{\nu}$ decay modes, respectively, and $t\bar{t}W$ production with its $W \to \ell\nu$ decay mode are important background processes. Special efforts are thus made to improve the precision of the background estimation, theoretically e. g. in Reference [167].

Complementary to associated $t\bar{t}$ production, the single top production in association with bosons provides sensitivity to the same couplings but in processes with electroweak top quark production. When considering more general deviations from the SM, e. g. in the framework of the SM effective field theory (SMEFT), associated $t\bar{t}$ production gets large contributions from modifications of the strong interaction which can conceal the effect from modifications of the electroweak top quark couplings. In Figure 3.3a, for example, a Feynman diagram for $t\bar{t}Z$ production is shown which depends on the strong triple-gluon and the top quark–gluon couplings in addition to the electroweak top quark–Z boson coupling. In contrast, associated single top quark production allows to directly access the electroweak couplings, including not only the top quark couplings, e. g. the top quark–Z boson coupling in tZq production as shown in Figure 3.3b, but also triple-boson couplings like the WWZ vertex in case of tZq production shown in Figure 3.3c [168, 169].

Associated single top production with a photon has been measured by the CMS experiment in the t-channel production mode, i. e. **tγq production**, at $\sqrt{s} = 13\,\text{TeV}$.

Using events with one muon from the top quark decay and a photon, evidence has been found for tγq production against a huge background of $t\bar{t}\gamma$ events [170].

Higgs bosons produced in association with a single top quark have been searched for by the CMS experiment in both the t-channel and the tW production modes, i. e. **tHq and tHW production**. Measurements of different decay channels at $\sqrt{s} = 13\,\text{TeV}$ have been combined and used to constrain the absolute value and sign of the top quark Yukawa coupling, complementary to the measurement of the absolute value in $t\bar{t}H$ production. No significant deviation from the SM expectation has been found [171].

Single top quark production in association with a Z boson has been observed at $\sqrt{s} = 13\,\text{TeV}$ by both the ATLAS and CMS experiments in the t-channel production mode, i. e. **tZq production**, using the $Z \rightarrow \ell^+\ell^-$ decay mode and against large background contributions from $t\bar{t}Z$ production. The measured cross sections are in agreement with the SM predictions [172, 173].

Finally, **four top quark production** has a very small predicted cross section of about 12 fb at $\sqrt{s} = 13\,\text{TeV}$ in the SM. As it receives contributions from intermediate Higgs bosons coupled to top quarks, it provides another probe of the top quark Yukawa coupling. Additionally, due to its low SM cross section, new physics modifications of $t\bar{t}t\bar{t}$ production can easily increase the production cross section significantly, and thus the four top quark signature has been used in new physics searches. The ATLAS and CMS experiments search for $t\bar{t}t\bar{t}$ production in different decay modes with between one and three leptons in the final state. However, no evidence has been found so far for $t\bar{t}t\bar{t}$ production, and the cross section limits are in agreement with the SM expectation [174–176].

In summary, many different associated top quark production modes have already been measured at the LHC. With the full Run 2 dataset, which has not been yet fully analysed for most of the processes, an unprecedented precision in the total cross section measurement was made and first differential measurements have been achieved. The results are used to evaluate the electroweak top quark couplings and to put constraints on new physics effects. So far, all results are found to be in agreement with the SM predictions. As both measurements and predictions will further improve in precision, it will be beneficial to adapt the analyses to a global strategy, like the SMEFT approach that targets the simultaneous measurement of all relevant couplings [177, 178].

Figure 3.4

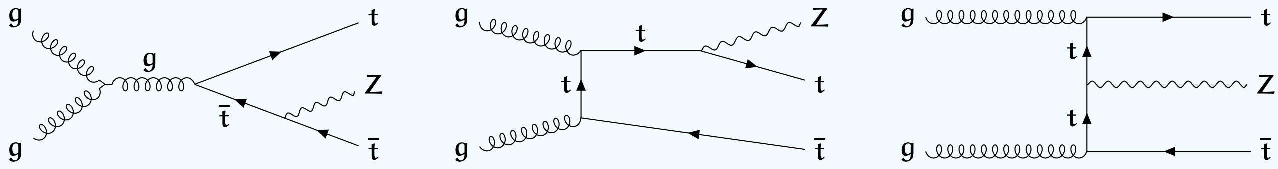

(a) strong production from gg initial state

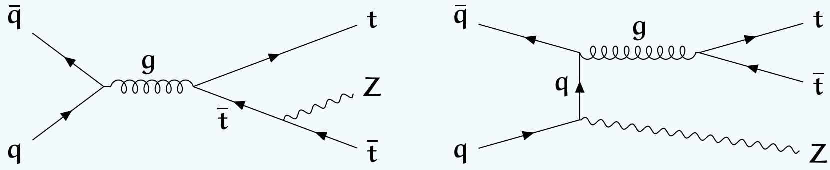

(b) strong production from $q\bar{q}$ initial state

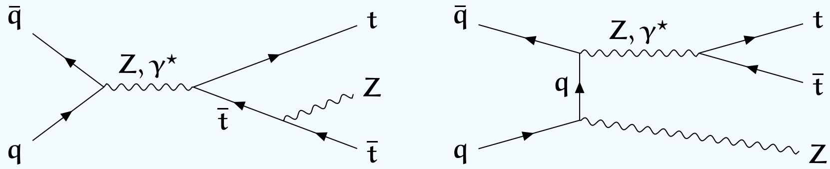

(c) electroweak production from $q\bar{q}$ initial state

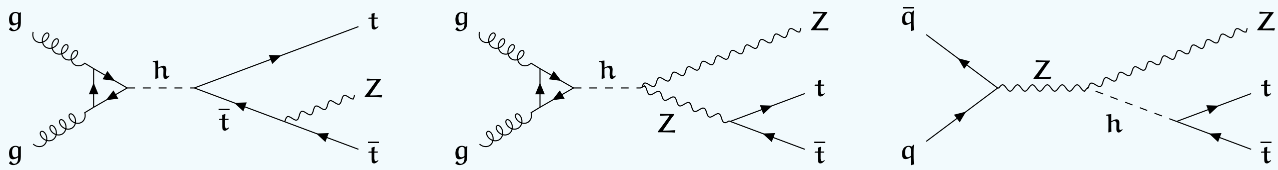

(d) production via a virtual Higgs boson

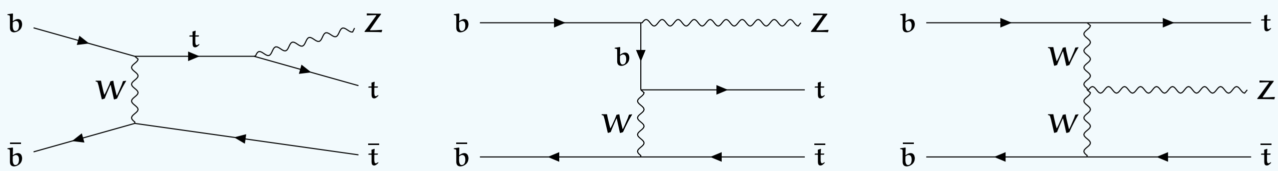

(e) electroweak production from $b\bar{b}$ initial state

Leading-order Feynman diagrams for $t\bar{t}Z$ production in proton-proton collisions. Diagrams that can be obtained by charge conjugation are omitted.

3.2. Cross section predictions for $t\bar{t}Z$ production

In the SM, the $t\bar{t}Z$ final state is produced in proton-proton collisions at leading order via diagrams as shown in Figure 3.4, where the dominant contributions are the strong production processes from gluon-gluon and quark-antiquark initial states. The production process has been described at NLO in QCD [179–181], matched to parton showers [72, 182, 183], and complemented with electroweak corrections at NLO [184, 185]. Corrections from soft gluon resummation have been computed at NNLL accuracy in two independent frameworks based on soft collinear effective theory [186, 187] and using the direct QCD approach [188–190]. The latter is used for the discussion in the following.

Figure 3.5

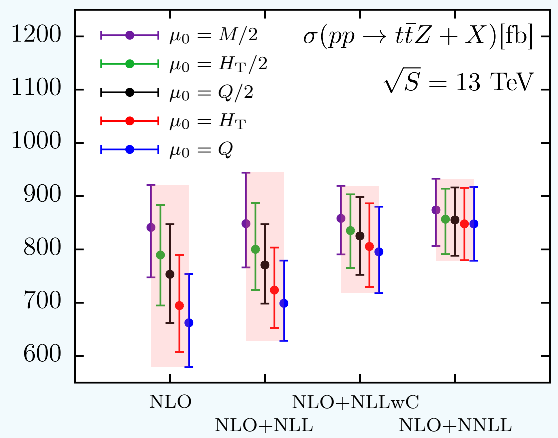

Total cross section prediction for different scale choices at different levels of accuracy, taken from Ref. [190].

The predicted total cross section for $t\bar{t}Z$ production at $\sqrt{s} = 13\,\text{TeV}$ is shown in Figure 3.5 at different levels of accuracy from NLO in QCD and electroweak theory up to the inclusion of full NNLL corrections. Different choices of the factorisation and renormalisation scales lead to different central values. The uncertainty of the prediction is assessed as the envelope of the variations of scales by a factor of 2 up and down, separately for both scales and also simultaneously in the same direction. The scale uncertainties are decreased with increasing accuracy from the NLO(QCD+EW) prediction to the full NLO+NNLL result, and also the agreement of the predictions for different scale choices improves, demonstrating a good stability of the theoretical prediction. The predicted cross section at NLO+NNLL accuracy is evaluated from the combination of the different scale choices to be:

$$\sigma(\text{pp} \to t\bar{t}Z)_{\text{theo}} = 859\,\text{fb}\,^{+8.6\,\%}_{-9.5\,\%} \pm 2.3\,\%, \tag{3.1}$$

where the first error is the scale uncertainty and the second error is the PDF uncertainty, as evaluated on the NLO(QCD+EW) prediction [190].

The authors of Reference [190] also provide differential cross section predictions for $t\bar{t}Z$ production at NLO+NNLL accuracy. Available observables are the following kinematic properties of the final state particles:

- the invariant masses of the $t\bar{t}Z$ system, $m(t\bar{t}Z)$, and of the $t\bar{t}$ system, $m(t\bar{t})$;

Figure 3.6

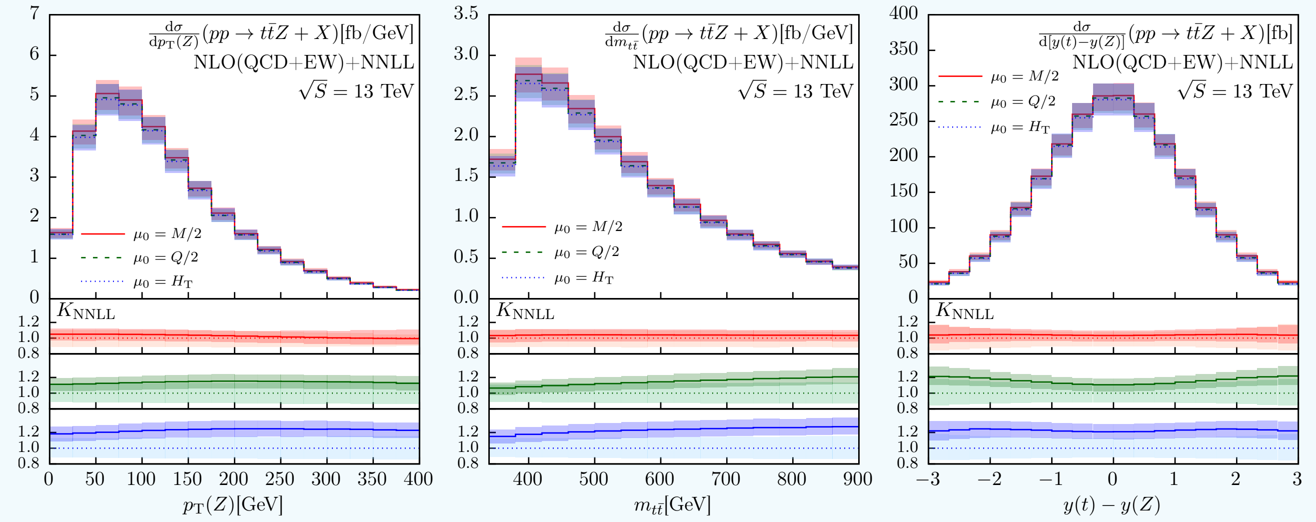

Differential cross section predictions for $t\bar{t}Z$ production at NLO+NNLL accuracy as a function of the Z boson transverse momentum (left), of the $t\bar{t}$ invariant mass (middle), and of the rapidity difference of top quark and Z boson (right), for different scale choices. The lower panels show the ratios between the NLO+NNLL and the NLO predictions for the respective scale choices. Taken from Ref. [190].

- the transverse momenta of the top quark, $p_T(t)$, and the Z boson, $p_T(Z)$;
- the rapidity differences between top quark and top antiquark, $y(t) - y(\bar{t})$, and between top quark and Z boson, $y(t) - y(Z)$; and
- the azimuthal angle differences between top quark and top antiquark, $\phi(t) - \phi(\bar{t})$, and between top quark and Z boson, $\phi(t) - \phi(Z)$.

Examples of the predictions for three observables are shown in Figure 3.6. As for the total cross section prediction, the scale uncertainty of the NLO+NNLL prediction is significantly reduced with respect to the NLO prediction. Since the ratios between the NLO+NNLL and the NLO prediction ("K factors") are not flat, differential cross section measurements can be used to probe the quality of the differential prediction at different accuracies.

The weak magnetic and electric dipole moments of the top quark–Z boson coupling are zero at tree-level in the SM and obtain small non-zero values through loop contributions. The impact of anomalous dipole moments, which modify the Lorentz structure of the interaction, has been studied at NLO in QCD including NLO corrections to the spin correlations in the top quark and Z boson decays. Results have been presented for the decay channel with three leptons from a leptonically decaying Z boson, $Z \to \ell^+\ell^-$, and the semileptonic decay of the $t\bar{t}$ system, including fiducial cuts that model the detector acceptance. Anomalous dipole moments increase the predicted total cross section, and

Figure 3.7

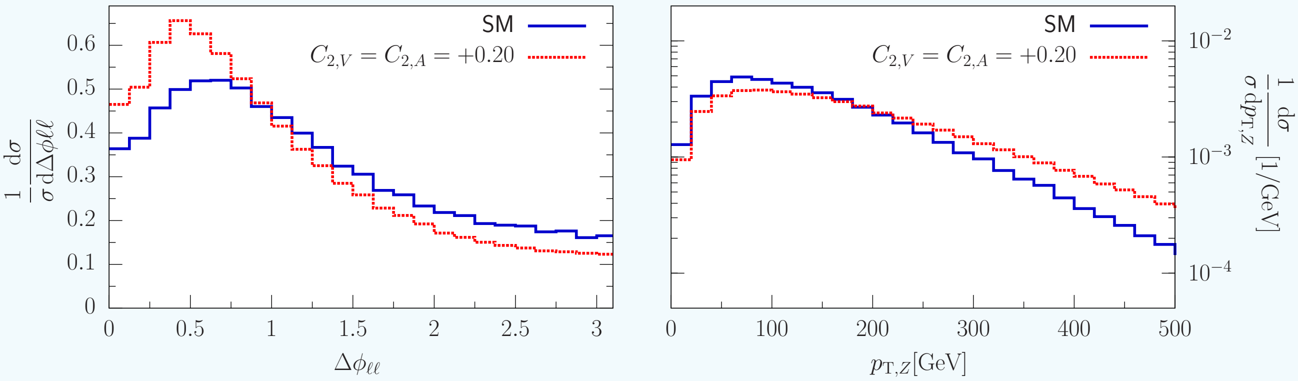

Differential cross section predictions for $t\bar{t}Z$ production in final states with three leptons as a function of the opening angle of the leptons from the Z boson decay (left) and the Z boson transverse momentum (right), for the SM (blue) and a scenario with anomalous dipole moments (red), taken from Ref. [152].

also induce significant changes to shapes of differential cross section predictions. In Figure 3.7, the differential predictions are shown for the transverse momentum of the Z boson, $p_T(Z)$, and for the azimuthal opening angle of the leptons originating from the Z boson decay, $\Delta\phi(\ell\ell)$ [150–152].

The two observables under study, $p_T(Z)$ and $\Delta\phi(\ell\ell)$, show a large correlation. To maximise the sensitivity of measurements with limited statistics to the new physics scenarios, it is useful to consider an observable that is boosted to the Z boson rest frame and is thus independent of $p_T(Z)$. With the boost defined as a function of laboratory-frame kinematics as

$$\gamma = \sqrt{1 + \left(\frac{p_T(\ell^+\ell^-)}{m(\ell^+\ell^-)}\right)^2 \cosh^2 \eta(\ell^+\ell^-)}, \quad (3.2)$$

it is found that the polar angle between the negatively charged lepton from the Z boson and the Z boson itself, $\theta(\ell^- Z)$, boosted to the Z boson rest frame as

$$\cos\theta^\star(Z) = \frac{-\beta + \cos\theta(\ell^- Z)}{1 - \beta\cos\theta(\ell^- Z)} \quad \text{with} \quad \beta = \sqrt{1 - \frac{1}{\gamma^2}}, \quad (3.3)$$

is a suitable observable [5].

Figure 3.8

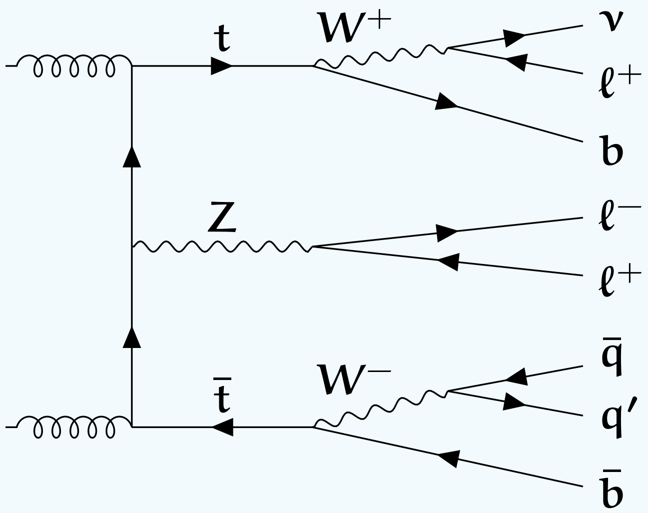

The three-lepton final states consists of
- three leptons, of which two are opposite-sign and same-flavour;
- at least four jets, of which two originate from bottom quarks; and
- missing transverse energy from one neutrino.

Example diagram for the decay of the $\mathrm{t\bar{t}Z}$ system into a final state with three leptons.

3.3. Measurements of $\mathrm{t\bar{t}Z}$ production

Run 1 measurements First searches for $\mathrm{t\bar{t}Z}$ production were performed at $\sqrt{s} = 7\,\mathrm{TeV}$ by the ATLAS and CMS experiments [191, 192], targeting the three-lepton final state as shown in Figure 3.8. In the CMS measurement, events are selected with three leptons or two same-sign leptons, where one lepton from the Z boson decay escaped detection. Here and in the following, "lepton" always refers to electrons and muons only. Evidence was found both for $\mathrm{t\bar{t}Z}$ production in three-lepton events and for $\mathrm{t\bar{t}Z} + \mathrm{t\bar{t}W}$ production in two-lepton events.

Observation of $\mathrm{t\bar{t}Z}$ production was reached by both experiments at $\sqrt{s} = 8\,\mathrm{TeV}$ [162, 163]. The analyses used events with two, three, or four leptons to simultaneously measure $\mathrm{t\bar{t}W}$ and $\mathrm{t\bar{t}Z}$ production in their respective leptonic decays. For $\mathrm{t\bar{t}Z}$ production, all decay modes of the $\mathrm{t\bar{t}}$ system are included, while $\mathrm{t\bar{t}W}$ production is measured with semileptonic and dileptonic $\mathrm{t\bar{t}}$ decays. The CMS measurement used boosted decision trees (BDTs) [193] to discriminate between signal and background events separately in different categories based on jet and lepton multiplicity. A fit to the binned likelihood function with nuisance parameters ("template fit") of the different BDT discriminator values was performed to extract the signal cross sections. The results were also used to evaluate constraints on the top quark–Z boson coupling.

Run 2 measurements Simultaneous measurements of $\mathrm{t\bar{t}W}$ and $\mathrm{t\bar{t}Z}$ production have also been performed by the ATLAS and CMS experiments at $\sqrt{s} = 13\,\mathrm{TeV}$ in final states with two, three, and four leptons, using about $36\,\mathrm{fb}^{-1}$ of data collected in 2015 & 2016 (ATLAS) or only in 2016 (CMS) [164–166]. In the CMS measurement, only the three-lepton and four-lepton final states are used for the extraction of the $\mathrm{t\bar{t}Z}$ signal. The $\mathrm{t\bar{t}W}$ signal is extract from same-sign two-lepton events, and a multivariate analysis (MVA) is used to improve the discrimination between signal and background events. The cross sections are determined with a template fit of the event yields in categories based on lepton, jet, and b jet multiplicity, which are split additionally for high and low values of the MVA discriminant for the two-lepton categories. The measured cross section of $\mathrm{t\bar{t}Z}$ production is

$$\sigma(\mathrm{pp} \to \mathrm{t\bar{t}Z})_{\mathrm{meas}} = 990\,^{+90}_{-80}\,(\mathrm{stat})\,^{+120}_{-100}\,(\mathrm{syst})\,\mathrm{fb}, \tag{3.4}$$

with a relative uncertainty of about 16 % [165].

The measurement of $\mathrm{t\bar{t}Z}$ production in final states with three and four leptons has been extended by the CMS experiment with data collected in 2017, yielding a total dataset of $77.5\,\mathrm{fb}^{-1}$. Following a similar analysis strategy, the inclusive cross section has been measured with unprecedented accuracy. Additionally, the result comprises a first differential measurement as a function of the leptonic observables $p_{\mathrm{T}}(\mathrm{Z})$ and $\cos\theta^{\star}(\mathrm{Z})$, using events with three leptons, and an interpretation of the results in terms of new physics models [E, 4, 5].

In the following chapters, an overview of the inclusive cross section measurement is given (Chapter VII), and differential cross section measurements in Z boson observables (Chapter VIII) and top quark observables (Chapter IX) are presented.

Other final states All measurements so far have been performed using the leptonic decay of the Z boson. Although these decays have the smallest branching ratio, the good reconstruction of leptons in the experiments allows for precise measurements and a good rejection of background events. Nevertheless, other channels have been considered recently as well. At the ATLAS experiment, a measurement of the $\mathrm{Z} \to \nu\bar{\nu}$ decay has been investigated, using the fully-hadronic decay of the $\mathrm{t\bar{t}}$ system and thus events with many jets and missing energy [194]. As part of the background studies for the measurement of $\mathrm{t\bar{t}H}$ production in the $\mathrm{H} \to \mathrm{b\bar{b}}$ channel, the measurement of $\mathrm{t\bar{t}Z}$ with the $\mathrm{Z} \to \mathrm{b\bar{b}}$ decay was investigated at the CMS experiment [195]. More results from these decay channels are expected with the upcoming larger datasets.

VII. Inclusive $t\bar{t}Z$ production cross section

In this chapter, an overview of the measurement of the inclusive $t\bar{t}Z$ production cross section in proton-proton collisions at $\sqrt{s} = 13\,\text{TeV}$ using data collected in 2016 & 2017 is given. Events are selected with three and four leptons, as described in Section 3.4. Background contributions are estimated from simulated events and with a data-driven method (Section 3.5). The systematic uncertainties of the measurement are discussed in Section 3.6, and the extraction of the measured cross section from a template fit to event categories in jet and b jet multiplicity is presented in Section 3.7.

This measurement has been published by the CMS experiment [E], and is also documented in the theses of Illia Khvastunov [4] and Daniel Spitzbart [5].

3.4. Event selection

Datasets The measurement is based on proton-proton collision data recorded in 2016 & 2017. Only data-taking periods in which the detector was fully operational are used. After this requirement, the combined dataset corresponds to an integrated luminosity of $77.5\,\text{fb}^{-1}$ [B, C], as listed in Table 3.1. The uncertainty in the integrated luminosity is 1.9 %, cf. Table 2.1.

Table 3.1

dataset	int. luminosity
2016	$35.9\,\text{fb}^{-1} \pm 2.5\,\%$
2017	$41.5\,\text{fb}^{-1} \pm 2.3\,\%$
combined	$77.5\,\text{fb}^{-1} \pm 1.9\,\%$

Integrated luminosity and relative uncertainty [B, C].

Both datasets are complemented with MC samples for signal and background processes, used to describe the signal selection efficiency, to provide predictions for the yields of some background processes, and to evaluate the closure of other background prediction methods. For each year, a separate set of MC samples is used, incorporating the specific detector conditions of the respective year in the detector response simulation. For the analysis, the number of MC events is scaled according to the integrated luminosity and the cross section as predicted by the SM such that its normalisation reflects the expected number of events.

Simulated events are reweighted to match the expected pileup distribution, computed from the measurement of the instantaneous luminosity and assuming an inelastic scattering cross section of 69.2 mb [196].

Trigger From the data samples, events that triggered by at least one out of a set of single-lepton, double-lepton, and triple-lepton HLT paths are selected for the measurement. The minimal transverse momentum thresholds of the single-lepton trigger paths in 2016 (2017) are 24 GeV (27 GeV) for muons, and 27 GeV (32 GeV) for electrons. The combination with double-lepton trigger paths increases the trigger efficiency for events with soft leptons, with minimal transverse momentum thresholds for the leading lepton of 17 GeV (23 GeV) for double-muon events (electron-muon and double-electron events), and down to 8 GeV for the trailing lepton. Finally, the triple-lepton trigger paths have a transverse momentum threshold of the leading lepton as low as 9 GeV, and thus increase the trigger efficiency for events with very soft transverse momentum spectra.

The trigger selection efficiency for events that pass the lepton selection described below is measured in data using an independent set of HLT paths as well as in MC samples. It is found to be above 98 % across all kinematic ranges in both years, with good agreement between data and MC samples. To account for residual differences between the efficiency in data and MC events, scale factors are applied to the MC prediction. The difference between the scale factors and unity is smaller than 2 % (3 %) in 2016 (2017).

Lepton selection The selection of electrons and muons from the reconstructed particle-flow objects of an event follows a strategy originally developed for a measurement of $\mathrm{t\bar{t}H}$ production in final states with multiple leptons [197, 198]. It was further developed in the context of this $\mathrm{t\bar{t}Z}$ production measurement and for the discovery of tZq production [172]. The main challenge of the lepton selection is to clearly distinguish "prompt" leptons originating from direct W and Z boson decays from "nonprompt" leptons, which include reconstructed lepton candidates from misidentified jets, from photon conversion, and from heavy-flavour hadron decays. To this end, three sets of criteria are applied to the lepton candidates, the "loose", "medium", and "tight" selection.

- Particle flow candidates for electrons and muons are preselected as loose leptons if they have a transverse momentum of $p_T > 10\,\text{GeV}$ and a pseudorapidity of $|\eta| < 2.5$ for electrons and $|\eta| < 2.4$ for muons, corresponding to the coverage of the relevant subdetectors. Further requirements are put on the impact parameter, i. e. the distance of closest approach between the lepton track and the leading interaction vertex, and on the relative isolation, defined as the scalar p_T sum of hadrons and photons in a cone around the lepton candidate direction [67]. Finally, a set of loose identification criteria specific to electrons and muons are applied, as described in Section 1.6. After this preselection, electron candidates are removed if they overlap with a muon candidate by $\Delta R = \sqrt{|\Delta\eta|^2 + |\Delta\phi|^2} < 0.05$.

- For the medium lepton selection, a jet within $\Delta R < 0.4$ of the lepton direction is selected as the "closest jet", if such a jet exists. The lepton fails the medium selection if the closest jet is tagged as originating from a b quark. Additionally, a medium lepton is required to either also pass the tight selection described below, or to fulfil requirements on the b tagging discriminator value and kinematics of the closest jet, as well as on the identification discriminator value in case of electrons, which is described in Section 1.6.

- For the tight selection, a multivariate analysis (MVA) discriminator is trained using boosted decision trees (BDTs) [193] as implemented in TMVA [199] to distinguish prompt and nonprompt leptons. Its input variables are observables of the lepton candidate (kinematics, relative isolation, impact parameter, and identification) and of the closest jet (kinematics, b tagging discriminator value, and tracking information). Medium leptons are selected as tight leptons if the MVA discriminator value passes a certain threshold. A tighter threshold is applied for leptons in three-lepton events than in four-lepton events, resulting in an efficiency of 90 % and 95 %, respectively, for prompt leptons from $t\bar{t}Z$ signal events to pass the tight lepton criterion, similar for electrons and muons.

The efficiencies of the lepton selection are measured with a "tag-and-probe" method [68, 69] separately in data and MC events, and the MC yields are reweighted to match the efficiency in data. These scale factors typically deviate from unity by about 1 % per lepton, but up to 10 % for low-momentum leptons with $p_T < 20\,\text{GeV}$.

After the selection of the individual leptons, events are selected for the measurement in the three-lepton and four-lepton channel. Three-lepton events are required to have exactly three tight leptons with transverse momenta of $p_T > 40$, 20, and 10 GeV. Four-lepton events are required to have exactly four tight leptons, where one lepton is required to have a transverse momentum of $p_T > 40\,\text{GeV}$. Additionally, two leptons are required to be of same flavour and opposite charge, and have an invariant mass compatible with the Z boson mass, $|m(\ell^+\ell^-) - 91\,\text{GeV}| < 10\,\text{GeV}$ for three-lepton events and $|m(\ell^+\ell^-) - 91\,\text{GeV}| < 20\,\text{GeV}$ for four-lepton events. The invariant mass criterion efficiently reduces background contamination from processes without a leptonically decaying Z boson. In the four-lepton channel, events are additionally rejected if they contain a second Z boson candidate. Furthermore, events are removed if any two leptons which passed the medium selection have a small invariant mass of $m(\ell\ell) < 12\,\text{GeV}$. This criterion rejects events with $\ell^+\ell^-$ pairs resulting from photon conversion, or where one lepton is a misidentified photon from the final state radiation of a prompt lepton.

Jet selection Reconstructed jets, with jet energy corrections and identification criteria applied as described in Section 1.6, are selected if they have a transverse momentum of $p_T > 30\,\text{GeV}$ and a pseudorapidity of $|\eta| < 2.4$. Additionally, a jet is removed from the event if it overlaps with any medium lepton by $\Delta R < 0.4$.

To identify jets originating from b quarks, the discriminator value of the DeepCSV b tagging algorithm is evaluated for all selected jets. A working point with 70 % efficiency for jets originating from b quarks, and 12 % (1 %) mistag probability for jets originating from charm quarks (light quarks and gluons) is used. Scale factors are applied to simulated events to match the b-tagging efficiency in data [64].

Events are required to have at least one jet. To improve discrimination between processes with and without top quarks, several categories are formed defined by the jet and b jet multiplicities. A "signal-enriched" selection is defined by requiring three-lepton events to have at least three jets of which at least one jet is b tagged, and four-lepton events to have at least two jets of which at least one jet is b tagged. In this selection, the purity of signal events is about 65 %.

3.5. Background predictions

Rare top quark production Irreducible backgrounds to $t\bar{t}Z$ events arise from processes with top quarks and additional prompt leptons in the final state. The contributions to the measured number of events for associated top quark pair production ($t\bar{t}H$, $t\bar{t}W$, $t\bar{t}VV$), associated single top quark production (tZq, tWZ, tHq, tHW), and four top quark production ($t\bar{t}t\bar{t}$) are estimated from MC samples. These processes are collectively referred to as "$t(\bar{t})X$".

Figure 3.9

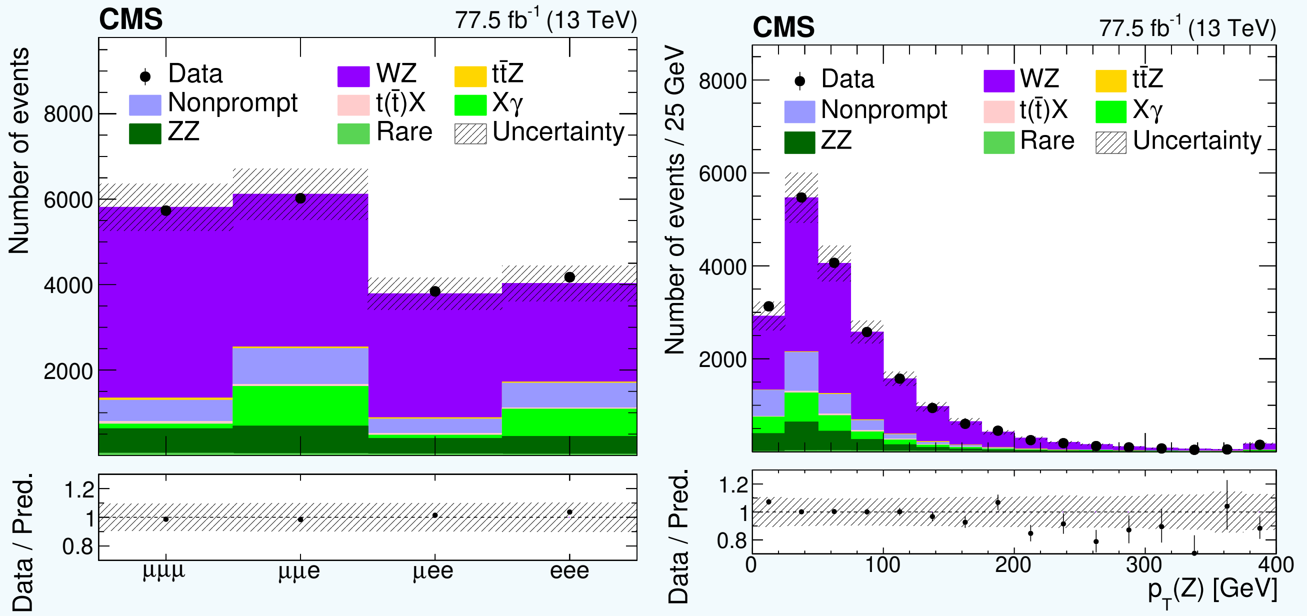

Observed (points) and predicted (shaded) event yields for the distribution of lepton flavour (left) and reconstructed Z boson transverse momentum (right) in the WZ control region, combined for the 2016 and 2017 datasets, taken from Ref. [E].

The number of simulated events is normalised to the predicted SM cross sections, which have a precision of about 11 % or smaller [72, 184, 200]. This precision is applied as uncertainty in the background normalisation, except for tZq production for which the precision of the recently measured cross section of about 15 % is used [172].

Diboson production Important backgrounds, especially in categories with small jet multiplicity, arise from the production of two bosons, with additional jets from initial-state radiation. In the three-lepton and four-lepton channel, WZ and ZZ production are the dominant diboson production channels. Both processes are predicted from MC samples, with a normalisation uncertainty of 10 % [201, 202]. Additionally, the MC prediction is validated in control regions.

For WZ production, a control region is defined by the three-lepton selection but with a veto on any b jet. In Figure 3.9, distributions for data and MC prediction are shown in the control region. Good agreement is observed between data and prediction, except for events with a large jet multiplicity. Thus, an additional normalisation uncertainty of 20 % is applied to WZ events with three or more jets.

Events with b jets can arise in WZ production especially through gluon splitting. Since a large underestimation of $g \to b\bar{b}$ has been observed in Run 1 measurements [203], a study of $Z + b\bar{b}$ events has been performed to check the modelling of gluon splitting. Good agreement of data and MC events at the level of 20 % has been found [5]. Using the ratio of WZ events that contain gluon splitting, an additional normalisation uncertainty of 8 % is assigned to the event yields with at least one b jet due to potential mismodelling of gluon splitting.

For ZZ production, a control region is defined by the four-lepton selection but with exactly two opposite-sign same-flavour lepton pairs with invariant masses compatible with the Z boson mass. This control region is very pure in ZZ events and shows good agreement between data and predicted event yields. Therefore, no additional uncertainty is assigned.

Processes with nonprompt leptons Background events with nonprompt leptons arise mainly from inclusive $t\bar{t}$ production, a process with a three orders of magnitude larger cross section. In $t\bar{t}$ events, a nonprompt lepton is wrongly combined with a prompt lepton of opposite flavour to form a Z boson candidate. In addition, Z + jets production plays a role, typically with the correctly reconstructed Z boson and a nonprompt lepton wrongly assigned to the semileptonic $t\bar{t}$ decay. Nonprompt lepton events are predicted from data, using the "fake rate method" that has been applied in previous measurements sensitive to nonprompt lepton backgrounds [165, 204].

The fake rate is defined as the probability for a nonprompt lepton that passed the medium selection to also pass the tight selection. It is measured in a QCD multijet selection separately for electrons and muons and as a function of their kinematics. Events that pass the full event selection but for one lepton which only passes the medium selection and fails the tight selection are scaled with the fake rate to predict the nonprompt background contributions in the signal regions [4].

Control regions to validate the nonprompt background estimation are defined both for $t\bar{t}$ and Z + jets events. The $t\bar{t}$ control region is defined by the three-lepton selection but without a Z boson candidate, i. e. with either no opposite-sign and same-flavour lepton pair, or with such a pair but with $|m(\ell^+\ell^-) - 91\,\text{GeV}| > 10\,\text{GeV}$. In Figure 3.10, distributions of data and MC predictions are shown for the $t\bar{t}$ control region. The Z + jets control region is defined by the three-lepton selection with no jets or exactly one jet, no b jet, and the requirement for both the missing transverse momentum and the transverse mass formed by the missing transverse momentum and the third lepton not used for the Z boson candidate to be smaller than 30 GeV. In both control regions,

Figure 3.10

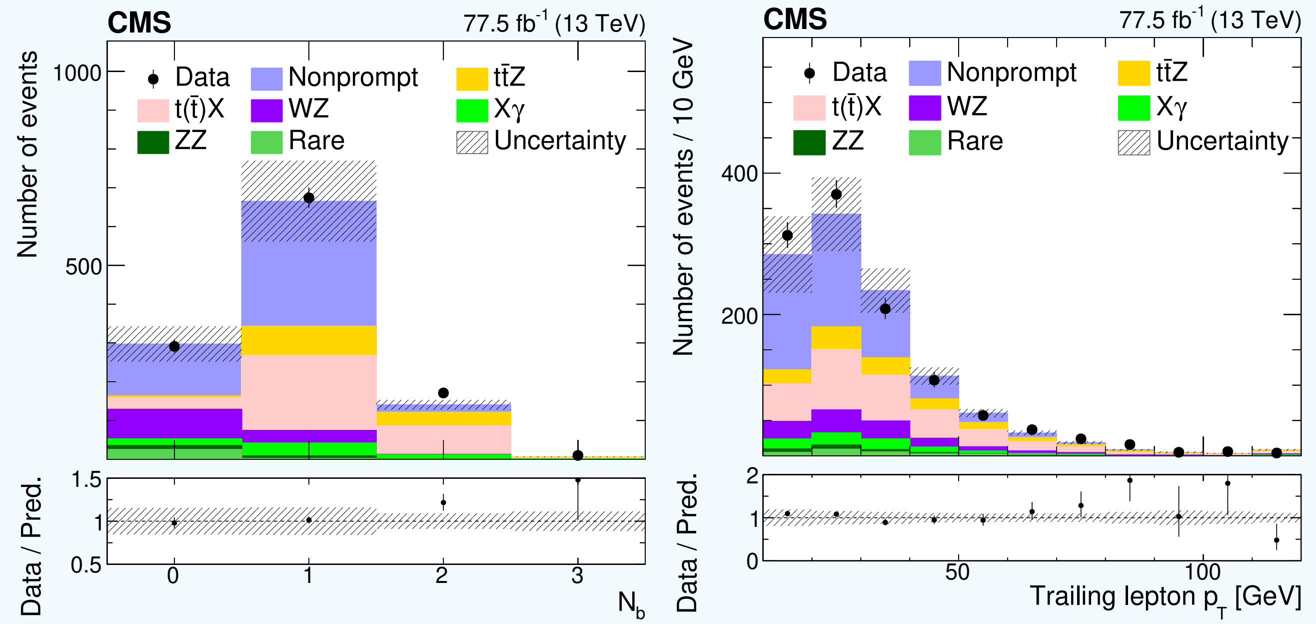

Observed (points) and predicted (shaded) event yields for the distribution of b jet multiplicity (left) and transverse momentum of the trailing lepton (right) in the $t\bar{t}$ control region, combined for the 2016 and 2017 datasets, taken from Ref. [E].

a good agreement between the estimated nonprompt background yields and the data is found.

A systematic uncertainty of 30 % is assigned to the nonprompt background normalisation. The statistical uncertainty from the event yields in the application region ranges between 5 % and 50 % for the different jet and b jet multiplicity regions.

Triboson production Events with three or four prompt leptons, including an opposite-sign and same-flavour pair compatible with the Z boson mass, also arise from the production of three heavy vector bosons, WWZ, WZZ, and ZZZ. Since the SM predicted cross sections are smaller than 200 fb [205], these processes are labelled “rare” and an uncertainty of 50 % is assigned to the normalisation of the MC prediction used for the background estimation. Due to the limited size of the MC samples, the statistical uncertainty in the triboson prediction of up to 100 % in some jet and b jet multiplicity regions has to be taken into account.

Processes with photon conversion Finally, background events with leptons arising from the conversion of photons are considered, including a dominant contribution from $Z\gamma$ production, as well as contributions from $W\gamma$, $t\bar{t}\gamma$, and $t\gamma q$ production. The background contributions are predicted from MC samples, and validated in a data control region defined by the three-lepton selection with the additional requirement that the invariant mass of all three leptons is compatible with the Z boson mass. Good agreement between data and the predicted yields is observed, and a normalisation uncertainty of 20 % is assigned [206, 207].

3.6. Systematic uncertainties

In the measurement of the inclusive $\mathrm{t\bar{t}Z}$ production cross section, several systematic effects affect the prediction of the signal selection efficiency and the background yields. The different uncertainty sources are discussed in the following, and are summarised in Table 3.2.

Integrated luminosity The relative uncertainty in the integrated luminosity is 2.5 % for the 2016 dataset [B] and 2.3 % for the 2017 dataset [C]. The uncertainties are partially correlated, as described in Table 2.1, resulting in an uncertainty of the combined dataset of 1.9 %. This measurement has been performed before the study of the correlation of the luminosity uncertainty between the datasets was completed, and thus uses the simplified assumption of uncorrelated measurements, resulting in an integrated luminosity uncertainty of the combined dataset of 1.7 %.

Trigger efficiency The statistical uncertainty in the trigger efficiency measurement is taken into account by corresponding variations of the predicted background yields. It has a value of 2 % in both years and is treated as uncorrelated between the two years.

Pileup modelling The modelling of pileup events in the MC predictions depends mainly on the value of the total inelastic scattering cross section which is known to a precision of 4.6 % [208]. To evaluate the impact on the cross section measurement, the MC samples of both years are simultaneously reweighted to pileup profiles with a cross section varied by $\pm 1\sigma$, resulting in variations of up to 2 % in the predicted event yields.

Table 3.2

uncertainty source	uncertainty range	correlation 2016/2017	impact on cross section
integrated luminosity	2.3–2.5 %	×	2 %
trigger efficiency	2 %	✓	2 %
pileup modelling	1–2 %	✓	1 %
lepton selection efficiency	4.5–6 %	∼	4 %
jet energy scale	1–9 %	✓	2 %
jet energy resolution	0–1 %	✓	< 1 %
b tagging efficiency	1–4 %	×	2 %
matrix element scale choice	1–4 %	✓	1 %
PDF choice	1–2 %	✓	< 1 %
parton shower modelling	1–8 %	✓	1 %
$t(\bar{t})X$ background prediction	11–15 %	✓	2 %
WZ background prediction	13–24 %	✓	3 %
ZZ background prediction	10 %	✓	1 %
nonprompt lepton background prediction	30–60 %	∼	1 %
triboson background prediction	50–100 %	∼	1 %
photon conversion background prediction	20 %	✓	1 %
total systematic uncertainty			6 %
statistical uncertainty			5 %
total uncertainty			8 %

Sources of systematic uncertainty in the inclusive cross section measurement with their respective sizes (second column) and their impact on the measured $t\bar{t}Z$ production cross section (fourth column). The third column indicates whether the uncertainty sources are treated as correlated (✓), uncorrelated (×), or partially correlated (∼) between the 2016 and 2017 datasets. Taken from Ref. [E].

Lepton selection efficiency Corrections to the lepton selection efficiency, as measured with the tag-and-probe method, have uncertainties due to limited statistics and due to the choice of the background modelling in tag-and-probe event samples. The resulting uncertainty on the predicted yields ranges between 4.5 % and 6 %, where the statistical contributions are treated as uncorrelated and the contributions related to background modelling are treated as correlated between 2016 and 2017. The lepton selection efficiency uncertainty has an impact on the $t\bar{t}Z$ cross section of about 4 % which is the largest contribution from a single uncertainty source.

Jet energy scale and resolution The scale and resolution corrections to the jet energy are varied within their uncertainties for each jet in the MC simulation, resulting in variations of up to 9 % of the predicted yields in some jet and b jet multiplicity regions. Both effects are treated as correlated between 2016 and 2017.

Efficiency of b tagging The corrections to MC event yields to match the b tagging efficiency in data are varied within uncertainties separately for jets originating from b and c quarks, and for jets originating from light quarks and gluons. The resulting variations of the predicted yields in different jet and b jet multiplicity regions range between 1 % and 4 %, and are treated as uncorrelated between 2016 and 2017.

Matrix element scale choice To estimate the impact of the choice of the renormalisation and factorisation scales in the matrix element calculation on the modelling of the signal and background acceptance and selection efficiency, the scales are varied by a factor of two up and down, separately and simultaneously [209, 210]. The envelope of the six variations is used to estimate the uncertainty on the central prediction, resulting in up to 4 % uncertainty in the predicted acceptance. This uncertainty due to the matrix element scale choice is treated as correlated between 2016 and 2017.

PDF choice Replicas of the nominal parton distribution functions (PDFs) used to generate the MC samples are evaluated to assess the impact of the PDF choice on the signal acceptance. Additionally, the choice of α_s is scaled up and down by its uncertainty. In combination [211], the impact on the cross section is smaller than 1 %.

Parton shower modelling To study the precision of the parton shower modelling, the scale of α_s in the simulation of initial-state (final-state) radiation is varied up and down by a factor of 2 ($\sqrt{2}$) [79]. The envelope of the variations is used as an uncertainty and takes values up to 8 % in the predicted yields of some jet and b jet multiplicity regions. Additionally, the colour reconnection model used in the parton shower [80–82] is compared to alternative colour reconnection models [212, 213], and the largest difference in the predicted yields is found to be 1.5 %. The parton shower modelling uncertainties are treated as correlated between 2016 and 2017.

Background normalisation The uncertainties in the normalisation of the background predictions are described in Section 3.5. They are treated as correlated between 2016 and 2017, except for the statistical uncertainties in the prediction of the nonprompt lepton background and triboson production processes.

3.7. Results

The cross section measurement is performed with a “template fit”, as described in References [214–217]. A binned likelihood function $L(r, \theta)$ is constructed as the product of the per-bin Poisson probability for the measurement of the number of events observed in data given the signal and background predictions in that bin. The bins are the categories in the number of jets and number of b jets, separately for the three-lepton and four-lepton channels, and separately for the 2016 and 2017 datasets. The signal strength parameter r scales the normalisation of the predicted signal yields. The symbol θ denotes a full set of nuisance parameters representing each source of systematic uncertainty including the normalisation of the background uncertainties. For each nuisance parameter, a factor is added to $L(r, \theta)$ evaluating the agreement between the current and nominal parameter value with respect to the assigned uncertainty.

The larger the value of the likelihood function, the better the data is described by the prediction assuming the current values of the signal strength parameter and the nuisance parameters. Thus, by maximising the likelihood function, an optimal description of data can be found, allowing to constrain systematic uncertainties, i. e. using the sensitivity of the chosen binning to some of the systematic uncertainty sources to reduce the assigned uncertainty. The parameter combination that maximises the likelihood function is denoted $(\hat{r}, \hat{\theta})$. Additionally, the nuisance parameter combination that maximises the likelihood function for a given signal strength parameter r is denoted $\hat{\theta}_r$. Using these two definitions, the profile likelihood ratio is defined as:

$$q(r) = -2 \ln \frac{L(r, \hat{\theta}_r)}{L(\hat{r}, \hat{\theta})}. \tag{3.5}$$

A minimisation of $q(r)$ yields the optimal value of the signal strength parameter, and an asymptotic approximation is employed to evaluate its uncertainty. In Figure 3.11, the event yields are shown for the jet and b jet multiplicity used in the template fit, but combined for the 2016 and 2017 datasets, using the signal and background normalisations as determined in the fit (“post-fit”).

The resulting measured cross section value is found to be:

$$\sigma(\mathrm{pp} \to \mathrm{t\bar{t}Z})_{\mathrm{meas}} = 950 \,\pm\, 50\,(\mathrm{stat}) \,\pm\, 60\,(\mathrm{syst})\,\mathrm{fb}. \tag{3.6}$$

It has a relative uncertainty of about 8 %, and thus constitutes the most precise measurement of the inclusive $t\bar{t}Z$ production cross section. It is found to be in good

Figure 3.11

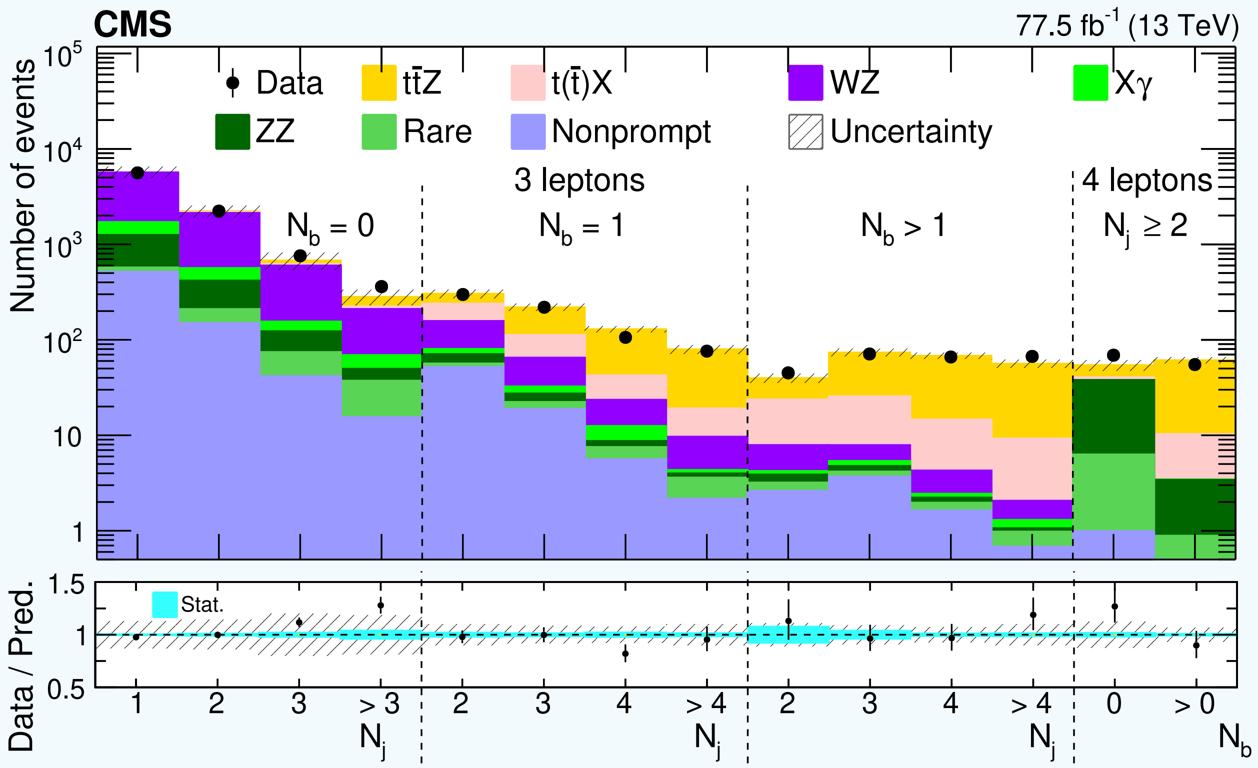

Observed (points) and predicted (shaded) event yields for different categories in lepton, jet, and b jet multiplicity, combined for the 2016 and 2017 dataset, taken from Ref. [E].

agreement with the predicted cross section at NLO+NNLL accuracy,

$$\sigma(\mathrm{pp} \to \mathrm{t\bar{t}Z})_{\mathrm{theo}} = 859\,\mathrm{fb}\,^{+8.6\,\%}_{-9.5\,\%}\,(\mathrm{scale}) \pm 2.3\,\%\,(\mathrm{PDF}), \tag{3.7}$$

described in Section 3.2, and the precision of the measurement is competitive to this state-of-the-art theory calculation.

Event yield distributions from some observables are shown in Figure 3.12 in the signal-enriched region, for the combined 2016 and 2017 datasets and using the post-fit predicted yields.

- The distribution of lepton flavours shows that the selection efficiency is slightly larger for prompt muons than for prompt electrons, resulting in about 35 % more selected triple-muon events than triple-electron events. In contrast, the contribution from backgrounds with nonprompt leptons is similar across the different lepton flavours.
- For the distribution of the dilepton invariant mass, the requirement of $|m(\ell^+\ell^-) - 91\,\mathrm{GeV}| < 10\,(20)\,\mathrm{GeV}$ for three-lepton (four-lepton) events is lifted. The bulk of

Figure 3.12

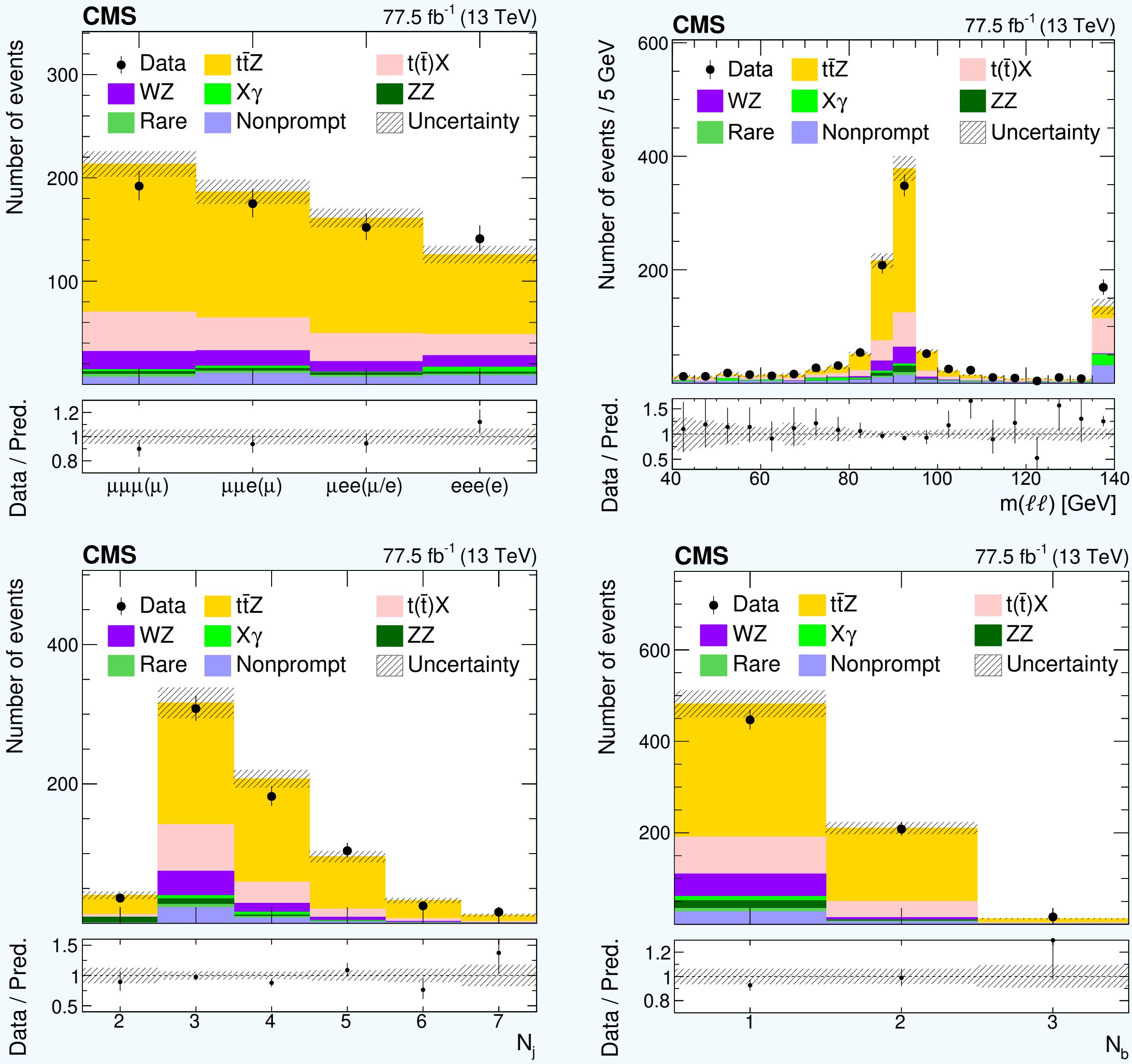

Observed (points) and predicted (shaded) event yields for the distribution of lepton flavour (upper left), dilepton invariant mass (upper right, without the Z boson mass cut applied), jet multiplicity (lower left), and b jet multiplicity (lower right) in the signal-enriched region, combined for the three-lepton and four-lepton channel, and for the 2016 and 2017 datasets, taken from Ref. [E].

Figure 3.13

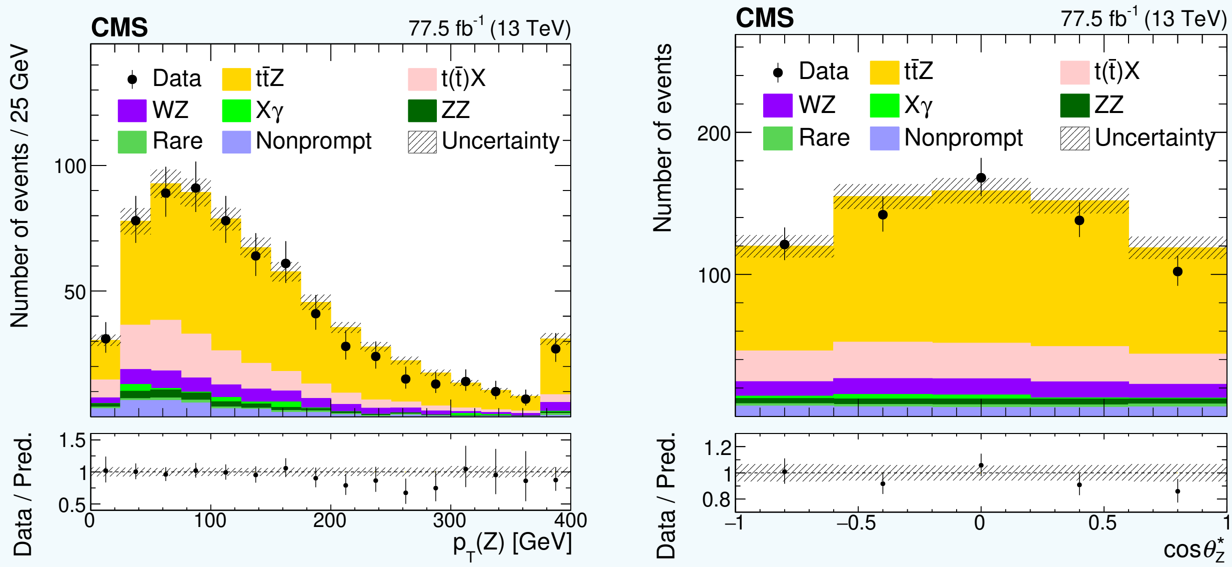

Observed (points) and predicted (shaded) event yields for the distribution of the Z boson transverse momentum (left) and the angle between the Z boson and its decay lepton, $\cos\theta^{\star}(\mathrm{Z})$, (right) in the signal-enriched region, combined for the three-lepton and four-lepton channel, and for the 2016 and 2017 datasets, taken from Ref. [E].

signal events as well as events from background processes with Z bosons (WZ, ZZ, and several processes from the t(t̄)X category) is found inside the mass window of the Z boson, and overall very few events are found outside.

- The distributions of the number of jets and number of b tagged jets show an increase in signal purity for events with larger multiplicity.

In all observables, a good post-fit agreement between measured data and predicted event yields is observed.

Similarly, the distributions of the observables $p_{\mathrm{T}}(\mathrm{Z})$ and $\cos\theta^{\star}(\mathrm{Z})$, sensitive to the Lorentz structure of the top quark–Z boson coupling as discussed in Section 3.2, are shown in Figure 3.13. The transverse momentum distribution peaks at values $50\,\mathrm{GeV} \lesssim p_{\mathrm{T}}(\mathrm{Z}) \lesssim 100\,\mathrm{GeV}$ and falls off for larger values, with similar behaviour for the signal and background predictions. For the angular distribution, about 30 % more events are observed in the central bin with $\cos\theta^{\star}(\mathrm{Z}) \approx 0$ than in each of the outer bins with $|\cos\theta^{\star}(\mathrm{Z})| \lesssim 1$. Here, the predictions for signal processes and other process with a Z boson show the same distribution while processes with nonprompt leptons are equally distributed over all bins in $\cos\theta^{\star}(\mathrm{Z})$.

An interpretation of this tt̄Z measurement in terms of new physics models has been performed, using a separate template fit with categories chosen in bins of $p_{\mathrm{T}}(\mathrm{Z})$ and $\cos\theta^{\star}(\mathrm{Z})$. The results are discussed in References [E, 5].

VIII. Differential $t\bar{t}Z$ production cross section in Z boson observables

In this chapter, a differential measurement of the $t\bar{t}Z$ production cross section as a function of Z boson observables is presented, using proton-proton collision data at $\sqrt{s} = 13\,\text{TeV}$ collected in 2016 & 2017. The observables have been chosen for their sensitivity to modifications of the top quark–Z boson coupling [5, 150–152].

For the measurement, the event selection and background predictions introduced in the previous chapter are used. The detector response to the Z boson observables under study and the unfolding procedure applied to correct for resolution and efficiency effects is discussed in Section 3.8. The differential cross section results are presented in Section 3.9.

This measurement is the first differential measurement of $t\bar{t}Z$ production and has been published by the CMS experiment [E]. It constitutes a main result of this thesis.

3.8. Detector response and unfolding

The number of observed $t\bar{t}Z$ events with an observable reconstructed in a bin j, x_j, with $1 < j < M$ bins in total, is distorted with respect to the true distribution of $t\bar{t}Z$ production events y_i, with generally independent bins $1 < j < M$, due to:

- the limited resolution of the detector reconstruction, including e. g. wrong assignments of reconstructed leptons to the Z boson decay;
- the limited efficiency of the detection of the final state particles and of the selection of $t\bar{t}Z$ production events, e. g. due to the coverage of the detector;
- background events that are indistinguishable from $t\bar{t}Z$ production events;
- statistical fluctuations due to the limited number of recorded collision events.

The relation between the true distribution y_i and the expectation value of the reconstructed distribution x_j, without statistical fluctuations, can be described as

$$x_j = \sum_{i=1}^{N} R_{ji} y_i + b_j. \tag{3.8}$$

Here, R_{ji} denotes the "response matrix" which describes the probability of an event from bin i of the true distribution to be reconstructed in bin j, and b_j is the number of background events reconstructed in bin j. For a diagonal response matrix with $N = M$, its diagonal entries thus describe the probability for an event to be reconstructed in the correct bin, and the off-diagonal elements give the probability for a migration to a different bin. The response matrix can be decomposed into

$$R_{ji} = \epsilon_i R'_{ji}, \tag{3.9}$$

where the efficiency ϵ_i describes the probability for an event to be reconstructed and selected at all, and the normalised resolution matrix R'_{ji} describes only the bin-to-bin migrations for selected events.

The response matrix can be computed from MC samples for $\mathrm{t\bar{t}Z}$ production that include a detector simulation. If both efficiency and resolution are sufficiently constant in each bin, the resulting matrix is independent of the shape of the SM prediction for the parton-level distribution [218].

For the construction of response matrices, the MC sample of $\mathrm{t\bar{t}Z}$ production events is used in which a Z boson decays to a pair of electrons or muons. The true distribution of events is evaluated on the observables obtained from the matrix-element calculation of the hard interaction including final state radiation and the decay of the Z boson to two leptons, but without the hadronisation of the coloured final state particles. Events are selected for the construction of the resolution matrix if they pass the selection criteria of the signal-enriched region in the three-lepton channel, i. e. if they have exactly three leptons, two of which are compatible with a Z boson decay, and three or more jets, of which at least one jet is b tagged, as described in Section 3.4. Signal events that fail this selection are used for the computation of the efficiency.

Here, a differential measurement as a function of the Z boson transverse momentum $p_{\mathrm{T}}(\mathrm{Z})$ and the angle between the Z boson and its decay lepton $\cos\theta^{\star}(\mathrm{Z})$, as defined in Section 3.2, is presented. In Figure 3.14, the resulting response matrices are shown, using MC events for the combined 2016 and 2017 dataset scaled according to the

Figure 3.14

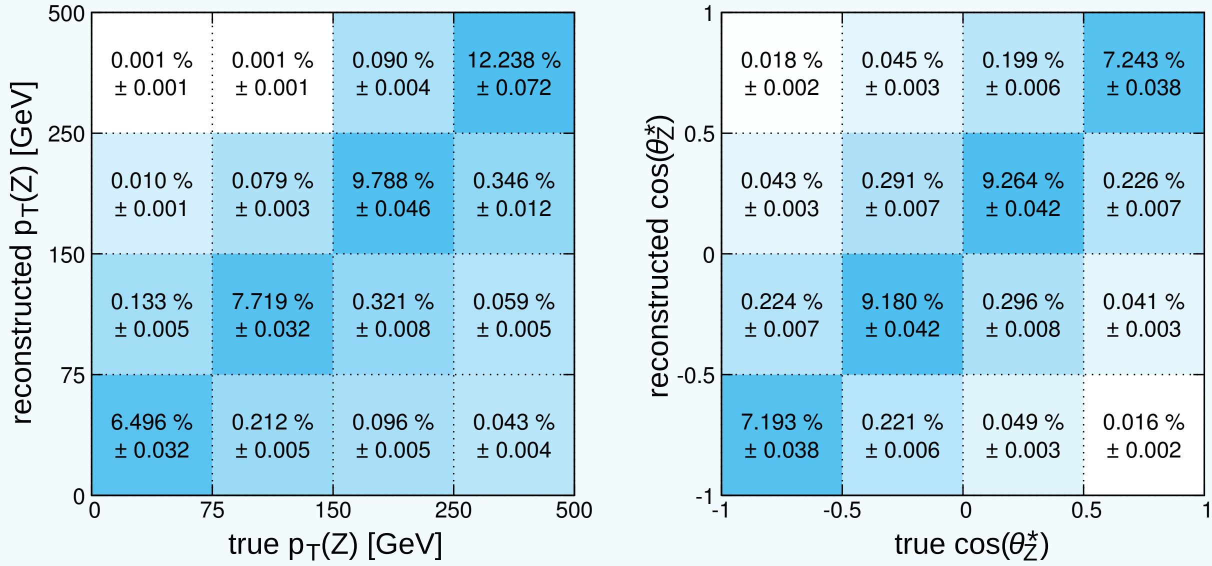

Response matrices describing bin-to-bin migrations from true bins to reconstructed bins for $p_{\mathrm{T}}(\mathrm{Z})$ (left) and $\cos\theta^{\star}(\mathrm{Z})$ (right), with statistical uncertainties due to the size of the MC samples.

respective integrated luminosities. The response matrices separately for each year alone are in good agreement with each other and with the combined result.

For the measurement of the observable $p_{\mathrm{T}}(\mathrm{Z})$, four bins are chosen with boundaries at 75, 150, and 250 GeV. In the figures, the last bin is represented as $250\,\mathrm{GeV} < p_{\mathrm{T}}(\mathrm{Z}) < 500\,\mathrm{GeV}$ but it also includes the “overflow” events with $p_{\mathrm{T}}(\mathrm{Z}) > 500\,\mathrm{GeV}$. This binning is the result of optimising the expected number of events in each bin while also reflecting the expected SM distribution with a peak at about 75 GeV and a long tail, as shown in Figure 3.6. The efficiency for signal events to be reconstructed and selected increases from about 6.6 % at low $p_{\mathrm{T}}(\mathrm{Z})$ to above 12.5 % at high $p_{\mathrm{T}}(\mathrm{Z})$, owing to the fact that the leptons from the decay of a high-momentum Z boson have a higher probability to pass the transverse momentum requirements.

For the measurement of the observable $\cos\theta^{\star}(\mathrm{Z})$, four equal-sized bins covering the full range of possible values between -1 and $+1$ are chosen. In the SM, Z bosons from t$\bar{\text{t}}$Z production are slightly longitudinally polarised, and thus slightly more events are expected at $\cos\theta^{\star}(\mathrm{Z}) \approx 0$ than at $|\cos\theta^{\star}(\mathrm{Z})| \approx 1$ [5]. The efficiency is about 9.8 % for the two central bins and about 7.5 % for the two outer bins, which is expected as the leptons from the decay of a highly polarised Z boson are more likely to have a low transverse momentum and thus fail the selection criteria.

To quantify the bin-to-bin migrations, the quantities "purity" and "stability" of the response are evaluated. Purity is the fraction of events in a reconstructed bin x_j that originate from the corresponding bin y_i,

$$\text{pur}_j = \frac{\sum_{y_i \supseteq x_j} N(\text{events in } x_j \text{ and } y_i)}{N(\text{events in } x_j)} \overset{\substack{\text{equal}\\ \text{bins}}}{=} \frac{N(\text{events in } x_j \text{ and } y_j)}{N(\text{events in } x_j)}. \tag{3.10}$$

Conversely, stability is the fraction of events in a true bin y_i that are also reconstructed in a corresponding bin x_j,

$$\text{stab}_i = \frac{\sum_{x_j \subseteq y_i} N(\text{events in } x_j \text{ and } y_i)}{N(\text{events in } y_i)} \overset{\substack{\text{equal}\\ \text{bins}}}{=} \frac{N(\text{events in } x_i \text{ and } y_i)}{N(\text{events in } y_i)}. \tag{3.11}$$

The good resolution of the lepton reconstruction with the CMS detector results in very high purities and stabilities of 94 % and higher in all bins of both observables.

With the measured event yields x_j in the bins of the reconstructed observables, their statistical uncertainties δ_j, and the predicted background yields b_j, a χ^2 expression is constructed from Equation (3.8) as

$$\chi^2(y) = \sum_{j=1}^{M} \frac{1}{\delta_j^2} \left(x_j - \sum_{i=1}^{N} R_{ji} y_i - b_j \right)^2 . \tag{3.12}$$

The value of χ^2 quantifies the agreement of the measured data with the true distribution y_i. A least-square minimisation, as implemented in the TUnfold software [219], provides the best estimator $\hat{y}_i$. The minimisation of Equation (3.12) is equivalent to

$$\hat{y}_i = \sum_{j=1}^{M} (R^{-1})_{ij} (x_j - b_j), \tag{3.13}$$

where R^{-1} is the inverse response matrix. The general approach to obtain an estimate for y_i from the measured data and the response matrix is known as "unfolding", and this specific method as "matrix inversion". It can be shown that matrix inversion provides an unbiased estimator with the smallest possible variance [218].

The unfolded number of events per bin $\hat{y}_i$ scaled with the branching ratio $\mathcal{B}$ of the leptonic Z boson decay and the integrated luminosity L gives the cross section integrated over the bin, and is divided by the bin width $\Delta\mathcal{O}_i$ to obtain the differential cross section σ_i:

$$\sigma_i = \frac{\hat{y}_i}{L \cdot \mathcal{B} \cdot \Delta\mathcal{O}_i} = \left.\frac{\Delta\sigma}{\Delta\mathcal{O}}\right|_{\text{bin } i} \approx \left.\frac{\mathrm{d}\sigma}{\mathrm{d}\mathcal{O}}\right|_{\substack{\text{central value}\\ \text{of bin } i}} . \tag{3.14}$$

Here, $\mathcal{B}(Z \to e^+e^-/\mu^+\mu^-) = 6.73\,\%$ is used [6].

3.9. Results

For the differential measurement, the event selection as described in Section 3.4 for the three-lepton channel is used. Only events that pass the selection criteria for the signal-enriched region, i. e. which have at least three jets of which at least one is b tagged, are considered. The background contributions are determined as described in Section 3.5.

The differential measurement is performed using the "pre-fit" predictions. While the template fit improves the understanding of systematic uncertainties and includes information from background-enriched regions to improve the description of the backgrounds, it also introduces correlations between the predicted background yields in different bins. For the differential measurement, the correlations between the event yields in the different bins have to be known, and this is not easily feasible using the template fit described in Section 3.7 alone. A proper approach to benefit from the uncertainty reduction by the template fit would be to perform a separate template fit in each bin of the differential observable, i. e. to split the $p_T(Z)$ and $\cos\theta^\star(Z)$ bins each into jet and b jet multiplicity categories. Given the currently large statistical uncertainties, such an approach is not necessary.

In Figure 3.15, the distribution of measured events and of the predicted backgrounds is shown for $p_T(Z)$ and $\cos\theta^\star(Z)$. In contrast to the distributions shown in Figure 3.13, the distributions here are presented, and used for the differential measurement, without applying a fit, using only the event selection for the three-lepton channel, and with the binning introduced in Section 3.8. The good description of the data by the MC predictions for signal and background event yields justifies the use of the pre-fit distributions.

The same sources of systematic uncertainty as for the inclusive measurement described in Section 3.6 are also considered for the differential measurement.

- To evaluate the uncertainty due to signal modelling, variations of the nominal response matrix are created for each alternative scale choice in the matrix element, in the parton distribution functions (PDFs), and in the parton shower simulation, as well as for each alternative PDF set. The unfolding is then repeated for each variation of the response matrix with the nominal data and background yields, and the resulting variations of the differential cross section are determined separately in

Figure 3.15

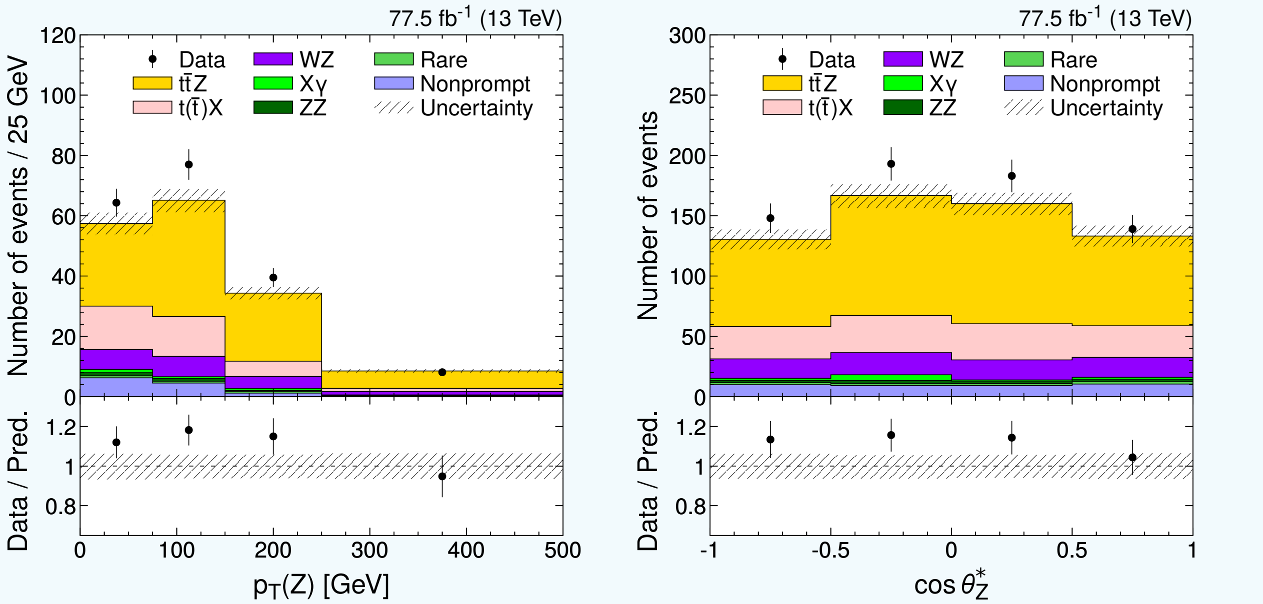

Observed (points) and predicted (shaded) event yields for the distribution of the Z boson transverse momentum (left) and the angle between the Z boson and its decay lepton, $\cos\theta^{\star}(\mathrm{Z})$, (right) in the signal-enriched region of the three-lepton selection, combined for the 2016 and 2017 datasets.

each bin. The per-bin uncertainty is estimated from the envelope of variations for each set of scale variations, and from the combination of variations for the alternative PDF sets.

- Background normalisation uncertainties do not affect the signal response. To evaluate their impact on the differential cross section, the event yields are scaled up and down for each background category and the unfolding is repeated with the nominal response matrix and the varied background predictions. Similarly, the integrated luminosity and trigger efficiency uncertainties are propagated by a simultaneous rescaling of all background yields. For the integrated luminosity, the variations of the unfolded distribution are combined with the corresponding variation of the integrated luminosity in Equation (3.14).

- The remaining experimental uncertainties—pileup modelling, lepton selection efficiency, jet energy scale and resolution, and b tagging efficiency—affect both the background yield predictions and the response to signal events. Since unfolding by matrix inversion as described in equation (3.13) is a linear operation, applying variations for these uncertainty sources to the response matrix or to the background-subtracted event yields gives the same result. Additional response matrix variations created from the same $\mathrm{t\bar{t}Z}$ MC sample would require a sufficient size of the sample

Table 3.3

$p_T(Z)$ range	absolute cross section	normalised cross section
0 GeV to 75 GeV	(3.85 ± 0.71) fb/GeV	$(4.08 \pm 0.48) \times 10^{-3}$/GeV
75 GeV to 150 GeV	(4.82 ± 0.65) fb/GeV	$(5.11 \pm 0.44) \times 10^{-3}$/GeV
150 GeV to 250 GeV	(2.12 ± 0.30) fb/GeV	$(2.24 \pm 0.26) \times 10^{-3}$/GeV
> 250 GeV	(0.33 ± 0.07) fb/GeV	$(0.35 \pm 0.06) \times 10^{-3}$/GeV

Measured absolute and normalised differential $t\bar{t}Z$ production cross section as a function of $p_T(Z)$.

Table 3.4

$\cos\theta^\star(Z)$ range	absolute cross section	normalised cross section
< -0.5	(230 ± 39) fb	0.249 ± 0.030
-0.5 to 0.0	(249 ± 38) fb	0.269 ± 0.030
0.0 to 0.5	(240 ± 34) fb	0.260 ± 0.028
> 0.5	(204 ± 38) fb	0.221 ± 0.031

Measured absolute and normalised differential $t\bar{t}Z$ production cross section as a function of $\cos\theta^\star(Z)$.

to ensure that they represent the systematic variation and are not dominated by statistical fluctuations present in the sample. Instead, the impact of the of the systematic uncertainties is evaluated on the predicted signal and background yields and applied as a variation to the measured data. The unfolding is then repeated with the nominal response matrix, the varied data, and the varied background event yields, and the systematic uncertainty is evaluated separately in each bin of the differential cross section.

The results from the unfolding of the measured distributions are shown in Figure 3.16. In addition to the absolute differential cross sections obtained as in Equation (3.14), the normalised differential cross sections, obtained by normalising the unfolded event yields with their sum, are shown. The values of all cross section measurements are also listed in Table 3.3 for $p_T(Z)$, and in Table 3.4 for $\cos\theta^\star(Z)$.

For the absolute cross section results, the statistical uncertainties range between 11 % and 17 %, and the total (statistical and systematic) uncertainties between 13 % and 17 %. Thus, the measurement is currently still limited by the limited number of events in data. For the normalised cross section, uncertainties that affect only the total $t\bar{t}Z$ production cross section, but not the shape of the differential distribution, cancel out, resulting in a much reduced systematic uncertainty, with total uncertainties between 9 % and 18 %.

Figure 3.16

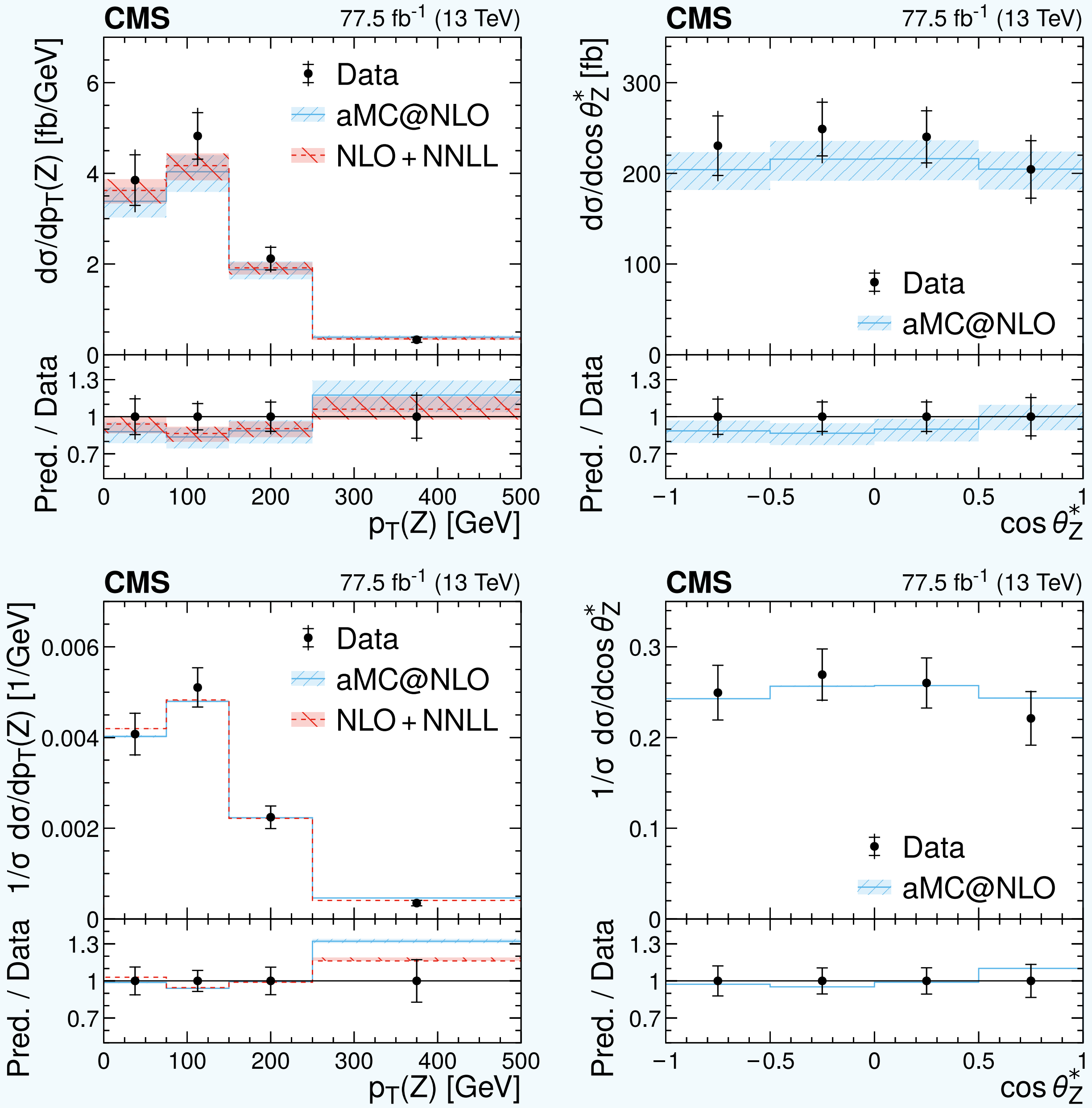

Absolute (upper row) and normalised (lower row) differential $t\bar{t}Z$ production cross sections as a function of the Z boson transverse momentum (left) and the angle between the Z boson and its decay lepton $\cos\theta^{\star}(Z)$ (right). Shown are the measured cross section (points), and the SM predictions (lines) at NLO accuracy [184, 185, 220] (blue) and at NLO+NNLL accuracy [188, 189] (red). The measurement shows the statistical (statistical and systematic) uncertainty with the inner (outer) error bars. Published in Ref. [E].

The measured differential cross sections are compared to SM predictions calculated to NLO accuracy [184, 185, 220] (both observables) and to NLO+NNLL accuracy [188, 189] (only $p_{\mathrm{T}}(\mathrm{Z})$). The predictions agree well with the data. Especially the shapes of the normalised cross sections are well described, while in the absolute cross sections the predictions are somewhat lower than the data, consistent with the results from the inclusive cross section measurement.

IX. Differential $t\bar{t}Z$ production cross section in top quark observables

In this chapter, a differential measurement of the $t\bar{t}Z$ production cross section as a function of top quark observables is presented, using proton-proton collision data at $\sqrt{s} = 13\,\text{TeV}$ collected in 2016–2018. The measurement of top quark observables allows to probe the modelling of the $t\bar{t}Z$ production process in perturbative QCD [190]. A kinematic reconstruction of the top quarks from their decay products requires a tighter event selection with exactly three leptons and at least four jets.

The event selection is described in Section 3.10. The kinematic reconstruction of the top quarks is discussed in Section 3.11, and the unfolding procedure applied to extract the differential cross section in Section 3.12. The differential cross section results are presented in Section 3.13, and an outlook on future measurements is given in Section 3.14.

This measurement constitutes a main result of this thesis.

3.10. Event selection and background predictions

This measurement follows a similar strategy as discussed in Chapters VII and VIII. In the following, the modified event selection and background estimations are described.

Datasets The combined 2016–2018 dataset corresponds to an integrated luminosity of $137\,\text{fb}^{-1}$, with a relative uncertainty of $1.8\,\%$ which takes the correlations between the uncertainties of the three datasets as described in Table 2.1 into account. Separate sets of MC samples for signal and background processes are used that reflect the detector conditions of the three years, and use updated detector calibrations for the 2016 and 2017 datasets with respect to the samples described in Section 3.4.

Trigger A combination of single-, double-, and triple-lepton HLT paths is used to select events from the data samples. A similarly high trigger selection efficiency as in Section 3.4 is expected for events that also pass the lepton selection. However, since the trigger efficiency measurement has not been repeated for the modified trigger and lepton selection, no scale factors are applied and an increased uncertainty of 4 % is assigned to the predicted background event yields.

Lepton selection A modified set of identification criteria are applied to discriminate between prompt and nonprompt leptons, developed in the context of the most recent $t\bar{t}H$ production measurement in multi-lepton final states [221]. The “loose”, ”medium”, and ”tight” selection criteria are described in the following.

- Loose electrons are selected with a transverse momentum of $p_T > 5\,\text{GeV}$ and a pseudorapidity of $|\eta| < 2.5$, and loose muons with $p_T > 7\,\text{GeV}$ and $|\eta| < 2.4$. In addition, loose leptons are required to fulfil criteria based on the impact parameter and the relative isolation, as well as specific identification criteria for electrons and muons. Electron candidates are removed if they overlap with a loose muon by $\Delta R < 0.3$.

- Medium leptons are required to have a transverse momentum of $p_T > 10\,\text{GeV}$. A jet is considered as the “closest jet” to a lepton if it uses the particle flow candidate from which the lepton has been reconstructed. If a lepton has a closest jet, the closest jet is required to not pass a b tagging criterion. Additionally, the lepton is either required to also pass the tight selection, or to fulfil a requirement on the relative isolation with respect to its closest jet.

- A modified MVA discriminator is trained for the selection of tight leptons, using observables of the lepton candidate and the closest jet as inputs. Tight leptons are required to pass a minimal threshold on the MVA discriminator value.

Scale factors to correct the selection efficiency in MC samples to match those in data are applied for the loose lepton selection. No scale factors are applied for the efficiency of the medium and tight lepton selection.

Events are required to have exactly three tight leptons with transverse momenta of $p_T > 40$, 20, and $10\,\text{GeV}$, and events with additional medium leptons are vetoed. Furthermore, a Z boson candidate is required, a lepton pair of same flavour and opposite charge with an invariant mass of $|m(\ell^+\ell^-) - 91\,\text{GeV}| < 10\,\text{GeV}$.

Jet selection Reconstructed jets are selected if they have a transverse momentum of $p_\mathrm{T} > 30\,\mathrm{GeV}$ and a pseudorapidity of $|\eta| < 2.5$. A jet is removed from the event if it is the closest jet to a medium lepton, as defined above.

Jets are tagged as b jets with the DeepJet discriminator value, using a working point with a mistag probability for light quark and gluon jets of 1 % and an efficiency of about 75 % for b quark jets [66].

Events are required to have at least four jets of which at least one jet is b tagged. This "signal-resolved" selection ensures that one jet can be assigned to each of the quarks from the semileptonic $\mathrm{t\bar{t}}$ decay.

Background predictions The contributions from the background processes as discussed in Section 3.5 are all predicted from simulated events. The grouping of the processes and the uncertainties assigned to the normalisation are modified with respect to the previous approach.

- Among the associated top quark production processes, the dominant background contributions arise from single top quark production with a Z boson, tZq and tWZ. Thus, these two processes are shown separately, and all other contributions are grouped as $\mathrm{t(\bar{t})X}$. A normalisation uncertainty of 15 % is assigned, corresponding to the uncertainty of the measured tZq cross section [172], except for a 30 % uncertainty assigned to the tWZ event yields due to ambiguities in the removal of $\mathrm{t\bar{t}Z}$ contributions in the cross section computation at NLO accuracy [222].
- Diboson and triboson production are grouped together as "VV(V)". The single most dominant contribution arises from WZ production. Combining the total WZ cross section uncertainty [201], the discrepancy observed at large jet multiplicities, and the potential mismodelling of gluon splitting [5], a normalisation uncertainty of 30 % is assigned to the event yields.
- The event yields from nonprompt lepton events are predicted using MC samples for $\mathrm{t\bar{t}}$ and Z + jets production, and are grouped together with the small contributions from photon conversion processes. The prediction of nonprompt lepton backgrounds from simulated events is estimated to be less precise than the data-driven determination using the fake rate method described in Section 3.5. Thus, a large normalisation uncertainty of 50 % is assigned.

The measured and predicted event yields are compared in Figure 3.17 for the three datasets and for the different lepton flavour categories. For all three years, the predicted

Figure 3.17

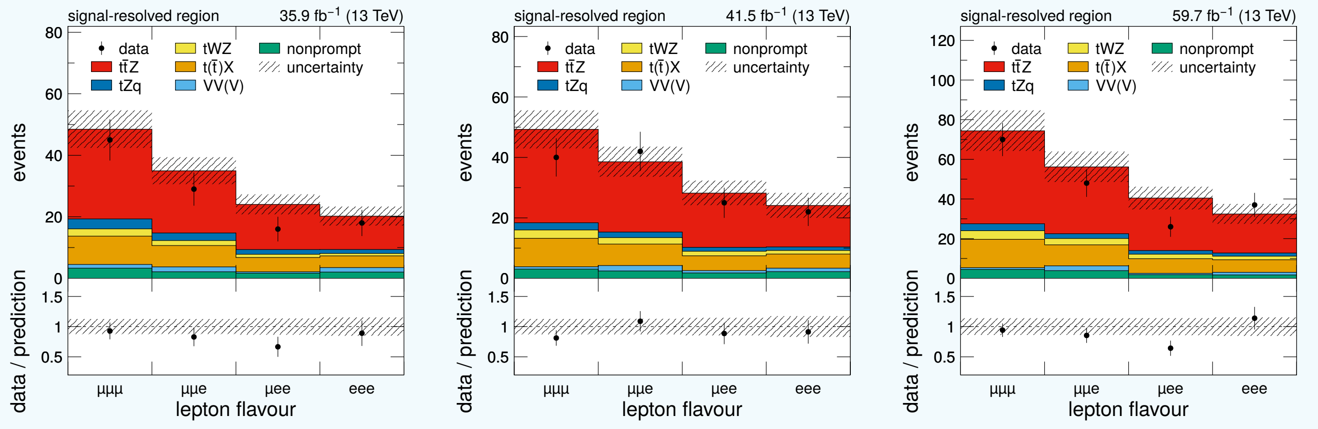

Observed (points) and predicted (shaded) event yields in the signal-resolved region for the distribution of the lepton flavours in the 2016 (left), 2017 (centre), and 2018 (right) datasets.

event yields are somewhat higher than the measured ones, in contrast to the pre-fit comparisons of the previous measurement. The predicted and measured event yields show very similar shapes for all datasets. The efficiency for the selection of muons is higher than for the selection of electrons, resulting in about twice as many triple-muon events compared to triple-electron events.

For the combined dataset, comparisons for several observables are shown in Figures 3.18 and 3.19. In general, a good agreement between measured and predicted shapes is found in all observables.

3.11. Top quark reconstruction

Kinematic reconstruction While the reconstruction of the Z boson four-momentum from the reconstructed $\ell^+\ell^-$ pair is straightforward, a reconstruction of the four-momenta of the top quarks from their decay products is more complicated. For the case of the semileptonic $t\bar{t}$ decay at leading-order, as shown in Figure 3.20, one lepton, one neutrino, and four quarks are present after the decays and before the start of hadronisation. This "parton-level" description is not observable, instead, modelling is required to connect the partons with the measured particles. Beyond the leading-order picture, additional partons, e. g. from gluon radiation, can be present and carry a fraction of the top quark momentum. Thus, a kinematic reconstruction based on the assignment of measured particles to intermediate partons has a limited precision but still provides sensitivity to the kinematic properties of the underlying partons [223].

Figure 3.18

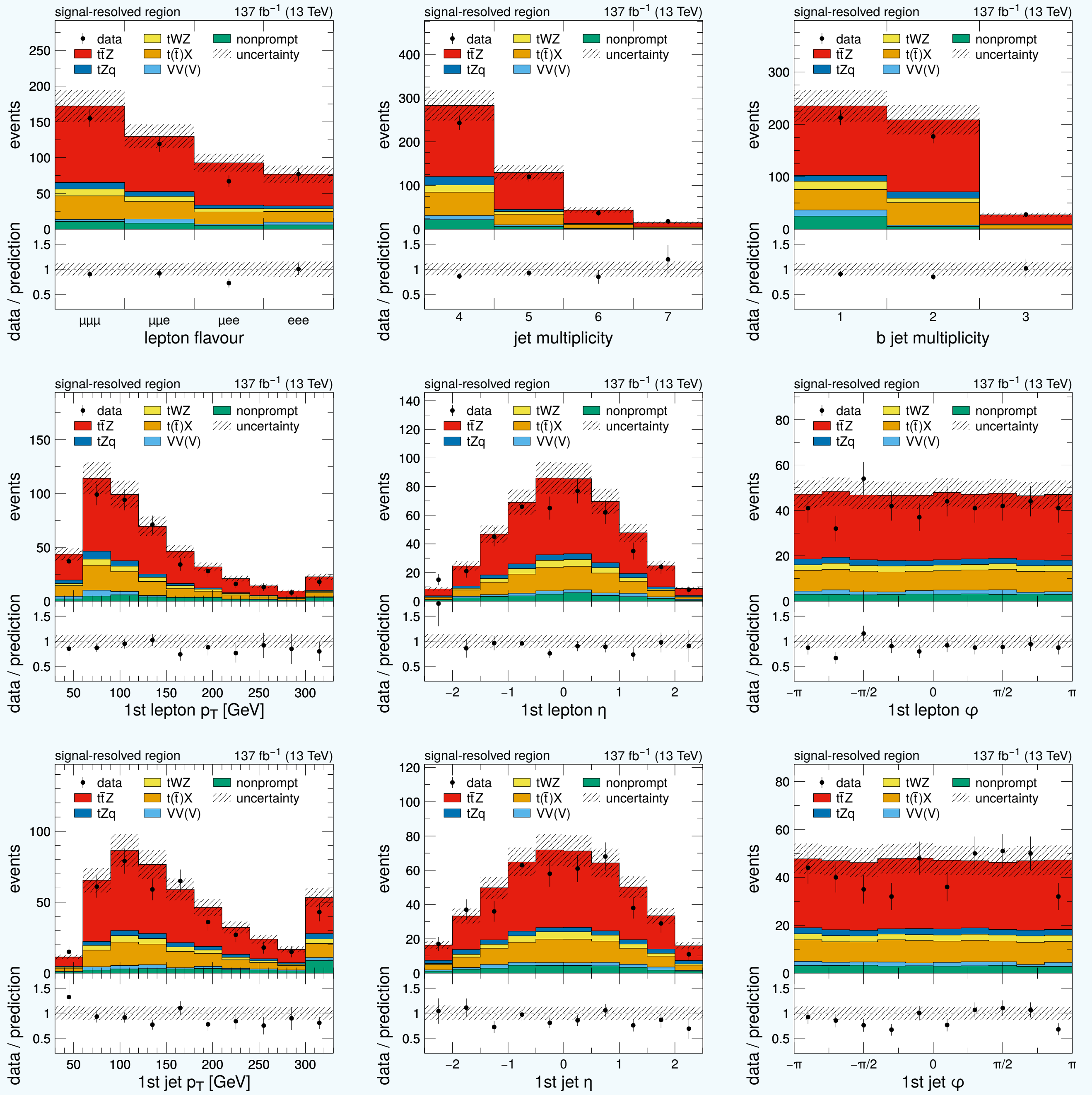

Observed (points) and predicted (shaded) event yields in the signal-resolved region for the distribution of: the lepton flavours (upper left), the number of jets (upper centre), the number of b jets (upper right); the transverse momentum (middle left), pseudorapidity (middle centre), and azimuthal angle (middle right) of the leading lepton; the transverse momentum (lower left), pseudorapidity (lower centre), and azimuthal angle (lower right) of the leading jet.

Figure 3.19

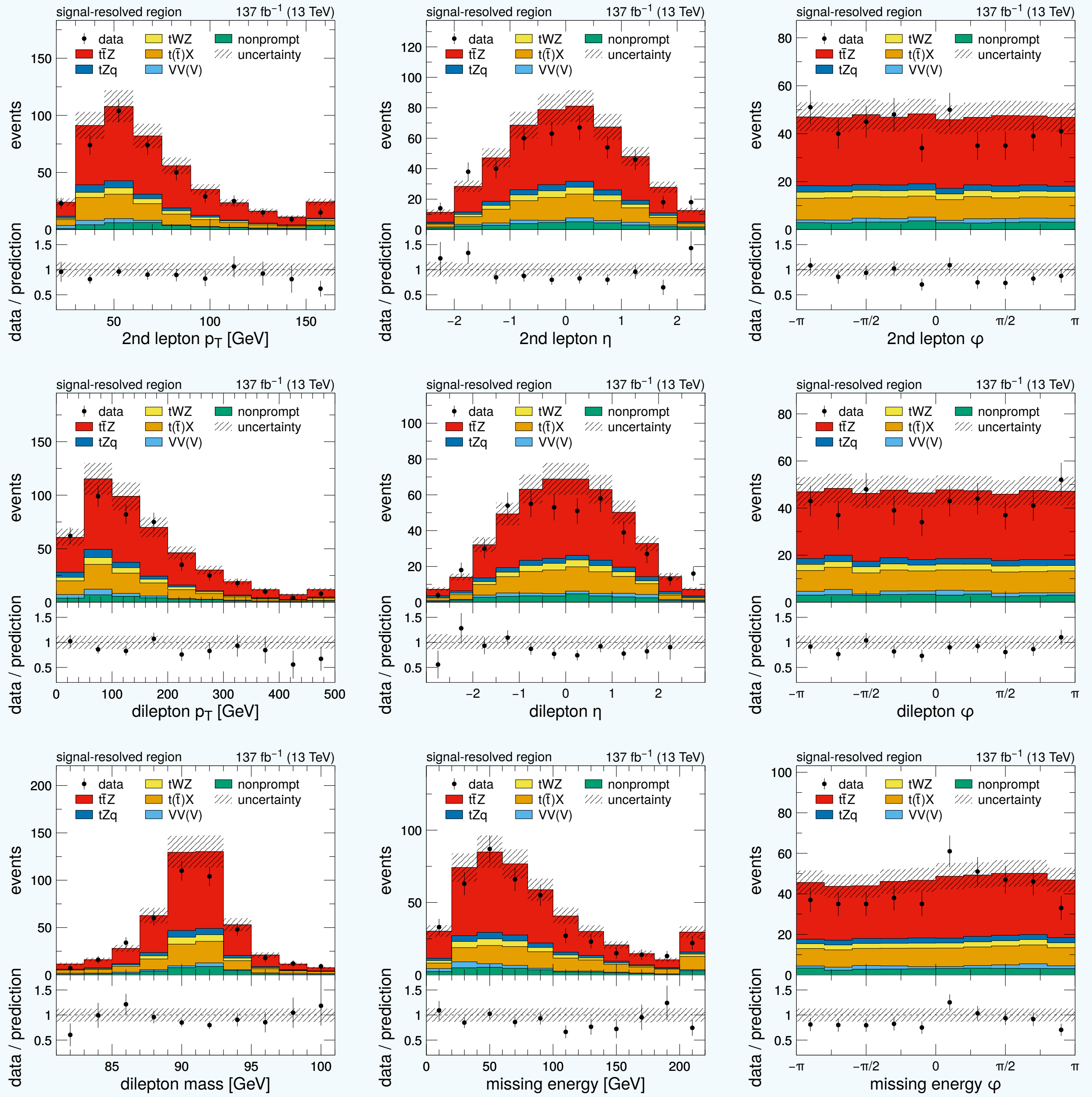

Observed (points) and predicted (shaded) event yields in the signal-resolved region for the distribution of: the transverse momentum (upper left), pseudorapidity (upper centre), and azimuthal angle (upper right) of the subleading lepton; the transverse momentum (middle left), pseudorapidity (middle centre), azimuthal angle (middle right), and invariant mass (lower left) of the dilepton system reconstructed as Z boson candidate; missing energy (lower centre) and its azimuthal angle (lower right).

Figure 3.20

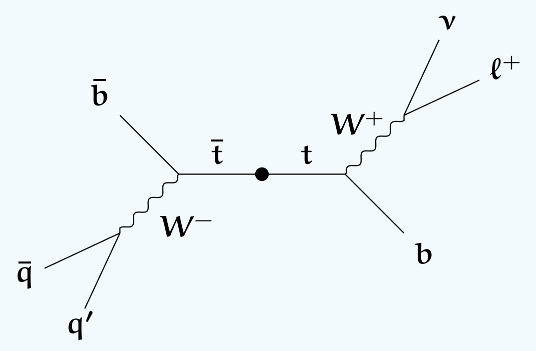

Schematic view of the semileptonic $t\bar{t}$ decay.

Two main challenges arise in the top quark reconstruction: the determination of the longitudinal neutrino momentum and the assignment of jets.

1. For the reconstruction of the leptonically decaying top quark, it is assumed that all missing transverse energy originates from the neutrino in the decay. However, no measurement is available for the longitudinal component of the neutrino momentum. Imposing the $W \to \ell\nu$ decay hypothesis on an event, the W boson mass $m(\mathrm{W}) = 80.38\,\mathrm{GeV}$ [6] is used to constrain the longitudinal component via the momentum-conservation equation:

$$(p_\ell + p_\nu)^2 = m_{\mathrm{W}}^2. \tag{3.15}$$

   This results in a quadratic equation for $p_{\nu,z}$ which can have two, one or no solutions. The precise formulation of the equation and its general solution can be found e. g. in Reference [224].
2. With four reconstructed jets and four partons from the top quark decays, there are twelve possible jet-parton assignments (an exchange of the two quarks from the W boson decay does not change the kinematic properties). The number of permutations can be reduced in events with b jets by considering only permutations where the b jets are assigned to the b quarks.

Three more mass constraints are formulated to evaluate how well a choice of jet-parton assignments together with a solution for the longitudinal neutrino momentum describe the hypothesis of a semileptonic decay of a $t\bar{t}$ system, namely

$$(p_\ell + p_\nu + p_{b,1})^2 = m_{\mathrm{t}}^2, \qquad (p_{j,1} + p_{j,2})^2 = m_{\mathrm{W}}^2, \qquad (p_{j,1} + p_{j,2} + p_{b,2})^2 = m_{\mathrm{t}}^2. \tag{3.16}$$

Noting that the resolutions of the measured four-momenta are limited, especially for the jets and the missing transverse momentum, a "kinematic fit" is performed in which the components of the measured four-momenta are allowed to vary within their experimental uncertainties to find a better description of the $t\bar{t}$ system [144].

Kinematic fit Here, a kinematic fit is performed with the KinFitter software [225], which has also been used in other measurements at the CMS experiment [226, 227]. For the four-momenta of all particles, a parameterisation in terms of transverse energy E_{T}, pseudorapidity η, and azimuthal angle ϕ is chosen,

$$E = E_\mathrm{T} \cosh\eta, \qquad \vec{p} = \begin{pmatrix} E_\mathrm{T}\cos\phi \\ E_\mathrm{T}\sin\phi \\ E_\mathrm{T}\sinh\eta \end{pmatrix}. \tag{3.17}$$

For the measured particles, the transverse energy is computed from the measured transverse momentum assuming a mass of 4.92 GeV [220] for jets assigned to the bottom quarks, and zero mass for all other particles. The measured ("meas") momentum components are fixed to their initial values, and a set of fitted four-momenta ("fit") are allowed to vary freely. The agreement between the fitted and measured momenta is quantified by the χ^2 function:

$$\chi^2 = \sum_i \left[\frac{(E_{\mathrm{T},i}^\mathrm{meas} - E_{\mathrm{T},i}^\mathrm{fit})^2}{\delta^2_{E_\mathrm{T},i}} + \frac{(\eta_i^\mathrm{meas} - \eta_i^\mathrm{fit})^2}{\delta^2_{\eta,i}} + \frac{(\phi_i^\mathrm{meas} - \phi_i^\mathrm{fit})^2}{\delta^2_{\phi,i}} \right], \tag{3.18}$$

using the resolutions δ of the respective particles. Lagrange multipliers λ_j are added for each mass constraint from Equations (3.15) and (3.16), resulting in the likelihood function:

$$\begin{aligned} \mathcal{L}(\{E_{\mathrm{T},i}^\mathrm{fit}, \eta_i^\mathrm{fit}, \phi_i^\mathrm{fit}\}, \{\lambda_j\}) = \chi^2 &+ \lambda_{\mathrm{W},1}(m_{\mathrm{W},1}^\mathrm{fit} - 80.38\,\mathrm{GeV}) + \lambda_{\mathrm{t},1}(m_{\mathrm{t},1}^\mathrm{fit} - 172.5\,\mathrm{GeV}) \\ &+ \lambda_{\mathrm{W},2}(m_{\mathrm{W},2}^\mathrm{fit} - 80.38\,\mathrm{GeV}) + \lambda_{\mathrm{t},2}(m_{\mathrm{t},2}^\mathrm{fit} - 172.5\,\mathrm{GeV}). \end{aligned} \tag{3.19}$$

A minimisation of the likelihood function provides the best-fit description of the $t\bar{t}$ system achievable with the chosen assignment of measured jets to partons, and the value of the likelihood function at the minimum is used to decide which assignment gives the best description of the $t\bar{t}$ hypothesis.

Experimental resolution A crucial input to the kinematic fit are the resolutions of the measured particles, which quantify how much the fitted momenta are allowed to deviate from the measured momenta. Since the goal of the kinematic fit is to reconstruct the parton-level four-momenta, the term "resolution" is not limited to the experimental resolutions of the detector measurements and reconstruction algorithms, but also includes the impact of hadronisation. For example, leptonically decaying b hadrons produce a neutrino which cannot be measured and is thus not part of the reconstructed b jet momentum, resulting in a discrepancy between the parton momentum and the measured momentum beyond the jet energy resolution. Additionally, these neutrinos are missing in the momentum balance of the event, resulting in a mismatch of measured missing transverse momentum and the momentum of the neutrino from the top quark decay.

The resolutions are studied in MC events using the parton four-momenta that were input to the hadronisation and detector simulation. To find the correct assignments between reconstructed particles (jets and leptons) and partons, a geometric matching is performed. Reconstructed leptons (jets) are assigned to a parton if they fulfil a distance criterion of $\Delta R < 0.1\,(0.2)$. For the resolution study, MC events are selected that contain a matched lepton, with correct flavour and charge, and four jets which are matched such that there is a jet assigned to each of the four quarks. No veto is applied on additional leptons or jets to include the impact of additional radiation or misreconstructions on the resolutions. Due to the size of the available MC samples, $\mathrm{t\bar{t}}$ production events in the semileptonic decay channel are used to derive the resolutions, and the results are validated with $\mathrm{t\bar{t}Z}$ production events in the three-lepton decay channel.

For the selected events, the agreement between parton momenta and measured momenta of electrons, muons, b jets, light jets (the jets assigned to the quarks from the hadronically decaying W boson), and missing momentum is analysed separately for E_{T}, η, and ϕ, and separately in categories of transverse energy and pseudorapidity. For the resolutions in η and ϕ, two pseudorapidity intervals are chosen corresponding to the barrel ($|\eta| < 1.479$) and endcap ($|\eta| > 1.479$) detector region. For the E_{T} resolution, pseudorapidity intervals are chosen in the barrel for the four ECAL supermodules (with transitions at $|\eta| = 0.435$, 0.783, 1.131), and in the endcap for the area without ($1.479 < |\eta| < 1.653$) and with ($|\eta| > 1.653$) the preshower detector. No division in pseudorapidity is done for the missing momentum resolution.

In Figure 3.21, examples for resolutions of jets and missing momentum are shown. The resolution is defined as the RMS of the distribution of deviations between true and measured value of the respective observable, separately in each (E_{T}, η) bin. For E_{T}, the relative discrepancy $(E_{\mathrm{T}}^{\mathrm{meas}} - E_{\mathrm{T}}^{\mathrm{parton}})/E_{\mathrm{T}}^{\mathrm{meas}}$ is presented, while absolute discrepancies are shown for η and ϕ.

The transverse energy resolution of jets improves from about 35 % for b jets and 28 % for light jets at the lowest energies to about 15 % at highest energies. The resolution is worse for b jets because of the typically larger multiplicity of particles with an, on average, lower transverse momentum compared to jets originating from light quarks or gluons, as well as by the probability to have neutrinos in the decay of the b hadron. Both types of jets have similar pseudorapidity and azimuthal angle resolutions, better than 0.06 and 0.06 rad in absolute values, which improve at higher transverse energy.

Figure 3.21

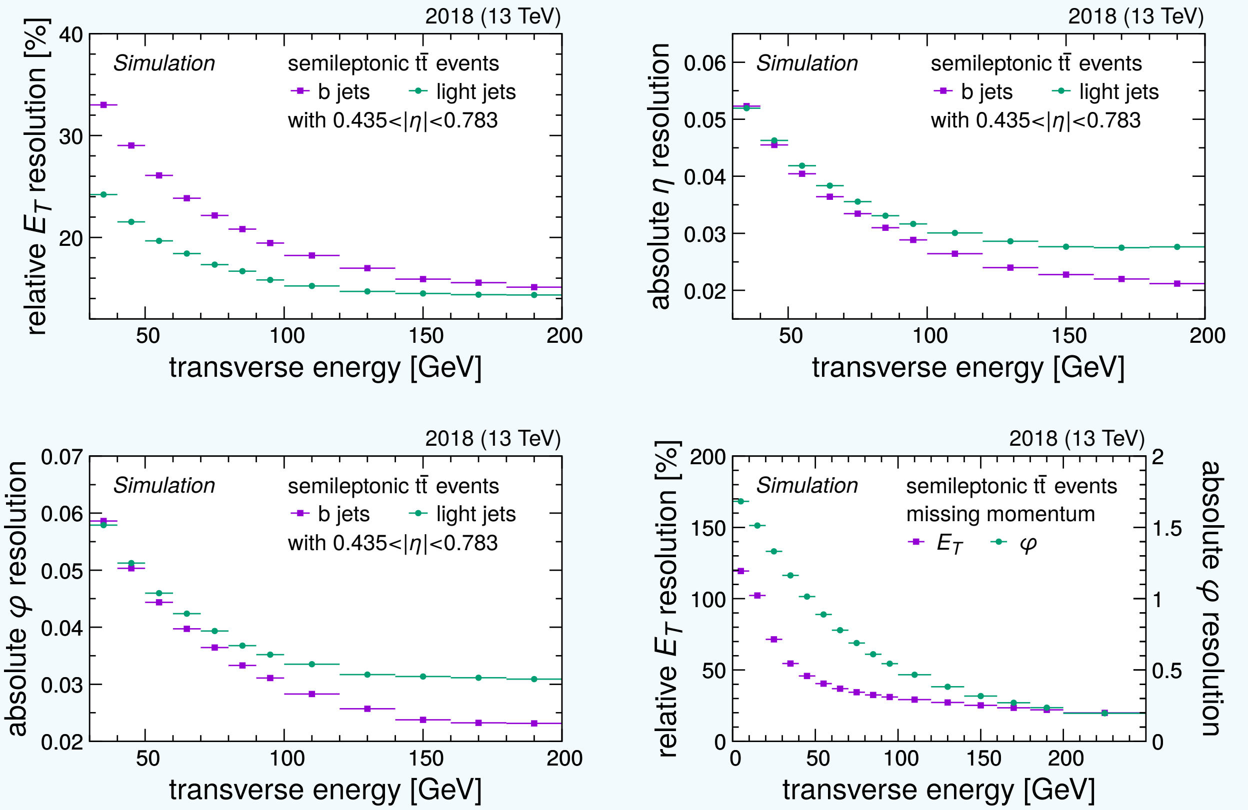

Resolution of jet E_T (upper left), η (upper right), and ϕ (lower left) for jets with $0.435 < |\eta| < 0.783$; and of E_T and ϕ of the missing momentum vector (lower right); as a function of transverse energy derived from simulated t$\bar{t}$ production events with semileptonic decays, using 2018 detector conditions.

Due to the simplifying assumption that the neutrino from the leptonic W boson decay is the only source of missing transverse momentum in the event, the resolution of the neutrino energy is larger than 150 % at lowest transverse energy values. For larger missing energy values, E_T and ϕ resolutions of 20 % and 0.2 rad are achieved.

In contrast, the resolutions of electrons and muons are very good. For electrons, where the momentum determination relies mainly on the calorimeter measurements, the E_T resolution is 1.5 % at highest energies and 9 % at lowest energy. For muons, where the momentum determination relies mainly on the reconstructed tracks, the resolution is between 2.5 % and 6 %, mainly depending on pseudorapidity and slightly better at lower energy. The pseudorapidity and azimuthal angle resolutions are better than 0.002 and 0.003 rad in absolute values, both for electrons and muons.

Table 3.5

true	1st bin		2nd bin		3rd bin		4th bin		
measured	**1st**	**2nd**	**3rd**	**4th**	**5th**	**6th**	**7th**	**8th**	
$m(\mathrm{t\bar{t}Z})$ [GeV]	436	580	640	720	800	890	1000	1150	1500
$m(\mathrm{t\bar{t}})$ [GeV]	345	400	440	485	540	610	700	850	1200
$p_{\mathrm{T}}(\mathrm{t})$ [GeV]	0	60	90	125	160	200	250	330	500
$\lvert\phi(\mathrm{t}) - \phi(\bar{\mathrm{t}})\rvert$	0	$\pi/4$	$\pi/2$	$5\pi/8$	$3\pi/4$	$13\pi/16$	$7\pi/8$	$15\pi/16$	π
$\lvert\phi(\mathrm{t}) - \phi(\mathrm{Z})\rvert$	0	$\pi/6$	$\pi/3$	$\pi/2$	$2\pi/3$	$3\pi/4$	$5\pi/6$	$11\pi/12$	π
$\lvert y(\mathrm{t}) - y(\bar{\mathrm{t}})\rvert$	0.0	0.25	0.5	0.75	1.0	1.25	1.5	2.1	3.0
$\lvert y(\mathrm{t}) - y(\mathrm{Z})\rvert$	0.0	0.25	0.5	0.75	1.0	1.25	1.5	2.0	3.0

Bin boundaries chosen for the true and measured observables.

Observables Seven observables that were studied in the differential cross section computation at NLO+NNLL accuracy [190] are measured here:

- the invariant mass of the $\mathrm{t\bar{t}Z}$ system, $m(\mathrm{t\bar{t}Z})$, and of the $\mathrm{t\bar{t}}$ system, $m(\mathrm{t\bar{t}})$;
- the transverse momentum of the top quark, $p_{\mathrm{T}}(\mathrm{t})$;
- the absolute value of the azimuthal angle difference between the top quark and the top antiquark, $\lvert\phi(\mathrm{t}) - \phi(\bar{\mathrm{t}})\rvert$, and between the top quark and the Z boson, $\lvert\phi(\mathrm{t}) - \phi(\mathrm{Z})\rvert$;
- the absolute value of the rapidity difference between the top quark and the top antiquark, $\lvert y(\mathrm{t}) - y(\bar{\mathrm{t}})\rvert$, and between the top quark and the Z boson, $\lvert y(\mathrm{t}) - y(\mathrm{Z})\rvert$.

The top quark (as opposed to the top antiquark) is identified via the charge of the lepton from the leptonically decaying top quark: If the lepton not used for the Z boson reconstruction has a positive charge, the kinematics of the leptonically decaying top quark are used (cf. Figure 3.20), otherwise the kinematics of the hadronically decaying top quark.

Eight and four bins are chosen for each measured and true observable, respectively, with bin boundaries as listed in Table 3.5. Each true bin corresponds to two bins for the measured observable. For the invariant masses, the lower bin boundaries of the first bins are chosen assuming values of 172.5 GeV and 91 GeV for the mass of top quarks and Z bosons. However, the first bins also include events with measured invariant masses lower than that. While the azimuthal angle differences are defined to have values strictly between $-\pi$ and π, all other observables have no strict upper limit but fall off at large values. The upper bin boundaries of the last bins are chosen such that less than 5% of the expected events lie outside the range. Events with values larger than the upper bin boundary of the last bins are then included in the last bins, but the nominal bin width is used to obtain the differential cross section in that bin.

Figure 3.22

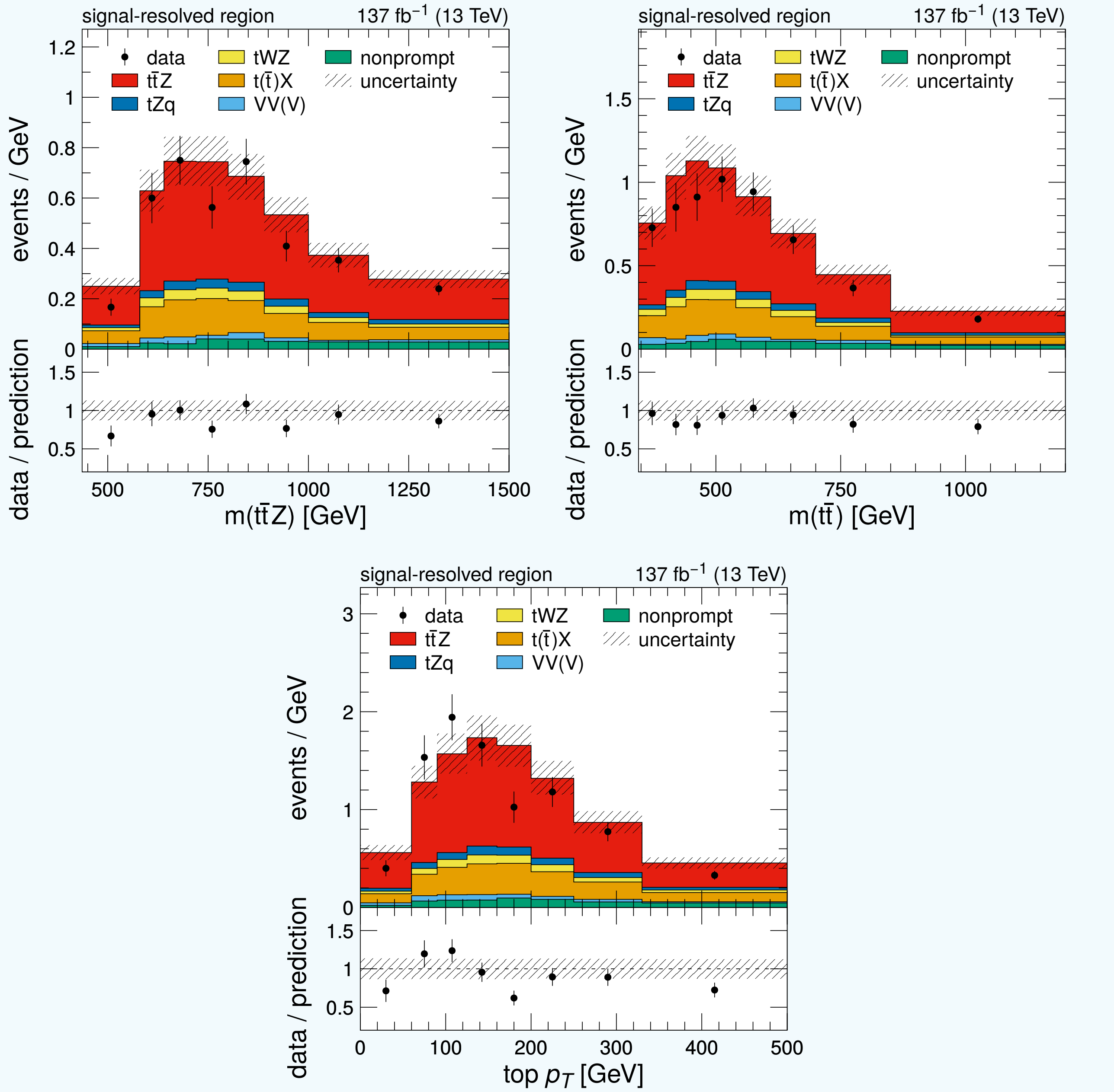

Observed (points) and predicted (shaded) event yields for the distribution of the invariant mass of the $t\bar{t}Z$ system (upper left), the invariant mass of the $t\bar{t}$ system (upper right), and the top quark transverse momentum (lower) in the signal-resolved region, combined for the 2016, 2017, and 2018 datasets.

Figure 3.23

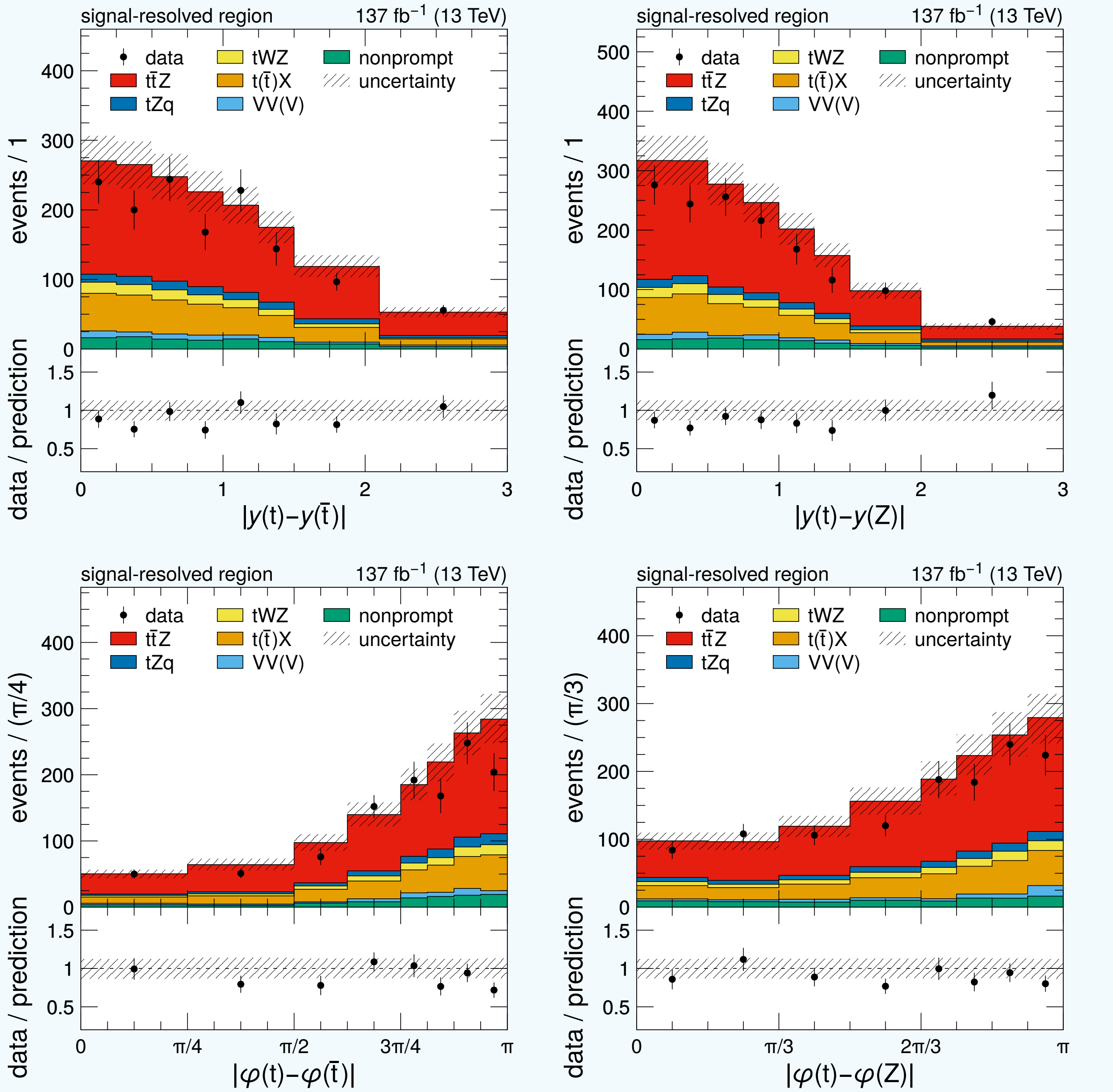

Observed (points) and predicted (shaded) event yields for the distribution of the rapidity difference (upper) and azimuthal angle difference (lower) between top quark and antiquark (left) and between top quark and Z boson (right) in the signal-resolved region, combined for the 2016, 2017, and 2018 datasets.

The measured distributions for these observables are shown in Figure 3.22 for the masses and momenta, and in Figure 3.23 for the rapidity and azimuthal angle differences. Within uncertainties, good agreement is observed between the measured data and the prediction for all observables.

Response For the computation of the response matrices, as described in Section 3.8, simulated $t\bar{t}Z$ events in the three-lepton decay channel are used. Only events that pass the selection criteria are considered for the computation of the resolution matrix. For the mass and momentum observables, the resulting resolution matrices are shown in Figure 3.24. The corresponding distributions of stability, purity, and efficiency are shown in Figure 3.25. Compared to the Z boson observables discussed in Section 3.8, much stronger bin-to-bin migrations are observed for the top quark observables.

Quantitatively, the stability, i. e. how many events from a true bin are reconstructed in one of the two corresponding measured bins, and the purity, i. e. how many measured events originate from the corresponding true bin, reach values as low as 45 % for $m(t\bar{t})$ and $p_T(t)$, and as low as 55 % for $m(t\bar{t}Z)$. As expected, the highest stability and purity values of about 85 % are reached in the first and last bins where migrations in only one direction are possible. The efficiency increases from about 16 % at low masses and momenta to 22 % at high values.

For the rapidity and azimuthal angle differences, the resolution matrices are shown in Figure 3.26, and the stability, purity, and efficiency distributions in Figure 3.27. For the observables involving the top quark and the Z boson, stability and purity range between 50 % and 75 %, profiting from the very good reconstruction of the Z boson kinematics. For the observables involving the two reconstructed top quarks, the lowest stability and purity values of 37 % are reached. The selection efficiency does not strongly depend on the value of the four observables and is about 20 % everywhere.

3.12. Regularised unfolding

In the simple unfolding approach by matrix inversion, strong bin-to-bin migrations lead to an amplification of statistical fluctuations which are present in any measurement. This was not a problem for the unfolding of the Z boson observables described in Section 3.8 since the bin-to-bin migrations were too small to cause an amplification of the statistical fluctuations larger than the statistical uncertainty.

Figure 3.24

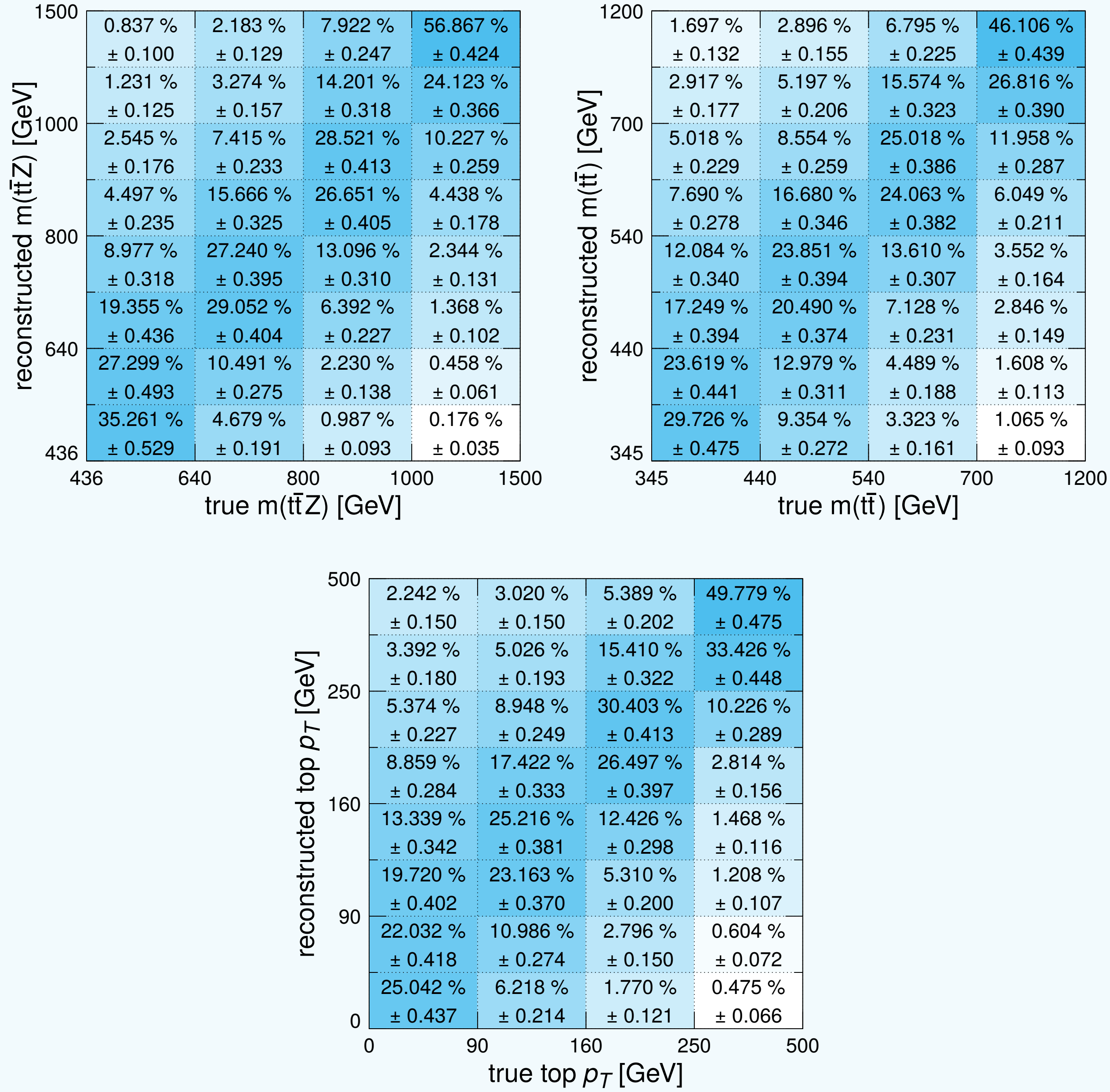

Resolution matrices describing bin-to-bin migrations from true bins to measured bins for the invariant mass of the $t\bar{t}Z$ system (upper left), the invariant mass of the $t\bar{t}$ system (upper right), and the top quark transverse momentum (lower), with statistical uncertainties due to the size of the MC samples.

Figure 3.25

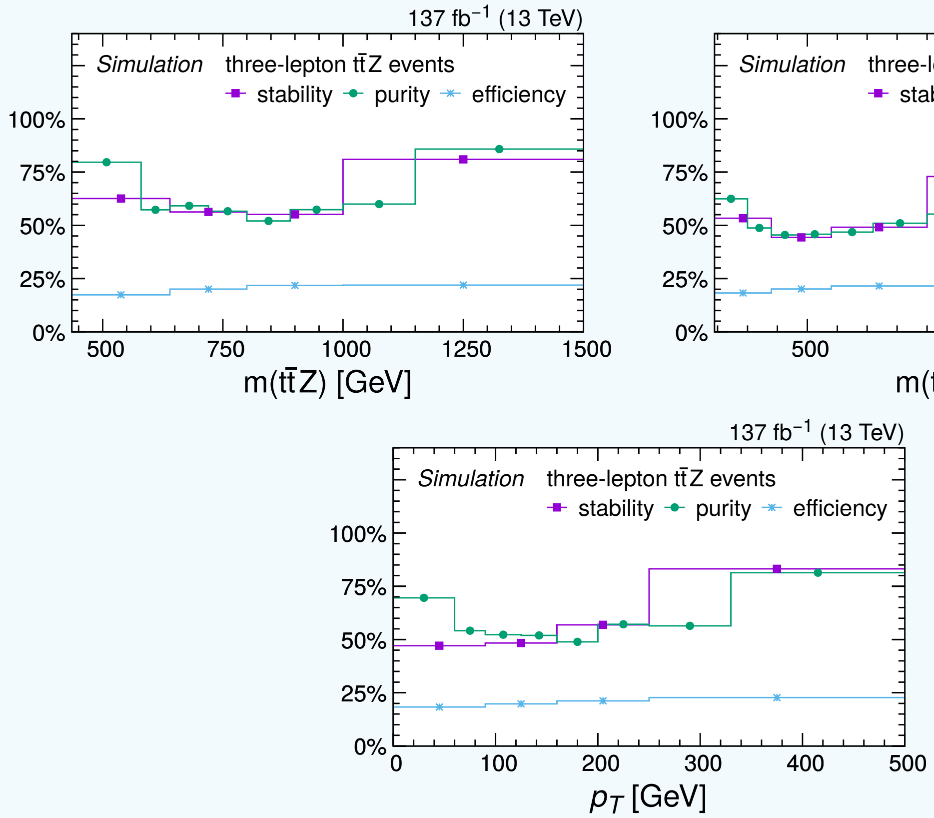

Stability, purity, and efficiency for the invariant mass of the $t\bar{t}Z$ system (upper left), the invariant mass of the $t\bar{t}$ system (upper right), and the top quark transverse momentum (lower).

Figure 3.26

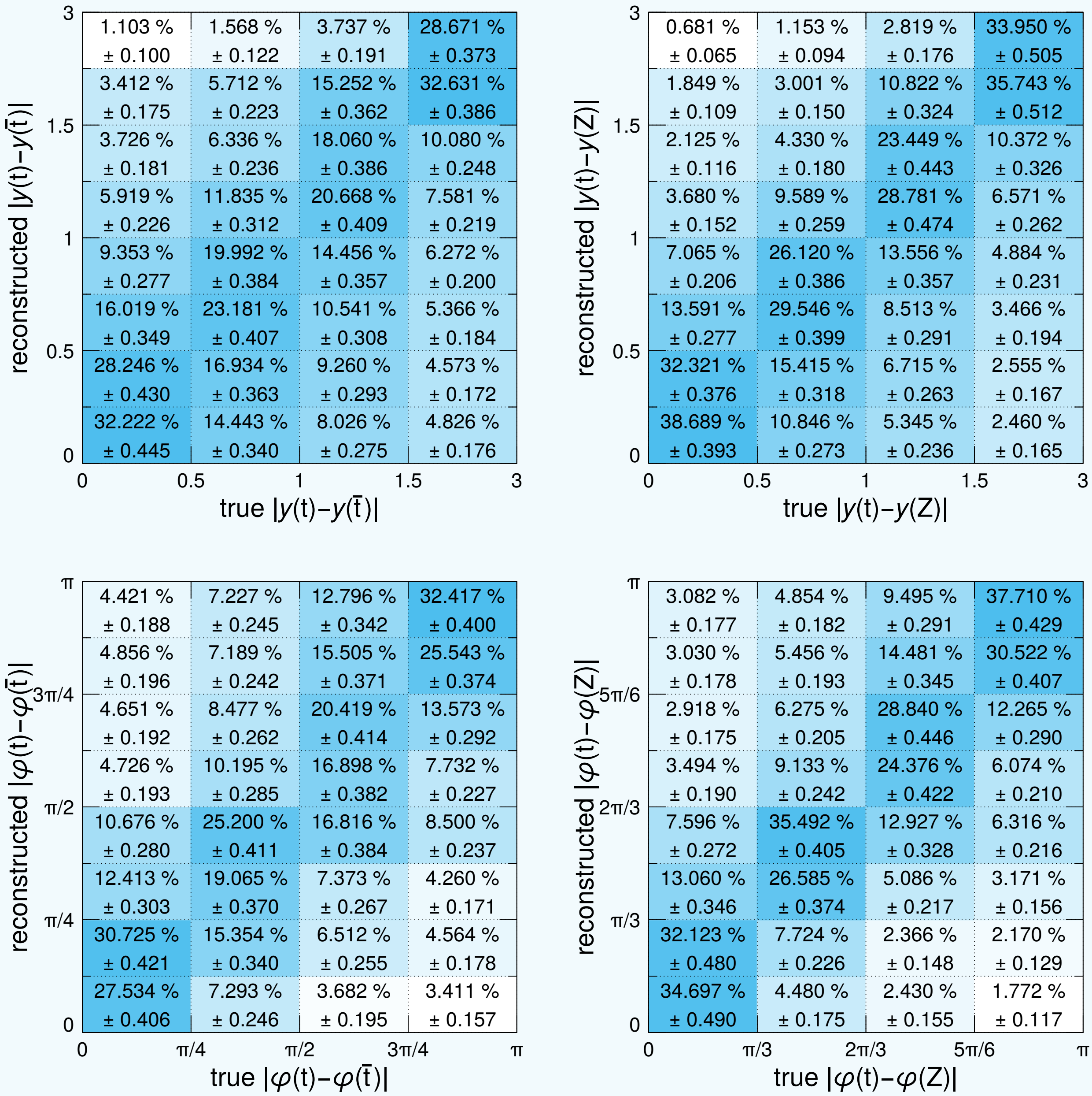

Resolution matrices describing bin-to-bin migrations from true bins to measured bins for the rapidity difference (upper) and azimuthal angle difference (lower) between top quark and antiquark (left) and between top quark and Z boson (right), with statistical uncertainties due to the size of the MC samples.

Figure 3.27

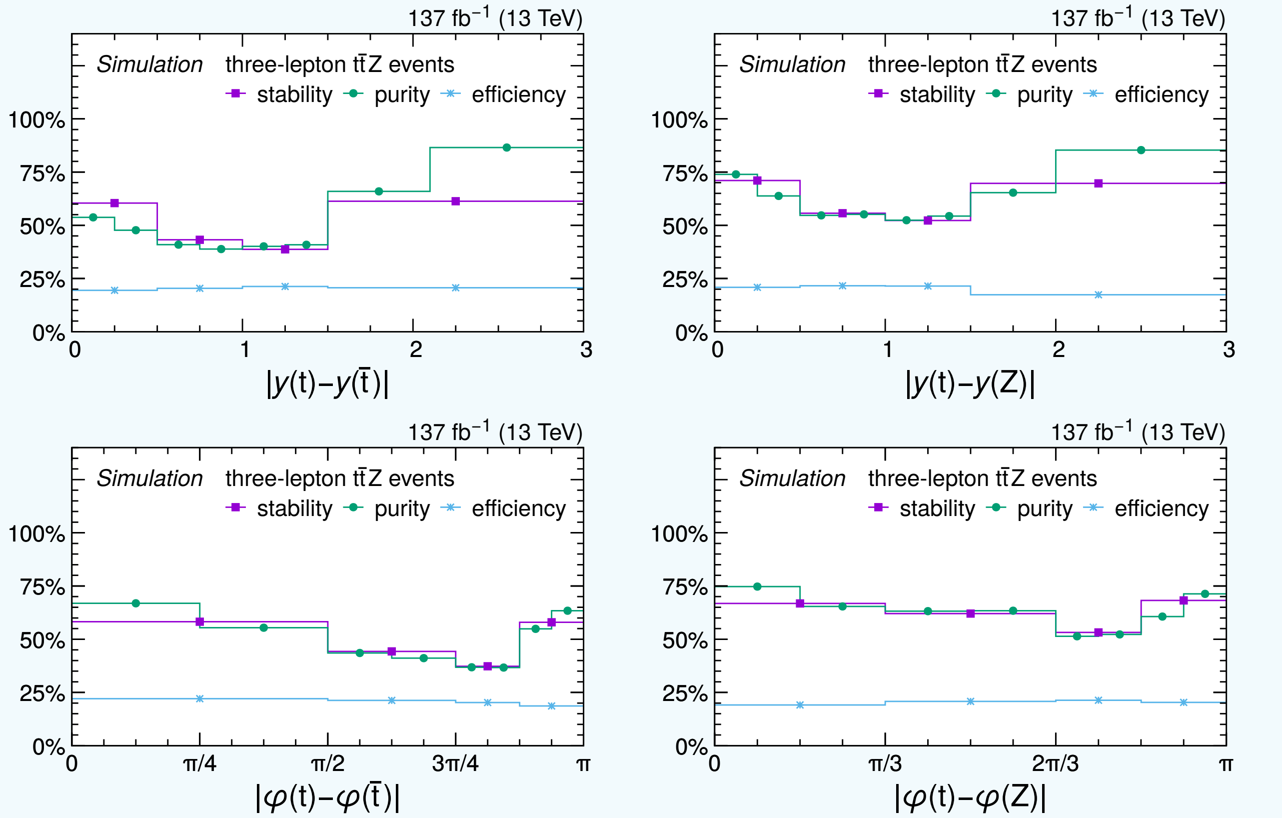

Stability, purity, and efficiency for the rapidity difference (upper) and azimuthal angle difference (lower) between top quark and antiquark (left) and between top quark and Z boson (right).

For the top quark observables introduced in Section 3.11, however, the strong bin-to-bin migrations, when amplified in the unfolding procedure, can cause unphysical solutions with large uncertainties and strong anti-correlations between neighbouring bins of the unfolded distribution. To mitigate this effect, the simple unfolding approach is extended with a "regularisation" requirement. This requirement is based on the assumption that any physical solution to the unfolding problem should be sufficiently smooth, and thus rejects solutions that have strong fluctuations. Regularisation necessarily introduces a bias in the unfolded distributions, and thus a careful balance between the strength of the regularisation and the bias of the unfolded distribution has to be found [218].

In this analysis, the mean square curvature of the unfolded distribution is used to quantify the smoothness of the unfolding result, an approach known as Tikhonov regularisation [228, 229]. For a continuous true event yield probability $y(\mathcal{O})$ as a function of some observable $\mathcal{O}$, the smoothness is defined as the integral over the squared second derivative:

$$\int \mathrm{d}\mathcal{O} \left(\frac{\mathrm{d}^2 y(\mathcal{O})}{\mathrm{d}\mathcal{O}^2} \right)^2 . \tag{3.20}$$

Requiring a smooth solution to the unfolding problem thus ensures an unfolded distribution with a small curvature. For the binned true event yields y_i with $i = 1, \ldots, N$, the discretisation of Equation (3.20) provides a regularisation function

$$\chi^2_{\mathrm{reg}}(y, \tau) = \tau^2 \sum_{i=1}^{N-2} (-y_i + 2y_{i+1} - y_{i+2})^2 \tag{3.21}$$

with a regularisation strength parameter τ, to be added to the χ^2 function defined in Equation (3.12) [218].

The regularisation of unfolding does not only affect the shape of the resulting distribution but can also change the total event yield. It is preferable to ensure that the total cross section obtained from a simple rescaling of the measured total event yield with the selection efficiency matches the integral over the differential cross section. To this end, an area constraint of the form

$$\chi^2_{\mathrm{area}}(y, \lambda) = \lambda \left(\sum_{j=1}^{M} (x_j - b_j) - \sum_{i=1}^{N} \epsilon_i y_i \right) \tag{3.22}$$

is added to the χ^2 function from Equation (3.12). Finding a stationary point with respect to the Lagrange multiplier λ enforces that the sum over the background-subtracted measured yields $x_j - b_j$ with $j = 1, \ldots, N$ is equal to the sum over the parton-level yields scaled with the per-bin selection efficiencies ϵ_i as defined in Equation (3.9) [219].

The total χ^2 function for regularised unfolding is thus

$$\tilde{\chi}^2(y, \tau, \lambda) = \chi^2(y) + \chi^2_{\mathrm{reg}}(y, \tau) + \chi^2_{\mathrm{area}}(y, \lambda). \tag{3.23}$$

Here, the unfolded event yield estimates y_i, the regularisation strength τ, and the area constraint multiplier λ are the free parameters. While the matrix inversion method works specifically for the case of the same number of bins for the reconstructed and the true observable, $N = M$, the regularised unfolding typically requires over-determination, i. e. more reconstructed bins than true bins, $M > N$, to find a suitable minimum of the χ^2 function.

The regularisation strength parameter τ should be chosen large enough to sufficiently suppress large fluctuations, but also small enough to minimise the bias of the unfolding result. Given the correlation matrix V of the unfolded result, the correlation coefficient ρ_{ij}, the global correlation coefficient ρ_i, and the average global correlation coefficient ρ_{avg} are defined as

$$\rho_{ij} = \frac{V_{ij}}{\sqrt{V_{ii} \cdot V_{jj}}}, \quad \rho_i = \sqrt{1 - \frac{1}{V_{ii} \cdot (V^{-1})_{ii}}}, \quad \rho_{\text{avg}} = \frac{1}{N}\sum_{i=1}^{N} \rho_i \quad [230]. \tag{3.24}$$

A suitable value of τ can be chosen by requiring that ρ_{avg} is minimal. Here, a τ scan is performed where the unfolding is repeated with different values of $\log_{10}\tau$. The minimum of the resulting distribution of ρ_{avg} is determined with a cubic interpolation [219].

A separate τ scan is performed for each of the seven observables, taking only the contributions of the statistical uncertainty to the covariance matrix of the unfolded result into account. In Figure 3.28, one example of a τ scan is shown. For small values of τ, the regularisation term has little impact on the unfolding result and the average global correlation corresponds to the unfolding result without regularisation. Conversely, for very large values of τ, the unfolded result is a distribution with zero curvature fully determined by the regularisation condition, resulting in maximal correlation between the bins. Around the local minimum, the regularisation strength is just strong enough to reduce the correlations with respect to the unregularised result but not so strong that additional correlations are introduced. For all observables, a clear minimum is found and subsequently used for the unfolding.

Figure 3.28

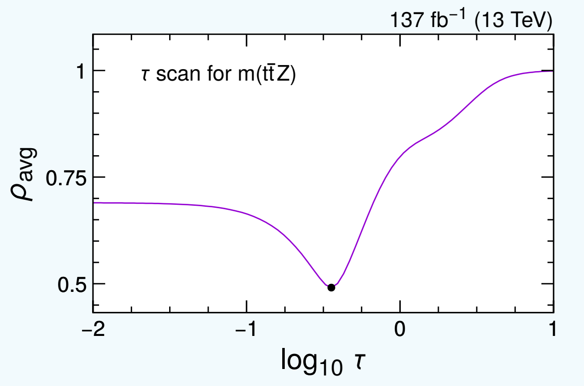

Average global correlation as a function of regularisation strength parameter for unfolding of $m(t\bar{t}Z)$.

3.13. Results

The differential cross section measurement is performed by applying regularised unfolding to the measured and predicted distributions of the seven observables obtained from a kinematic reconstruction of the $t\bar{t}$ system. The regularisation strength is determined from a minimisation of the average global correlation, separately for each observable. As described in Section 3.9, systematic uncertainties are evaluated by a repetition of the unfolding with different types of variations.

- The theoretical uncertainties related to the modelling of the $\mathrm{t\bar{t}Z}$ production process are evaluated by repeating the unfolding with different response matrices obtained with different scale choices (matrix element, PDF, parton shower) and with different PDF sets.
- The background normalisation uncertainties as well as the uncertainties in the integrated luminosity and the trigger efficiency are propagated as variations of the background yields which are subtracted before the unfolding.
- The remaining experimental uncertainties—pileup modelling, lepton selection efficiency, jet energy scale and resolution, b tagging efficiency, and unclustered energy uncertainty in the missing transverse momentum computation—are applied by a variation of the measured event yields according to the variation of the simulated signal and background yields.

The normalised differential cross sections and the corresponding correlation matrices for the $\mathrm{t\bar{t}Z}$ and $\mathrm{t\bar{t}}$ invariant masses are shown in Figure 3.29, and for the top quark transverse momentum in Figure 3.30. Similarly, the results for the rapidity differences and azimuthal angle differences are shown in Figure 3.31 and Figure 3.32, respectively, each with respect to the top quark and antiquark, and to the top quark and the Z boson. In Table 3.6, the measured cross section values are summarised for all seven observables.

In general, the results are limited by the statistical uncertainty of the measured event yields. The statistical component of the uncertainty in the cross section is typically between 15 % and 30 %, and reaches more than 60 % in one bin of the differential cross section as a function of $|y(\mathrm{t}) - y(\mathrm{Z})|$. In comparison, the combined systematic uncertainty per bin is not larger than 13 % and can be as small as 2 %. The largest systematic sources contributing to the uncertainty are the background normalisations, the MC statistics of the signal sample used to derive the response matrix, the jet energy corrections, and the lepton efficiencies. In all distributions, strong anticorrelations are observed between the measured cross section values in different bins, as expected when unfolding distributions of limited purity.

From the invariant masses and momenta, the differential cross section as a function of the $\mathrm{t\bar{t}Z}$ invariant mass, $m(\mathrm{t\bar{t}Z})$ has the best precision, with relative per-bin uncertainties between 18 % and 32 %. All three distributions show somewhat large anticorrelations between some bins. Within uncertainties, the predictions agree with the measured cross section values, where the best agreement is found for $m(\mathrm{t\bar{t}Z})$. For the distribution of the top quark transverse momentum, the predicted spectrum is somewhat softer compared to the measured values, similar to the discrepancies observed in differential

Figure 3.29

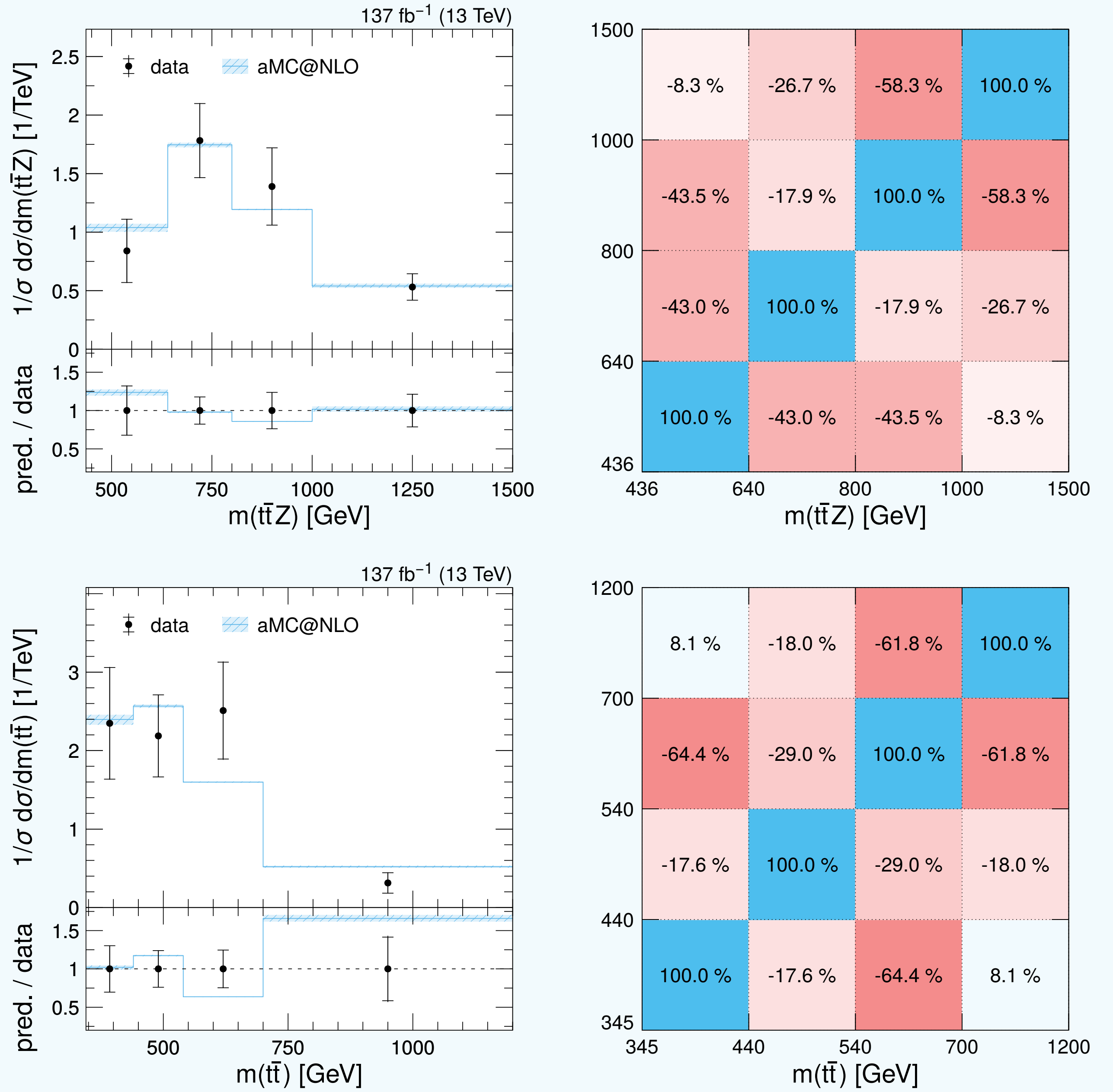

Left: Normalised differential $t\bar{t}Z$ production cross section as a function of the invariant mass of the $t\bar{t}Z$ system (upper row), and the invariant mass of the $t\bar{t}$ system (lower row). Shown are the measured cross section (points), and the SM predictions (lines) at NLO accuracy [184, 185, 220]. The measurement shows the statistical (statistical and systematic) uncertainty with the inner (outer) error bars.
Right: Corresponding correlation matrices.

Figure 3.30

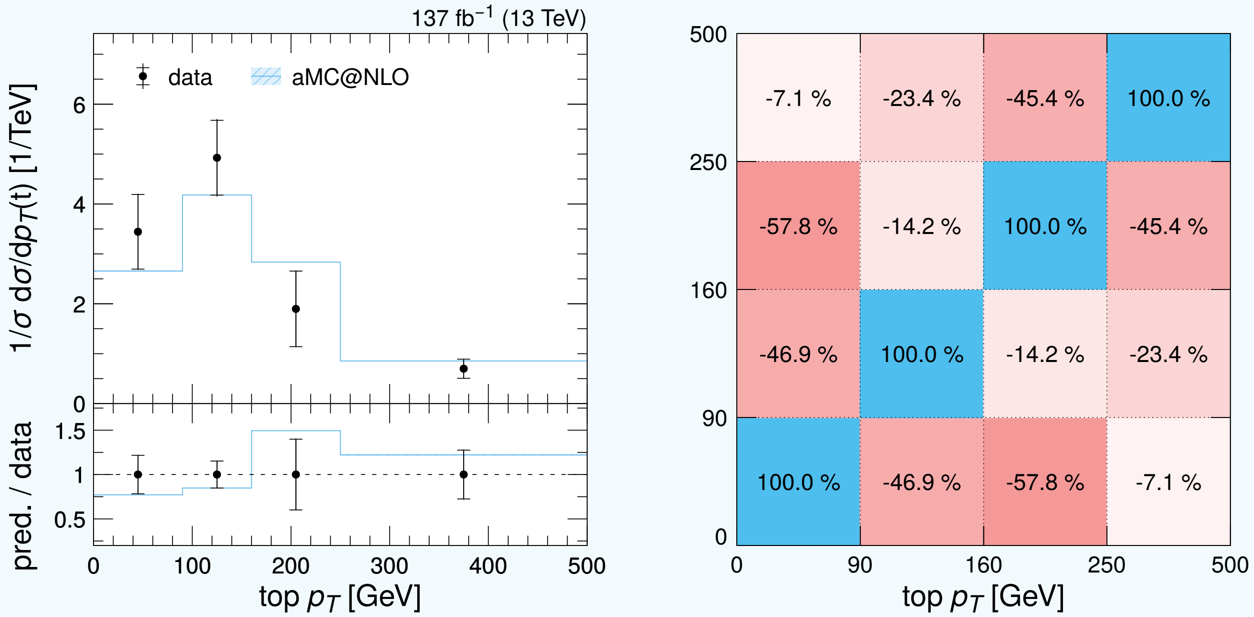

Left: Normalised differential $\mathrm{t\bar{t}Z}$ production cross section as a function of the the top quark transverse momentum. Shown is the measured cross section (points), and the SM prediction (lines) at NLO accuracy [184, 185, 220]. The measurement shows the statistical (statistical and systematic) uncertainty with the inner (outer) error bars. Right: Corresponding correlation matrix.

measurements of the $\mathrm{t\bar{t}}$ production cross section as a function of the top quark p_T [146], but not statistically significant.

From the rapidity and azimuthal angle differences, the differential cross section as a function of the azimuthal angle difference between top quark and Z boson, $|\phi(\mathrm{t}) - \phi(\mathrm{Z})|$, has the best precision, with relative per-bin uncertainties between 21 % and 33 %. The largest uncertainties are reached for the rapidity differences, $|y(\mathrm{t}) - y(\mathrm{\bar{t}})|$ and $|y(\mathrm{t}) - y(\mathrm{Z})|$, with relative per-bin uncertainties of up to 50 % and 70 %. Especially the third bin of the $|y(\mathrm{t}) - y(\mathrm{Z})|$ distribution shows a much smaller measured cross section value than expected from the SM prediction. Since the event yield distribution, shown in Figure 3.23, does not exhibit a particular deficit in the corresponding bins resembling the structure found in the unfolded distribution, this difference is not understood and will require further studies.

Figure 3.31

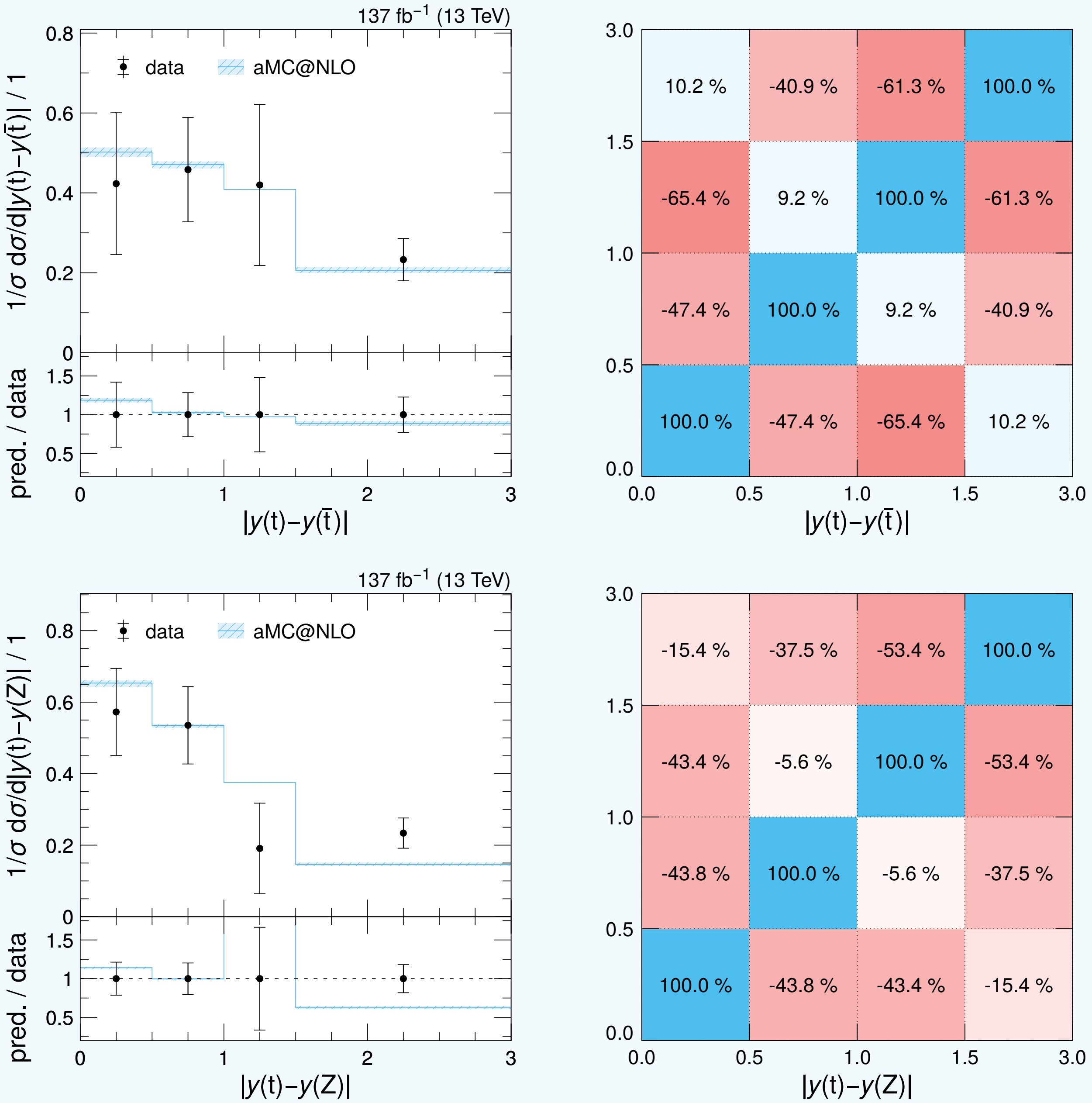

Left: Normalised differential $t\bar{t}Z$ production cross section as a function of the rapidity difference between top quark and antiquark (upper row), and between top quark and Z boson (lower row). Shown are the measured cross section (points), and the SM predictions (lines) at NLO accuracy [184, 185, 220]. The measurement shows the statistical (statistical and systematic) uncertainty with the inner (outer) error bars. Right: Corresponding correlation matrices.

Figure 3.32

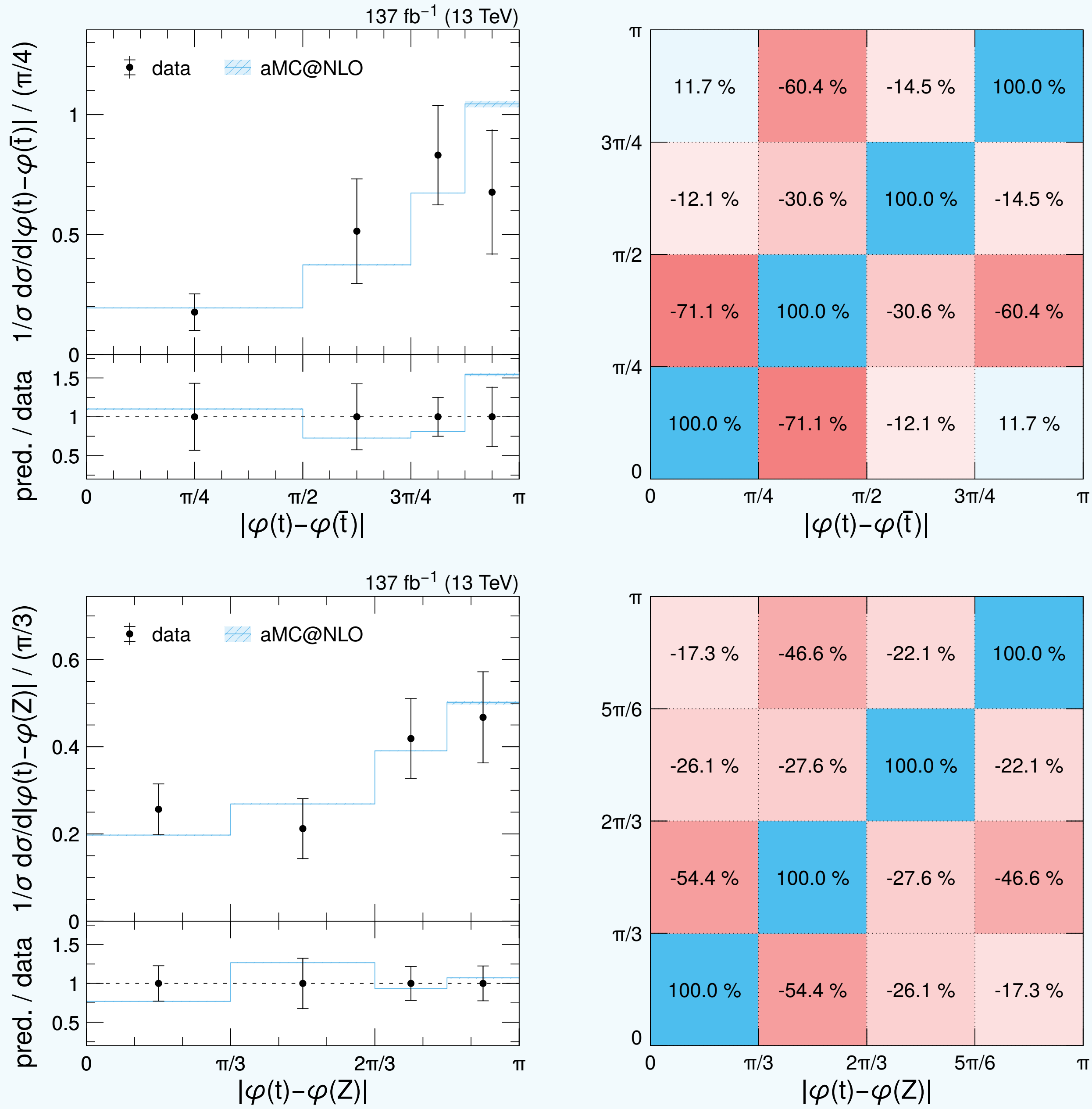

Left: Normalised differential $t\bar{t}Z$ production cross section as a function of the azimuthal angle difference between top quark and antiquark (upper row), and between top quark and Z boson (lower row). Shown are the measured cross section (points), and the SM predictions (lines) at NLO accuracy [184, 185, 220]. The measurement shows the statistical (statistical and systematic) uncertainty with the inner (outer) error bars.
Right: Corresponding correlation matrices.

Table 3.6

observable	1st bin	2nd bin	3rd bin	4th bin	unit
$m(\mathrm{t\bar{t}Z})$	0.84 ± 0.27	1.78 ± 0.32	1.39 ± 0.33	0.53 ± 0.11	/ TeV
$m(\mathrm{t\bar{t}})$	2.35 ± 0.72	2.19 ± 0.53	2.51 ± 0.63	0.31 ± 0.14	/ TeV
$p_\mathrm{T}(\mathrm{t})$	3.44 ± 0.76	4.93 ± 0.78	1.90 ± 0.77	0.70 ± 0.20	/ TeV
$\lvert y(\mathrm{t}) - y(\mathrm{\bar{t}})\rvert$	0.42 ± 0.18	0.46 ± 0.13	0.42 ± 0.20	0.23 ± 0.05	/ 1
$\lvert y(\mathrm{t}) - y(\mathrm{Z})\rvert$	0.57 ± 0.12	0.54 ± 0.11	0.19 ± 0.13	0.23 ± 0.04	/ 1
$\lvert \phi(\mathrm{t}) - \phi(\mathrm{\bar{t}})\rvert$	0.18 ± 0.08	0.51 ± 0.22	0.83 ± 0.21	0.68 ± 0.26	/ $(\pi/4)$
$\lvert \phi(\mathrm{t}) - \phi(\mathrm{Z})\rvert$	0.26 ± 0.06	0.21 ± 0.07	0.42 ± 0.09	0.47 ± 0.11	/ $(\pi/3)$

Measured normalised differential $\mathrm{t\bar{t}Z}$ production cross section as a function of top quark observables.

3.14. Outlook

In this thesis, the first differential measurement of the $\mathrm{t\bar{t}Z}$ production cross section as a function of kinematic observables of the Z boson has been performed using the 2016 & 2017 dataset. Furthermore, an extended differential measurement as a function of kinematic observables involving the $\mathrm{t\bar{t}}$ system, or both the Z boson and the $\mathrm{t\bar{t}}$ system, has been developed and applied to the 2016–2018 dataset. These results demonstrate that it is viable to use the three-lepton decay channel of the $\mathrm{t\bar{t}Z}$ final state to access the studied observables, even if the precision is currently still limited by large statistical uncertainties.

The statistical uncertainty of the differential cross section measurements will improve with the data recorded in the upcoming Run 3 of the LHC and ultimately at the HL-LHC. In Figure 3.33, a projection is shown for the expected performance of the $\mathrm{t\bar{t}Z}$ production measurement in the Z boson observables, using the expected HL-LHC dataset. The large event yields will significantly improve the precision and allow for differential cross section measurements to be sensitive to small deviations from the SM prediction [231]. Nevertheless, improvements of the analysis strategy are conceivable which will increase the available signal event yields as well, especially for the measurement of the top quark observables.

For the kinematic reconstruction, as it has been applied in this measurement, four reconstructed jets are required. This way, one jet can be assigned to each quark from the semileptonic $\mathrm{t\bar{t}}$ decay. It has been demonstrated that a **kinematic reconstruction with only three jets**, where one quark does not result in a measured jet due to its low momentum, the limited detector acceptance, or the reconstruction efficiency, is also feasible and provides a good measurement of the top quark kinematic properties [232,

Figure 3.33

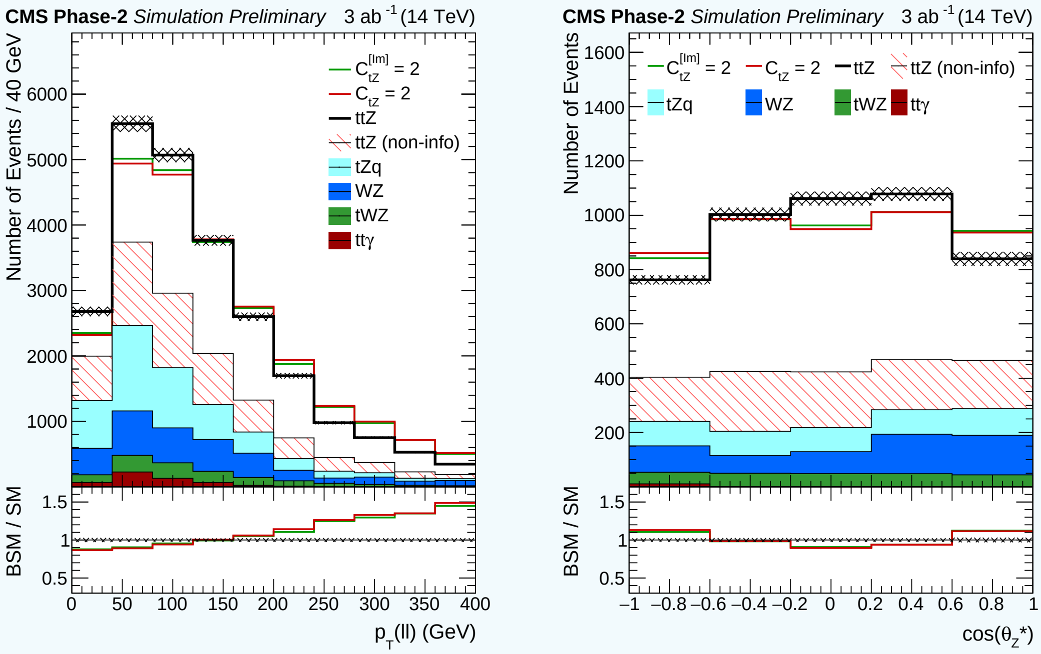

Event yields for the Z boson transverse momentum (left), and the angle between Z boson and its decay lepton, boosted to the Z boson rest frame, for $p_T(Z) > 200\,\mathrm{GeV}$, (right) expected for a $\mathrm{t\bar{t}Z}$ production measurement with $3\,\mathrm{ab}^{-1}$ of proton-proton collision data at $\sqrt{s} = 14\,\mathrm{TeV}$ collected at the HL-LHC, taken from Ref. [231].

233]. Extending the event selection here to include events with three jets would nearly double the total event yields, and increase the signal event yields by about 70 %. However, the impact of the missing jet on the resolution of the observables that are studied here and thus on the feasibility of the unfolding method for this class of events requires further study.

In the inclusive $\mathrm{t\bar{t}Z}$ cross section measurement, the **four-lepton channel**, where the Z boson decays leptonically and the $\mathrm{t\bar{t}}$ system decays to two b quarks, two leptons, and two neutrinos, provided a very pure selection of events with low background contributions, but also with a much smaller total number of events than the three-lepton channel. For the differential measurement as a function of Z boson observables, including the four-lepton channel is easily feasible. For the kinematic reconstruction of the $\mathrm{t\bar{t}}$ system, however, a more elaborate approach is needed to obtain the momenta of the two neutrinos from only one missing transverse momentum measurement [146, 234, 235].

In contrast, the kinematic reconstruction of the $\mathrm{t\bar{t}}$ system in the **two-lepton channel**, where the Z boson decays leptonically and the $\mathrm{t\bar{t}}$ system decays to six quarks, simplifies to a combinatorial problem since no unmeasured particles are needed. A selection with two leptons, however, has much larger background contributions from $t\bar{t}$ and $Z+$jets production, such that larger systematic uncertainties are expected [166].

Furthermore, improvements in the **estimation and rejection of background events** could facilitate a loosened event selection with an increased selection efficiency for $t\bar{t}Z$ signal events.

- As the event selection is driven by the need to discriminate between prompt and nonprompt leptons, a data-driven estimation of the nonprompt lepton background contributions, as described in Section 3.5, with a simultaneous optimisation of lepton selection criteria and background estimation parameters, could entail a higher efficiency for the selection of prompt leptons from $t\bar{t}Z$ events, resulting in an overall higher signal selection efficiency.
- A template fit, as described in Section 3.7, could be applied in each bin of the measured observables. In order to do this, additional selections enriched in background processes would be added to the measurement, resulting in a more precise estimation of the background contributions as well as in larger total signal event yields due to the $t\bar{t}Z$ signal contributions to the looser selections.

Ultimately, a strategy to be considered is a simultaneous measurement of several associated top quark production processes. Using multiclassification techniques to distinguish between background events on one hand and multiple signal processes on the other hand, a simultaneous measurement e. g. of the $t\bar{t}Z$, tZq, and tWZ production cross sections would be feasible. This would improve the precision of the cross section measurement itself, as a larger dataset than a selection optimised for only one process would be used, but would also allow for a well-defined interpretation of the cross section results in terms of new physics models which simultaneously affect all three processes.

Conclusions

Summary

In this thesis, measurements of the integrated luminosity with the CMS experiment, and inclusive and differential cross section measurements of top quark pair production in association with a Z boson ($t\bar{t}Z$) in proton-proton collisions at $\sqrt{s} = 13\,\text{TeV}$ with the CMS experiment have been presented.

The **luminosity measurement** of the CMS experiment is calibrated with the Van der Meer (VdM) method. It uses beam separation scans called VdM scans to obtain a precise luminosity measurement in a specific LHC fill, which in turn is used to estimate the visible cross section of a specific luminosity detector. Systematic uncertainties arise in the calibration due to several experimental effects, including the knowledge of the length scale of the beam separation, and the assumption of factorisable beam proton densities.

The length scale calibration with constant-separation length scale scans provides a precise estimation of the length scale factor used in the VdM method. With a correction for time-dependent drifts of the proton beams away from their nominal positions, the obtained results are substantially improved with respect to previous applications of the method.

In the beam-imaging method, data from four beam-imaging scans are used to reconstruct the transverse proton densities of the two beams. The results are then used to derive a correction for the factorisation bias of the VdM method. In this thesis, the beam-imaging method was extended to include improved beam proton density models. The experimental results were scrutinised with a dedicated closure test using simulated datasets. The updated factorisation bias estimates have a significantly improved uncertainty compared to the preliminary results, and will be included in an upcoming publication of the integrated luminosity measurement for the 2015 & 2016 datasets of the CMS experiment.

The **measurement of the $t\bar{t}Z$ production cross section** provides a first direct probe of the top quark–Z boson coupling and can be used to constrain contributions from physics beyond the standard model (SM) to this coupling. A measurement of the inclusive cross section in events with three and four leptons has been performed, using a dataset corresponding to an integrated luminosity of $77.5\,\mathrm{fb}^{-1}$ collected in 2016 & 2017. The measured inclusive cross section of $\sigma(\mathrm{pp} \to t\bar{t}Z)_{\mathrm{meas}} = 950 \pm 50\,(\mathrm{stat}) \pm 60\,(\mathrm{syst})\,\mathrm{fb}$ is in good agreement with the SM prediction, and with a precision of about 8 % competitive to state-of-the-art theory calculations.

In addition, a differential $t\bar{t}Z$ production cross section measurement has been performed for the first time, using events with three leptons and at least three jets. The Z boson is identified in its decay to two oppositely charged leptons, and the differential cross section is presented as a function of the Z boson transverse momentum as well as of the angle between the Z boson and its decay lepton, boosted to the Z boson rest frame. Good agreement of the shape of the differential cross sections with the SM predictions is observed.

Finally, a differential $t\bar{t}Z$ production cross section measurement as a function of top quark observables has been performed, using the full Run 2 dataset corresponding to an integrated luminosity of $137\,\mathrm{fb}^{-1}$ collected in 2016–2018, and a tighter event selection with three leptons and at least four jets. The kinematic properties of the semileptonically decaying $t\bar{t}$ system are reconstructed with a kinematic fit. The differential cross section is presented as a function of the invariant masses of the $t\bar{t}Z$ and the $t\bar{t}$ system, the transverse momentum of the top quark, and of the rapidity and azimuthal angle differences each between the top quark and antiquark, and between the top quark and the Z boson. All results are found to be in agreement with the SM predictions. This is a very first measurement of these observables in $t\bar{t}Z$ production, and several optimisation options have been discussed.

Outlook

Experimental particle physics continues to evolve towards larger datasets at the highest reachable energies, in the quest to understand the limitations of the SM and to find signs of physics beyond the SM. With the upcoming Run 3 of the LHC, more proton-proton collision data will be collected at a potentially higher centre-of-mass energy. By the end of the 2030's, a dataset corresponding to an integrated luminosity of about $3\,\mathrm{ab}^{-1}$ is expected to be delivered to the CMS experiment at the High-Luminosity LHC

(HL-LHC) [50], with a factor of five to seven larger instantaneous luminosity than currently achieved. Beyond the LHC, proposals for linear electron-positron colliders offer remarkable possibilities for future top quark research [236].

In the near future, the larger instantaneous luminosities to be expected at the LHC will be a challenge to the extrapolation of the luminosity calibration and thus to the precision of the luminosity measurements. New methods are being developed to address the extrapolation uncertainties, and further improvements of the calibration techniques will be required to achieve an overall good precision.

An important aspect of the luminosity calibration is the performance of the beam-imaging method. While an enormous improvement of the calibration precision has been demonstrated in this thesis for the 2015 & 2016 datasets, the application of the same method to the 2017 & 2018 datasets did not provide a fully satisfactory calibration result and hints at larger non-factorisation effects in the transverse beam proton densities. Thus, further studies of other experimental effects potentially impacting the beam-imaging scan data, further improvements of the method itself, and the development of and comparison with complementary methods for the estimation of the factorisation bias are required.

The measurement of the $\mathrm{t\bar{t}Z}$ production cross section will, in contrast, improve with larger available datasets as more events improve the statistical uncertainties and help in studies of the systematic uncertainties. Thus, the improved precision will allow for differential cross section measurements to be sensitive to small deviations from the SM prediction, as predicted by some beyond-the-SM models.

But also the currently applied methods can be further developed to improve the results of the differential cross section measurement. Possible approaches include an extension of the kinematic reconstruction to events with less jets, the inclusion of other decay channels of the $\mathrm{t\bar{t}}$ system, and more precise strategies for the estimation of background contributions. Ultimately, a simultaneous measurement of several similar processes like $\mathrm{t\bar{t}Z}$, tZq, and tWZ production will help to improve the precision of the respective cross section measurements and will facilitate a well-defined interpretation in terms of new physics models which simultaneously affect all three processes.

Appendix

A. Acknowledgements

I am deeply grateful to my supervisors Andreas Meyer and Johannes Haller for having me as their student. Thanks for your guidance and support in my research, and for the constant reminders to not sell myself short!

My work on the calibration of the luminosity measurement would not have been possible without the help of many people in the CMS Luminosity POG and BRIL DPG. I am especially thankful to Jakob Salfeld-Nebgen for the close collaboration at the start of my PhD, and to Georgios Krintiras and Chris Palmer for continuous fruitful exchange.

The measurements of $t\bar{t}Z$ production emerged from a close collaboration with the colleagues in Ghent and Vienna. My special thanks go to Illia Khvastunov and Didar Dobur in Ghent, also for your hospitality, and to Daniel Spitzbart and Robert Schoefbeck in Vienna. Thanks also to the convenors of the CMS Top Quark PAG and the subgroups for their support.

At DESY, I have been lucky to work with Angela Giraldi, Rafael Sosa, and Oleksii Turkot on luminosity projects. Many thanks to Till Arndt for his help in the early days, and to Valerie Scheurer, Nicolas Tonon, and David Walter for their help in the final days of my $t\bar{t}Z$ measurements. Various other people in the CMS Top group, the CMS BRIL/Lumi group, the PR department, and beyond contributed to the excellent atmosphere during and after work in Hamburg. Thanks to all of you!

I received generous support from the DESY CMS group and the group leaders Matthias Kasemann and Elisabetta Gallo for the attendance of schools, conferences, and workshops, for which I am grateful. All of my travels would have been much less fun without my travel companions, especially Anna Benecke, Matteo Defranchis, Simon Kurz, and Paul Schütze.

Throughout my PhD, I have relied on the emotional support and friendship of many other people, from school and university days, from politics and church, in Hamburg and outside. Finally, I am grateful to Susanne, Marian, Annelie, and Caroline, my loving family. And to my father Rolf—even if you did not live to see this thesis, I would not be here without you.

B. Bibliography

List of publications

[A] CMS Collaboration. *CMS luminosity measurement for the 2015 data-taking period.* Physics Analysis Summary, CERN, 2016. Updated in February 2017. CMS-PAS-LUM-15-001. CDS: 2138682.

[B] CMS Collaboration. *CMS luminosity measurements for the 2016 data taking period.* Physics Analysis Summary, CERN, 2017. CMS-PAS-LUM-17-001. CDS: 2257069.

[C] CMS Collaboration. *CMS luminosity measurement for the 2017 data-taking period at* $\sqrt{s} = 13\,\text{TeV}$. Physics Analysis Summary, CERN, 2018. CMS-PAS-LUM-17-004. CDS: 2621960.

[D] CMS Collaboration. *CMS luminosity measurement using 2016 proton-nucleus collisions at* $\sqrt{s_{\text{NN}}} = 8.16\,\text{TeV}$. Physics Analysis Summary, CERN, 2018. CMS-PAS-LUM-17-002. CDS: 2628652.

[E] Albert Sirunyan et al. (CMS Collaboration). *Measurement of top quark pair production in association with a Z boson in proton-proton collisions at* $\sqrt{s} = 13\,\text{TeV}$. JHEP 03 (2020) 056. DOI: 10.1007/JHEP03(2020)056. ARXIV: 1907.11270 [hep-ex].

[F] CMS Collaboration. *CMS luminosity measurement for the 2018 data-taking period at* $\sqrt{s} = 13\,\text{TeV}$. Physics Analysis Summary, CERN, 2019. CMS-PAS-LUM-18-002. CDS: 2676164.

[G] CMS Collaboration. *Nonfactorization in Van der Meer scans in Run 2.* Detector Performance Note, CERN, 2019. CMS-DP-2019-019. CDS: 2681801.

[H] Joscha Knolle (ATLAS & CMS Collaborations). *Rare top quark production at the LHC:* $\text{t}\bar{\text{t}}\text{Z}$, $\text{t}\bar{\text{t}}\text{W}$, $\text{t}\bar{\text{t}}\gamma$, tZq, $\text{t}\gamma\text{q}$, *and* $\text{t}\bar{\text{t}}\text{t}\bar{\text{t}}$. In: *Proc. 27th Int. Workshop on Deep-Inelastic Scattering and Related Subjects*, Turin, Italy, May 2019. PoS (DIS2019) 157. DOI: 10.22323/1.352.0157.

[I] Joscha Knolle (CMS Collaboration). *The factorization bias in the Van der Meer method: Run 2 experiences at the CMS experiment.* In: *Proc. LHC Lumi Days 2019*, Prévessin, France, June 2019. CMS-CR-2019-129. ARXIV: 1910.14066 [hep-ex]. CDS: 2698258.

[J] Joscha Knolle (CMS Collaboration). *Differential measurement of* $\text{t}\bar{\text{t}}\text{Z}$ *production at* $\sqrt{s} = 13\,\text{TeV}$ *with the CMS experiment.* In: *Proc. 12th Int. Workshop on Top Quark Physics (TOP2019)*, Beijing, China, September 2019. CMS-CR-2019-256. ARXIV: 1911.12714 [hep-ex]. CDS: 2703395.

[K] Kirill Grevtsov, Judith Katzy, Joscha Knolle, and Andreas Meyer. *Top quarks and Higgs or Z bosons.* 2020. In: Ilka Flegel, Manfred Fleischer, and Thomas Konstandin (editors). *Particle physics 2019: Highlights and annual report.* DESY, Hamburg, Germany, 2020. DOI: 10.3204/PUBDB-2019-05176.

References

[1] Nicolaus Stenonis. *Prooemium demonstrationum anatomicarum in theatro Hafniensi*. 1673. In: Wilhelm Maar (editor). *Nicolai Stenonis opera philosophica*. Volume 2. Vilhelm Tryde, Copenhagen, Denmark, 1910. URL: https://www.biusante.parisdescartes.fr/histmed/medica/cote?09371x02.

[2] Georges Aad et al. (ATLAS Collaboration). *Observation of a new particle in the search for the standard model Higgs boson with the ATLAS detector at the LHC*. Phys. Lett. B 716 (2012) 1. DOI: 10.1016/j.physletb.2012.08.020. ARXIV: 1207.7214 [hep-ex].

[3] Serguei Chatrchyan et al. (CMS Collaboration). *Observation of a new boson at a mass of* 125 GeV *with the CMS experiment at the LHC*. Phys. Lett. B 716 (2012) 30. DOI: 10.1016/j.physletb.2012.08.021. ARXIV: 1207.7235 [hep-ex].

[4] Illia Khvastunov. *Search for supersymmetry and the measurement of the top pair production in association with a* W *or a* Z *boson with the CMS detector at the LHC*. PhD thesis, Ghent University, 2019. URL: http://hdl.handle.net/1854/LU-8633661.

[5] Daniel Spitzbart. *Search for supersymmetric partners and anomalous couplings of the top quark with the CMS experiment*. PhD thesis, Vienna University of Technology, 2019. URL: https://resolver.obvsg.at/urn:nbn:at:at-ubtuw:1-129830.

[6] Masaharu Tanabashi et al. (Particle Data Group). *Review of particle physics*. Phys. Rev. D 98 (2018) 030001 and 2019 update. DOI: 10.1103/PhysRevD.98.030001. URL: http://pdg.lbl.gov.

[7] Nabila Aghanim et al. (Planck Collaboration). *Planck 2018 results. VI. Cosmological parameters*. 2018. ARXIV: 1807.06209 [astro-ph.CO]. Submitted to A&A.

[8] Sheldon Glashow. *Partial-symmetries of weak interactions*. Nucl. Phys. 22 (1961) 579. DOI: 10.1016/0029-5582(61)90469-2.

[9] Murray Gell-Mann. *The eightfold way: a theory of strong interaction symmetry*. Technical Report, California Institute of Technology, 1961. CTSL-20. DOI: 10.2172/4008239.

[10] Peter Higgs. *Broken symmetries, massless particles and gauge fields*. Phys. Lett. 12 (1964) 132. DOI: 10.1016/0031-9163(64)91136-9.

[11] François Englert and Robert Brout. *Broken symmetry and the mass of gauge vector mesons*. Phys. Rev. Lett. 13 (1964) 321. DOI: 10.1103/PhysRevLett.13.321.

[12] Peter Higgs. *Broken symmetries and the masses of gauge bosons*. Phys. Rev. Lett. 13 (1964) 508. DOI: 10.1103/PhysRevLett.13.508.

[13] Gerald Guralnik, Carl Hagen, and Tom Kibble. *Global conservation laws and massless particles*. Phys. Rev. Lett. 13 (1964) 585. DOI: 10.1103/PhysRevLett.13.585.

[14] Steven Weinberg. *A model of leptons*. Phys. Rev. Lett. 19 (1967) 1264. DOI: 10.1103/PhysRevLett.19.1264.

[15] Abdus Salam. *Weak and electromagnetic interactions*. In: *Proc. 8th Nobel Symposium*, Lerum, Sweden, May 1968. Almquist and Wiksell, Stockholm, Sweden, 1968.

[16] Michael Peskin and Daniel Schroeder. *An introduction to quantum field theory*. Addison-Wesley, Reading MA, US, 1995.

[17] David Griffiths. *Introduction to elementary particles*. 2nd, revised edition. Wiley-VCH, Weinheim, Germany, 2008.

[18] Maarten Boonekamp, Stefan Dittmaier, and Matthias Mozer. *Electroweak standard model physics*. 2015. DOI: 10.1007/978-3-319-15001-7_4. In: Thomas Schörner-Sadenius (editor). *The Large Hadron Collider. Harvest of Run 1*. Springer International Publishing, Cham, Switzerland, 2015.

[19] Tancredi Carli, Klaus Rabbertz, and Steffen Schumann. *Studies of quantum chromodynamics at the LHC*. 2015. DOI: 10.1007/978-3-319-15001-7_5. ARXIV: 1506.03239 [hep-ex]. In: Thomas Schörner-Sadenius (editor). *The Large Hadron Collider. Harvest of Run 1*. Springer International Publishing, Cham, Switzerland, 2015.

[20] Karl Jakobs, Günter Quast, and Georg Weiglein. *Higgs-boson physics at the LHC*. 2015. DOI: 10.1007/978-3-319-15001-7_6. In: Thomas Schörner-Sadenius (editor). *The Large Hadron Collider. Harvest of Run 1*. Springer International Publishing, Cham, Switzerland, 2015.

[21] Joshua Ellis. *TikZ-Feynman: Feynman diagrams with TikZ*. Comput. Phys. Commun. 210 (2017) 103. DOI: 10.1016/j.cpc.2016.08.019. ARXIV: 1601.05437 [hep-ph].

[22] Richard Ball et al. (NNPDF Collaboration). *Parton distributions from high-precision collider data*. Eur. Phys. J. C 77 (2017) 663. DOI: 10.1140/epjc/s10052-017-5199-5. ARXIV: 1706.00428 [hep-ph].

[23] Halina Abramowicz et al. (H1 & ZEUS Collaborations). *Combination of measurements of inclusive deep inelastic* $\mathrm{e}^{\pm}\mathrm{p}$ *scattering cross sections and QCD analysis of HERA data*. Eur. Phys. J. C 75 (2015) 580. DOI: 10.1140/epjc/s10052-015-3710-4. ARXIV: 1506.06042 [hep-ex].

[24] Matteo Cacciari, Gavin Salam, and Gregory Soyez. *The anti-*k_{T} *jet clustering algorithm*. JHEP 04 (2008) 063. DOI: 10.1088/1126-6708/2008/04/063. ARXIV: 0802.1189 [hep-ph].

[25] Matteo Cacciari, Gavin Salam, and Gregory Soyez. *FastJet user manual*. Eur. Phys. J. C 72 (2012) 1896. DOI: 10.1140/epjc/s10052-012-1896-2. ARXIV: 1111.6097 [hep-ph].

[26] Maurizio Acciarri et al. (L3 Collaboration). *Measurement of the running of the fine-structure constant*. Phys. Lett. B 476 (2000) 40. DOI: 10.1016/S0370-2693(00)00122-2. ARXIV: hep-ex/0002035.

[27] Yoshiyuki Fukuda et al. (Super-Kamiokande Collaboration). *Evidence for oscillation of atmospheric neutrinos*. Phys. Rev. Lett. 81 (1998) 1562. DOI: 10.1103/PhysRevLett.81.1562. ARXIV: hep-ex/9807003.

[28] Rushdy Ahmad et al. (SNO Collaboration). *Measurement of the rate of* $\nu_{\mathrm{e}} + \mathrm{d} \rightarrow \mathrm{p} + \mathrm{p} + \mathrm{e}^{-}$ *interactions produced by* $^{8}\mathrm{B}$ *solar neutrinos at the Sudbury Neutrino Observatory*. Phys. Rev. Lett. 87 (2001) 071301. DOI: 10.1103/PhysRevLett.87.071301. ARXIV: nucl-ex/0106015.

[29] Nicola Cabibbo. *Unitary symmetry and leptonic decays*. Phys. Rev. Lett. 10 (1963) 531. DOI: 10.1103/PhysRevLett.10.531.

[30] Sheldon Glashow, John Iliopoulos, and Luciano Maiani. *Weak interactions with lepton-hadron symmetry*. Phys. Rev. D 2 (1970) 1285. DOI: 10.1103/PhysRevD.2.1285.

[31] Makoto Kobayashi and Toshihide Maskawa. *CP-violation in the renormalizable theory of weak interaction*. Prog. Theor. Phys. 49 (1973) 652. DOI: 10.1143/PTP.49.652.

[32] Rabindra Mohapatra and Alexei Smirnov. *Neutrino mass and new physics*. Ann. Rev. Nucl. Part. Sci. 56 (2006) 569. DOI: 10.1146/annurev.nucl.56.080805.140534. ARXIV: hep-ph/0603118.

[33] Fritz Zwicky. *Die Rotverschiebung von extragalaktischen Nebeln*. Helv. Phys. Acta 6 (1933) 110.

[34] Gianfranco Bertone, Dan Hooper, and Joseph Silk. *Particle dark matter: evidence, candidates and constraints*. Phys. Rept. 405 (2005) 279. DOI: 10.1016/j.physrep.2004.08.031. ARXIV: hep-ph/0404175.

[35] Werner Bernreuther. *CP violation and baryogenesis*. Lect. Notes Phys. 591 (2002) 237. DOI: 10.1007/3-540-47895-7_7. ARXIV: hep-ph/0205279.

[36] Hermann Nicolai. *Quantum gravity: the view from particle physics*. Fundam. Theor. Phys. 177 (2014) 369. DOI: 10.1007/978-3-319-06349-2_18. ARXIV: 1301.5481 [gr-qc].

[37] Ian Aitchison. *Supersymmetry in particle physics. An elementary introduction*. Cambridge University Press, Cambridge, UK, 2007. DOI: 10.1017/CBO9780511619250.

[38] Lisa Randall and Raman Sundrum. *Large mass hierarchy from small extra dimension*. Phys. Rev. Lett. 83 (1999) 3370. DOI: 10.1103/PhysRevLett.83.3370. ARXIV: hep-ph/9905221.

[39] Steven Weinberg. *Effective gauge theories*. Phys. Lett. B 91 (1980) 51. DOI: 10.1016/0370-2693(80)90660-7.

[40] Wilfried Buchmüller and Daniel Wyler. *Effective lagrangian analysis of new interactions and flavour conservation*. Nucl. Phys. B 268 (1986) 621. DOI: 10.1016/0550-3213(86)90262-2.

[41] Bohdan Grzadkowski et al. *Dimension-six terms in the standard model Lagrangian*. JHEP 10 (2010) 085. DOI: 10.1007/JHEP10(2010)085. ARXIV: 1008.4884 [hep-ph].

[42] Roderik Bruce et al. *Reaching record-low $\beta^{\star}$ at the CERN Large Hadron Collider using a novel scheme of collimator settings and optics*. Nucl. Instrum. Meth. A 848 (2017) 19. DOI: 10.1016/j.nima.2016.12.039.

[43] Lyndon Evans and Philip Bryant (editors). *LHC machine*. JINST 3 (2008) S08001. DOI: 10.1088/1748-0221/3/08/S08001.

[44] Georges Aad et al. (ATLAS Collaboration). *The ATLAS experiment at the CERN Large Hadron Collider*. JINST 3 (2008) S08003. DOI: 10.1088/1748-0221/3/08/S08003.

[45] Serguei Chatrchyan et al. (CMS Collaboration). *The CMS experiment at the CERN LHC*. JINST 3 (2008) S08004. DOI: 10.1088/1748-0221/3/08/S08004.

[46] Augusto Alves et al. (LHCb Collaboration). *The LHCb detector at the LHC*. JINST 3 (2008) S08005. DOI: 10.1088/1748-0221/3/08/S08005.

[47] Kenneth Aamodt et al. (ALICE Collaboration). *The ALICE experiment at the CERN LHC*. JINST 3 (2008) S08002. DOI: 10.1088/1748-0221/3/08/S08002.

[48] John Jowett. *Colliding heavy ions in the LHC*. In: *Proc. 9th Int. Particle Accelerator Conference (IPAC18)*, Vancouver BC, Canada, April 2018. DOI: 10.18429/JACoW-IPAC2018-TUXGBD2. CERN-ACC-2018-121. CDS: 2648704.

[49] Giorgio Apollinari et al. *High-Luminosity Large Hadron Collider (HL-LHC)*. Technical Design Report. CERN Yellow Reports: Monographs 4 (2017). DOI: 10.23731/CYRM-2017-004. CDS: 2284929.

[50] Andrea Dainese et al. *Physics of the HL-LHC, and perspectives at the HE-LHC*. CERN Yellow Reports: Monographs 7 (2019). DOI: 10.23731/CYRM-2019-007. CDS: 2703572.

[51] Tai Sakuma and Thomas McCauley. *Detector and event visualization with SketchUp at the CMS experiment*. In: *Proc. 20th Int. Conference on Computing in High Energy and Nuclear Physics (CHEP2013)*, Amsterdam, Netherlands, October 2013. J. Phys. Conf. Ser. 513 (2014) 022032. DOI: 10.1088/1742-6596/513/2/022032. ARXIV: 1311.4942 [physics.ins-det].

[52] Ingrid-Maria Gregor and Arno Straessner. *The LHC detectors*. 2015. DOI: 10.1007/978-3-319-15001-7_3. In: Thomas Schörner-Sadenius (editor). *The Large Hadron Collider. Harvest of Run 1*. Springer International Publishing, Cham, Switzerland, 2015.

[53] Albert Sirunyan et al. (CMS Collaboration). *Particle-flow reconstruction and global event description with the CMS detector*. JINST 12 (2017) P10003. DOI: 10.1088/1748-0221/12/10/P10003. ARXIV: 1706.04965 [physics.ins-det].

[54] Aaron Dominguez et al. (CMS Collaboration). *CMS Technical Design Report for the pixel detector upgrade*. CERN, 2012. CMS-TDR-011. CDS: 1481838.

[55] Martin Lipinski (CMS Collaboration). *The Phase-1 upgrade of the CMS pixel detector*. In: *Proc. Int. Conference on Instrumentation for Colliding Beam Physics (INSTR17)*, Novosibirsk, Russia, February 2017. JINST 12 (2017) C07009. DOI: 10.1088/1748-0221/12/07/C07009. CMS-CR-2017-135. CDS: 2265423.

[56] Vardan Khachatryan et al. (CMS Collaboration). *The CMS trigger system*. JINST 12 (2017) P01020. DOI: 10.1088/1748-0221/12/01/P01020. ARXIV: 1609.02366 [physics.ins-det].

[57] Albert Sirunyan et al. (CMS Collaboration). *Pileup mitigation at CMS in* 13 TeV *data*. 2020. ARXIV: 2003.00503 [hep-ex]. Accepted for publication in JINST.

[58] Serguei Chatrchyan et al. (CMS Collaboration). *Description and performance of track and primary-vertex reconstruction with the CMS tracker*. JINST 9 (2014) P10009. DOI: 10.1088/1748-0221/9/10/P10009. ARXIV: 1405.6569 [physics.ins-det].

[59] Georgios Krintiras. Personal communication, April 2017.

[60] CMS Collaboration. *Jet algorithms performance in* 13 TeV *data*. Physics Analysis Summary, CERN, 2017. CMS-PAS-JME-16-003. CDS: 2256875.

[61] Matteo Cacciari, Gavin Salam, and Gregory Soyez. *The catchment area of jets*. JHEP 04 (2008) 005. DOI: 10.1088/1126-6708/2008/04/005. ARXIV: 0802.1188 [hep-ph].

[62] Matteo Cacciari and Gavin Salam. *Pileup subtraction using jet areas*. Phys. Lett. B 659 (2008) 119. DOI: 10.1016/j.physletb.2007.09.077. ARXIV: 0707.1378 [hep-ph].

[63] Vardan Khachatryan et al. (CMS Collaboration). *Jet energy scale and resolution in the CMS experiment in* pp *collisions at* 8 TeV. JINST 12 (2017) P02014. DOI: 10.1088/1748-0221/12/02/P02014. ARXIV: 1607.03663 [hep-ex].

[64] Albert Sirunyan et al. (CMS Collaboration). *Identification of heavy-flavour jets with the CMS detector in pp collisions at* 13 TeV. JINST 13 (2018) P05011. DOI: 10.1088/1748-0221/13/05/P05011. ARXIV: 1712.07158 [physics.ins-det].

[65] Mauro Verzetti (CMS Collaboration). *Machine learning techniques for jet flavour identification at CMS*. In: *Proc. 23rd Int. Conference on Computing in High Energy and Nuclear Physics (CHEP2018)*, Sofia, Bulgaria, July 2018. EPJ Web Conf. 214 (2019) 06010. DOI: 10.1051/epjconf/201921406010.

[66] CMS Collaboration. *CMS Phase 1 heavy flavour identification performance and developments*. Detector Performance Note, CERN, 2017. CMS-DP-2017-013. CDS: 2263802.

[67] Keith Rehermann and Brock Tweedie. *Efficient identification of boosted semileptonic top quarks at the LHC*. JHEP 03 (2011) 059. DOI: 10.1007/JHEP03(2011)059. ARXIV: 1007.2221 [hep-ph].

[68] Albert Sirunyan et al. (CMS Collaboration). *Performance of the CMS muon detector and muon reconstruction with proton-proton collisions at* $\sqrt{s} = 13\,\mathrm{TeV}$. JINST 13 (2018) P06015. DOI: 10.1088/1748-0221/13/06/P06015. ARXIV: 1804.04528 [physics.ins-det].

[69] Vardan Khachatryan et al. (CMS Collaboration). *Performance of electron reconstruction and selection with the CMS detector in proton-proton collisions at* $\sqrt{s} = 8\,\mathrm{TeV}$. JINST 10 (2015) P06005. DOI: 10.1088/1748-0221/10/06/P06005. ARXIV: 1502.02701 [physics.ins-det].

[70] Albert Sirunyan et al. (CMS Collaboration). *Performance of missing transverse momentum reconstruction in proton-proton collisions at* $\sqrt{s} = 13\,\mathrm{TeV}$ *using the CMS detector*. JINST 14 (2019) P07004. DOI: 10.1088/1748-0221/14/07/P07004. ARXIV: 1903.06078 [hep-ex].

[71] Nicholas Metropolis and Stanisław Ulam. *The Monte Carlo method*. J. Am. Stat. Assoc. 44 (1949) 247. DOI: 10.1080/01621459.1949.10483310.

[72] Johan Alwall et al. *The automated computation of tree-level and next-to-leading order differential cross sections, and their matching to parton shower simulations*. JHEP 07 (2014) 079. DOI: 10.1007/JHEP07(2014)079. ARXIV: 1405.0301 [hep-ph].

[73] Simone Alioli et al. *A general framework for implementing NLO calculations in shower Monte Carlo programs: the POWHEG BOX*. JHEP 06 (2010) 043. DOI: 10.1007/JHEP06(2010)043. ARXIV: 1002.2581 [hep-ph].

[74] Heribertus Hartanto et al. *Higgs boson production in association with top quarks in the POWHEG BOX*. Phys. Rev. D 91 (2015) 094003. DOI: 10.1103/PhysRevD.91.094003. ARXIV: 1501.04498 [hep-ph].

[75] Richard Ball et al. (NNPDF Collaboration). *Parton distributions for the LHC run II*. JHEP 04 (2015) 040. DOI: 10.1007/JHEP04(2015)040. ARXIV: 1410.8849 [hep-ph].

[76] Torbjörn Sjöstrand, Stephen Mrenna, and Peter Skands. *A brief introduction to PYTHIA 8.1*. Comput. Phys. Commun. 178 (2008) 852. DOI: 10.1016/j.cpc.2008.01.036. ARXIV: 0710.3820 [hep-ph].

[77] Torbjörn Sjöstrand et al. *An introduction to PYTHIA 8.2*. Comput. Phys. Commun. 191 (2015) 159. DOI: 10.1016/j.cpc.2015.01.024. ARXIV: 1410.3012 [hep-ph].

[78] Rikkert Frederix and Stefano Frixione. *Merging meets matching in MC@NLO*. JHEP 12 (2012) 061. DOI: 10.1007/JHEP12(2012)061. ARXIV: 1209.6215 [hep-ph].

[79] Peter Skands, Stefano Carrazza, and Juan Rojo. *Tuning PYTHIA 8.1: the Monash 2013 tune*. Eur. Phys. J. C 74 (2014) 3024. DOI: 10.1140/epjc/s10052-014-3024-y. ARXIV: 1404.5630 [hep-ph].

[80] Vardan Khachatryan et al. (CMS Collaboration). *Event generator tunes obtained from underlying event and multiparton scattering measurements*. Eur. Phys. J. C 76 (2016) 155. DOI: 10.1140/epjc/s10052-016-3988-x. ARXIV: 1512.00815 [hep-ex].

[81] Albert Sirunyan et al. (CMS Collaboration). *Extraction and validation of a new set of CMS PYTHIA8 tunes from underlying-event measurements*. Eur. Phys. J. C 80 (2020) 4. DOI: 10.1140/epjc/s10052-019-7499-4. ARXIV: 1903.12179 [hep-ex].

[82] CMS Collaboration. *Investigations of the impact of parton shower tuning in Pythia 8 in the modelling of* $t\bar{t}$ *at* $\sqrt{s} = 8$ *and* 13 TeV. Physics Analysis Summary, CERN, 2016. CMS-PAS-TOP-16-021. CDS: 2235192.

[83] Stefano Agostinelli et al. (GEANT4 Collaboration). *GEANT4—a simulation toolkit*. Nucl. Instrum. Meth. A 506 (2003) 250. DOI: 10.1016/S0168-9002(03)01368-8. CERN-IT-2002-003. CDS: 602040.

[84] CMS Collaboration. *Public CMS luminosity information*. CERN TWiki, 2019. URL: https://twiki.cern.ch/CMSPublic/LumiPublicResults (accessed on 08/03/2020).

[85] Michelangelo Mangano. *Motivations and precision targets for an accurate luminosity determination at the LHC*. In: *Proc. LHC Lumi Days: LHC workshop on LHC luminosity calibration*, Geneva, Switzerland, January 2011. CERN-Proceedings-2011-001. CDS: 1357612.

[86] Helmut Burkhardt and Per Grafström. *Absolute luminosity from machine parameters*. Technical Report, CERN, 2007. LHC-PROJECT-Report-1019. CDS: 1056691.

[87] Didier Bédérède et al. *SICAL — a high precision silicon-tungsten luminosity calorimeter for ALEPH*. Nucl. Instrum. Meth. A 365 (1995) 117. DOI: 10.1016/0168-9002(95)00409-2. CERN-PPE-95-017. CDS: 277894.

[88] Tiziano Camporesi et al. *Luminosity measurement in 1994 with the STIC detector*. Technical Report, CERN, 1997. DELPHI-97-8 PHYS 667. CDS: 2629467.

[89] Ian Brock et al. *Luminosity measurement in the L3 detector at LEP*. Nucl. Instrum. Meth. A 381 (1996) 236. DOI: 10.1016/S0168-9002(96)00734-6. CERN-PPE-96-089. CDS: 307585.

[90] Giovanni Abbiendi et al. (OPAL Collaboration). *Precision luminosity for* Z^0 *line shape measurements with a silicon-tungsten calorimeter*. Eur. Phys. J. C 14 (2000) 373. DOI: 10.1007/s100520000353. ARXIV: hep-ex/9910066.

[91] Fernando Abudinén et al. (Belle II Collaboration). *Measurement of the integrated luminosity of the Phase 2 data of the Belle II experiment*. Chin. Phys. C 44 (2020) 021001. DOI: 10.1088/1674-1137/44/2/021001. ARXIV: 1910.05365 [hep-ex].

[92] Medina Ablikim et al. (BESIII Collaboration). *Precision measurement of the integrated luminosity of the data taken by BESIII at center-of-mass energies between* 3.810 GeV *and* 4.600 GeV. Chin. Phys. C 39 (2015) 093001. DOI: 10.1088/1674-1137/39/9/093001. ARXIV: 1503.03408 [hep-ex].

[93] Medina Ablikim et al. (BESIII Collaboration). *Luminosity measurements for the R scan experiment at BESIII*. Chin. Phys. C 41 (2017) 063001. DOI: 10.1088/1674-1137/41/6/063001. ARXIV: 1702.04977 [hep-ex].

[94] Medina Ablikim et al. (BESIII Collaboration). *Measurement of integrated luminosity and center-of-mass energy of data taken by BESIII at* $\sqrt{s} = 2.125$ GeV. Chin. Phys. C 41 (2017) 113001. DOI: 10.1088/1674-1137/41/11/113001. ARXIV: 1705.09722 [hep-ex].

[95] Francisc Aaron et al. (H1 Collaboration). *Determination of the integrated luminosity at HERA using elastic QED Compton events*. Eur. Phys. J. C 72 (2012) 2163. DOI: 10.1140/epjc/s10052-012-2163-2. ARXIV: 1205.2448 [hep-ex]. Erratum: Eur. Phys. J. C 74 (2012) 2733. DOI: 10.1140/epjc/s10052-014-2733-6.

[96] Leszek Adamczyk et al. (ZEUS Collaboration). *Measurement of the luminosity in the ZEUS experiment at HERA II*. Nucl. Instrum. Meth. A 744 (2014) 80. DOI: 10.1016/j.nima.2014.01.053. ARXIV: 1306.1391 [physics.ins-det].

[97] Simon van der Meer. *Calibration of the effective beam height in the ISR*. Technical Report, CERN, 1968. CERN-ISR-PO-68-31. CDS: 296752.

[98] Carlo Rubbia. *Measurement of the luminosity of* $p\bar{p}$ *collider with a (generalized) Van der Meer method*. Technical Report, CERN, 1977. CERN-pp-Note-38. CDS: 1025746.

[99] Per Grafström and Witold Kozanecki. *Luminosity determination at proton colliders*. Prog. Part. Nucl. Phys. 81 (2015) 97. DOI: 10.1016/j.ppnp.2014.11.002.

[100] Ugo Amaldi et al. *Precision measurement of proton-proton total cross section at the CERN Intersecting Storage Rings*. Nucl. Phys. B 145 (1978) 367. DOI: 10.1016/0550-3213(78)90090-1.

[101] Liza Baksay et al. *Measurements of the proton-proton total cross section and small angle elastic scattering at ISR energies*. Nucl. Phys. B 141 (1978) 1. DOI: 10.1016/0550-3213(78)90331-0. Erratum: Nucl. Phys. B 148 (1979) 538. DOI: 10.1016/0550-3213(79)90149-4.

[102] Giovanni Carboni et al. *Precise measurements of proton-antiproton and proton-proton total cross sections at the CERN Intersecting Storage Rings*. Nucl. Phys. B 254 (1985) 697. DOI: 10.1016/0550-3213(85)90242-1. CERN-EP-84-163. CDS: 156499.

[103] Norman Amos et al. *Measurement of small-angle antiproton-proton and proton-proton elastic scattering at the CERN Intersecting Storage Rings*. Nucl. Phys. B 262 (1985) 689. DOI: 10.1016/0550-3213(85)90511-5. CERN-EP-85-94. CDS: 160391.

[104] Corinne Augier et al. (UA4/2 Collaboration). *Measurement of the proton-antiproton total cross section at the* $Sp\bar{p}S$ *by a luminosity dependent method*. Phys. Lett. B 344 (1995) 451. DOI: 10.1016/0370-2693(94)01485-U. CERN-PPE-94-160. CDS: 270586.

[105] Brendan Casey et al. *The DØ Run IIb luminosity measurement*. Nucl. Instrum. Meth. A 698 (2013) 208. DOI: 10.1016/j.nima.2012.08.095. ARXIV: 1204.0461 [hep-ex].

[106] Angelika Drees. *Analysis of Vernier scans during the PP2PP run in 2009* (pp *at* 100 GeV/beam). Technical Report, BNL, 2011. BNL-96818-2011-IR. DOI: 10.2172/1039649.

[107] CMS Collaboration. *CMS luminosity based on pixel cluster counting. Summer 2013 update*. Physics Analysis Summary, CERN, 2013. CMS-PAS-LUM-13-001. CDS: 1598864.

[108] Roel Aaij et al. (LHCb Collaboration). *Precision luminosity measurements at LHCb*. JINST 9 (2014) P12005. DOI: 10.1088/1748-0221/9/12/P12005. ARXIV: 1410.0149 [hep-ex].

[109] Morad Aaboud et al. (ATLAS Collaboration). *Luminosity determination in* pp *collisions at* $\sqrt{s} = 8$ TeV *using the ATLAS detector at the LHC*. Eur. Phys. J. C 76 (2016) 653. DOI: 10.1140/epjc/s10052-016-4466-1. ARXIV: 1608.03953 [hep-ex].

[110] ALICE Collaboration. *ALICE luminosity determination for* pp *collisions at* $\sqrt{s} =$ 8 TeV. Public Note, CERN, 2017. ALICE-PUBLIC-2017-002. CDS: 2255216.

[111] ALICE Collaboration. *ALICE luminosity determination for* pp *collisions at* $\sqrt{s} = 13\,\text{TeV}$. Public Note, CERN, 2016. ALICE-PUBLIC-2016-002. CDS: 2160174.

[112] ATLAS Collaboration. *Luminosity determination in* pp *collisions at* $\sqrt{s} = 13\,\text{TeV}$ *using the ATLAS detector at the LHC*. Conference Note, CERN, 2019. ATLAS-CONF-2019-021. CDS: 2677054.

[113] Jakob Salfeld-Nebgen and Daniel Marlow. *Data-driven precision luminosity measurements with* Z *bosons at the LHC and HL-LHC*. JINST 13 (2018) P12016. DOI: 10.1088/1748-0221/13/12/P12016. ARXIV: 1806.02184 [hep-ex].

[114] Albert Sirunyan et al. (CMS Collaboration). *The Phase-2 upgrade of the CMS beam radiation, instrumentation, and luminosity detectors*. Conceptual Design Report, CERN, 2020. CMS-NOTE-2019-008. CDS: 2706512.

[115] CMS Collaboration. *CMS luminosity calibration for the* pp *reference run at* $\sqrt{s} = 5.02\,\text{TeV}$. Physics Analysis Summary, CERN, 2016. CMS-PAS-LUM-16-001. CDS: 2235781.

[116] Colin Barschel et al. *Results of the LHC DCCT calibration studies*. Technical Report, CERN, 2012. CERN-ATS-Note-2012-026 PERF. CDS: 1425904.

[117] Gabriel Anders et al. *Study of the relative LHC bunch populations for luminosity calibration*. Technical Report, CERN, 2012. CERN-ATS-Note-2012-028 PERF. CDS: 1427726.

[118] Andrea Alici et al. *Study of the LHC ghost charge and satellite bunches for luminosity calibration*. Technical Report, CERN, 2012. CERN-ATS-Note-2012-029 PERF. CDS: 1427728.

[119] Oleksii Turkot. Personal communication, February 2020.

[120] Witold Kozanecki. *Impact of orbit perturbations on luminosity calibrations*. In: *Proc. LHC Lumi Days 2019*, Prévessin, France, June 2019. URL: https://indico.cern.ch/event/813285/contributions/3406092. In preparation.

[121] Witold Kozanecki, Tatiana Pieloni, and Jorg Wenninger. *Observation of beam-beam deflections with LHC orbit data*. Technical Report, CERN, 2013. CERN-ACC-NOTE-2013-0006. CDS: 1581723.

[122] Anton Babaev (CMS Collaboration). *Beam-dynamic effects at the CMS BRIL van der Meer scans*. In: *Proc. 12th Int. Symposium on Radiation from Relativistic Electrons in Periodic Structures (RREPS17)*, Hamburg, Germany, September 2017. JINST 13 (2018) C03028. DOI: 10.1088/1748-0221/13/03/C03028. CMS-CR-2017-415. CDS: 2304750.

[123] Vladislav Balagura. *Beam-beam correction in vdM scans*. In: *Proc. LHC Lumi Days 2019*, Prévessin, France, June 2019. URL: https://indico.cern.ch/event/813285/contributions/3406102. In preparation.

[124] Tatiana Pieloni and Claudia Tambasco. *Beam-beam effects in Van der Meer scans: COMBI and TRAIN beam-beam corrections*. In: *Proc. LHC Lumi Days 2019*, Prévessin, France, June 2019. URL: https://indico.cern.ch/event/813285/contributions/3406103. In preparation.

[125] Olena Karacheban (CMS Collaboration). *Long-term monitoring of delivered luminosity and calibration stability in the CMS experiment*. In: *Proc. LHC Lumi Days 2019*, Prévessin, France, June 2019. URL: https://indico.cern.ch/event/813285/contributions/3406108.

[126] Marco Zanetti. *Beams scan based absolute normalizaton of the CMS luminosity measurement.* In: *Proc. LHC Lumi Days: LHC workshop on LHC luminosity calibration*, Geneva, Switzerland, January 2011. CERN-Proceedings-2011-001. CDS: 1357856.

[127] Christopher Palmer. Personal communication, May 2019.

[128] Markus Klute, Catherine Medlock, and Jakob Salfeld-Nebgen. *Beam imaging and luminosity calibration.* JINST 12 (2017) 03. DOI: 10.1088/1748-0221/12/03/P03018. ARXIV: 1603.03566 [hep-ex].

[129] Samuel Webb. *Factorisation of beams in van der Meer scans and measurements of the ϕ^*_η distribution of $\mathrm{Z} \to \mathrm{e}^+\mathrm{e}^-$ events in pp collisions at $\sqrt{s} = 8\,\mathrm{TeV}$ with the ATLAS detector.* PhD thesis, University of Manchester, 2015. CERN-THESIS-2015-054. CDS: 2020875.

[130] Mateusz Dyndal (ATLAS & ALICE Collaborations). *Non factorisation in ATLAS and ALICE vdM scans: experience in Run 2, impact on luminosity calibration.* In: *Proc. LHC Lumi Days 2019*, Prévessin, France, June 2019. ATL-DAPR-PROC-2019-002. CDS: 2701733.

[131] Massimiliano Ferro-Luzzi. *Proposal for an absolute luminosity determination in colliding beam experiments using vertex detection of beam-gas interactions.* Nucl. Instrum. Meth. A 553 (2005) 388. DOI: 10.1016/j.nima.2005.07.010. CERN-PH-EP-2005-023. CDS: 844569.

[132] Colin Barschel. *Precision luminosity measurement at LHCb with beam-gas imaging.* PhD thesis, RWTH Aachen University, 2014. CERN-THESIS-2013-301. CDS: 1693671.

[133] Paul Bromiley. *Products and convolutions of Gaussian probability density functions.* Technical Report, University of Manchester, 2003. Updated in June 2018. TINA-Memo-2003-003. URL: http://www.tina-vision.net/docs/memos/2003-003.pdf.

[134] André Parent, Michel Morin, and Pierre Lavigne. *Propagation of super-Gaussian field distributions.* Opt. Quant. Electron. 24 (1992) S1071. DOI: 10.1007/BF01588606.

[135] Wouter Verkerke and David Kirkby. *The RooFit toolkit for data modeling.* In: *Proc. Statistical Problems in Particle Physics, Astrophysics and Cosmology (PHYSTAT05)*, Oxford, UK, September 2005. URL: https://www.physics.ox.ac.uk/phystat05/proceedings.

[136] Rafael Molina et al. *Image restoration in astronomy: a Bayesian perspective.* IEEE Signal Proc. Mag. 18 (2001) 2. DOI: 10.1109/79.916318.

[137] CMS Collaboration. *Summaries of CMS cross section measurements.* CERN TWiki, 2020. URL: https://twiki.cern.ch/CMSPublic/PhysicsResultsCombined (accessed on 08/03/2020).

[138] Fumio Abe et al. (CDF Collaboration). *Observation of top quark production in $\mathrm{p\bar{p}}$ collisions with the Collider Detector at Fermilab.* Phys. Rev. Lett. 74 (1995) 2626. DOI: 10.1103/PhysRevLett.74.2626. ARXIV: hep-ex/9503002.

[139] Shahriar Abachi et al. (DØ Collaboration). *Observation of the top quark.* Phys. Rev. Lett. 74 (1995) 2632. DOI: 10.1103/PhysRevLett.74.2632. ARXIV: hep-ex/9503003.

[140] Giuseppe Degrassi et al. *Higgs mass and vacuum stability in the standard model at NNLO.* JHEP 08 (2012) 098. DOI: 10.1007/JHEP08(2012)098. ARXIV: 1205.6497 [hep-ph].

[141] Sergey Alekhin, Abdelhak Djouadi, and Sven-Olaf Moch. *The top quark and Higgs boson masses and the stability of the electroweak vacuum*. Phys. Lett. B 716 (2012) 214. DOI: 10.1016/j.physletb.2012.08.024. ARXIV: 1207.0980 [hep-ph].

[142] Vittorio Del Duca and Eric Laenen. *Top physics at the LHC*. Int. J. Mod. Phys. A 30 (2015) 1530063. DOI: 10.1142/S0217751X1530063X. ARXIV: 1510.06690 [hep-ph].

[143] Andreas Meyer (ATLAS, CDF, CMS & DØ Collaborations). *Top quark properties*. In: *Proc. 27th International Symposium on Lepton Photon Interactions at High Energies*, Ljubljana, Slovenia, August 2015. PoS (LeptonPhoton2015) 028. DOI: 10.22323/1.245.0028. ARXIV: 1511.07172 [hep-ex].

[144] Ulrich Husemann. *Top-quark physics: Status and prospects*. Prog. Part. Nucl. Phys. 95 (2017) 48. DOI: 10.1016/j.ppnp.2017.03.002. ARXIV: 1704.01356 [hep-ex].

[145] Albert Sirunyan et al. (CMS Collaboration). *Measurement of the* $\mathrm{t\bar{t}}$ *production cross section, the top quark mass, and the strong coupling constant using dilepton events in* pp *collisions at* $\sqrt{s} = 13\,\mathrm{TeV}$. Eur. Phys. J. C 79 (2019) 368. DOI: 10.1140/epjc/s10052-019-6863-8. ARXIV: 1812.10505 [hep-ex].

[146] Albert Sirunyan et al. (CMS Collaboration). *Measurements of* $\mathrm{t\bar{t}}$ *differential cross sections in proton-proton collisions at* $\sqrt{s} = 13\,\mathrm{TeV}$ *using events containing two leptons*. JHEP 02 (2019) 149. DOI: 10.1007/JHEP02(2019)149. ARXIV: 1811.06625 [hep-ex].

[147] Albert Sirunyan et al. (CMS Collaboration). *Measurement of* $\mathrm{t\bar{t}}$ *normalised multi-differential cross sections in* pp *collisions at* $\sqrt{s} = 13\,\mathrm{TeV}$*, and simultaneous determination of the strong coupling strength, top quark pole mass, and parton distribution functions*. 2019. ARXIV: 1904.05237 [hep-ex]. Accepted for publication in Eur. Phys. J. C.

[148] Albert Sirunyan et al. (CMS Collaboration). *Measurement of differential cross sections and charge ratios for t-channel single top quark production proton-proton collisions at* $\sqrt{s} = 13\,\mathrm{TeV}$. Eur. Phys. J. C 80 (2020) 370. DOI: 10.1140/epjc/s10052-020-7858-1. ARXIV: 1907.08330 [hep-ex].

[149] Albert Sirunyan et al. (CMS Collaboration). *Measurement of the production cross section for single top quarks in association with* W *bosons in proton-proton collisions at* $\sqrt{s} = 13\,\mathrm{TeV}$. JHEP 10 (2018) 117. DOI: 10.1007/JHEP10(2018)117. ARXIV: 1805.07399 [hep-ex].

[150] Raoul Röntsch and Markus Schulze. *Constraining couplings of top quarks to the* Z *boson in* $\mathrm{t\bar{t}}$+Z *production at the LHC*. JHEP 07 (2014) 091. DOI: 10.1007/JHEP07(2014)091. ARXIV: 1404.1005 [hep-ph]. Erratum: JHEP 09 (2015) 132. DOI: 10.1007/JHEP09(2015)132.

[151] Raoul Röntsch and Markus Schulze. *Constraining the top-*Z *coupling through* $\mathrm{t\bar{t}Z}$ *production at the LHC*. In: *Proc. 37th International Conference on High Energy Physics (ICHEP14)*, Valencia, Spain, July 2014. Nucl. Part. Phys. Proc. 273-275 (2016) 2311. DOI: 10.1016/j.nuclphysbps.2015.09.377.

[152] Raoul Röntsch and Markus Schulze. *Probing top-*Z *dipole moments at the LHC and ILC*. JHEP 08 (2015) 044. DOI: 10.1007/JHEP08(2015)044. ARXIV: 1501.05939 [hep-ph].

[153] Olga Bessidskaia Bylund et al. *Probing top quark neutral couplings in the standard model effective field theory at NLO in QCD*. JHEP 05 (2016) 052. DOI: 10.1007/JHEP05(2016)052. ARXIV: 1601.08193 [hep-ph].

[154] Markus Schulze and Yotam Soreq. *Pinning down electroweak dipole operators of the top quark*. Eur. Phys. J. C 76 (2016) 466. DOI: 10.1140/epjc/s10052-016-4263-x. ARXIV: 1603.08911 [hep-ph].

[155] Fabio Maltoni, Eleni Vryonidou, and Cen Zhang. *Higgs production in association with a top-antitop pair in the standard model effective field theory at NLO in QCD*. JHEP 10 (2016) 123. DOI: 10.1007/JHEP10(2016)123. ARXIV: 1607.05330 [hep-ph].

[156] Timo Aaltonen et al. (CDF Collaboration). *Evidence for* $\mathrm{t\bar{t}}\gamma$ *production and measurement of* $\sigma_{\mathrm{t\bar{t}}\gamma}/\sigma_{\mathrm{t\bar{t}}}$. Phys. Rev. D 84 (2011) 031104. DOI: 10.1103/PhysRevD.84.031104. ARXIV: 1106.3970 [hep-ex].

[157] Georges Aad et al. (ATLAS Collaboration). *Observation of top-quark pair production in association with a photon and measurement of the* $\mathrm{t\bar{t}}\gamma$ *production cross section in* pp *collisions at* $\sqrt{s} = 7\,\mathrm{TeV}$ *using the ATLAS detector*. Phys. Rev. D 91 (2015) 072007. DOI: 10.1103/PhysRevD.91.072007. ARXIV: 1502.00586 [hep-ex].

[158] Morad Aaboud et al. (ATLAS Collaboration). *Measurements of inclusive and differential fiducial cross-sections of* $\mathrm{t\bar{t}}\gamma$ *production in leptonic final states at* $\sqrt{s} = 13\,\mathrm{TeV}$ *in ATLAS*. Eur. Phys. J. C 79 (2019) 382. DOI: 10.1140/epjc/s10052-019-6849-6. ARXIV: 1812.01697 [hep-ex].

[159] Georges Aad et al. (ATLAS Collaboration). *Measurements of inclusive and differential cross-sections of combined* $\mathrm{t\bar{t}}\gamma$ *and* $\mathrm{tW}\gamma$ *production in the* $\mathrm{e}\mu$ *channel at* 13 TeV *with the ATLAS detector*. 2020. ARXIV: 2007.06946 [hep-ex]. Submitted to JHEP.

[160] Albert Sirunyan et al. (CMS Collaboration). *Observation of* $\mathrm{t\bar{t}H}$ *production*. Phys. Rev. Lett. 120 (2018) 231801. DOI: 10.1103/PhysRevLett.120.231801. ARXIV: 1804.02610 [hep-ex].

[161] Morad Aaboud et al. (ATLAS Collaboration). *Observation of Higgs boson production in association with a top quark pair at the LHC with the ATLAS detector*. Phys. Lett. B 784 (2018) 173. DOI: 10.1016/j.physletb.2018.07.035. ARXIV: 1806.00425 [hep-ex].

[162] Georges Aad et al. (ATLAS Collaboration). *Measurement of the* $\mathrm{t\bar{t}W}$ *and* $\mathrm{t\bar{t}Z}$ *production cross sections in* pp *collisions at* $\sqrt{s} = 8\,\mathrm{TeV}$ *with the ATLAS detector*. JHEP 11 (2015) 172. DOI: 10.1007/JHEP11(2015)172. ARXIV: 1509.05276 [hep-ex].

[163] Vardan Khachatryan et al. (CMS Collaboration). *Observation of top quark pairs produced in association with a vector boson in* pp *collisions at* $\sqrt{s} = 8\,\mathrm{TeV}$. JHEP 01 (2016) 096. DOI: 10.1007/JHEP01(2016)096. ARXIV: 1510.01131 [hep-ex].

[164] Morad Aaboud et al. (ATLAS Collaboration). *Measurement of the* $\mathrm{t\bar{t}Z}$ *and* $\mathrm{t\bar{t}W}$ *production cross sections in multilepton final states using* $3.2\,\mathrm{fb}^{-1}$ *of* pp *collisions at* $\sqrt{s} = 13\,\mathrm{TeV}$ *with the ATLAS detector*. Eur. Phys. J. C 77 (2017) 40. DOI: 10.1140/epjc/s10052-016-4574-y. ARXIV: 1609.01599 [hep-ex].

[165] Albert Sirunyan et al. (CMS Collaboration). *Measurement of the cross section for top quark pair production in association with a* W *or* Z *boson in proton-proton collisions at* $\sqrt{s} = 13\,\mathrm{TeV}$. JHEP 08 (2018) 011. DOI: 10.1007/JHEP08(2018)011. ARXIV: 1711.02547 [hep-ex].

[166] Morad Aaboud et al. (ATLAS Collaboration). *Measurement of the* $\mathrm{t\bar{t}Z}$ *and* $\mathrm{t\bar{t}W}$ *cross sections in proton-proton collisions at* $\sqrt{s} = 13\,\mathrm{TeV}$ *with the ATLAS detector*. Phys. Rev. D 99 (2019) 072009. DOI: 10.1103/PhysRevD.99.072009. ARXIV: 1901.03584 [hep-ex].

[167] Giuseppe Bevilacqua et al. *Towards constraining dark matter at the LHC: Higher order QCD predictions for* $\mathrm{t\bar{t}} + \mathrm{Z}$ $(\mathrm{Z} \to \nu_\ell \bar{\nu}_\ell)$. JHEP 11 (2019) 001. DOI: 10.1007/JHEP11(2019)001. ARXIV: 1907.09359 [hep-ph].

[168] Celine Degrande et al. *Single-top associated production with a* Z *or* H *boson at the LHC: the SMEFT interpretation.* JHEP 10 (2018) 005. DOI: 10.1007/JHEP10(2018)005. ARXIV: 1804.07773 [hep-ph].

[169] Fabio Maltoni, Luca Mantani, and Ken Mimasu. *Top-quark electroweak interactions at high energy.* JHEP 10 (2019) 004. DOI: 10.1007/JHEP10(2019)004. ARXIV: 1904.05637 [hep-ph].

[170] Albert Sirunyan et al. (CMS Collaboration). *Evidence for the associated production of a single top quark and a photon in proton-proton collisions at* $\sqrt{s} = 13\,\mathrm{TeV}$. Phys. Rev. Lett. 121 (2018) 221802. DOI: 10.1103/PhysRevLett.121.221802. ARXIV: 1808.02913 [hep-ex].

[171] Albert Sirunyan et al. (CMS Collaboration). *Search for associated production of a Higgs boson and a single top quark in proton-proton collisions at* $\sqrt{s} = 13\,\mathrm{TeV}$. Phys. Rev. D 99 (2019) 092005. DOI: 10.1103/PhysRevD.99.092005. ARXIV: 1811.09696 [hep-ex].

[172] Albert Sirunyan et al. (CMS Collaboration). *Observation of single top quark production in association with a* Z *boson in proton-proton collisions at* $\sqrt{s} = 13\,\mathrm{TeV}$. Phys. Rev. Lett. 122 (2019) 132003. DOI: 10.1103/PhysRevLett.122.132003. ARXIV: 1812.05900 [hep-ex].

[173] Georges Aad et al. (ATLAS Collaboration). *Observation of the associated production of a top quark and a* Z *boson in* pp *collisions at* $\sqrt{s} = 13\,\mathrm{TeV}$ *with the ATLAS detector.* JHEP 07 (2020) 124. DOI: 10.1007/JHEP07(2020)124. ARXIV: 2002.07546 [hep-ex].

[174] Morad Aaboud et al. (ATLAS Collaboration). *Search for four-top-quark production in the single-lepton and opposite-sign dilepton final states in* pp *collisions at* $\sqrt{s} = 13\,\mathrm{TeV}$ *with the ATLAS detector.* Phys. Rev. D 99 (2019) 052009. DOI: 10.1103/PhysRevD.99.052009. ARXIV: 1811.02305 [hep-ex].

[175] Albert Sirunyan et al. (CMS Collaboration). *Search for the production of four top quarks in the single-lepton and opposite-sign dilepton final states in proton-proton collisions at* $\sqrt{s} = 13\,\mathrm{TeV}$. JHEP 11 (2019) 082. DOI: 10.1007/JHEP11(2019)082. ARXIV: 1906.02805 [hep-ex].

[176] Albert Sirunyan et al. (CMS Collaboration). *Search for production of four top quarks in final states with same-sign or multiple leptons in proton-proton collisions at* $\sqrt{s} = 13\,\mathrm{TeV}$. Eur. Phys. J. C 80 (2020) 75. DOI: 10.1140/epjc/s10052-019-7593-7. ARXIV: 1908.06463 [hep-ex].

[177] Juan Aguilar-Saavedra et al. *Interpreting top-quark LHC measurements in the standard-model effective field theory.* LHCTopWG note, CERN, 2018. CERN-LPCC-2018-01. ARXIV: 1802.07237 [hep-ph]. CDS: 2305783.

[178] Nathan Hartland et al. *A Monte Carlo global analysis of the standard model effective field theory: the top quark sector.* JHEP 04 (2019) 100. DOI: 10.1007/JHEP04(2019)100. ARXIV: 1901.05965 [hep-ph].

[179] Achilleas Lazopoulos, Kirill Melnikov, and Frank Petriello. *NLO QCD corrections to the production of* $\mathrm{t\bar{t}Z}$ *in gluon fusion.* Phys. Rev. D 77 (2008) 034021. DOI: 10.1103/PhysRevD.77.034021. ARXIV: 0709.4044 [hep-ph].

[180] Achilleas Lazopoulos et al. *Next-to-leading order QCD corrections to* $t\bar{t}Z$ *production at the LHC*. Phys. Lett. B 666 (2008) 62. DOI: 10.1016/j.physletb.2008.06.073. ARXIV: 0804.2220 [hep-ph].

[181] Adam Kardos, Zoltán Trócsányi, and Costas Papadopoulos. *Top quark pair production in association with a Z-boson at next-to-leading-order accuracy*. Phys. Rev. D 85 (2012) 054015. DOI: 10.1103/PhysRevD.85.054015. ARXIV: 1111.0610 [hep-ph].

[182] Maria-Vittoria Garzelli et al. $t\bar{t}W^{\pm} + t\bar{t}Z$ *hadroproduction at NLO accuracy in QCD with parton shower and hadronization effects*. JHEP 11 (2012) 056. DOI: 10.1007/JHEP11(2012)056. ARXIV: 1208.2665 [hep-ph].

[183] Fabio Maltoni, Davide Pagani, and Ioannis Tsinikos. *Associated production of a top-quark pair with vector bosons at NLO in QCD: impact on* $t\bar{t}H$ *searches at the LHC*. JHEP 02 (2016) 113. DOI: 10.1007/JHEP02(2016)113. ARXIV: 1507.05640 [hep-ph].

[184] Stefano Frixione et al. *Electroweak and QCD corrections to top-pair hadroproduction in association with heavy bosons*. JHEP 06 (2015) 184. DOI: 10.1007/JHEP06(2015)184. ARXIV: 1504.03446 [hep-ph].

[185] Rikkert Frederix et al. *The automation of next-to-leading order electroweak calculations*. JHEP 07 (2018) 185. DOI: 10.1007/JHEP07(2018)185. ARXIV: 1804.10017 [hep-ph].

[186] Alessandro Broggio et al. *Associated production of a top pair and a Z boson at the LHC to NNLL accuracy*. JHEP 04 (2017) 105. DOI: 10.1007/JHEP04(2017)105. ARXIV: 1702.00800 [hep-ph].

[187] Alessandro Broggio et al. *Top-quark pair hadroproduction in association with a heavy boson at NLO+NNLL including EW corrections*. JHEP 08 (2019) 039. DOI: 10.1007/JHEP08(2019)039. ARXIV: 1907.04343 [hep-ph].

[188] Anna Kulesza et al. *Associated production of a top quark pair with a heavy electroweak gauge boson at NLO+NNLL accuracy*. Eur. Phys. J. C 79 (2019) 249. DOI: 10.1140/epjc/s10052-019-6746-z. ARXIV: 1812.08622 [hep-ph].

[189] Anna Kulesza et al. *Associated top-pair production with a heavy boson production through NLO+NNLL accuracy at the LHC*. In: *Proc. 54th Rencontres de Moriond, QCD and High Energy Interactions*, La Thuile, Italy, March 2019. ARXIV: 1905.07815 [hep-ph].

[190] Anna Kulesza et al. *Associated top quark pair production with a heavy boson: differential cross sections at NLO+NNLL accuracy*. Eur. Phys. J. C 80 (2020) 428. DOI: 10.1140/epjc/s10052-020-7987-6. ARXIV: 2001.03031 [hep-ph].

[191] ATLAS Collaboration. *Search for* $t\bar{t}Z$ *production in the three lepton final state with* $4.7\,\text{fb}^{-1}$ *of* $\sqrt{s} = 7\,\text{TeV}$ pp *collision data collected by the ATLAS detector*. Conference Note, CERN, 2012. ATLAS-CONF-2012-126. CDS: 1474643.

[192] Serguei Chatrchyan et al. (CMS Collaboration). *Measurement of associated production of vector bosons and top quark-antiquark pairs in* pp *collisions at* $\sqrt{s} = 7\,\text{TeV}$. Phys. Rev. Lett. 110 (2013) 172002. DOI: 10.1103/PhysRevLett.110.172002. ARXIV: 1303.3239 [hep-ex].

[193] Byron Roe et al. *Boosted decision trees as an alternative to artificial neural networks for particle identification*. Nucl. Instrum. Meth. A 543 (2005) 577. DOI: 10.1016/j.nima.2004.12.018. ARXIV: physics/0408124 [physics.data-an].

[194] Marie Reinecke. *A measurement of the cross section of* $\mathrm{t\bar{t}Z}$ *with two neutrinos in the final state at* 13 TeV *with the ATLAS detector*. Master's thesis, University of Göttingen, 2018. `II.Physik-UniGö-MSc-2018/02`. URL: `https://www.uni-goettingen.de/de/document/download/7bcdd38a90b86825d45ab442d0ca931a.pdf/MSc_Reinecke_Marie.pdf`.

[195] Jan van der Linden. *Limit on* $\mathrm{t\bar{t}} + \mathrm{Z}$ *production in the* $\mathrm{Z} \rightarrow \mathrm{b\bar{b}}$ *channel at the CMS experiment*. Master's thesis, Karlsruhe Institute of Technology, 2019. `CERN-THESIS-2019-234`. CDS: 2703587.

[196] Albert Sirunyan et al. (CMS Collaboration). *Measurement of the inelastic proton-proton cross section at* $\sqrt{s} = 13\,\mathrm{TeV}$. JHEP 07 (2018) 161. DOI: `10.1007/JHEP07(2018)161`. ARXIV: `1802.02613 [hep-ex]`.

[197] Albert Sirunyan et al. (CMS Collaboration). *Evidence for associated production of a Higgs boson with a top quark pair in final states with electrons, muons, and hadronically decaying* τ *leptons at* $\sqrt{s} = 13\,\mathrm{TeV}$. JHEP 08 (2018) 066. DOI: `10.1007/JHEP08(2018)066`. ARXIV: `1803.05485 [hep-ex]`.

[198] CMS Collaboration. *Measurement of the associated production of a Higgs boson with a top quark pair in final states with electrons, muons and hadronically decaying* τ *leptons in data recorded in 2017 at* $\sqrt{s} = 13\,\mathrm{TeV}$. Physics Analysis Summary, CERN, 2018. `CMS-PAS-HIG-18-019`. CDS: 2649199.

[199] Andreas Höcker et al. *TMVA – Toolkit for multivariate data analysis*. Technical Report, CERN, 2007. `CERN-OPEN-2007-007`. ARXIV: `physics/0703039 [physics.data-an]`. CDS: 1019880.

[200] John Campbell, Keith Ellis, and Raoul Röntsch. *Single top production in association with a* Z *boson at the LHC*. Phys. Rev. D 87 (2013) 114006. DOI: `10.1103/PhysRevD.87.114006`. ARXIV: `1302.3856 [hep-ph]`.

[201] Albert Sirunyan et al. (CMS Collaboration). *Measurements of the* $\mathrm{pp} \rightarrow \mathrm{WZ}$ *inclusive and differential production cross sections and constraints on charged anomalous triple gauge couplings at* $\sqrt{s} = 13\,\mathrm{TeV}$. JHEP 04 (2019) 122. DOI: `10.1007/JHEP04(2019)122`. ARXIV: `1901.03428 [hep-ex]`.

[202] Albert Sirunyan et al. (CMS Collaboration). *Measurement of differential cross sections for* Z *boson pair production in association with jets at* $\sqrt{s} = 8$ *and* 13 TeV. Phys. Lett. B 789 (2019) 19. DOI: `10.1016/j.physletb.2018.11.007`. ARXIV: `1806.11073 [hep-ex]`.

[203] Serguei Chatrchyan et al. (CMS Collaboration). *Measurement of the cross section and angular correlations for associated production of a* Z *boson with* b *hadrons in* pp *collisions at* $\sqrt{s} = 7\,\mathrm{TeV}$. JHEP 12 (2013) 039. DOI: `10.1007/JHEP12(2013)039`. ARXIV: `1310.1349 [hep-ex]`.

[204] Vardan Khachatryan et al. (CMS Collaboration). *Search for new physics in same-sign dilepton events in proton-proton collisions at* $\sqrt{s} = 13\,\mathrm{TeV}$. Eur. Phys. J. C 76 (2016) 439. DOI: `10.1140/epjc/s10052-016-4261-z`. ARXIV: `1605.03171 [hep-ex]`.

[205] Dao Thi Nhung, Le Duc Ninh, and Marcus Weber. *NLO corrections to* WWZ *production at the LHC*. JHEP 12 (2013) 096. DOI: `10.1007/JHEP12(2013)096`. ARXIV: `1307.7403 [hep-ph]`.

[206] Vardan Khachatryan et al. (CMS Collaboration). *Measurement of the* Zγ *production cross section in* pp *collisions at* 8 TeV *and search for anomalous triple gauge boson couplings*. JHEP 04 (2015) 164. DOI: 10.1007/JHEP04(2015)164. ARXIV: 1502.05664 [hep-ex].

[207] Vardan Khachatryan et al. (CMS Collaboration). *Measurement of the cross section for electroweak production of* Zγ *in association with two jets and constraints on anomalous quartic gauge couplings in proton-proton collisions at* $\sqrt{s} = 8$ TeV. Phys. Lett. B 770 (2017) 380. DOI: 10.1016/j.physletb.2017.04.071. ARXIV: 1702.03025 [hep-ex].

[208] Morad Aaboud et al. (ATLAS Collaboration). *Measurement of the inelastic proton-proton cross section at* $\sqrt{s} = 13$ TeV *with the ATLAS detector at the LHC*. Phys. Rev. Lett. 117 (2016) 182002. DOI: 10.1103/PhysRevLett.117.182002. ARXIV: 1606.02625 [hep-ex].

[209] Matteo Cacciari et al. *The* $\mathrm{t\bar{t}}$ *cross section at* 1.8 *and* 1.96 TeV: *a study of the systematics due to parton densities and scale dependence*. JHEP 04 (2004) 068. DOI: 10.1088/1126-6708/2004/04/068. ARXIV: hep-ph/0303085.

[210] Stefano Catani et al. *Soft-gluon resummation for Higgs boson production at hadron colliders*. JHEP 07 (2003) 028. DOI: 10.1088/1126-6708/2003/07/028. ARXIV: hep-ph/0306211.

[211] Jon Butterworth et al. *PDF4LHC recommendations for LHC Run II*. J. Phys. G 43 (2016) 023001. DOI: 10.1088/0954-3899/43/2/023001. ARXIV: 1510.03865 [hep-ph].

[212] Spyros Argyropoulos and Torbjörn Sjöstrand. *Effects of color reconnection on* $\mathrm{t\bar{t}}$ *final states at the LHC*. JHEP 11 (2014) 043. DOI: 10.1007/JHEP11(2014)043. ARXIV: 1407.6653 [hep-ph].

[213] Jesper Christiansen and Peter Skands. *String formation beyong leading colour*. JHEP 08 (2015) 003. DOI: 10.1007/JHEP08(2015)003. ARXIV: 1505.01681 [hep-ph].

[214] Thomas Junk. *Confidence level computation for combining searches with small statistics*. Nucl. Instrum. Meth. A 434 (1999) 435. DOI: 10.1016/S0168-9002(99)00498-2. ARXIV: hep-ex/9902006.

[215] Alexander Read. *Presentation of search results: the* CL_s *technique*. In: *Proc. Advanced Statistical Techniques in Particle Physics*, Durham, UK, March 2002. J. Phys. G 28 (2002) 2693. DOI: 10.1088/0954-3899/28/10/313. URL: http://www.ippp.dur.ac.uk/Workshops/02/statistics/proceedings/read.pdf.

[216] ATLAS & CMS Collaborations & LHC Higgs Combination Group. *Procedure for the LHC Higgs boson search combination in Summer 2011*. Technical Report, CERN, 2011. ATL-PHY-PUB-2011-011. CMS-NOTE-2011-005. CDS: 1379837.

[217] Glen Cowan et al. *Asymptotic formulae for likelihood-based tests of new physics*. Eur. Phys. J. C 71 (2011) 1554. DOI: 10.1140/epjc/s10052-011-1554-0. ARXIV: 1007.1727 [physics.data-an]. Erratum: Eur. Phys. J. C 73 (2013) 2501. DOI: 10.1140/epjc/s10052-013-2501-z.

[218] Glen Cowan. *Statistical data analysis*. Clarendon Press, Oxford, UK, 1998.

[219] Stefan Schmitt. *TUnfold, an algorithm for correcting migration effects in high energy physics*. JINST 7 (2012) T10003. DOI: 10.1088/1748-0221/7/10/T10003. ARXIV: 1205.6201 [physics.data-an].

[220] Daniel de Florian et al. (LHC Higgs Cross Section Working Group). *Handbook of LHC Higgs cross sections: 4. Deciphering the nature of the Higgs sector*. CERN Yellow Reports: Monographs 2 (2017). DOI: 10.23731/CYRM-2017-002. ARXIV: 1610.07922 [hep-ph].

[221] CMS Collaboration. *Higgs boson production in association with top quarks in final states with electrons, muons, and hadronically decaying tau leptons at* $\sqrt{s} = 13\,\text{TeV}$. Physics Analysis Summary, CERN, 2020. CMS-PAS-HIG-19-008. CDS: 2725523.

[222] Olga Bessidskaia Bylund. *Top quark and heavy vector boson associated production at the ATLAS experiment: Modelling, measurements and effective field theory*. PhD thesis, Stockholm University, 2017. URL: http://www.diva-portal.org/smash/record.jsf?pid=diva2%3A1142616.

[223] Braden Abbott et al. (DØ Collaboration). *Direct measurement of the top quark mass by the DØ Collaboration*. Phys. Rev. D 58 (1998) 052001. DOI: 10.1103/PhysRevD.58.052001. ARXIV: hep-ex/9801025.

[224] Jiří Kvita. *Study of methods of resolved top quark reconstruction in semileptonic* $\mathrm{t\bar{t}}$ *decay*. Nucl. Instrum. Meth. A 900 (2018) 84. DOI: 10.1016/j.nima.2018.05.059. ARXIV: 1806.05463 [hep-ex].

[225] Jorgen D'Hondt et al. *Fitting of event topologies with external kinematic constraints in CMS*. Technical Report, CERN, 2006. CMS-NOTE-2006-023. CDS: 926540.

[226] Albert Sirunyan et al. (CMS Collaboration). *Measurement of the top quark mass in the all-jets final state at* $\sqrt{s} = 13\,\text{TeV}$ *and combination with the lepton+jets channel*. Eur. Phys. J. C 79 (2019) 313. DOI: 10.1140/epjc/s10052-019-6788-2. ARXIV: 1812.10534 [hep-ex].

[227] Melanie Eich. *Kinematic fits in* $\mathrm{t\bar{t}}$ *resonance searches*. Master's thesis, University of Hamburg, 2017. URL: http://www.iexp.uni-hamburg.de/groups/pd/contents/index/index-132.html?q=theses/kinematic-fits-tbart-resonance-searches.

[228] David Phillips. *A technique for the numerical solution of certain integral equations of the first kind*. J. ACM 9 (1962) 84. DOI: 10.1145/321105.321114.

[229] Andrei Tikhonov. *On the solution of ill-posed problems and the method of regularization*. Dokl. Akad. Nauk SSSR 151 (1963) 3.

[230] Stefan Schmitt. *Data unfolding methods in high energy physics*. In: *Proc. 12th Conference on Quark Confinement and the Hadron Spectrum (Confinement XII)*, Thessaloniki, Greece, August 2016. EPJ Web Conf. 137 (2017) 11008. DOI: 10.1051/epjconf/201713711008. ARXIV: 1611.01927 [physics.data-an].

[231] CMS Collaboration. *Anomalous couplings in the* $\mathrm{t\bar{t}} + \mathrm{Z}$ *final state at the HL-LHC*. Physics Analysis Summary, CERN, 2018. CMS-PAS-FTR-18-036. CDS: 2652018.

[232] Regina Demina, Amnon Harel, and Douglas Orbaker. *Reconstructing* $\mathrm{t\bar{t}}$ *events with one lost jet*. Nucl. Instrum. Meth. A 788 (2015) 128. DOI: 10.1016/j.nima.2015.03.069. ARXIV: 1310.3263 [hep-ex].

[233] Albert Sirunyan et al. (CMS Collaboration). *Measurement of the top quark Yukawa coupling from* $\mathrm{t\bar{t}}$ *kinematic distributions in the lepton+jets final state in proton-proton collisions at* $\sqrt{s} = 13\,\text{TeV}$. Phys. Rev. D 100 (2019) 072007. DOI: 10.1103/PhysRevD.100.072007. ARXIV: 1907.01590 [hep-ex].

[234] Burton Betchart, Regina Demina, and Amnon Harel. *Analytic solutions for neutrino momenta in decay of top quarks*. Nucl. Instrum. Meth. A 736 (2014) 169. DOI: 10.1016/j.nima.2013.10.039. arXiv: 1305.1878 [hep-ph].

[235] Albert Sirunyan et al. (CMS Collaboration). *Search for heavy Higgs bosons decaying to a top quark pair in proton-proton collisions at* $\sqrt{s} = 13\,\text{TeV}$. 2020. DOI: 10.1007/JHEP04(2020)171. arXiv: 1908.01115 [hep-ex].

[236] Marcel Vos et al. *Top physics at high-energy lepton colliders*. Workshop summary, Instituto de Física Corpuscular, 2016. IFIC-16-12. arXiv: 1604.08122 [hep-ex].